



**MILITARY APPLICATIONS OF  
HIGH-ALTITUDE SATELLITE ORBITS IN A  
MULTI-BODY DYNAMICAL ENVIRONMENT  
USING NUMERICAL METHODS AND  
DYNAMICAL SYSTEMS THEORY**

THESIS

Meredith M. Wilmer, 2d Lt, USAF  
AFIT-ENY-MS-16-M-247

**DEPARTMENT OF THE AIR FORCE  
AIR UNIVERSITY**

***AIR FORCE INSTITUTE OF TECHNOLOGY***

**Wright-Patterson Air Force Base, Ohio**

DISTRIBUTION STATEMENT A  
APPROVED FOR PUBLIC RELEASE; DISTRIBUTION UNLIMITED

The views expressed in this document are those of the author and do not reflect the official policy or position of the United States Air Force, the United States Department of Defense or the United States Government. This material is declared a work of the U.S. Government and is not subject to copyright protection in the United States.

AFIT-ENY-MS-16-M-247

MILITARY APPLICATIONS OF HIGH-ALTITUDE SATELLITE ORBITS IN A  
MULTI-BODY DYNAMICAL ENVIRONMENT USING NUMERICAL  
METHODS AND DYNAMICAL SYSTEMS THEORY

THESIS

Presented to the Faculty  
Department of Aeronautics and Astronautics  
Graduate School of Engineering and Management  
Air Force Institute of Technology  
Air University  
Air Education and Training Command  
in Partial Fulfillment of the Requirements for the  
Degree of Master of Science in Astronautical Engineering

Meredith M. Wilmer, B.S.

2d Lt, USAF

March 2016

DISTRIBUTION STATEMENT A  
APPROVED FOR PUBLIC RELEASE; DISTRIBUTION UNLIMITED

AFIT-ENY-MS-16-M-247

MILITARY APPLICATIONS OF HIGH-ALTITUDE SATELLITE ORBITS IN A  
MULTI-BODY DYNAMICAL ENVIRONMENT USING NUMERICAL  
METHODS AND DYNAMICAL SYSTEMS THEORY

THESIS

Meredith M. Wilmer, B.S.  
2d Lt, USAF

Committee Membership:

Maj Christopher D. Geisel, Ph.D.  
Chair

William E. Wiesel, Ph.D.  
Member

Richard G. Cobb, Ph.D.  
Member

Maj Stuart A. Stanton, Ph.D.  
Member

## Abstract

The circular restricted three-body problem (CR3BP) is a simplified dynamical model for a satellite under the gravitational influence of both the Earth and the Moon, maintaining closer fidelity to the gravitational environment experienced by a high-altitude Earth-orbiting spacecraft than modeling in the Earth-satellite two-body problem. Resonant orbit arcs are used to determine an initial guess to input into an algorithm that computes a trajectory solution with specific design requirements and constraints. A test case uses this method to compute a lunar “fly-by” transfer solution requiring less  $\Delta V$  than two-body transfer methods and offers an unusual pathway that adds an “unpredictability” element to the design. Multiple-shooting and pseudo-arclength continuation methods are used to target trajectories and compute periodic orbits in the CR3BP to within a satisfactory tolerance. Invariant manifolds associated with an unstable periodic orbit around a libration point in the Earth-Moon system are used as unpredictable transfer pathways when traveling from one Earth orbit to another, utilizing a map-based design process. Periapsis Poincaré maps are also constructed to characterize the observed behaviors of orbits in the Earth-Moon system for a specified time, demonstrating utility for both designing trajectories with desired end characteristics and predicting an unknown spacecraft’s future behavior. This investigation uses numerical methods and Dynamical Systems Theory concepts that are typically showcased for missions traveling beyond Earth orbits and the Earth-Moon system, and these tools are successfully applied to missions between Earth orbits. All transfers are successfully designed to require similar or less  $\Delta V$  than traditional methods and to offer unpredictable pathways for military utility. In addition to showcasing modern tools for Earth-centric missions, examining problems in a rotating frame and

representing information with Poincaré maps is shown to give valuable visual insight for mission planners. Using a map-based method is also found to present a vast collection of transfer opportunities for mission design.

AFIT-ENY-MS-16-M-247

*“Ad infinitum et ultra.”*

*Bombus Lux-Anno*

## Acknowledgments

First, I would like to express my incredible gratitude to my family. Your support, encouragement, and tail-wagging have made my educational pursuits and career choices possible. And to my other half, I cannot begin to express how grateful I am to have you by my (distant) side.

I would also like to give my sincerest thanks to my adviser, Maj Geisel. Your high expectations, attention to detail, and dedication to your students has been instrumental to our research. It has been an honor to be a member of your first generation of thesis advisees.

Lastly, I'd like to give a special thanks to the other Astrodynamics and Space Applications research group members, 2d Lt Chip Zurita and 1st Lt Scott Biehl. Your feedback and continual patience with me has meant the world to me, and I hope to work with you both again sometime in the future.

Meredith M. Wilmer



# Table of Contents

	Page
Abstract .....	iv
Acknowledgments .....	vi
List of Figures .....	ix
List of Tables .....	xv
1. Introduction .....	1
1.1 Overview .....	1
1.2 Expanding Design Options .....	2
1.3 Motivation from the AsiaSat-3/HGS-1 “Rescue” Mission .....	4
1.4 Military Relevance of High-Altitude Missions and Modeling in a Multi-Body Environment .....	6
1.5 Thesis Problem Statement and Document Overview .....	9
1.5.1 Problem Statement .....	9
1.5.2 Thesis Overview .....	10
1.6 Chapter 1 Summary .....	13
2. Background on the Fundamentals of the CR3BP Using Numerical Methods .....	15
2.1 Historical Overview of Astrodynamics .....	15
2.2 General and Special Perturbations .....	18
2.3 Numerical Integration .....	20
2.4 Simplifying Assumptions of the Circular Restricted Three-Body Problem .....	22
2.4.1 The Two-Body Problem .....	23
2.4.2 The Circular Restricted Three-Body Problem .....	28
2.5 Equations of Motion and Nondimensionalization .....	29
2.6 Coordinate Transformation of Vectors in the Barycentric Rotating Frame to/from the Earth-Centered Inertial Frame of the CR3BP .....	38
2.7 Integral of the Motion .....	43
2.8 Equilibrium Solutions .....	48
2.9 Symmetry Properties .....	55
2.10 Motion Near the Equilibrium Points .....	57
2.11 State Transition Matrix .....	66
2.12 Periodic Orbits .....	69
2.13 Dynamical Systems Theory .....	74
2.14 Invariant Manifolds .....	78

	Page
2.15 Resonant Orbits .....	87
2.16 Poincaré Maps .....	91
2.17 Chapter 2 Summary .....	100
3. Design Methodology and Numerical Tools .....	102
3.1 Targeting Strategies .....	103
3.2 Continuation Methods .....	110
3.3 Periapsis Poincaré Maps .....	119
3.3.1 Periapsis Poincaré Maps Representing Stable and Unstable Invariant Manifold Trajectories .....	121
3.3.2 Periapsis Poincaré Maps Displaying Near-Earth Trajectories .....	121
3.4 Chapter 3 Summary .....	122
4. Test Cases: Results and Analysis .....	124
4.1 Test Case I: “Rescue” Mission .....	125
4.1.1 Test Case I: Analysis .....	138
4.1.2 Test Case I: Contingency Options .....	141
4.2 Test Case II: Planar Orbit Transfer Design .....	147
4.2.1 Test Case II: Analysis .....	162
4.2.2 Test Case II: Contingency Options .....	164
4.3 Test Case III: Periapsis Poincaré Maps for Predicting Behaviors .....	165
4.3.1 Test Case III: Analysis .....	170
4.4 Chapter 4 Summary .....	176
5. Summary, Conclusions, and Future Work .....	179
5.1 Summary .....	179
5.2 The Employment of Numerical Methods and Dynamical Systems Theory Are Essential for Contemporary Mission Design .....	182
5.3 The Barycentric Rotating Frame Gives Significant Insight .....	183
5.4 Specific Solutions Originate from a Vast Collection of Mission Options with Map-Based Design .....	185
5.5 Recommendations for Future Work .....	186
Bibliography .....	193

## List of Figures

Figure		Page
1	Notional Representation of the Six Classical Orbital Elements with Respect to Earth's Equatorial Plane: Right Ascension of the Ascending Node ( $\Omega$ ), Argument of Perigee ( $\omega$ ), Inclination ( $i$ ), True Anomaly ( $\nu$ ), Semi-major Axis ( $a$ ), and Eccentricity Vector (with Magnitude $e$ ). . . . .	26
2	$n$ -Body Problem Setup in Inertial Frame. . . . .	30
3	Three-Body Problem Setup in Inertial Frame. . . . .	32
4	Definition of Barycentric Rotating Frame in CR3BP. . . . .	33
5	Numerically Integrated Spacecraft Trajectory in (a) Barycentric Rotating Frame (Integration time = 7 nondimensional units (about 30 days)), (b) Earth-Centered Inertial Frame (Integration time = 7 nondimensional units (about 30 days)), (c) Barycentric Rotating Frame (Integration time = 32 nondimensional units (about 139 days), and (d) Earth-Centered Inertial Frame (Integration time = 32 nondimensional units (about 139 days)) in CR3BP. . . . .	40
6	Tracking Numerical Error with Jacobi Constant for 7 Nondimensional Units (About 30 days) (Left: Trajectory in Configuration Space, Right: Error Along Trajectory). . . . .	46
7	Tracking Numerical Error with Jacobi Constant for 15 Revolutions of the Primaries (About 1.12 Years) (Left: Trajectory in Configuration Space, Right: Error Along Trajectory). . . . .	47
8	Zoomed View Near Moon Region Showing Impact of Spacecraft Trajectory at 22.32 Nondimensional Time Units (About 95 Days). . . . .	47
9	Earth-Moon CR3BP Libration Point Locations in Barycentric Rotating Frame. . . . .	49

Figure		Page
10	Earth-Moon CR3BP Libration Point Locations in Barycentric Rotating Frame with Associated Distances from the Primaries. ....	50
11	Zero Velocity Curves in Barycentric Rotating Frame of CR3BP for (a) $JC = 3.3 < JC_{L1}$ , (b) $JC = JC_{L1} = 3.188341126426104$ , (c) $JC = 3.179 < JC_{L1}$ , (d) $JC = 3.1 < JC_{L2}$ , (e) $JC = 3.0 < JC_{L3}$ , and (f) $JC = 2.9 < JC_{L45}$ . ....	54
12	Notional Variation of a Nearby Trajectory with Respect to a Reference Trajectory by Isochronous Correspondence. ....	58
13	Notional Variation of a Nearby Trajectory with Respect to a Reference Trajectory by Normal Correspondence (Adapted from Szebehely [1]). ....	70
14	Notional Representation of the Dynamical “Flow” Near a 2-D Saddle Equilibrium Point. ....	79
15	Stable and Unstable Invariant Manifold “Tube” Approximations Associated with Unstable Periodic $L_1$ Lyapunov Orbit in Barycentric Rotating Frame. ....	84
16	Zoomed View of Stable and Unstable Invariant Manifold “Tube” Approximations Associated with Unstable Periodic $L_1$ Lyapunov Orbit in Barycentric Rotating Frame. ....	85
17	Member of Periodic 4:1 Resonant Orbit Family in Barycentric Rotating and Inertial Frames. ....	90
18	Notional Representation of a Poincaré Surface of Section. ....	96
19	Poincaré Map for Earth-Moon System, $JC = 3.1$ , 60 Trajectories Numerically Integrated for 150 Revolutions of the Primaries (About 11 Years). ....	98
20	Periodic Orbit Targeted By Single-Shooting With Initial Guess from Poincaré Map for Earth-Moon System, $JC = 3.1$ , Integration Time = 1.356 nondimensional units (About 6 days). ....	99

Figure		Page
21	Notional Multiple-Shooting Targeting Process with Fixed Initial and Final Positions. ....	108
22	Notional Multiple-Shooting Targeting Process with Forced Continuity in Position and Velocity.....	108
23	Several Members in Planar $L_1$ Lyapunov Orbit Family in Barycentric Rotating Frame. ....	111
24	Planar and Axial Members of Periodic 4:3 Resonant Orbit Family. ....	118
25	Zoomed View of Notional Mission Setup for Initial Geosynchronous Transfer Orbit (GTO) Transfer to Final Geosynchronous Orbit (GEO). ....	126
26	Notional Mission Setup of Earth and Moon Positions for Initial Geosynchronous Transfer Orbit (GTO) Transfer to Final Geosynchronous Orbit (GEO) via Lunar Fly-By. ....	127
27	Planar and Axial Members of Periodic 4:3 Resonant Orbit Family. ....	128
28	Orbit Chosen from Collection of Planar and 3-D 4:3 Resonant Orbit Families to Produce Initial Guess Patch-Points for Multiple-Shooting Algorithm.....	130
29	Orbit Chosen from Collection of Planar and 3-D 4:3 Resonant Orbit Families to Produce Initial Guess Patch-Points for Multiple-Shooting Algorithm in Earth-Centered Inertial Frame. ....	131
30	Converged Spacecraft Trajectory Transferring from Initial GTO to Final GEO via Lunar Fly-by in Barycentric Rotating Frame. ....	133
31	Converged Spacecraft Trajectory Transferring from Initial GTO to Final GEO via Lunar Fly-by in Earth-Centric Inertial Frame (Left: 3-D Inertial View, Right: Inertial x-y View).....	134
32	Osculating Elements of Full Transfer Mission from an Initial Geosynchronous Transfer Orbit (GTO) to Final Geosynchronous Orbit (GEO) via Lunar Fly-By. ....	137

Figure	Page
33	Lunar Fly-by Trajectory Propagated for 5 Revolutions of the Primaries in Barycentric Rotating Frame. .... 142
34	Trajectory Transferring from Initial GTO to Final LEO via Lunar Fly-by in Barycentric Rotating Frame ( $x$ - $y$ view). .... 143
35	Trajectory Transferring from Initial GTO to Final LEO via Lunar Fly-by in Earth-Centered Inertial Frame (Left: 3-D View, Right: $x$ - $y$ view). .... 144
36	Zoomed View of Notional Mission Setup for Transfer from Initial “Tundra” Orbit (green) to Final “GEO” (red), Both in the Plane of the Primaries. .... 148
37	Initial “Tundra” Orbit in Barycentric Rotating Frame of the CR3BP. .... 150
38	Initial “Tundra” Orbit in Earth-Centered Inertial Frame of the CR3BP. .... 150
39	Stable and Unstable Invariant Manifold “Tube” Approximations Associated with Unstable Periodic $L_1$ Lyapunov Orbit in Barycentric Rotating Frame ( $JC = 3.1327$ ). .... 151
40	Zoomed View of $L_1$ Region with Stable and Unstable Invariant Manifold “Tube” Approximations Associated with Unstable Periodic $L_1$ Lyapunov Orbit in Barycentric Rotating Frame ( $JC = 3.1327$ ). .... 152
41	Periapsis Poincaré Map for Stable and Unstable Invariant Manifold Approximations Associated with Unstable Periodic Lyapunov Orbit About Earth-Moon $L_1$ in Barycentric Rotating Frame, $JC = 3.1327$ , 80 Trajectories Numerically Integrated for 300 Revolutions of the Primaries (About 22 Years). .... 153
42	Zoomed View of Periapsis Poincaré Map for Stable and Unstable Invariant Manifold Approximations Associated with Unstable Periodic $L_1$ Lyapunov Orbit in Barycentric Rotating Frame, Showing “Tundra” Altitude Locations, $JC = 3.1327$ , 80 Trajectories Numerically Integrated for 300 Revolutions of the Primaries (About 22 Years). .... 154

Figure	Page
43	Maneuver from Initial “Tundra” Orbit to Stable Manifold Trajectory in Barycentric Rotating Frame. .... 155
44	Zoomed View of Periapsis Poincaré Map for Stable and Unstable Invariant Manifold Approximations Associated with Unstable Periodic $L_1$ Lyapunov Orbit in Barycentric Rotating Frame, Showing “Intersection” Point Location Between Manifold Trajectories (80 Trajectories Numerically Integrated for 300 Revolutions of the Primaries (About 22 Years), $JC = 3.1327$ ). .... 157
45	Zoomed View of Periapsis Poincaré Map for Stable and Unstable Invariant Manifold Approximations Associated with Unstable Periodic $L_1$ Lyapunov Orbit in Barycentric Rotating Frame, Showing “GEO” Altitude Regions, $JC = 3.1327$ , 80 Trajectories Numerically Integrated for 300 Revolutions of the Primaries (About 22 Years). .... 158
47	Full Transfer Plan from Initial “Tundra” Orbit to Final “GEO” Orbit Using Stable and Unstable Manifold Trajectories in Earth-Centered Inertial Frame. .... 159
46	Full Transfer Plan from Initial “Tundra” Orbit to Final “GEO” Orbit Using Stable and Unstable Manifold Trajectories in Barycentric Rotating Frame. .... 160
48	Periapsis Poincaré Map, $JC = 2.95$ , 36 Trajectories Numerically Integrated for 155 Revolutions of the Primaries (About 11.5 Years), Cyan=Trajectories Departing $L_1$ “Gateway,” Green=Trajectories “Bounded” for Integration Time, Blue=Trajectories that Impact Earth. .... 167
49	Zoomed View of Periapsis Poincaré Map, $JC = 2.95$ , 36 Trajectories Numerically Integrated for 155 Revolutions of the Primaries (About 11.5 Years), Cyan=Trajectories Departing $L_1$ “Gateway,” Green=Trajectories “Bounded” for Integration Time, Blue=Trajectories that Impact Earth. .... 168

Figure		Page
50	Periapsis Poincaré Map, $JC = 2.95, 3.0$ , and $3.1$ , 36 Trajectories Numerically Integrated for 15 Revolutions of the Primaries (About 1.12 Years), Cyan=Trajectories Departing $L_1$ “Gateway,” Green=Trajectories “Bounded” for Integration Time, Blue=Trajectories that Impact Earth (Left: Barycentric Rotating Frame, Right: Zoomed View).....	169
51	Periapsis Poincaré Map for 36 Trajectories Numerically Integrated for 15 Revolutions of the Primaries (About 1.12 Years), $JC = 3.15$ , Shown with Example Trajectories Corresponding to Initial Conditions for a (a) Bounded Trajectory, (b) Escape Trajectory Through the $L_1$ “Gateway,” and (c) Impact Trajectory. Cyan=Trajectories Departing $L_1$ “Gateway,” Green=Trajectories “Bounded” for Integration Time, Blue=Trajectories that Impact Earth. ....	170
52	Periapsis Poincaré Map for 36 Trajectories Numerically Integrated for 15 Revolutions of the Primaries, or 1.12 Years ( $JC = 3.15$ and $JC = 3.2$ ), Cyan=Trajectories Departing $L_1$ “Gateway,” Green=Trajectories “Bounded” for Integration Time, Blue=Trajectories that Impact Earth (Left: Barycentric Rotating Frame, Right: Zoomed View).....	171
53	Escape Trajectory Through the $L_1$ “Gateway” in the Barycentric Rotating Frame and Earth-Centered Inertial Frame. ....	173
54	Earth-Moon Periapsis Poincaré Map Showing Possible Structure (a) Barycentric Rotating Frame (b) Zoomed View of Barycentric Rotating Frame ( $JC = 3.17$ , Integration Time = 15 Revolutions of the Primaries), Cyan=Trajectories Departing $L_1$ “Gateway,” Green=Trajectories “Bounded” for Integration Time, Blue=Trajectories that Impact Earth. ....	188



## List of Tables

Table		Page
1	Jacobi Constant Values and Rotating Frame Coordinates of the Equilibrium Points in the Earth-Moon, Sun-Earth, and Equal Primary Mass Systems in the CR3BP .....	52
2	Compared Values for Two-body Calculations, the AsiaSat-3/HGS-1 “Nominal Trajectory” from Ocampo’s Analysis, and the Converged Design Using a Resonant Arc as an Initial Guess for a Multiple-Shooting Scheme. ....	135
3	Times, Altitudes, Inclinations, and Final Maneuver $\Delta V$ Values of Approximate Returns to Inclined “GEO” or LEO by a Lunar Fly-By Transfer Trajectory Propagated for 1.25 Years Since First Maneuver. ....	145
4	Times, Altitudes, Inclinations, and Final Maneuver $\Delta V$ Values of Approximate Returns to LEO by a Lunar Fly-By Transfer Trajectory Propagated for 5 Years Since First Maneuver. ....	146
5	Values for Two-Body Calculations for a Transfer from Planar “Tundra” Orbit to Planar “GEO” as Compared to Design Utilizing Invariant Manifold Trajectories for Transfer .....	161

# MILITARY APPLICATIONS OF HIGH-ALTITUDE SATELLITE ORBITS IN A MULTI-BODY DYNAMICAL ENVIRONMENT USING NUMERICAL METHODS AND DYNAMICAL SYSTEMS THEORY

## 1. Introduction

### 1.1 Overview

Considering orbital transfers, a multi-body dynamical environment, modern numerical algorithms, and unconventional design methods are essential to exploring transfer options with reduced fuel expenditure ( $\Delta V$ ) and favorable, more unpredictable trajectory pathways.

The first chapter in the current investigation lays the groundwork for three specific orbital mission design test cases examining unconventional, high-altitude pathways as a means for transferring from one Earth orbit to another. The first case uses a resonant orbit arc to generate an initial guess for a targeting algorithm that computes a transfer between a highly inclined geosynchronous transfer orbit and a geostationary orbit for less cost (less  $\Delta V$ ) than standard transfer methods. The second case exploits concepts from Dynamical Systems Theory, using visual insight gained from a periapsis Poincaré map to design a transfer between orbits in the Earth-Moon plane. The third test case inspects periapsis Poincaré maps to obtain visual information about the future whereabouts of a spacecraft, aiding in both orbit design and in the prediction of an unknown spacecraft's behavior.

In the following first chapter, a discussion of expanding the available design space is presented, emphasizing the possibility of low- $\Delta V$ , innovative design options deter-

mined by modeling in a multi-body environment, using a variety of numerical tools, and utilizing concepts from Dynamical Systems Theory. An example of a successful real-world scenario is described, motivating the present investigation by exhibiting how using the gravity of the Moon (with two lunar “fly-bys”) led to a transfer between two Earth orbits and required less  $\Delta V$  than standard methods. The military applicability of the tools, procedures, and test cases used in the present investigation is also offered, examining the goals and objectives listed in Department of Defense literature. Finally, a definitive problem statement is listed, specific terminology is defined, and an outline of the remaining chapters is given.

## 1.2 Expanding Design Options

Every day, new scientific discoveries and technological advancements in space systems increase capabilities and potential for progress in space exploration. With the launches of *Sputnik I* in October 1957 and *Explorer I* in January 1958 and the subsequent “Space Race” that ensued between the Soviet Union and United States, there has been a military presence in space, aiming to take advantage of the “ultimate high ground” [2]. Space operations are now a regular military priority, and space mission design—designing the trajectories used to get a spacecraft from one point to another, or a combination thereof—is a vital part of each program. The mission design process is not unlike other military problem solving strategies in that there is a protocol to follow. The Air Force Smart Operations for the 21st Century (AFSO21) program applies to all problem solving associated with the Air Force mission and provides the framework for the 8-Step Problem Solving Model. All steps in the model fall under the categories: “Observe,” “Orient,” “Decide,” and “Act” (also known as Col John Boyd’s OODA Loop [3]) [4]. The fifth step in the process, “develop countermeasures,” is found under “Decide” [4]. This is the step that can bring military mission design to

the next level. The 927th Air Refueling Wing at MacDill Air Force Base gives further guidance on the importance of the fifth step: “Pilots examine all the possibilities for counter measures so they can head the problem off at the pass before it affects their mission...Lay out all of your options so you can examine the possibilities before deciding which one would be best to get you where you want to go” [5]. Applying this model to spaceflight dynamics, a mission designer must fully understand the problem and explore all possibilities for solutions. Simplified information and mission design capability limitations can restrain problem-solvers when it comes to orbital dynamics. Victor G. Szebehely, a remarkable theorist of celestial mechanics, agreed with these thoughts. He began his first book by stating: “The purpose of dynamics is to characterize the totality of possible motions of a given dynamical system” [1]. The U.S. military can benefit from a wider understanding of modern methods in astrodynamics that expand the design space options.

Once in Earth orbit, conventional methods for impulsive maneuvers of a spacecraft are generally both expensive and follow predictable trajectory pathways. However, there are alternative, innovative methods that can be used to transfer a spacecraft from one point to another for similar or potentially less  $\Delta V$  and with less predictable pathways that may be advantageous for military missions. Some spacecraft trajectories in the design problems presented in this investigation may travel to extremely high altitudes, making it necessary to use a higher-fidelity system model that considers gravitational effects beyond what is reflected in analysis of a simple Earth-satellite (two-body) environment. Tools for this type of design have been developed by looking at the motion of, and nearby, different orbits by the means of Dynamical Systems Theory (DST). The main applications of DST are based on the notion of using invariant manifold structures associated with unstable periodic orbits as low-cost (low- $\Delta V$ ) transfer options. Manifolds are examined in the present investigation to transfer from

one potential military mission orbit to another near-Earth orbit. Strategies also include numerical methods such as implementing numerical integration and generating Poincaré maps, exploiting what is known about the equations of motion for the system and displaying available solutions. The present investigation examines multiple scenarios involving spacecraft traveling from one Earth orbit to another in a multi-body environment, as well as characterizing the potential motions in the vicinity of the Earth, basing design on DST strategies and numerical tools.

### 1.3 Motivation from the AsiaSat-3/HGS-1 “Rescue” Mission

Innovative spaceflight projects have emerged in the space community that draw upon the mission design tools based in a multi-body dynamical model, offering a comparison to those projects designed with the standard orbital model involving solely the Earth and a near-Earth satellite. The “rescue” story of AsiaSat-3/HGS-1 offers an inspiring account of how using the gravity of the Moon assisted in placing the satellite in a favorable Earth orbit after a rocket malfunction left it in a highly inclined, highly eccentric, and ultimately unusable orbit. The Hughes Global Services 1 spacecraft HGS-1 (originally AsiaSat-3, as it was built and launched for Asia Satellite Communications Ltd. by Hughes Spacecraft Company) had a fourth stage rocket that was supposed to perform a combined plane change and circularization burn from the spacecraft’s geosynchronous transfer orbit. Unfortunately, the satellite was left in an unusable orbit when the Proton rocket failed to execute the maneuver properly, and mission failure was declared at this point [6]. The total  $\Delta V$  to perform a combined plane change maneuver at apogee was calculated to be 2.42 km/sec. There was not enough propellant on board for such a maneuver, and the best possible orbit produced with the available fuel via conventional trajectory methods was a  $16^\circ$  inclined orbit with unfavorable right ascension of the ascending node, and even then, there would

not be enough fuel left for the necessary stationkeeping [6].

Representatives from Innovative Orbital Design and Microcosm Inc and the Hughes Spacecraft Company Senior Orbital Analyst proposed a “rescue” plan. They wanted to execute an injection maneuver to place the satellite in an orbit that would send it beyond 1.5 million km from the Earth to then travel around the Moon and perform a circularization maneuver as it came back with zero inclination [6]. The nominal transfer time was eight days, and the  $\Delta V$  required was within the spacecraft’s capability at just 1.815 km/sec [6]. Further studies also showed that a second lunar fly-by would lead to a more favorable, lower initial inclination in the final geosynchronous orbit. Advantages of the lunar fly-by option over standard trajectory methods included shorter trip time, near continuous communication, and lower overall  $\Delta V$  cost. The “rescue” mission was declared a success after two lunar fly-bys, achieving a final inclination of  $8^\circ$  and favorable ascending node that decreased inclination to the desired  $0^\circ$  over the next several years [6]. The “rescue” mission designed using a multi-body model was not only a successful mission accomplished, but it was groundbreaking in that the design used an unconventional pathway to complete the same task as a combined plane change and circularization maneuver to end up in the final geostationary orbit, but for much less  $\Delta V$ . This example shows how searching for a solution in an expanded design space may lead to valuable transfer options. A similar example is developed and compared to this mission in Section 4.1, using a design method that utilizes resonant arcs. This “rescue” mission is one of many possible examples where the Moon’s dynamics can be used for Earth-centered orbital operations with favorable  $\Delta V$  values. The following section describes how using the tools and examining the type of scenarios presented in this investigation align with specific military objectives.

## 1.4 Military Relevance of High-Altitude Missions and Modeling in a Multi-Body Environment

The National Research Council's *Continuing Kepler's Quest: Assessing Air Force Space Command's Astrodynamics Standards* explains that satellite systems sometimes experience unpredictable or chaotic behavior, which is expected in nonlinear systems and is reflected in the solutions of the multi-body equations of motion. Given as examples are satellite systems in orbits starting in standard conditions that "experience dissimilar dynamical futures," with diverging predicted and actual orbits, or systems with unexpected variance when predicting collisions [7]. Chaotic behaviors are also seen in satellite systems, and as the distance between the Earth's surface and a spacecraft increases, the more apparent these dynamical behaviors become. Showing spacecraft motion with a two-body model leads to a basic understanding of near-Earth behavior and usually provides a decent fit for the exhibited motion, at least as a reference solution. Additionally, there are Earth's oblateness effects, air drag, as well as other small perturbations to consider to formulate a better model; however, as a spacecraft travels farther from the Earth, starting near geosynchronous orbit altitudes, lunar and solar perturbations become the dominant perturbations on the spacecraft's motion. While its motion near these altitudes may still be modeled with lunar and solar gravitational influences as small perturbations on two-body motion, as the spacecraft moves even further out, its dynamics change drastically, and the gravitational effects of other bodies in the solar system may no longer be modeled as mere perturbations on two-body motion. The two-body model trajectories are no longer sufficient, even as reference solutions. Not only would the motion at higher altitudes not fit well with the two-body model, but the motion actually exhibited may be completely unpredictable if chaos is present [8]. At this point, a transition to a higher-fidelity model is necessary. The circular restricted three-body problem

(CR3BP) introduces a third body into the model, and the resulting dynamics are a more accurate representation of the possible motion for these missions than the standard two-body problem. Unlike the two-body problem (2BP), the CR3BP does not have a known closed-form analytical solution; therefore, alternative methods are explored to better suit the nonlinear dynamics [8]. Justifications for using the CR3BP to expand the design options and implementing numerical tools and DST concepts are documented in the following military literature.

In addition to its correspondence with the OODA/AFSO21 Model, the modern methods for orbital mission design presented in this investigation are supported by the United States Joint Chiefs of Staff *Joint Publication 3-14: Space Operations* (JP3-14) and the United States Air Force Chief Scientist Report *Technology Horizons* [9, 10]. To support the U.S. military’s joint goals of space operations, expanding the design space with a multi-body dynamical environment and applying the methods explored in this investigation directly relate to the contributions detailed in Chapter II of JP3-14, entitled *Space Mission Areas* [9]. Specifically applicable are the functional capabilities listed under Section B: *Space Force Enhancement*, particularly environmental monitoring, and in Section C: *Space Support*, markedly under satellite operations and maneuvering.

Operating in a higher-altitude environment and choosing trajectories that visit other bodies and locations in the Earth-Moon and Sun-Earth systems allow extensive and unique opportunities for environmental monitoring as mentioned in Section B of JP3–14 [9]. Just a few areas include monitoring and sampling of the near-Earth space environment and magnetosphere, the Earth environment’s interaction with the solar wind, the solar wind in the outer space environment, and regions near celestial bodies like the Sun, Moon, and Earth. Satellite operations and maneuvering as described in Section C are supported by this investigation as the opportunity is explored for



lower- $\Delta V$  transfers from one point in the solar system to another (as demonstrated by the AsiaSat-3/HGS-1 mission), theoretically “free” (zero- $\Delta V$ ) transfers or other advantageous maneuvers between trajectories on invariant manifolds, and opportunities for small burns along a spacecraft trajectory that may result in a completely different orbit than the original due to chaotic behavior [9].

Traveling to and around different locations in the Earth-Moon and other systems may also increase capability for systems designed for space weather monitoring, orbital environment characterization, complex environment visualization, and many others, all of which are listed as Key Technology Areas (KTAs) under Potential Capability Area (PCA) 30: *Improved Orbital Conjunction Prediction*, which will enable technology-derived capabilities that can respond to the strategic, budget, and technology environments. According to the document, each KTA is an “essential component of the science and technology that the Air Force will need for the strategic environment, enduring realities, and over-arching themes that define the 2010-30 time frame and beyond” [10]. A variety of significant missions can utilize the different trajectories and behaviors possible in a higher-fidelity, multi-body dynamical model.

Other potential applications of the tools in the present investigation include missions that start in the near-Earth environment and travel outward to high-altitude Earth orbits; the Moon; and libration points of the Earth-Moon and Sun-Earth systems, as well as stable and unstable periodic orbits around them. Achieving successful operations through and at these locations in the tactical environment may theoretically include missions for various reconnaissance, surveillance, navigation, and command, control, and communication functions. Missions that travel in irregular patterns and require only slight maneuvers to drastically change the shape of a trajectory can also serve as a useful platform for missions desiring decreased predictability. An orbit modeled in the CR3BP may initially appear as a typical 2BP orbit in the

inertial frame as it begins its path along a trajectory. However, integrating the trajectory further and looking in a different frame of reference may reveal completely different behavior than expected or specific structures that indicate different behaviors. Furthermore, missions in the CR3BP that use the gravity of the Moon, visit different locations in the Earth-Moon system, or have specific, regular patterns and shapes seen in the CR3BP’s rotating frame may seem unremarkable when seen in the inertial frame. The potential unpredictability of the example orbits in this study will be discussed further in the later sections when comparing trajectories in different frames of reference.

## 1.5 Thesis Problem Statement and Document Overview

As discussed, the 2BP no longer provides a decent dynamical model to provide a reference solution as a spacecraft travels beyond geosynchronous orbit altitudes and the lunar gravitational field cannot be modeled as a small perturbation on two-body motion. Innovative methods can be applied to Earth-Moon dynamics to aid in mission design. As described by *Continuing Kepler’s Quest*: “The connections between the abstract theory of dynamical systems and practical and applied spaceflight have yielded an expansive growth in the ability to design (previously undiscovered) efficient and practical transfers within a highly perturbed, multi-body environment” [7]. In this investigation, different characteristics of and the specific findings in the CR3BP are exploited to design mission scenarios with alternative methods to conventional 2BP procedures.

### 1.5.1 Problem Statement

The objective of this investigation is to showcase a variety of numerical tools and concepts from Dynamical Systems Theory in a multi-body environment to show

how unconventional, innovative mission design solutions can provide ways to transfer spacecraft between Earth-centered orbits. This investigation aims to find solutions that require similar or less  $\Delta V$  when compared to standard methods, provide unpredictable pathways through the Earth-Moon system that may be advantageous to military operations, and offer visual insight into the possible motions for design problems.

### 1.5.2 Thesis Overview

This thesis is organized into chapters that provide the background information and design methodology that ultimately lead to the setup, design, and analysis of three specific orbital mission test cases. For all intensive computations and algorithms, MATLAB<sup>®</sup> was used to produce numerical solutions and to generate Poincaré maps. The following overview details this organization and defines key terms and assumptions particular to this investigation.

- Chapter 2: A historical overview of the contributions to the field of astrodynamics is provided, as well as a description for numerical integration, general and special perturbations, DST, Poincaré maps, and resonant orbits. Also explained in this chapter are the simplifying assumptions for the CR3BP, derivation of the 2BP and CR3BP equations of motion, nondimensionalization of units definition, transformations to/from the barycentric rotating and Earth-centered inertial frames of the CR3BP, and description of the one known integral of the motion admitted by the CR3BP and its implications. The specific features seen in the rotating frame of the CR3BP are described as well, including the equilibrium solutions and the motion near them, specific symmetry properties, the State Transition Matrix used for numerical tasks, and periodic orbits. In this chapter, mathematical descriptions of both the 2BP and CR3BP are given, and both refer

to an expression labeled “ $\mu$ .” In the 2BP, the gravitational parameter,  $\mu$ , refers to the total mass of the system multiplied by the gravitational constant. In the CR3BP, the mass ratio,  $\mu$ , refers to a specifically defined ratio of the mass of the smaller primary body to the total system mass. Further explanation of these definitions are found in Chapter 2, but the difference is mentioned here for clarification. Also notice that the geocentric equatorial inertial reference frame defined in the context of the 2BP and orbital elements is different than the Earth-centered inertial frame of the CR3BP defined later in this chapter. Both are inertial frames defined at the center of the Earth, with the geocentric equatorial inertial frame defined in relation to the Earth’s equator and the stars, and the Earth-centered inertial frame of the CR3BP based on the Moon’s orbit about the Earth and a direction in inertial space based on the initial position of the Moon at some epoch.

- Chapter 3: A description of the various numerical tools employed to aid in overall mission design, including periapsis Poincaré maps, single- and multiple-shooting targeting algorithms, and single-parameter and pseudo-arclength continuation procedures are derived and explained relative to the context of this investigation. Poincaré maps, multiple-shooting, and pseudo-arclength continuation algorithms are constructed specifically to track and record periapses on trajectories to connect the tools and produce a simple overall design method. In this chapter, a “periapse” is defined in both the 2BP and the CR3BP; there is a distinction between the definitions, so unless otherwise noted, a “periapse” in this investigation refers to the CR3BP definition.
- Chapter 4: Three test cases are explained to showcase the design methods. None of the converged solutions found in this investigation are claimed to be optimal, but they do provide possible solutions and offer favorable  $\Delta V$  values.

Taking advantage of the natural change in orbital parameters, a high-altitude resonant orbit arc is used in Test Case I as an initial guess in designing a high-altitude transfer from a highly inclined geosynchronous transfer orbit to a zero-inclination geostationary orbit (GEO). The transfer design is compared to the AsiaSat-3/HGS-1 “nominal trajectory” as defined by the Hughes Spacecraft Company’s Chief Technologist at that time, Cesar Ocampo.

In Test Case II, a periapsis Poincaré map is utilized to plan transfer opportunities between Earth orbits using invariant manifold trajectories associated with unstable periodic orbits. The initial “Tundra” and final “GEO” orbits in Test Case II, as well as the transfer trajectories between them, are all in the plane of the Earth and Moon. The chosen initial orbit is referred to as a “Tundra” orbit solely because it shares the apogee and perigee altitudes of a typical Tundra orbit, which in the real world is actually inclined at  $63.4^\circ$  with respect to the Earth’s equatorial plane [11]. The characteristics shared with the “Tundra” orbit in Test Case II include the altitude information and having an orbital period equal to one sidereal day. The “GEO” orbit in Test Case II is referred to as such since it is a circular orbit *near* GEO altitude, but since this final orbit lies in the plane of the Earth and Moon, its inclination with respect to the Earth’s equatorial plane is not zero, as it would be for geostationary orbit (like in Test Case I). Due to the nature of the design process chosen, the final “GEO” altitude is also slightly smaller than actual geostationary altitude. The relevance of these orbits as initial and final mission orbits is discussed in the test case, but the reference to “Tundra” and “GEO” orbits are defined here for clarity.

In Test Case III, orbits are also observed in the Earth interior region of the Earth-Moon CR3BP on periapsis Poincaré maps as a method for predicting

the behavior of a trajectory based on its periapse locations. A discussion is presented that uses the classification of trajectory behavior at some later time from a map to easily foresee where an unknown spacecraft may be or may end up depending on its initial or current conditions. These maps are evaluated as a tool that can be used for mission designers to choose initial conditions from the map based on desired end conditions, as well as a method to predict the future behavior of an unknown spacecraft based on a guess for its observed current or initial conditions.

The feasibility of the designs in each test case are evaluated, and the approaches of “warfighting mission assurance” as defined by the Office of the Assistant Secretary of Defense for Homeland Defense and Global Security is also discussed in this chapter [12]. The analysis and discussion of utilizing different contingency options, as well as the idea of gaining insight about an unknown spacecraft’s trajectory are explored as advantages to improve mission assurance.

- Chapter 5: A summary of the completed work is presented, along with conclusions drawn from both the design processes used and the results generated from simulations, as well as recommendations for future work that build on the outcomes of this investigation.

## **1.6 Chapter 1 Summary**

Military space operations can be advanced by implementing unconventional trajectory design methods to transfer spacecraft between orbits. A summary of the “rescue” story of AsiaSat-3/HGS-1 motivates the exploration of innovative solutions that lower required  $\Delta V$  and compute less predictable trajectories, as two fly-bys around the Moon inserted the stranded spacecraft in a favorable orbit for less cost than conventional methods. Considering more solution options by looking at an ex-

panded design space and using advanced tools and numerical methods aligns with the Air Force OODA Loop in “develop[ing] countermeasures,” as well as with the goals in the highlighted sections of JP3-14 and *Technology Horizons*. Further study of a multi-body dynamical environment, numerical methods, and Dynamical Systems Theory as they apply to military space applications leads to increased understanding of what is possible in a complex dynamical model, which aids in producing innovative solutions in mission design. Before specific scenarios are detailed and analyzed, a background of the CR3BP and the associated design methods are required.

## 2. Background on the Fundamentals of the CR3BP Using Numerical Methods

In order to fully develop the ideas in this investigation, a brief historical background and an explanation of each topic presented in the test cases are necessary. This chapter summarizes the major contributions to the field of astrodynamics that make the research in this investigation possible and lays the foundation for modeling in a multi-body environment. The dynamical model used in the current investigation, the circular restricted three-body problem (CR3BP), is introduced and derived, and explanations are provided for perturbation theories, numerical integration, and coordinate transformations to/from different reference frames. Details specific to the CR3BP are also introduced, including the one known integral of the motion admitted by the CR3BP, the model's equilibrium solutions and the motion near them, the State Transition Matrix (STM) developed from the equations of motion and equations of variation, periodic solutions, invariant manifolds, resonant orbits, and Poincaré maps.

### 2.1 Historical Overview of Astrodynamics

The school of thought that led to the development of celestial mechanics began in approximately 300 B.C. with Aristotle's ponderings about the natural state of matter, or if one existed. Although he wrongly believed that the center of the Earth was a "natural place" toward which each celestial body was striving and that "if there exists a motion, there must be a force," his thinking sparked others to explore the concepts and develop the principles that are fundamental to spaceflight dynamics [13]. In 100 A.D., Claudius Ptolemy proposed that the planets moved in circles with epicycles with the Earth near the center of the system [14]. In 1543 Nicolaus Copernicus published his heliocentric model of the solar system, showing how the planets moved about the Sun at the system center rather than the Earth [13]. The Copernican revolution



followed, opening the door for others to make more extensive observations. Galileo developed the Law of Inertia and the concept of acceleration, publishing his findings in 1610 and laying the study of celestial dynamics on a truly scientific foundation [13]. Johannes Kepler used Tycho Brahe's observations to develop his laws of planetary motion [14]:

- (1) The solar system is a Sun-centered system where the planets travel in ellipses with the Sun at one focus instead of in circles with epicycles about the Earth (published 1609) [13, 14].
- (2) A line that connects a planet to the Sun sweeps out equal areas in equal times (published in 1609) [13].
- (3) The period of a planet's orbit around the Sun is proportional to the semi-major axis of the ellipse raised to the  $\frac{3}{2}$  power, with a constant of proportionality that is the same for all the planets (published in 1619) [8].

In the late 1600s, Isaac Newton explained the dynamics behind Kepler's observational kinematics [13]. Building the foundation of dynamics are his laws of motion:

- (1) Every body at rest or in straight-line motion remains in that state unless acted upon by a net applied force [8, 15].
- (2) The sum of the applied forces on a body is equal to the time rate of change of momentum of the body [8].
- (3) For every applied force, there is an equal and opposite reaction force [8].

Newton's Law of Gravitation is also worth noting, describing how the magnitude of "the gravitational force  $[F]$  acting between two bodies [with masses  $m_1$  and  $m_2$ ] is proportional to the product of the masses and is inversely proportional to the square

of the distance between them [where  $r$  is the distance],” [8, 15], or:

$$F = G \frac{m_1 m_2}{r^2}, \quad (1)$$

where  $G$  is the gravitational constant ( $6.674 \times 10^{-11} N \cdot (\frac{m}{kg})^2$ ). Newton used Kepler’s laws of planetary motion and his own Law of Gravitation to derive the equations of motion for the two-body problem and determine the solution [13]. Modern military use of celestial mechanics started in 1767 when the Astronomer Royal Maskelyne used Leonard Euler’s lunar theory as the basis for the lunar ephemeris in the British Nautical Almanac, which was used by the British Navy for navigation [1]. Officially published in 1772, Euler’s lunar theories made the first contribution to the development of the CR3BP as he solved the problem of two fixed centers of force, using Newton’s Law of Gravitation to describe the motion of two fixed masses acting on a third body [1]. He also notably introduced the synodic, or rotating, coordinate system, which led to Jacobi’s discovery of the integral admitted by the equations of motion in 1836 [1]. Also known as the “Jacobian Integral” or defined in terms of the “Jacobi Constant,” the integral connects the speed of the third body in the CR3BP to its location. The existence of the integral implies certain accessible and “forbidden” regions of motion for the third body, which George William Hill further examined in his work in 1878, making a significant contribution to the field with the introduction of “zero velocity curves and surfaces” [1].

In 1765, Euler discovered the first three of the five equilibrium solutions in the CR3BP, the collinear points, and in 1772, Joseph Louis Lagrange discovered the last two, the triangular points [8, 16]. Altogether they are called the “Lagrange points,” or “libration points” [8, 16]. These five points are positions where the gravitational forces are “balanced” between the two primary masses in the rotating frame [16]. Motion near the equilibrium solutions became a focal point of study when looking at possi-

ble motions in the CR3BP. Completing his three-part treatise *Méthodes Nouvelles* in 1899, Henri Poincaré’s contributions focused on the qualitative rather than quantitative approach to celestial mechanics [1]. His work examined the stability of the solar system, and he used the simplified, restricted three-body problem as his model [17]. He analyzed the local and global behavior of the dynamical system of the CR3BP. His research laid the groundwork for many methods used in modern Dynamical Systems Theory, including methods that will be discussed later, such as first-return maps, or Poincaré maps, stability theory for periodic orbits, the concept of dynamical chaos, and manifold dynamics. George David Birkhoff expanded Poincaré’s work to examine the dynamical theories further. For example, in 1927 he showed the existence of an infinite number of periodic solutions to the restricted three-body problem [18]. In order to introduce the methods used in this research, various ways to handle the perturbations caused by gravitational bodies in addition to the Earth are discussed.

## 2.2 General and Special Perturbations

Since the CR3BP has no known closed-form analytical solution, other engineering methods are explored to find useful dynamical information. General and special perturbations offer two different avenues in approaching the problem. General perturbation methods are seen frequently in classical celestial mechanics and use series expansions as a fundamental tool in a mathematical exploration of problems [1]. General perturbations uses analytical expressions to approximate perturbations and initial conditions for problems [19]. Analysis with the theory of general perturbations provides a series solution for small third-body perturbations, however it proves to be unhelpful when needing an accurate representation of the full dynamics. Even though this method produces a convergent series, the characteristics and properties of the system cannot be derived from this general solution [1]. Though a higher-fidelity

model is needed to represent the dynamics for a spacecraft under the gravitational influence of both the Earth and the Moon, general perturbations is helpful when it *is* valid to assume that third-body effects are just small perturbations on the motion. Analytical approximations are used to investigate the motion in the vicinity of the libration points in the CR3BP, and there are also useful approximations for certain periodic solutions in the CR3BP. However, when a situation arises that includes perturbations not easily expressed by a simple algebraic formula, special perturbations may provide insight [19].

Special perturbations is the term used by astrodynamicists when referring to the “special” resulting orbit generated by numerically integrating the equations of motion in an orbital problem [20]. Numerical approaches are commonly used when trying to find a particular solution, for instance trying to find a solution to the  $n$ -body problem, rather than for studying the behavior of the entire system or nearby solutions [1]. As a mission designer studies a problem, a wide range of solutions must first be considered in order to find the best solution for the problem. Taking a numerical approach, a region of interest is selected, and practical initial conditions are used to compute the group of possible orbits in the region. The disadvantage here is obviously the ruling out of potential useful orbits or families of orbits because they did not stem from the range of initial conditions used to establish the set of possible solutions [1]. Also note that any numerical process also comes with an amount of error, which is discussed further in the next section.

Numerical methods are associated with experimentation, and through time, these experiments have only been as advanced as the available computational power. In this way, numerical methods are becoming more relevant as technology improves. Numerical studies can also reveal new dynamical motion in the CR3BP that cannot be found or inferred in the 2BP. Periodic, quasi-periodic, or chaotic motion may

be observed from integrating the CR3BP equations of motion. Applications using numerical methods can provide insight into the inner mechanics of a nonlinear system like the CR3BP and may inspire new design methods. Formulating the problem as seen from a rotating frame with the primary system gives insight into distinctive structures that contain new dynamical information. One known integral of the motion is admitted by the CR3BP, termed the “Jacobi Constant” ( $JC$ ) [1]. When looking at the phase space of the problem, the  $JC$  reduces the dimension of the problem by one. Considering a spacecraft in the Earth-Moon system with zero velocity, the  $JC$  then defines curves or surfaces of zero velocity that serve as the boundary between an “accessible region” where a spacecraft could potentially travel and a “forbidden region” where spacecraft motion is not physically possible in the CR3BP at that energy-level [1]. Numerical integration provides the means necessary for implementing special perturbations into the analysis of a spacecraft’s particular solution, or its trajectory, in the CR3BP.

### 2.3 Numerical Integration

Andrew Claude de la Chèrie Crommelin and Philip Herbert Cowell computed the 1910 return of Halley’s Comet using numerical integration to produce their prediction [21]. Their calculation was accurate within three days, an astounding feat during that time [21]. Direct numerical integration of the equations of motion in inertial, rectangular coordinates in orbital mechanics is still referred to as Cowell’s Method, after the mathematician with a specialty in the dynamics of motion [20, 21]. Most targeting schemes and continuation methods in the present investigation converge to solutions within an error tolerance of  $10^{-12}$  nondimensional units. This tolerance corresponds to the specifically defined error vector in each numerical algorithm derived for the specific problems in the current investigation. As an example, this tolerance

translates to an accuracy within 0.03844 cm in position across an entire error vector of distances, and it represents a total error of 0.0000001025 cm/s across an entire error vector of velocities. With this definition of the convergence criterion, accuracy at each specific point is different, but the total error over all points in the error vector corresponds to the tolerance value. These accuracies may offer even more accuracy than is necessary close to the Earth and may be useful further out in the system, but this is assuming that acceptable accuracy is still maintained at the end of the integration [20]. Summing miniscule errors from rounding and truncation in the inner-arithmetic of the integrator leads to decreased accuracy toward the end of integration. With all integrators, there is a build-up of error that grows with the integration time. Therefore, the limitation of numerical integration in this analysis must be noted; short periods may produce dependable solutions to within a given integration tolerance, but the accuracy achieved with longer periods of integration may become less trustworthy. When chaotic behavior is observed in the system, numerical error can cause significant changes. The more chaos the system experiences, the more sensitive the resulting trajectories can be to their initial conditions.

This investigation's numerical simulations were created using MATLAB<sup>®</sup> [22]. The integrators used for numerically integrating spacecraft trajectories are the built-in MATLAB<sup>®</sup> functions, *ode45* and *ode113* [22]. The *ode45* function is an explicit Runge-Kutta integrator based on a Dormand-Prince (4, 5) pair, which uses a step control method that works well in many problems [23]. In this investigation, *ode45* is used for integrating small numbers of trajectories in a single simulation [24]. For quicker algorithm run-time of more computationally intensive algorithms, a predictor-corrector implemented from Adams-Bashforth-Moulton methods, *ode113*, was used [24]. In the present investigation, this integrator is used for simulations that integrate larger numbers of spacecraft trajectories, such as for Poincaré maps. Both *ode45* and

*ode113* also require initial conditions. Since the outputs of the numerical simulations using these functions do not compute exact (zero error) solutions, ways to track error along with the integration are useful. A known integral of the motion for a system or another known constant value given by the mathematics can serve as metrics to track the numerical error as the trajectory is computed. It is also important to note that the numerical simulations of the CR3BP are time-invariant. This is useful for numerical integration of trajectories, since the solution for a specific time interval is the same as a solution for an equivalent interval that begins at a different start time [1]. In order to model spacecraft trajectories using numerical integration, the gravitational environment of the CR3BP is first defined.

## 2.4 Simplifying Assumptions of the Circular Restricted Three-Body Problem

The problem of two bodies in orbital mechanics involves two bodies with spherically symmetric mass distributions that are treated as point masses, orbiting under their mutual gravitational attraction. It has a closed-form analytical solution in terms of conic sections: circles, ellipses, parabolas, hyperbolas, and straight lines [8]. The circular restricted three-body problem defines the expanded design space in this investigation and introduces the gravitational forces of a third body, such as the Moon (or Sun) in an Earth-spacecraft situation. This additional body increases the complexity of the solution space significantly. Under certain conditions, when the spacecraft is relatively close to one of the primary bodies, the CR3BP describes basic 2BP motion with a perturbing effect [8, 25]. When the additional gravitational influence is no longer just a small perturbation, as Wiesel states is the “fundamental assumption of perturbation theory,” other models must be considered [20]. The general  $n$ -body problem examines the orbits of a system of  $n$  masses whose motion is influenced by

their own gravitational fields [8]. According to Newton’s Law of Gravitation (equation (1)), the force of gravity between masses is proportional to the product of the masses and inversely proportional to the square of the distance between them [8]. The dynamical system depicting motion as observed by an inertial frame has  $3n$  degrees of freedom; a system of  $6n$  first-order (or  $3n$  second-order) differential equations describes the motion. When  $n = 1$ , the solution is trivial and is described by Newton’s first law. For  $n = 2$ , there is a closed-form solution.

### 2.4.1 The Two-Body Problem

The two-body problem (2BP) setup describes two bodies modeled as point masses that are moving under the forces of their mutual gravitational attraction. It is also convenient to consider the restricted 2BP, in which the smaller of the two masses is assumed to be negligible in comparison to the significantly larger mass of the other body. Note that a more in-depth derivation of the 2BP equations of motion and their solution is provided by many authors, including Szebehely and Wiesel [8, 15]. In the inertial formulation of the problem where  $n = 2$ , the equations of motion represent six second-order, nonlinear, coupled ordinary differential equations, and twelve constants of the motion are required to solve the problem [8]. Reformulating the problem to define the *relative* motion between the two masses, which is no longer an inertial construction of the problem, the relative equation of motion for the two-body problem is:

$$\ddot{\vec{r}} = \frac{-\mu\vec{r}}{r^3}, \quad (2)$$

where  $\vec{r}$  is defined as the position vector of the body with smaller mass with respect to the body with larger mass,  $\ddot{\vec{r}}$  is its second time derivative, and

$$\mu = G(M + m), \quad (3)$$



where  $G$  is the gravitational constant,  $M$  is the larger mass, and  $m$  is the smaller mass. Note that the frame of differentiation for these vectors is still an inertial frame. From this point forward in the development, the solution for the *restricted* 2BP is derived, in which the smaller mass is assumed to be negligible compared to the larger mass ( $m \ll M$ ). The system barycenter is then at the center of the larger mass and serves as an inertially-fixed point. Considering the Earth-spacecraft 2BP as an example, the center of the Earth serves as the inertially-fixed origin of the inertial frame for the restricted 2BP, but note this does not hold true for the general 2BP.

The relative equation of motion in equation (2) decouples the relative-position problem from the problem of the position of the system in inertial space. At this point, six integrals of the motion are needed to solve the problem, and they can all be found. Taking the dot product of each side of equation (2) with the first time derivative of the position vector,  $\dot{\vec{r}}$ , leads to finding the law of conservation of energy (and the first constant of the motion) through the “vis-viva” equation,

$$\varepsilon = \frac{1}{2}v^2 - \frac{\mu}{r}, \quad (4)$$

where  $\varepsilon$  is the conserved value, specific mechanical energy, or the total energy per unit mass of  $m$  for the restricted 2BP,  $v = \|\dot{\vec{r}}\|$ , and  $r = \|\vec{r}\|$ . Note that for the general 2BP,  $\varepsilon$  is the total energy per unit reduced mass, where  $m_{reduced} = \frac{m_1 m_2}{m_1 + m_2}$ .

Taking a cross product of each side of equation (2) with the radius vector,  $\vec{r}$ , leads to the conservation of angular momentum [8]. The resultant definition of specific angular momentum,  $\vec{H}$ , is

$$\vec{r} \times \dot{\vec{r}} = \vec{H}. \quad (5)$$

The three resulting constants of the motion are the components of the angular momentum vector per unit mass of  $m$  for the restricted 2BP. The final two constants

of the motion needed to solve the 2BP are found by taking the cross product of equation (2) with  $\vec{H}$ . Performing the cross product and integrating the result, this yields

$$\dot{\vec{r}} \times \vec{H} - \mu \frac{\vec{r}}{r} = \mu \vec{e}, \quad (6)$$

where  $\vec{e}$  is the constant eccentricity vector. This vector gives two additional, independent constants of the motion since the definition of the angular momentum vector already determined the plane of the orbit where  $\vec{e}$  resides [8]. Taking the dot product of both sides of equation (6) with  $\vec{r}$  gives the solution to the 2BP, the polar form of a conic section with the center of the primary body at one focus:

$$r = \frac{H^2/\mu}{1 + e \cos(\nu)} = \frac{p}{1 + e \cos(\nu)}, \quad (7)$$

where  $H = \|\vec{H}\|$ ,  $p$  is the semi-latus rectum (half the chord through one focus, parallel to the directrix [26]), and  $\nu$  is the angle between vectors  $\vec{r}$  and  $\vec{e}$ , or the true anomaly. This equation implies that all solution trajectories in the 2BP are in terms of conic sections: closed circular and elliptical orbits, parabolic, hyperbolic, and also straight-line trajectories [8, 15]. Note that  $p = a(1 - e^2)$  for circles, ellipses, and hyperbolas, where  $a$  is the semi-major axis (half the distance of an elliptical orbit's long axis) and  $e = \|\vec{e}\|$ . The 2BP is typically used in problems involving the Earth (the larger mass) and a satellite (the negligible mass). Most Earth satellites remain in closed circular or elliptical trajectories about the Earth, for which a set of classical orbital elements may be defined with respect to the Earth's equatorial plane. A notional representation of these elements for an elliptical Earth orbit is seen in Figure 1. Earth orbits in the 2BP are also commonly defined with respect to the geocentric equatorial inertial frame. This reference frame describes inertial, orthogonal directions originating at the center of the Earth, represented by unit vectors,  $\hat{i}$ ,  $\hat{j}$ , and  $\hat{k}$ . The  $\hat{i}$  direction lies

in the Earth's equatorial plane, pointing to the first point of Aries,  $\gamma$ , or from the center of the Earth to the Sun on the first day of Spring in the northern hemisphere (the vernal equinox) [27]. The  $\hat{k}$  direction points through the Earth's north pole, and the  $\hat{j}$  direction completes the right-handed set. Note that this frame is different from the Earth-centered inertial frame of the CR3BP, defined in the next section.

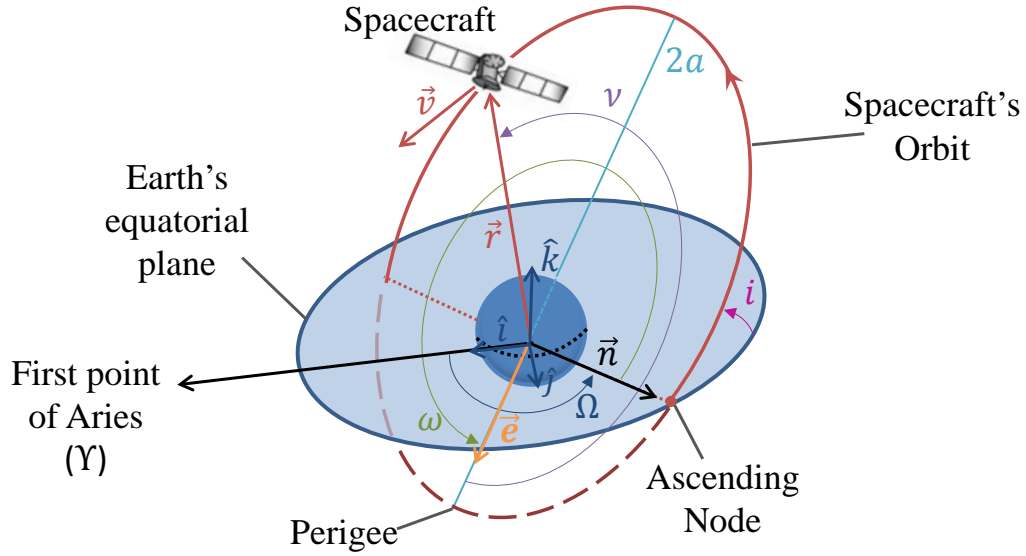


**Figure 1. Notional Representation of the Six Classical Orbital Elements with Respect to Earth's Equatorial Plane: Right Ascension of the Ascending Node ( $\Omega$ ), Argument of Perigee ( $\omega$ ), Inclination ( $i$ ), True Anomaly ( $\nu$ ), Semi-major Axis ( $a$ ), and Eccentricity Vector (with Magnitude  $e$ ).**

In Figure 1, the classical orbital elements are defined for an elliptical orbit with respect to the Earth's equatorial plane. The right ascension of the ascending node ( $\Omega$ ) is defined with respect to the first point of Aries,  $\gamma$ , which is a point considered to be sufficiently inertial among the approximately “fixed” stars [8]. The angle  $\Omega$  is measured in the eastward direction, defining the location of where the orbit crosses from south to north (its ascending node) [8]. The argument of perigee ( $\omega$ ) is the angle in the orbital plane between the line of nodes (the nodal vector,  $\vec{n}$  in Figure 1) and the vector between the center of the Earth to the orbit's point of perigee, which is

also the eccentricity vector,  $\vec{e}$  [8]. The inclination ( $i$ ) is the angle between the Earth's equatorial plane and the orbital plane. The true anomaly ( $\nu$ ), as mentioned before, is the angle between the eccentricity vector,  $\vec{e}$  and the radius vector,  $\vec{r}$ . The semi-major axis ( $a$ ) is the length of half of the long axis of the orbit, labeled  $2a$  in Figure 1. The eccentricity ( $e$ ) in general defines the type of conic section, and it describes the shape of closed orbits. This set of orbital elements can completely define an orbit solution in the 2BP [8]. Note that for orbits that lie in the equatorial plane,  $\Omega$  is undefined, and for circular orbits,  $\omega$  and  $\nu$  are undefined. Alternate orbital elements can then be used to define an orbit. Longitude of perigee ( $\Pi$ ) is used to define the perigee location in the equatorial case (if the orbit is not also circular), argument of latitude ( $u$ ) defines the position vector from the ascending node for circular orbits (if the orbit is not also equatorial), and true longitude ( $l$ ) defines the spacecraft location for orbits that are both equatorial and circular [8, 32].

Closed satellite orbits also have a defined orbital period,  $P_{2BP}$ , which is expressed by,

$$P_{2BP} = 2\pi\sqrt{\frac{a^3}{\mu}}. \quad (8)$$

The orbital mean motion, or the mean angular frequency of the orbit,  $n_{2BP}$ , is defined,

$$n_{2BP} = \sqrt{\frac{\mu}{a^3}}. \quad (9)$$

These quantities are also defined in terms of the CR3BP in Section 2.5. Though they are derived in the 2BP, the orbital elements can also be useful in the analysis of trajectories in the CR3BP. In Section 4.1.1, “osculating” orbital elements are used to examine a transfer solution by determining the instantaneous orbital elements at each time step along the numerically integrated trajectory in the CR3BP. While the *restricted* 2BP was derived above, the solution describing conic sections, the

relationships in equations (8) and (9), and the constants of the motion extend to the *general* 2BP. In the next section (Section 2.4.2), the CR3BP uses the general 2BP to describe the motion of the two larger masses considered in the model.

### 2.4.2 The Circular Restricted Three-Body Problem

In the  $n$ -body problem, when  $n = 3$ , no closed-form analytical solution is known [8]. The addition of just one more body indicates that eighteen integrals of the motion are needed to solve the problem, while the  $n$ -body problem in general has only ten known integrals of the motion: energy provides one, the conservation of linear momentum gives six, and the conservation of angular momentum offers three [8]. In the 2BP derivation, decoupling the relative problem of two bodies from the initial 2BP of the system in inertial space provided enough integrals of the motion to solve the problem. Unfortunately, the same process of reformulating the problem to describe the relative motion of the bodies does not provide enough integrals of the motion to solve the three-body problem. Simplifying assumptions are made in order to gain more insight into the problem.

As in the two-body problem, in the general three-body problem, all bodies are modeled as point masses and the gravitational forces of each are assumed to influence the motion of the others. The two most massive of the three bodies are labeled  $P_1$  and  $P_2$ , and if the two primaries are of unequal masses, the most massive is called  $P_1$ , by convention. The third and least massive body is  $P_3$ . For the *restricted* three-body problem, the mass of the third body,  $m_3$ , is assumed to be negligible when compared to the masses of the primary bodies,  $m_1$  and  $m_2$ , respectively for  $P_1$  and  $P_2$  ( $m_3 \ll m_1, m_2$ ) [1, 25]. With this assumption, the gravitational field of  $P_3$  does not influence the motion of the primaries. This leads to the assumption that the motion of  $P_1$  and  $P_2$  is, in general, described by conics in the primaries' own isolated, solved

two-body system. The final simplifying assumption is that  $P_1$  and  $P_2$  have circular orbits about their barycenter,  $B$  [1, 25]. In general, the circular orbit assumption is not necessary, but simplifies the analysis. Thus, the circular restricted three-body problem is defined.

## 2.5 Equations of Motion and Nondimensionalization

Since  $P_1$  and  $P_2$  move in circular orbits about the system barycenter,  $B$ , their orbital motion is described by the two-body equation of motion. The differential equations of motion (EOMs) defined in the CR3BP govern the motion of  $P_3$  as it is influenced by the movement of the primaries [1, 25]. The EOMs for the general  $n$ -body problem are defined by:

$$m_i \ddot{\vec{r}}_i = -G \sum_{j=1, j \neq i}^n \frac{m_i m_j}{r_{ji}^3} \vec{r}_{ji}, \quad (10)$$

where  $P_i$  and  $P_q$  (defined with respect to an inertial frame with position vectors  $\vec{r}_i$  and  $\vec{r}_q$ , respectively) are two of  $n$  total particles in a system,  $G$  is the universal gravitational constant,  $\vec{r}_{ji} = \vec{r}_i - \vec{r}_j$ , and  $r_{ji} = \|\vec{r}_{ji}\|$ . The  $n$ -body system setup is described as seen by an inertial observer in Figure 2.

The governing equation of motion for  $\ddot{\vec{r}}_{qi}$ , representing the relative motion of two bodies ( $P_i$  with respect to  $P_q$ ), is then

$$\ddot{\vec{r}}_{qi} + G \frac{(m_i + m_q)}{r_{qi}^3} \vec{r}_{qi} = G \sum_{j=1, j \neq i, q}^n m_j \left( \frac{\vec{r}_{ij}}{r_{ij}^3} - \frac{\vec{r}_{qj}}{r_{qj}^3} \right). \quad (11)$$

The first term on the left hand side (LHS) of equation (11),  $\ddot{\vec{r}}_{qi}$ , is the acceleration of the relative vector of  $P_i$  with respect to  $P_q$ , and the remaining expression on the LHS is the so-called “dominate” acceleration term (though not necessarily the

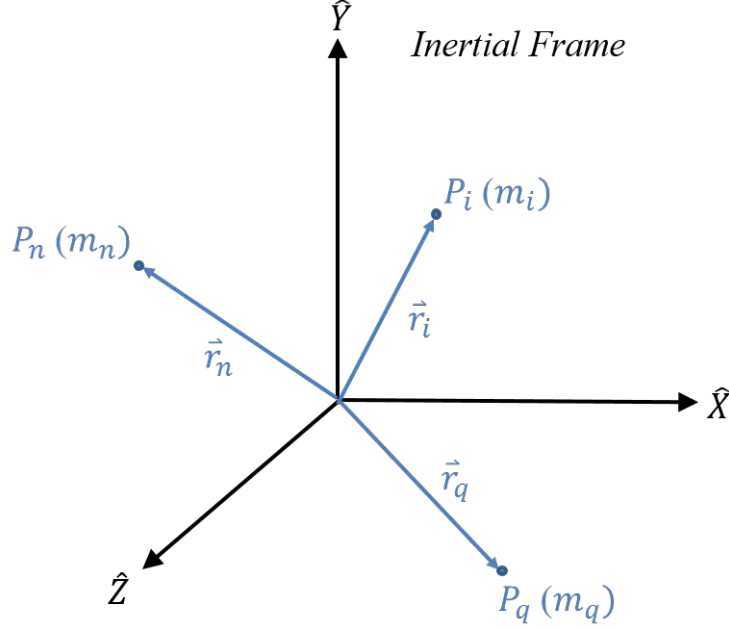


**Figure 2.  $n$ -Body Problem Setup in Inertial Frame.**

largest perturbing term) [25]. On the right hand side (RHS), the term with  $\vec{r}_{ij}$  in the numerator represents the direct perturbing acceleration of all other bodies and forces in the system gravitationally pulling on  $P_i$ . The term with  $\vec{r}_{qj}$  in the numerator on the RHS is the indirect perturbing acceleration of all bodies and forces that have a gravitational pull on  $P_q$  [8, 25]. Note that if all perturbations were to be removed from the system, the RHS of equation (11) is equal to zero and the equation describes solvable two-body relative motion. However, if even one additional gravity field (one additional body) is added to the system, there is mathematically no longer a closed-form analytical solution [1, 8, 25]. To explore the relative formulation of the three-body problem, consider the system of the Earth ( $P_1$ ), Sun ( $P_2$ ), and Moon ( $P_3$ ). When considering a third body, the relative equations of motion (following the form in equation (11)) must be solved for the relative motion of the Moon with respect to the Earth,  $\ddot{\vec{r}}_{13}$ , and the relative motion of the Moon with respect to the Sun,  $\ddot{\vec{r}}_{23}$ ,

seen below.

$$\ddot{\vec{r}}_{13} + G \frac{(m_1 + m_3)}{r_{13}^3} \vec{r}_{13} = Gm_2 \left( \frac{\vec{r}_{32}}{r_{32}^3} - \frac{\vec{r}_{12}}{r_{12}^3} \right), \quad (12)$$

where the term with  $\vec{r}_{32}$  in the numerator represents the Sun's perturbation on the Moon (direct perturbation term), and the term with  $\vec{r}_{12}$  in the numerator represents the Sun's perturbation on the Earth (indirect perturbation term).

$$\ddot{\vec{r}}_{23} + G \frac{(m_2 + m_3)}{r_{23}^3} \vec{r}_{23} = Gm_1 \left( \frac{\vec{r}_{31}}{r_{31}^3} - \frac{\vec{r}_{21}}{r_{21}^3} \right), \quad (13)$$

where the term with  $\vec{r}_{31}$  in the numerator represents the Earth's perturbation on the Moon (direct perturbation term), and the term with  $\vec{r}_{21}$  in the numerator represents the Earth's perturbation on the Sun (indirect perturbation term). The third relative equation of motion ( $\ddot{\vec{r}}_{12}$ ), may be defined by the relation  $\ddot{\vec{r}}_{12} = \ddot{\vec{r}}_{13} + \ddot{\vec{r}}_{32}$ . Therefore, to solve this relative formulation of the three-body problem, the relative EOMs must be solved simultaneously, requiring twelve integrals of the motion. Since there are only ten integrals of the motion available, the relative formulation of the three-body problem does not aid in finding a solution. When solving the two-body problem, reformulating the problem in terms of a relative equation of motion is significant enough to afford a solution, but doing so in the three-body problem still leaves the problem unsolved.

Returning to the general  $n$ -body equations of motion in equation (10) and considering  $n = 3$  bodies, the equation of motion for the third body becomes

$$m_3 \ddot{\vec{r}}_3 = -G \frac{m_3 m_1}{r_{13}^3} \vec{r}_{13} - G \frac{m_3 m_2}{r_{23}^3} \vec{r}_{23}, \quad (14)$$

and the equations of motion for  $P_1$  and  $P_2$  follow similar form:

$$m_1 \ddot{\vec{r}}_1 = -G \frac{m_2 m_1}{r_{21}^3} \vec{r}_{21} - G \frac{m_3 m_1}{r_{31}^3} \vec{r}_{31} \quad (15)$$



$$m_2 \ddot{\vec{r}}_2 = -G \frac{m_1 m_2}{r_{12}^3} \vec{r}_{12} - G \frac{m_3 m_2}{r_{32}^3} \vec{r}_{32} \quad (16)$$

Let  $\hat{\mathbf{X}}$ ,  $\hat{\mathbf{Y}}$ , and  $\hat{\mathbf{Z}}$  define the orthogonal unit vectors of the inertial frame where the  $\hat{\mathbf{X}}$ - $\hat{\mathbf{Y}}$  plane is the fixed plane of mutual primary motion. An illustration of the three-body system setup in the inertial frame originating at the system Barycenter,  $B$ , is seen in Figure 3.

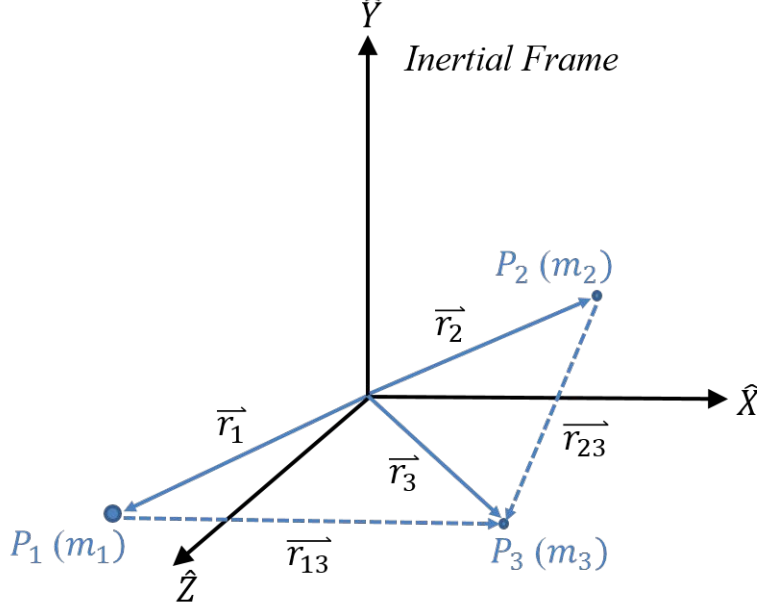


**Figure 3. Three-Body Problem Setup in Inertial Frame.**

Notice that the vector EOMs for each body must be solved simultaneously and will require eighteen integrals of the motion to obtain a closed-form analytical solution. Only ten integrals of the motion are available, therefore solving the system in this form is not possible. In summary, neither the relative equations of motion (requiring twelve integrals of the motion) nor the inertial equations of motion (requiring eighteen integrals of the motion) for the general problem of three bodies offer a formulation that allows a solution to the problem to be found (with ten known integrals of the motion available).

Variables are redefined in order to look at the problem in a synodic, or rotating,

frame with orthogonal unit vectors  $\hat{\mathbf{x}}$ ,  $\hat{\mathbf{y}}$ , and  $\hat{\mathbf{z}}$  centered at  $B$ . By convention, the  $\hat{\mathbf{x}}$  direction points through the primaries from  $P_1$  to the direction of  $P_2$ . Observing the rotating frame,  $R$ , as it is defined with respect to the inertial frame,  $I$ , both the  $\hat{\mathbf{Z}}$  and  $\hat{\mathbf{z}}$  components are along the angular momentum vector of the two-body system of the primaries. The  $\hat{\mathbf{y}}$  direction of  $R$  then completes the orthogonal set of the barycentric rotating frame. The orientation of  $R$  with respect to  $I$  is described by the angle,  $\theta$ . Since the primaries are in circular orbits,  $\theta$  is changing at a constant rate,  $\dot{\theta}$ , which is the angular velocity of the primary system. This constant is also the mean motion of the circular orbits of the primaries,  $N$ . For simplicity, let  $\vec{D} = \vec{r}_{13}$  and  $\vec{R} = \vec{r}_{23}$ . The vector from  $B$  to  $P_3$  is defined as  $\vec{p}$ . The system setup of the barycentric rotating frame as it relates to the inertial frame is illustrated in Figure 4.

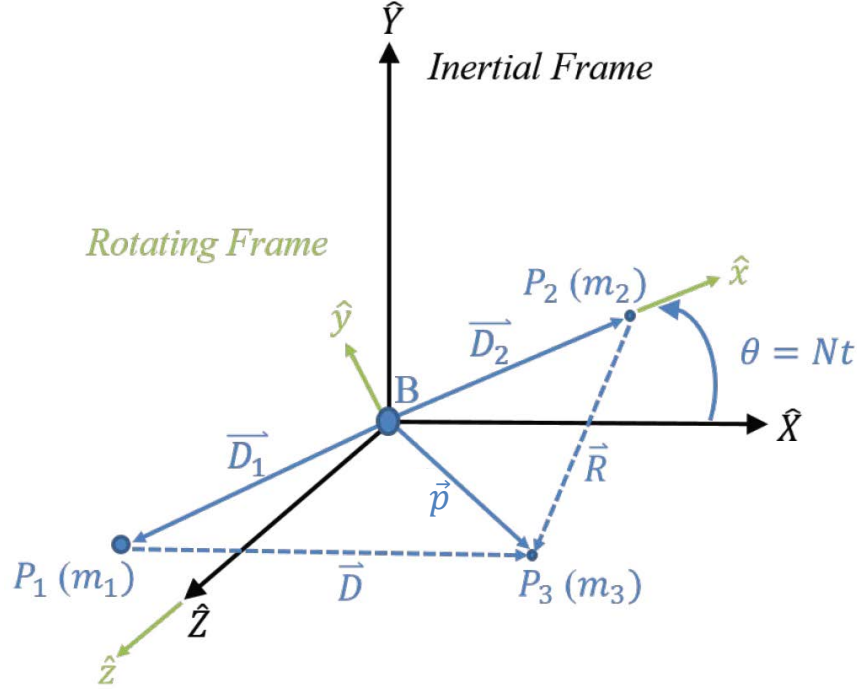


**Figure 4. Definition of Barycentric Rotating Frame in CR3BP with Respect to Inertial Frame.**

The variables in the CR3BP are often defined with nondimensional units. Nondimensional units are useful in numerical simulations since computers have a limited

number of digits for each computed value that they can represent with a given precision floating point number [28]. A numerical simulation can only handle numbers that are within certain limits based on the achievable precision, or numbers that are not too small or too large for the system to deal with [28]. In numerical simulations dealing with a large variety of calculations, values near the center of these limits (close to the value of one) are typically chosen [28]. For this reason, in this investigation, nondimensional mean motion,  $n$ , and the nondimensional gravitational constant,  $G$ , are normalized with unity value. Nondimensional units also help the mission planner to compare different CR3BP systems of bodies with different masses and distances. For the discussion hereafter, time derivatives with respect to dimensional time are expressed with the following notation:  $\dot{\mathbf{p}}''$ . Time derivatives with respect to nondimensional time, on the other hand, are expressed as:  $\ddot{\mathbf{p}}$ . The dimensional universal gravitational constant is labeled  $\tilde{G}$ , while the nondimensional version is expressed  $G$ . Also note that several dimensional and nondimensional variables are defined with upper and lower case variables, respectively (one exception being dimensional  $\mathbf{p}$  and nondimensional  $\mathbf{p}$ ). Equation (14) may then be expressed as:

$$m_3 \dot{\mathbf{p}}'' = -\tilde{G} \frac{m_3 m_1}{D^3} \vec{D} - \tilde{G} \frac{m_3 m_2}{R^3} \vec{R}, \quad (17)$$

where  $D = \|\vec{D}\|$  and  $R = \|\vec{R}\|$ . There is a set of specifically defined values, or “characteristic quantities” that serves to define a nondimensional system of variables. Each characteristic quantity, denoted with an asterisk (\*), is defined in the equations below.

$$l^* = D_1 + D_2, \quad (18)$$

where  $D_i = \|\vec{D}_i\|$  is constant with the assumption of circular orbits.

$$m^* = m_1 + m_2 \quad (19)$$

$$t^* = \sqrt{\frac{(D_1 + D_2)^3}{\tilde{G}(m_1 + m_2)}} = \sqrt{\frac{l^{*3}}{\tilde{G}m^*}} = \frac{1}{n}, \quad (20)$$

selected such that  $G = 1$ , and where  $n$  = nondimensional mean motion. Note that equation (20) is equivalent to the time it takes for  $P_3$  to travel one radian, and by extension, one orbital period,  $P$ , of  $P_3$  in the CR3BP. This is given by:

$$P = 2\pi t^* = \frac{2\pi}{n} = 2\pi, \quad (21)$$

since nondimensional mean motion,  $n$ , is normalized to one. Because  $l^*$  is assumed to be equal to the two-body semi-major axis of the primaries' orbit,

$$\tilde{G}m^* = \tilde{G}m_1 + \tilde{G}m_2, \quad (22)$$

and the mass ratio,  $\mu$ , may be defined:

$$\mu = \frac{m_2}{m_1 + m_2} = \frac{\tilde{G}m_2}{\tilde{G}(m_1 + m_2)} = \frac{m_2}{m^*}. \quad (23)$$

Each dimensional quantity in question may be expressed as a nondimensional quantity by dividing it by the appropriate characteristic quantity expression. For instance, nondimensional time,  $t$ , can be computed from dimensional time,  $T$ , by:

$$t = \frac{T}{t^*}. \quad (24)$$

Other important definitions include the characteristic quantity expression for velocity,

$\frac{l^*}{t^*}$ , and the following mass relations:

$$\frac{m_2}{m^*} = \mu \quad (25)$$

$$\frac{m_1 + m_2}{m^*} = 1 \quad (26)$$

$$\frac{m_1}{m^*} = 1 - \mu \quad (27)$$

To derive the nondimensional equations of motion, equation (17) is divided by  $m_3$ , and expressing the equation in nondimensional variables, the result is:

$${}_I \ddot{\vec{\rho}} = \frac{-(1 - \mu)\vec{d}}{d^3} - \frac{\mu\vec{r}}{r^3}, \quad (28)$$

where  $\vec{d}$  = nondimensional  $\vec{D}$  and  $\vec{r}$  = nondimensional  $\vec{R}$ . Notice the equation of motion for  $P_3$  above (equation (28)) still describes an *inertial* second derivative with respect to time. Recall the rotating frame definition of position for  $P_3$ ,

$$\vec{\rho} = x\hat{x} + y\hat{y} + z\hat{z}, \quad (29)$$

and similarly,

$${}^R \dot{\vec{\rho}} = \dot{x}\hat{x} + \dot{y}\hat{y} + \dot{z}\hat{z}, \quad (30)$$

which is the relative velocity of  $P_3$  in the rotating frame (where the frame of differentiation is the rotating frame). The “transport theorem” is applied in this investigation when taking the inertial derivative of any vector,  $\vec{a}$ , that is expressed in the rotating frame, using the angular velocity of the rotating frame with respect to the inertial frame,  $\vec{\omega}^{RI}$  [25, 29]:

$${}_I \frac{d}{dt}(\vec{a}) = {}^R \frac{d}{dt}(\vec{a}) + \vec{\omega}^{RI} \times (\vec{a}) \quad (31)$$

By applying the “transport theorem” (equation (31)) twice, equation (28) may be

written as three scalar, second order (nondimensional) ordinary differential equations that describe the motion for  $P_3$ :

$$\ddot{x} - 2n\dot{y} - n^2x = \frac{-(1-\mu)(x+\mu)}{d^3} - \frac{\mu(x-1+\mu)}{r^3} \quad (32)$$

$$\ddot{y} + 2n\dot{x} - n^2y = \frac{-(1-\mu)y}{d^3} - \frac{\mu y}{r^3} \quad (33)$$

$$\ddot{z} = \frac{-(1-\mu)z}{d^3} - \frac{\mu z}{r^3}, \quad (34)$$

where  $d = \sqrt{(x+\mu)^2 + y^2 + z^2}$  and  $r = \sqrt{(x-1+\mu)^2 + y^2 + z^2}$ . In this investigation, since circular orbits are assumed,  $n = 1$  for these equations. Recall the angle  $\theta = Nt$ , defining the barycentric rotating frame as it relates to the inertial frame with dimensional mean motion and dimensional time in Figure 4. Nondimensionalizing and substituting  $n = 1$ , the rotation angle,  $\theta$ , between the rotating and inertial frames is found to be equal to nondimensional time,  $t$ . This also implies that one orbital period of the primaries is  $2\pi$  nondimensional units. The instantaneous nondimensional time derivative of this angle,  $\dot{\theta}$  is then found to be:

$$\dot{\theta} = \frac{d\theta}{dt} = \frac{d(nt)}{dt} = n = 1. \quad (35)$$

In order to solve the equations of motion defined in the rotating frame (equations (32)-(34)), six integrals of the motion would be required, but only one is known to exist (see Section 2.7). For this reason, the equations of motion are numerically integrated in this investigation, creating simulations of possible trajectories of  $P_3$  in the Earth-Moon CR3BP. In general, 3-D motion of the third body is possible. Notice, however, that a spacecraft with an initial position and velocity in the plane of the primaries ( $x$ - $y$  plane) *remains* in the plane for all finite time unless perturbed out-of-plane. For this reason, the CR3BP can be considered as a planar (2-D) problem or a

full spatial (3-D) problem.

## 2.6 Coordinate Transformation of Vectors in the Barycentric Rotating Frame to/from the Earth-Centered Inertial Frame of the CR3BP

Although plotting trajectories in the rotating reference frame of the Earth-Moon system is useful for missions utilizing certain applications such as resonant orbits and libration point dynamics, it is important to visualize the same trajectories in the Earth-centered inertial reference frame of the CR3BP. Different from the geocentric equatorial inertial frame, the inertial frame of the CR3BP is defined at the center of the Earth with its  $X$ - $Y$  plane aligned with the  $x$ - $y$  plane of the primaries. At the initial time,  $t_0$ , the  $\hat{X}$  direction is aligned with the  $\hat{x}$  direction of the rotating frame. Some of the shapes and behaviors of trajectories noticeable in the rotating frame may not appear so obvious from the inertial perspective. This characteristic is apparent in Figure 5. Figures 5 (a) and 5 (b) show the same spacecraft trajectory in the rotating and inertial frames, respectively. Both are numerically integrated trajectories propagated for 7 nondimensional time units, or about 30 days. These figures show a trajectory that appears as a slightly perturbed, higher-altitude two-body orbit in the inertial frame. From observing Figures 5 (a) and 5 (b), the rotating frame shows a trajectory that does not seem like a periodic orbit in the rotating frame, but that follows some sort of pattern as it orbits the Earth. Figures 5 (c) and 5 (d) show the same trajectory, propagated for 32 nondimensional time units, or about 139 days (4.6 months). While the trajectory initially appears to be staying close to a two-body orbit, longer propagation and examination in the rotating frame shows that a spacecraft following this trajectory diverges from the two-body orbit at 9 nondimensional units (39 days) and travels around the  $L_1$  libration point (see section 2.8 for further discussion on libration points), and then orbits around the

Moon for about 90 days before coming back near the Earth with total time equal to about 30 nondimensional time units (129 days). This type of trajectory has numerous potential applications for Moon missions, as a spacecraft on this trajectory naturally and repeatedly orbits about both the Earth and Moon.

Examining the orbit in the inertial frame has little indication of the dramatic change until the trajectory actually changes, and even when it does, the orbits about the libration point and the Moon are not obvious at first. Viewing the same trajectory in the rotating frame clearly shows these behaviors at first glance. Notice Figure 5 shows “forbidden regions” in each rotating frame plot. The curves surrounding the “forbidden” sections represent the physical position of where a spacecraft in the CR3BP has zero velocity as defined by the CR3BP’s one known integral of the motion, the Jacobi Constant (see Section 2.7). The “forbidden regions” represent where the possible velocity for a spacecraft has a nonphysical value ( $v^2 < 0$ ). These curves of zero velocity serve as a preview for the explanation of the integral of the motion and its implications, defined in the next section.

Recognizing this type of behavior in the rotating frame gives advantage to the mission planner in terms of “predictability” for spacecraft orbits. It may be possible to predict a future location, orbit shape, or general trajectory behavior by examining trajectories in a different frame. Recognizing resonant orbit arcs and spacecraft trajectories traveling near the equilibrium points in the rotating frame can possibly help to predict where a spacecraft on the trajectory will be some time in the future. Further discussion of the predictability aspect of frame perspective is found in Section 4.3.1.

The following discussion on how to transform a trajectory in the barycentric rotating frame to the Earth-centered inertial frame is based on Haapala’s development for the same transformation [30]. Recall from Figure 4 that  $\vec{\rho}$  is defined as the vector



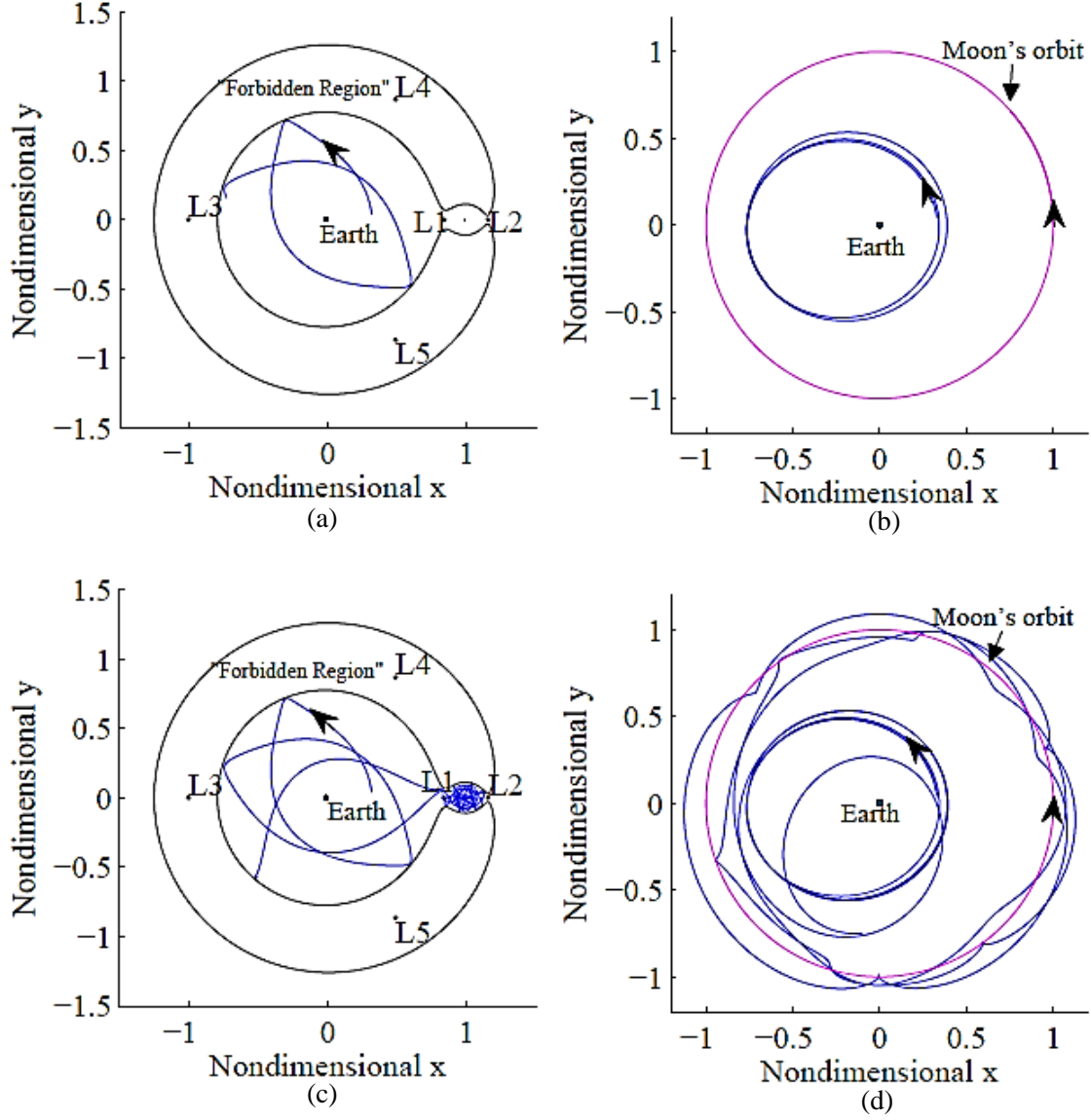


Figure 5. Numerically Integrated Spacecraft Trajectory in (a) Barycentric Rotating Frame (Integration time = 7 nondimensional units (about 30 days)), (b) Earth-Centered Inertial Frame (Integration time = 7 nondimensional units (about 30 days)), (c) Barycentric Rotating Frame (Integration time = 32 nondimensional units (about 139 days)), and (d) Earth-Centered Inertial Frame (Integration time = 32 nondimensional units (about 139 days)) in CR3BP.

from the system barycenter to  $P_3$ , and  $\theta$  is defined as the orientation angle from the  $X$ -axis of the inertial frame to the  $x$ -axis of the rotating frame. the Earth-centered inertial frame is initially aligned with the rotating frame (at initial time,  $t_0$ ), and therefore  $\theta$  changes at a constant rate and is also equal to the nondimensional time,  $t$ . The Direction Cosine Matrix (DCM),  $R^{RI}$ , rotates the position vector of  $P_3$  from the rotating frame to the inertial frame [8]. The DCM rotates the vector it pre-multiplies about the common  $z$ -axis between both frames. As defined below,  $R^{RI}$  is an explicit function of nondimensional time,  $t$ .

$$R^{RI} = \begin{bmatrix} \cos(t - t_0) & -\sin(t - t_0) & 0 \\ \sin(t - t_0) & \cos(t - t_0) & 0 \\ 0 & 0 & 1 \end{bmatrix} \quad (36)$$

The inverse transformation  $(R^{RI})^{-1} = R^{RI}$  is the DCM that rotates vectors from inertial to rotating coordinates. Expressing the state vector,  $\vec{X}$ , in both inertial and rotating coordinates is often useful. The expressions for the position and velocity vectors that make up the rotating frame state vector definition used in the simulations in this investigation,  $\vec{X}^R$ , are shown below, where  $\vec{\rho}$  is the position of  $P_3$  in the rotating frame. The vector  ${}^I\dot{\vec{\rho}}$  is the velocity of  $P_3$  in the rotating frame, found by employing the “transport theorem” (equation (31)) to  $\vec{\rho}$ .

$$\vec{\rho} = x\hat{x} + y\hat{y} + z\hat{z} \quad (37)$$

$${}^I\dot{\vec{\rho}} = \dot{\vec{\rho}} = (\dot{x} - ny)\hat{x} + (\dot{y} + nx)\hat{y} + \dot{z}\hat{z}, \quad (38)$$

where  $n = 1$  with the assumption of circular orbits, and

$$\vec{\mathbf{X}}^R = \begin{bmatrix} \vec{\rho} \\ \dot{\vec{\rho}} \end{bmatrix}. \quad (39)$$

Transforming the state vector in the rotating frame to Earth-centered inertial coordinates uses the same DCM as before, as well as its time derivative,  $\dot{R}^{RI}$ , [30]:

$$\vec{\mathbf{X}}^I = \begin{bmatrix} R^{RI} & 0_{3 \times 3} \\ \dot{R}^{RI} & R^{RI} \end{bmatrix} [\vec{\mathbf{X}}^R + \mu \hat{\mathbf{x}}], \quad (40)$$

where

$$\dot{R}^{RI} = \begin{bmatrix} -\sin(t - t_0) & -\cos(t - t_0) & 0 \\ \cos(t - t_0) & -\sin(t - t_0) & 0 \\ 0 & 0 & 0 \end{bmatrix} \quad (41)$$

and  $(\vec{\mathbf{X}}^R + \mu \hat{\mathbf{x}})$  translates the coordinates from the barycentric frame to the Earth-centric frame with a shift in the  $\hat{\mathbf{x}}$  direction. The inverse of this transformation matrix gives the transformation from the inertial to rotating frame. Element by element, the transformation from the barycentric rotating frame to the Earth-centric inertial frame is:

$$X = (x + \mu)\cos(t) - y\sin(t) \quad (42)$$

$$Y = (x + \mu)\sin(t) + y\cos(t) \quad (43)$$

$$Z = z \quad (44)$$

$$\dot{X} = -(x + \mu)\sin(t) - y\cos(t) + \dot{x}\cos(t) - \dot{y}\sin(t) \quad (45)$$

$$\dot{Y} = (x + \mu)\cos(t) - y\sin(t) + \dot{x}\sin(t) + \dot{y}\cos(t) \quad (46)$$

$$\dot{Z} = \dot{z} \quad (47)$$

Note that some authors consider  $P_2$ -centric inertial frames for analysis, which would result in a shift in the  $-\hat{\mathbf{x}}$  direction by  $1 - \mu$  to account for the translation between frames before multiplying by the  $6 \times 6$  matrix in equation (40).

## 2.7 Integral of the Motion

When desiring to look at the dynamics in the rotating frame, adding a third body will still give a conservative system of forces as it does in the inertial frame. This implies that an energy (or energy-like) constant may exist [1, 25]. It is possible to derive the integral of the motion associated with the differential equations in equations (32)-(34). Note that in general, this integral is not a property of the system, but an aspect of the synodic formulation of the problem. The EOMs in equations (32)-(34) can be further simplified by defining the scalar “pseudopotential,”  $U^*$  in the rotating frame:

$$U^* = \frac{(1 - \mu)}{d} + \frac{\mu}{r} + \frac{1}{2}n^2(x^2 + y^2), \quad (48)$$

where  $n = 1$  with the assumption of circular orbits. The scalar CR3BP EOMs describing the motion of  $P_3$  can then be defined in terms of the pseudopotential:

$$\ddot{x} - 2\dot{y} = U_x^* \quad (49)$$

$$\ddot{y} + 2\dot{x} = U_y^* \quad (50)$$

$$\ddot{z} = U_z^*, \quad (51)$$

where  $U_x^* = \frac{\partial U^*}{\partial x}$ ,  $U_y^* = \frac{\partial U^*}{\partial y}$ , and  $U_z^* = \frac{\partial U^*}{\partial z}$ . In theory, all the needed information is available to mathematically solve the EOMs above (equations (49)-(51)), but this may prove to be difficult, as these equations are highly nonlinear and highly coupled.

As an earlier explanation mentioned, the inertial formulation of the three-body problem requires eighteen constants of the motion to be solved, and the relative formulation requires twelve. Looking at the problem in the rotating frame gives three second-order ordinary differential equations for the motion of  $P_3$  under the gravitational influence of the primaries (equations (49)-(51)), which requires six integrals of the motion to solve. Though it does not completely solve the problem, the CR3BP admits one known integral of the motion, named the Jacobi Integral (or Jacobi Constant), leading to numerous implications [1,25,31]. Carl Gustav Jacob Jacobi discovered the integral of the motion by looking at the equations of motion in the synodic coordinate system described above, [1,25].

To derive the integral, the scalar dot products of the differential equations of motion (equations (49)-(51)) and the relative velocity of  $P_3$  in  $R$  (equation (30)) are calculated and then summed to yield the following:

$$\dot{x}\ddot{x} + \dot{y}\ddot{y} + \dot{z}\ddot{z} = \frac{dU^*}{dt} \quad (52)$$

Equation (52) is then directly integrated over nondimensional time,  $t$ , and the result is,

$$\frac{1}{2}(\dot{x}^2 + \dot{y}^2 + \dot{z}^2) = U^* + C, \quad (53)$$

where  $C$  is the constant of integration. For convenience,  $C$  is defined such that  $C = \frac{-JC}{2}$ , where  $JC$  is the Jacobi Constant. Recognizing  $(\dot{x}^2 + \dot{y}^2 + \dot{z}^2) = \|\dot{\vec{r}}\|^2 = v^2$ , where  $v$  is the relative speed of  $P_3$  in the rotating frame,  $JC$  is then expressed in the form,

$$JC = 2U^* - v^2. \quad (54)$$

Expanding the expression,

$$JC = x^2 + y^2 + \frac{2(1-\mu)}{d} + \frac{2\mu}{r} - v^2. \quad (55)$$

Note that other authors may define  $JC$  differently with relation to the constant of integration,  $C$ . The definition in the current investigation is chosen such that  $JC = -2H$ , where  $H$  is the Hamiltonian of the system [1,25,32]. As seen in equation (55) above, a given  $JC$  value connects the speed of  $P_3$  with its location. Considering a spacecraft in the Earth-Moon CR3BP at a given position and velocity, the value of  $JC$  is established by its conditions [31]. As a spacecraft moves through the space, changing in position and velocity, the integration constant associated with the trajectory does not vary. Examining equation (54), the magnitude of the velocity vector is squared, implying that calculating the position and velocity coordinates on a spacecraft trajectory from a known  $JC$  yields a solution for both positive and negative values of velocity [31]. Also notice that in general the  $JC$  can be positive or negative, but it will always be positive when velocity of the spacecraft is zero. In equation (55),  $x^2 > 0$ ,  $y^2 > 0$ , and the last two terms will always be positive since  $0 < \mu < 1$  and  $d$  and  $r$  are positive distances, yielding a positive value when  $v = 0$ .

As seen in the relationship with the system pseudopotential (equation (54)), the  $JC$  is a quantity that is inversely related to system energy level. As the  $JC$  increases, the system energy level decreases, and vice versa. Since the  $JC$  remains constant for the duration of any trajectory, it may also be calculated along a trajectory as the trajectory is numerically integrated in order to track changes and therefore assess the error in the simulation [31]. Examining the same spacecraft trajectory as in Figure 5, the error of the  $JC$  along the spacecraft trajectory is seen for integration times of about 31 days and 1.12 years in Figures 6 and 7. In these figures, zero Jacobi Constant error would correspond to zero change in the  $JC$ , and therefore no error

in the numerical simulation. In Figure 6, as integration time increases, the error's absolute value also increases.

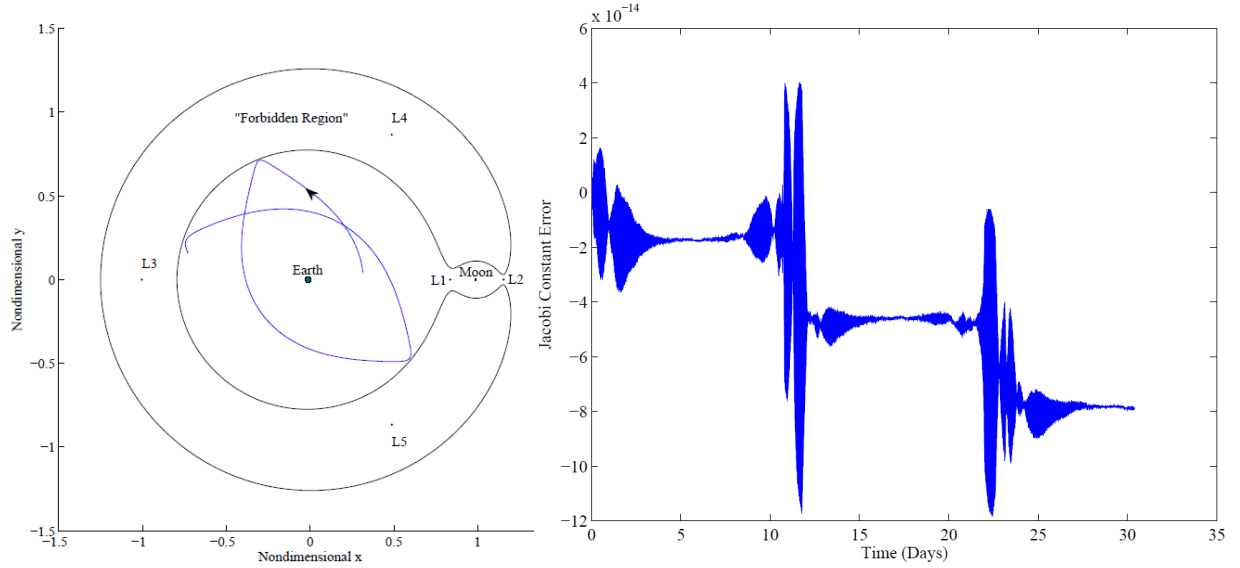


**Figure 6. Tracking Numerical Error with Jacobi Constant for 7 Nondimensional Units (About 30 days) (Left: Trajectory in Configuration Space, Right: Error Along Trajectory).**

The error is seen to sharply increase when the spacecraft approaches the Earth and tends to settle when the spacecraft is farther away from the primary. The greatest amount of error seen in this example is observed around 12 days, at a point along the trajectory when the spacecraft is closer to the Earth. The value of this maximum is  $16 \times 10^{-14}$ , which is comparable to the integration tolerance in this simulation of  $10^{-13}$  nondimensional units. In Figure 7, a longer integration time is observed (15 revolutions of the primaries or 1.12 years). The  $JC$  error is seen to reach roughly  $20 \times 10^{-12}$  at about 95 days. At this point, the trajectory impacts the Moon, as seen in Figure 8.

The close proximity to the primaries causes a rapid build-up in the numerical integration error. Long-duration numerical integration also shows the build-up of the integration error over time. Since in general, chaos is present in the CR3BP, error in numerical simulations can make a substantial difference when resulting trajectories

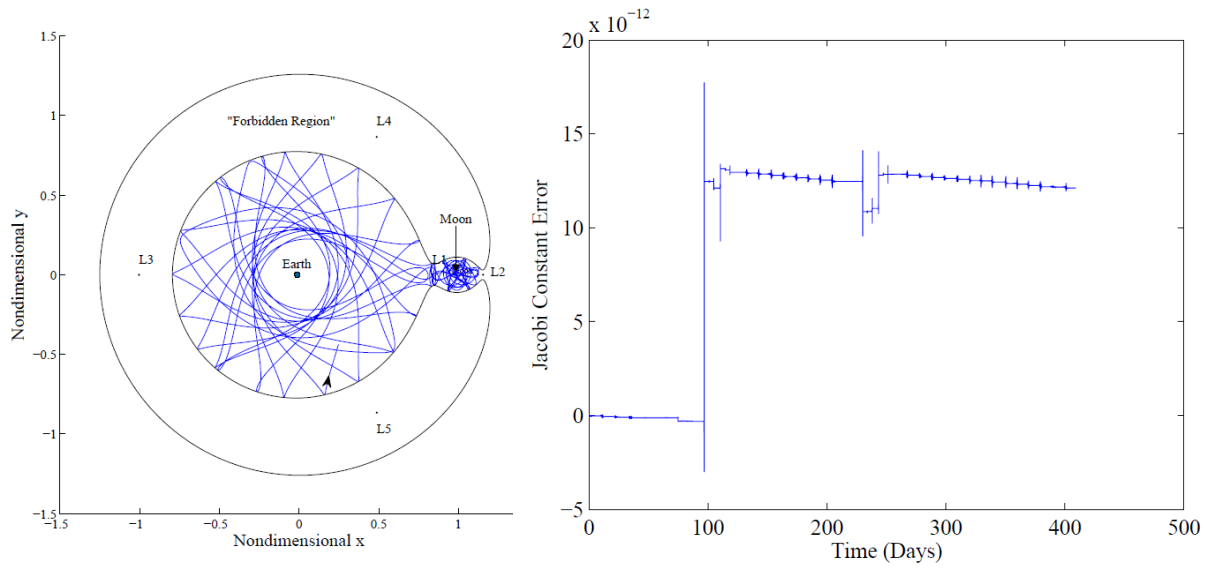


**Figure 7. Tracking Numerical Error with Jacobi Constant for 15 Revolutions of the Primaries (About 1.12 Years) (Left: Trajectory in Configuration Space, Right: Error Along Trajectory).**

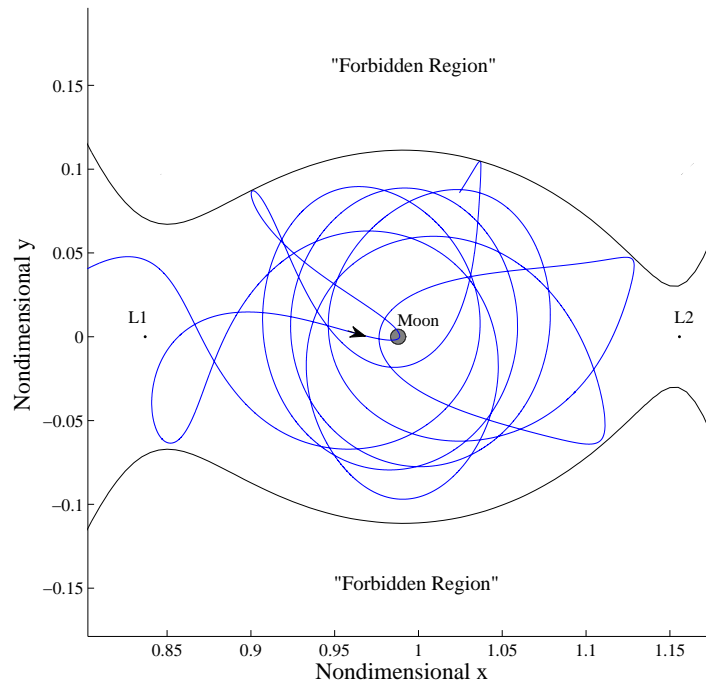


**Figure 8. Zoomed View Near Moon Region Showing Impact of Spacecraft Trajectory at 22.32 Nondimensional Time Units (About 95 Days).**



are particularly sensitive to the initial conditions. Tracking this error can be used as a metric for how trustworthy the results of numerical integration are for different scenarios.

## 2.8 Equilibrium Solutions

Searching for particular solutions for the CR3BP equations of motion (equations (49)-(51)) by examining the system when the first and second derivatives are equal to zero leads to five constant equilibrium solutions in the rotating frame. As stated earlier, the equilibrium solutions, libration points, or Lagrange points are the locations of balanced gravitational forces in the rotating frame where the attractive forces of  $P_1$  and  $P_2$  are equal to the centripetal force of  $P_3$  as it rotates with the primaries [1, 25]. As observed from the rotating frame, each of the five libration points ( $L_1$  through  $L_5$ ) are stationary, with zero velocity and acceleration. If  $P_3$  were to be placed with zero initial velocity in the rotating frame exactly at the location of any of these points,  $P_3$  would theoretically stay at that position with zero relative motion in the rotating system [1, 25]. The first three points are collinear with the primaries on the  $x$ -axis of the rotating frame, and the last two points, the triangular points, have symmetric positions off the  $x$ -axis that form equilateral triangles with the primaries. The locations of  $L_1$  through  $L_5$  in the rotating frame of the Earth-Moon system are indicated in Figure 9. Note that although five libration points are found in each system evaluated in the CR3BP, this investigation focuses on the equilibrium points in the Earth-Moon CR3BP.

The mathematical conditions for each equilibrium point in any CR3BP system include having zero velocity and zero acceleration in the rotating frame, and  $\vec{\nabla}U^* = \vec{0}$  [1, 25]. To solve for the exact libration point locations of the triangular points, recall the EOMs defined in terms of partial derivatives of the pseudopotential in

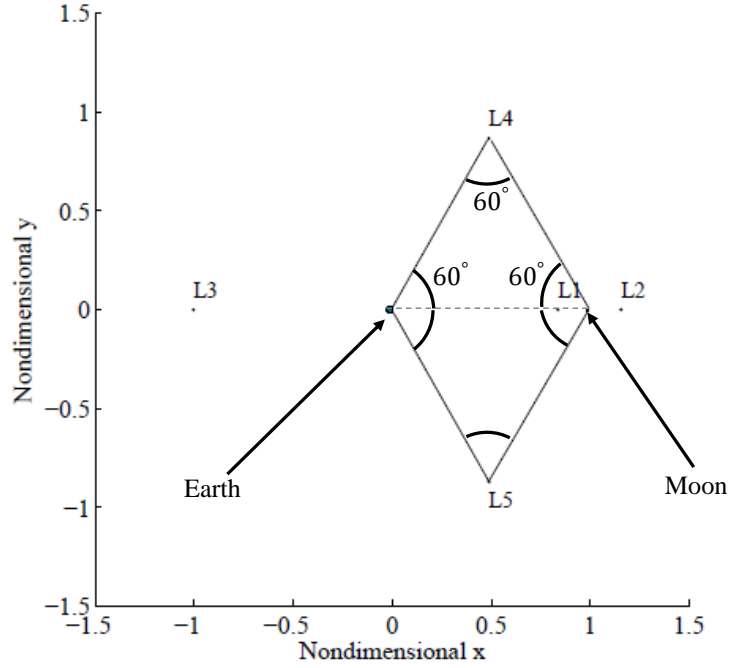


**Figure 9. Earth-Moon CR3BP Libration Point Locations in Barycentric Rotating Frame.**

equations (49)-(51). Note that because the coefficients for  $z$  in the  $z$ -partial of the pseudopotential (equation (51)) are nonzero,  $z$  must be zero for each libration point. Therefore, all of the equilibrium solutions are fixed in the  $x$ - $y$  plane. Starting with the  $y$ -component equation, each component of the pseudopotential function is set equal to zero and constant coordinates for each equilibrium solution are computed. Setting equation (50) equal to zero yields  $y = 0$ , true for each of the three collinear points, and  $y_{L4,5} = \pm \frac{\sqrt{3}}{2}$ , where the positive value corresponds to  $L_4$ , and the negative corresponds to  $L_5$  [1]. Solving for the  $x$ -coordinates for the triangular points,  $y_{L4,5}$  is substituted into equation (49) and set to zero, resulting in  $x_{L4,5} = \frac{1}{2} - \mu$ . One way to determine the  $x$ -coordinates of the collinear libration points in the barycentric rotating frame is through an iterative scheme. Each location is defined in terms of a variable,  $\gamma_i$  defining the  $L_1$ ,  $L_2$ , and  $L_3$  locations from the nearest primary, illustrated and defined in Figure 10.

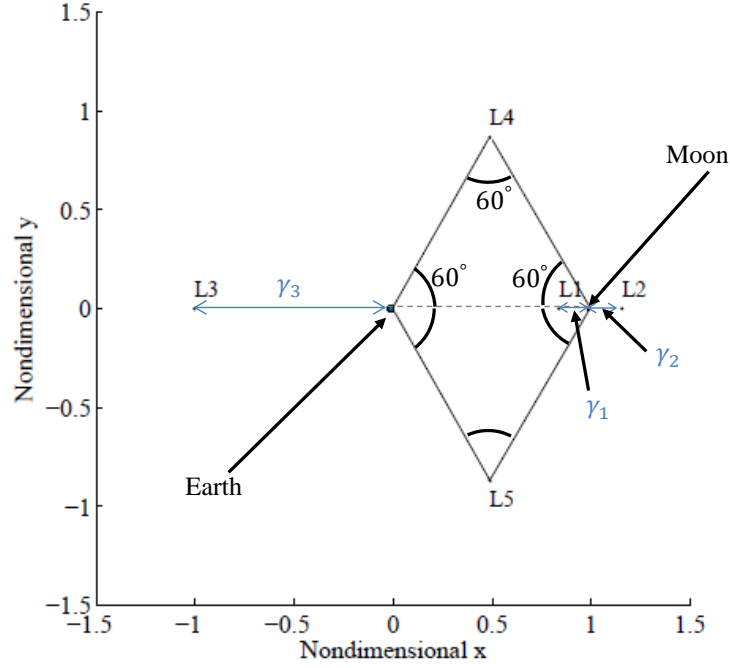


**Figure 10. Earth-Moon CR3BP Libration Point Locations in Barycentric Rotating Frame with Associated Distances from the Primaries.**

From the equilibrium conditions for each point,  $\ddot{x} = \ddot{y} = \ddot{z} = \dot{x} = \dot{y} = \dot{z} = 0$  and from the analysis above,  $z_{L1,2,3} = y_{L1,2,3} = 0$ . Substituting this information and the  $x$ -coordinate location in terms of  $\gamma_2$  into equation (49), the equation is set equal to zero, and the  $x$ -value for  $L_2$  is computed.

$$\frac{1 - \mu}{(1 + \gamma_2)^2} + \frac{\mu}{\gamma_2^2} = 1 - \mu + \gamma_2, \quad (56)$$

where

$$x_{L_2} = 1 - \mu + \gamma_2. \quad (57)$$

Equation (56) is solved iteratively using a Newton-Raphson algorithm with update equation,

$$x_{n+1} = x_n - \frac{f(x)}{f'(x)}, \quad (58)$$

where  $x_{n+1}$  is the next computed value for the  $x$ -coordinate,  $x_n$  is the previous value,

$$f(\gamma_2) = \frac{1 - \mu}{(1 + \gamma_2)^2} + \frac{\mu}{\gamma_2^2} - 1 + \mu - \gamma_2, \quad (59)$$

and

$$f'(\gamma_2) = \frac{-2(1 - \mu)}{(1 + \gamma_2)^3} - \frac{2\mu}{\gamma_2^3} - 1. \quad (60)$$

In order to start the process, the Hill radius,  $r_h$  (similar to the “radius of the sphere of activity” of  $m_2$ , or the Roche limit when  $r$  is the maximum permitted size of  $m_2$ ), is the initial input for  $x_n$ , which is considered a decent initial guess for small  $\mu$  [8].

$$r_H \simeq \left( \frac{m_2}{3m_1} \right)^{\frac{1}{3}} \quad (61)$$

The Newton-Raphson iterative process continues until a solution value has converged to within the given tolerance of  $10^{-12}$  nondimensional units in this work, corresponding to an accurate location to within 0.03844 cm. The  $x$ -coordinates of  $L_1$  and  $L_3$  are completed in similar processes. The comparison of the coordinates of the libration points in the barycentric rotating frame are listed for both the Earth-Moon and Sun-Earth systems in Table 1.

**Table 1. Jacobi Constant Values and Rotating Frame Coordinates of the Equilibrium Points in the Earth-Moon, Sun-Earth, and Equal Primary Mass Systems in the CR3BP**

Libration Point	Rotating Coordinates in Earth-Moon System in Nondimensional Units [km]	Earth-Moon System Jacobi Constant Value	Rotating Coordinates in Sun-Earth System in Nondimensional Units [km]	Sun-Earth System Jacobi Constant Value	Rotating Coordinates in System of Primaries with Equal Mass in Nondimensional Units	Equal Mass System Jacobi Constant Value
$L_1$	$x = 0.836915121142417$ [321, 710.173] $y = 0$ $z = 0$	3.1883411264261000	$x = 0.990026587821958$ [148, 095, 559.635] $y = 0$ $z = 0$	3.00089069490319	$x = 0$ $y = 0$ $z = 0$	4.0
$L_2$	$x = 1.155682169063840$ [444, 244.226] $y = 0$ $z = 0$	3.17216046839511	$x = 1.01003412254119$ [151, 088, 435.874] $y = 0$ $z = 0$	3.00088669021457	$x = 1.19840614455492$ $y = 0$ $z = 0$	3.45679622408615
$L_3$	$x = -1.00506264620232$ [-386, 346.081] $y = 0$ $z = 0$	3.01214715162089	$x = -1.00000125145253$ [-149, 587, 644.202] $y = 0$ $z = 0$	3.00000300348589	$x = -1.19840614455492$ $y = 0$ $z = 0$	3.45679622408615
$L_4$	$x = 0.487849413449431$ [187, 529.315] $y = 0.866025403784439$ [332, 900.165] $z = 0$	2.98799705020295	$x = 0.499996996513926$ [74, 793, 279.216] $y = 0.866025403784439$ [129, 546, 537.850] $z = 0$	2.99999699652295	$x = 0$ $y = 0.866025403784439$ $z = 0$	2.75
$L_5$	$x = 0.48784941344943$ [187, 529.315] $y = -0.866025403784439$ [-332, 900.165] $z = 0$	2.98799705020295	$x = 0.499996996513926$ [74, 793, 279.216] $y = -0.866025403784439$ [-129, 546, 537.850] $z = 0$	2.99999699652295	$x = 0$ $y = -0.866025403784439$ $z = 0$	2.75

Equations (49)-(51) facilitate solving for the libration point locations depending on the system mass ratio value,  $\mu$ . As  $\mu$  increases (the closer  $P_1$  and  $P_2$  are in mass), the distance from  $P_2$  to  $L_1$  and  $L_2$  increases, and the distance from  $P_1$  to  $L_3$  decreases. Table 1 shows the qualitative differences in coordinates for the Earth-Moon, Sun-Earth, and equal primary mass systems of the CR3BP. Jacobi Constant values also vary across the libration points. As seen in Table 1, a larger value of  $JC$  corresponds to a lower energy level. The table shows that energy levels increase as  $JC_{L_1} > JC_{L_2} > JC_{L_3} > JC_{L_4} = JC_{L_5}$  for the Earth-Moon system, so the lowest energy level of the five libration points corresponds with  $L_1$ , and the highest energy level is associated with  $L_4$  and  $L_5$ .

The concept of a  $JC$  also establishes “forbidden regions” in the configuration space where the spacecraft may not enter unless  $JC$  is changed [1,31]. The first application of the concept of “forbidden regions” was used by Hill in 1878 when he proved that the Moon is “permanently attached” to the Earth while obeying a constant  $JC$  throughout its orbit about the Earth in the Sun-Earth-Moon CR3BP [15,31]. The “forbidden regions” are defined by the boundaries where the square of the velocity changes sign, or when  $v^2 = 0$  [31]. Inside the “forbidden region,”  $v^2 < 0$ , so a spacecraft would be required to have an imaginary speed, or a nonphysical value. The “accessible regions” that allow spacecraft motion lie outside these boundaries, where  $v^2 > 0$ . These “zero velocity curves” (ZVCs) are observed as curves in the planar problem and surfaces in the three dimensional case, termed “zero velocity surfaces” (ZVSs) [31]. For a given  $JC$ , there is an infinite number of position component combinations ( $x$ ,  $y$ , and  $z$ ) that will satisfy equation (55). The ZVCs and ZVSs represented by equation (55) encompass these solutions. An example of ZVCs corresponding to specific  $JC$  values in the CR3BP for the Earth-Moon system are seen in Figure 11.

The curves and surfaces seem to evolve for various increasing or decreasing values

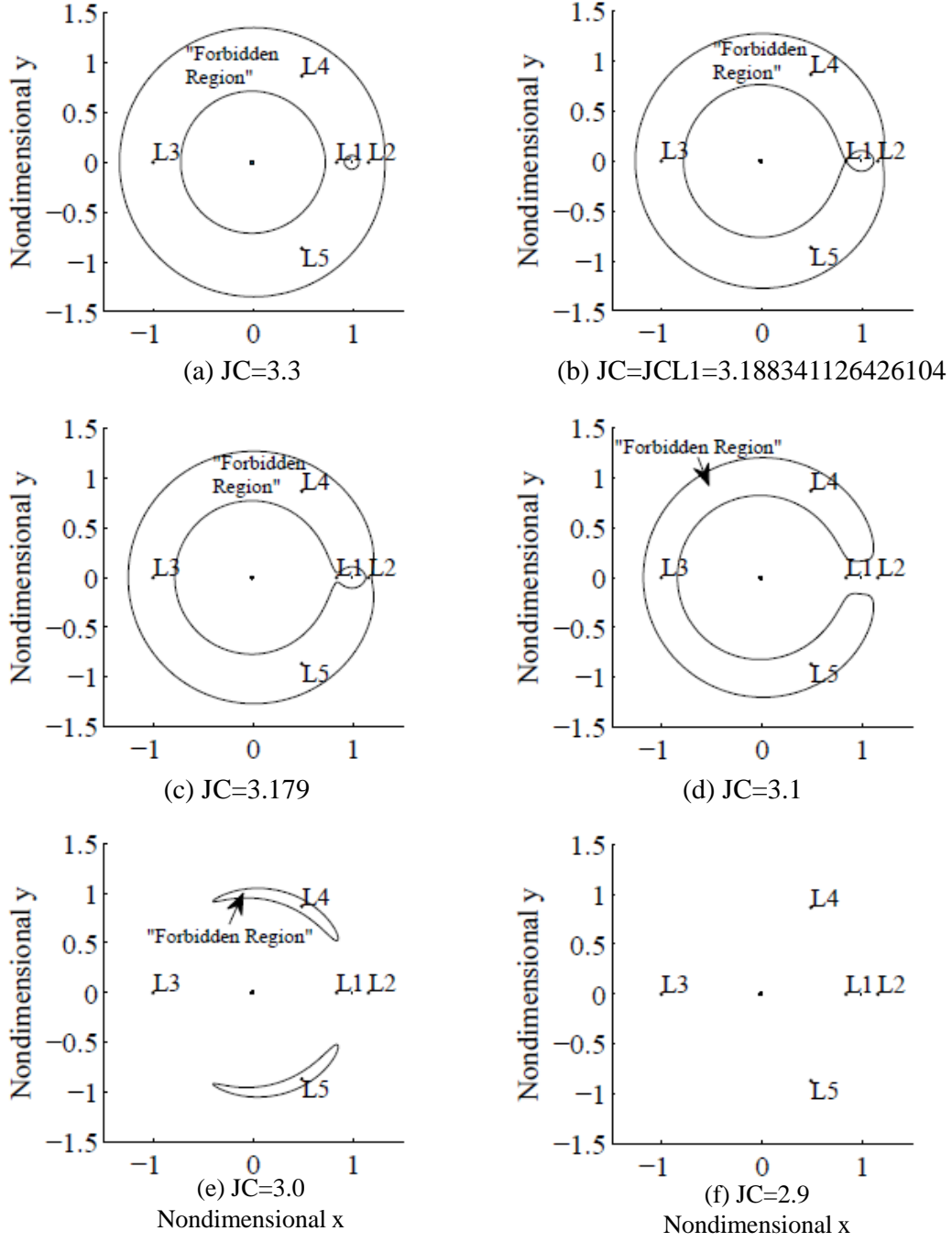


Figure 11. Zero Velocity Curves in Barycentric Rotating Frame of CR3BP for (a)  $JC = 3.3 < J_{CL1}$ , (b)  $JC = J_{CL1} = 3.188341126426104$ , (c)  $JC = 3.179 < J_{CL1}$ , (d)  $JC = 3.1 < J_{CL2}$ , (e)  $JC = 3.0 < J_{CL3}$ , and (f)  $JC = 2.9 < J_{CL45}$ .

of  $JC$ . Hill was the first to work with the ZVCs and ZVSs, but it was Karl Bohlin who first plotted them for the restricted problem in 1887 [31]. For large values of  $JC$  ( $JC > JC_{L_1}$  in the Earth-Moon system), or “low” energy levels, the ZVC accessible regions constitute three distinct curves: one accessible region around the Earth, one around the Moon, and the “exterior” region that lies outside the “forbidden region” (seen in Figure 11 (a)). As the  $JC$  decreases, the ZVCs near the Earth and Moon regions increase in size and the outer curve of the “forbidden region” decreases. When  $JC = JC_{L_1}$ , the curves near the primaries meet exactly at  $L_1$  (Figure 11 (b)). As the  $JC$  decreases further (or as energy level increases), the  $L_1$  “gateway” opens, and a spacecraft starting its trajectory within the interior Earth region of the ZVCs may pass through the  $L_1$  “gateway” and travel around the Moon region, but the spacecraft will never escape the vicinity of the Earth-Moon system by crossing the ZVC boundary without a change in  $JC$  (or energy level) (Figure 11 (c)). Similarly, when  $JC < JC_{L_2}$ , the  $L_2$  “gateway” creates an opening between the “interior” region of the primaries to the “exterior” region beyond the ZVC “forbidden region,” allowing a spacecraft to depart the vicinity of the Earth and Moon (Figure 11 (d)). As the  $JC$  decreases further, the “gateways” to  $L_3$  (Figure 11 (e)) and eventually  $L_4$  and  $L_5$  become accessible (Figure 11 (f)). As the  $JC$  decreases lower than  $JC_{L_4} = JC_{L_5}$ , the evolving curves disappear from the plane, and motion within the plane is no longer bounded. In general, there may still be “forbidden regions” defined by symmetric ZVSs above and below the plane.

## 2.9 Symmetry Properties

Displaying information in the rotating frame of the CR3BP reveals two symmetry properties in the problem, which prove to be useful from a design standpoint. The first symmetry is seen about the  $x$ - $y$  plane (or the plane of the primaries’ motion) [1]. If a



solution trajectory to the CR3BP EOMs (equations (49)-(51)) contains a state of the form:  $[x(t) \ y(t) \ z(t) \ \dot{x}(t) \ \dot{y}(t) \ \dot{z}(t)]^T$ , then another solution exists below the plane of the primaries, with state:  $[x(t) \ y(t) \ -z(t) \ \dot{x}(t) \ \dot{y}(t) \ -\dot{z}(t)]^T$ , and the same follows for all points along the trajectory. The second property is an inherent symmetry in time and also the  $x$ - $z$  plane [1]. In practice, this means that if there is a solution in forward (positive) time and of the form  $[x(t) \ y(t) \ z(t) \ \dot{x}(t) \ \dot{y}(t) \ \dot{z}(t)]^T$ , then the EOMs also yield a solution of the form  $[x(-t) \ -y(-t) \ z(-t) \ -\dot{x}(-t) \ \dot{y}(-t) \ -\dot{z}(-t)]^T$  in negative time. These symmetries are commonly exploited when searching for periodic solutions. Observing this property, Roy states a “Mirror Theorem”:

If  $n$  point masses are acted upon by their mutual gravitational forces only, and at a certain epoch each radius vector from the center of mass of the system is perpendicular to every velocity vector, then the orbit of each mass after that epoch is a mirror image of its orbit prior to that epoch. Such a configuration of radius and velocity vectors is called a mirror configuration [33].

He explains that the second statement is a corollary to the first, and if the  $n$  point masses are only moving according to their mutual gravitational forces, and if a mirror configuration occurs at two separate times along the path, the trajectory is periodic [33].

As an example of one practical application using a symmetry property, a mission designer can compute a periodic orbit in the planar CR3BP that is symmetric in the  $x$ - $y$  plane by the second symmetry property mentioned above. A targeting scheme may utilize an algorithm that will integrate a solution with initial conditions with one perpendicular crossing on the  $x$ -axis until another perpendicular crossing of the  $x$ -axis is reached. Once the targeting scheme converges on a solution for the “top” half of the orbit, the symmetric properties of the CR3BP show that the “bottom” half of the periodic orbit is the mirror image of the “top” over the  $x$ -axis. This ability to reflect

a converged solution from a numerical simulation allows for shorter integration time, convenient both for simulations with longer computational times and for decreasing the numerical error during integration.

## 2.10 Motion Near the Equilibrium Points

While an analytical solution is not available for the CR3BP, a linear stability analysis can be useful for finding an approximate solution near an equilibrium point or a specific trajectory as a reference [1,25]. While exact solutions cannot be yielded, examining linearized equations with small perturbations may give information about how the nonlinear system behaves [1,25]. The stability of the solutions gives indication of the “flow” in the vicinity of the references and the boundedness of the motion [1, 25, 34]. To characterize the motion near the equilibrium solutions of the CR3BP, the variational equations of motion are defined. Recall equations (49)-(51), describing a nonlinear, autonomous, continuous-time system. In general, these EOMs may be written

$$\dot{\vec{X}} = \vec{f}(\vec{X}, t), \quad (62)$$

where  $\vec{f}$  is a smooth function that defines a vector field in  $\mathbb{R}^n$ . A nearby trajectory solution ( $\vec{X}(t)$ ) is equal to some reference solution ( $\vec{X}^*(t)$ ) plus a small variation from that reference ( $\delta\vec{X}(t)$ ), or  $\vec{X}(t) = \vec{X}^*(t) + \delta\vec{X}(t)$ . The method of variation used in this analysis uses isochronous correspondence, meaning same “time” [1]. This method computes a variation that gives a solution,  $\vec{X}(t)$ , occurring at the same time,  $t$ , at which the state,  $\vec{X}^*(t)$ , occurs on the reference trajectory, illustrated in Figure 12 [1].

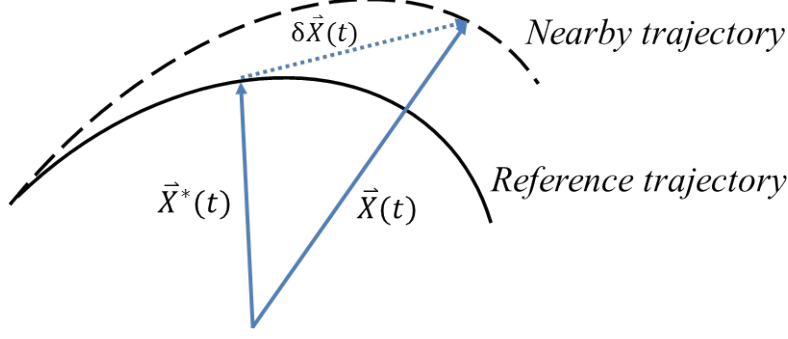


**Figure 12. Notional Variation of a Nearby Trajectory with Respect to a Reference Trajectory by Isochronous Correspondence.**

Perturbing the original state at the initial time ( $t = 0 = t_0$ ), the reference solution at the initial time is of the form  $\vec{X}_0 = [x_0(t) \ y_0(t) \ z_0(t) \ \dot{x}_0(t) \ \dot{y}_0(t) \ \dot{z}_0(t)]^T$ , with small perturbations,  $\zeta(t)$ ,  $\eta(t)$ , and  $\xi(t)$ . This yields the nearby solutions:

$$x(t) = x_0(t) + \xi(t) \quad (63)$$

$$y(t) = y_0(t) + \eta(t) \quad (64)$$

$$z(t) = z_0(t) + \zeta(t) \quad (65)$$

The variational equations of motion are derived by inserting the perturbed solutions into the equations of motion and evaluating at the reference solution. Since the perturbations are assumed to be small, the RHS of each equation is expanded linearly using a first-order Taylor Series Approximation [35], giving the result:

$$\ddot{x}_0(t) + \ddot{\xi}(t) - 2\dot{y}_0(t) - 2\dot{\eta} = \left. \frac{\partial U^*}{\partial x} \right|_{\vec{X}_0} + \left. \frac{\partial^2 U^*}{\partial x^2} \right|_{\vec{X}_0} \xi + \left. \frac{\partial^2 U^*}{\partial x \partial y} \right|_{\vec{X}_0} \eta + \left. \frac{\partial^2 U^*}{\partial x \partial z} \right|_{\vec{X}_0} \zeta + \dots \quad (66)$$

$$\ddot{y}_0(t) + \ddot{\eta}(t) + 2\dot{x}_0(t) + 2\dot{\xi} = \left. \frac{\partial U^*}{\partial y} \right|_{\vec{X}_0} + \left. \frac{\partial^2 U^*}{\partial y \partial x} \right|_{\vec{X}_0} \xi + \left. \frac{\partial^2 U^*}{\partial y^2} \right|_{\vec{X}_0} \eta + \left. \frac{\partial^2 U^*}{\partial y \partial z} \right|_{\vec{X}_0} \zeta + \dots \quad (67)$$

$$\ddot{z}_0(t) + \ddot{\zeta}(t) = \left. \frac{\partial U^*}{\partial z} \right|_{\vec{X}_0} + \left. \frac{\partial^2 U^*}{\partial z \partial x} \right|_{\vec{X}_0} \xi + \left. \frac{\partial^2 U^*}{\partial z \partial y} \right|_{\vec{X}_0} \eta + \left. \frac{\partial^2 U^*}{\partial z^2} \right|_{\vec{X}_0} \zeta + \dots, \quad (68)$$

where  $\frac{\partial^2}{\partial x \partial y} = \frac{\partial^2}{\partial y \partial x}$ ,  $\frac{\partial^2}{\partial y \partial z} = \frac{\partial^2}{\partial z \partial y}$ , and  $\frac{\partial^2}{\partial x \partial z} = \frac{\partial^2}{\partial z \partial x}$  since the system is continuous, and each expression also includes higher order terms that are neglected in this linear approximation. Also note that  $U^*(t)$ ,  $x(t)$ ,  $y(t)$ , and  $z(t)$  are all functions of time in general, but the time terms, “(t),” are left off for simplicity from this point forward in this investigation. The reference terms (those corresponding with the original solution) on the LHS and the first term in the linear expansion on the RHS in each equation are equivalent by the original equations of motion. Using the same abbreviation for the partial derivative of  $U^*$  as in equations (49)-(51) in Section 2.7 and simplifying further, the linearized variational equations of motion for small perturbations, evaluated at a reference solution are below:

$$\ddot{\xi} - 2\dot{\eta} = U^*_{xx}|_{\vec{X}_0} \xi + U^*_{xy}|_{\vec{X}_0} \eta + U^*_{xz}|_{\vec{X}_0} \zeta \quad (69)$$

$$\ddot{\eta} + 2\dot{\xi} = U^*_{xy}|_{\vec{X}_0} \xi + U^*_{yy}|_{\vec{X}_0} \eta + U^*_{yz}|_{\vec{X}_0} \zeta \quad (70)$$

$$\ddot{\zeta} = U^*_{xz}|_{\vec{X}_0} \xi + U^*_{yz}|_{\vec{X}_0} \eta + U^*_{zz}|_{\vec{X}_0} \zeta \quad (71)$$

Equations (69)-(71) are the variational EOMs that represent the linearized motion of perturbations near a reference solution. Since the perturbations are assumed to be small, these EOMs are also a decent approximation of the nonlinear dynamical “flow” near the reference [25, 32]. The following methodology for examining the linear system is based on development by Geisel [25, 32]. Since solutions to the EOMs are expressed in the form  $[x \ y \ z \ \dot{x} \ \dot{y} \ \dot{z}]^T = [\vec{r} \ \vec{v}]^T$ , where position  $\vec{r} = [x \ y \ z]^T$ , and velocity  $\vec{v} = [\dot{x} \ \dot{y} \ \dot{z}]^T$ , the variations of position and velocity may be expressed  $\delta \vec{X} = [\delta \vec{r} \ \delta \vec{v}]^T = [\delta x \ \delta y \ \delta z \ \delta \dot{x} \ \delta \dot{y} \ \delta \dot{z}]^T = [\xi \ \eta \ \zeta \ \dot{\xi} \ \dot{\eta} \ \dot{\zeta}]^T$  [32]. The variational equations can then be written in first-order differential form of a linear system,

$$\delta \dot{\vec{X}} = A(t) \delta \vec{X}, \quad (72)$$

where  $A(t)$ , defined below in equation (73), is the Jacobian matrix of  $\vec{f}$ , and in general, is not constant [25, 32].

$$A(t) = \begin{bmatrix} 0_{3 \times 3} & I_{3 \times 3} \\ B & \Omega \end{bmatrix}, \quad (73)$$

where  $0_{3 \times 3}$  is the  $3 \times 3$  null matrix,  $I_{3 \times 3}$  is the  $3 \times 3$  identity matrix,

$$B = \begin{bmatrix} U_{xx}^* & U_{xy}^* & U_{xz}^* \\ U_{xy}^* & U_{yy}^* & U_{yz}^* \\ U_{xz}^* & U_{yz}^* & U_{zz}^* \end{bmatrix}, \quad (74)$$

and,

$$\Omega = \begin{bmatrix} 0 & 2 & 0 \\ -2 & 0 & 0 \\ 0 & 0 & 0 \end{bmatrix}. \quad (75)$$

Defining the reference solution as an equilibrium solution of the CR3BP, a nearby solution is described,

$$\vec{X} = \vec{X}_{eq} + \delta \vec{X}, \quad (76)$$

where  $\vec{X}_{eq}$  represents the state vector at the libration point. Linearizing the system with reference to the equilibrium point gives equation (72), where

$$A = \begin{bmatrix} 0_{3 \times 3} & I_{3 \times 3} \\ B_{eq} & \Omega \end{bmatrix} \quad (77)$$

and,

$$B_{eq} = \begin{bmatrix} U_{xx0}^* & U_{xy0}^* & 0 \\ U_{xy0}^* & U_{yy0}^* & 0 \\ 0 & 0 & U_{zz0}^* \end{bmatrix}, \quad (78)$$

where  $U_{pq0}^*$  represents the second partial derivative evaluated at the equilibrium point [30]. Note that in this special case, the  $A$  matrix is a constant matrix [8]. The  $A$  matrix is used to calculate a characteristic equation for the system, from which the eigenvalues are examined to determine stability [13, 25]. Since each libration point lies within the  $x$ - $y$  plane ( $z_i = 0$ ),  $U_{xz0}^* = U_{zx0}^* = U_{yz0}^* = U_{zy0}^* = 0$  and  $U_{zz0}^* < 0$ . The linear variational equations are written,

$$\ddot{\xi} - 2\dot{\eta} = U_{xx0}^*\xi + U_{xy0}^*\eta \quad (79)$$

$$\ddot{\eta} + 2\dot{\xi} = U_{yx0}^*\xi + U_{yy0}^*\eta \quad (80)$$

$$\ddot{\zeta} = U_{zz0}^*\zeta \quad (81)$$

It is clear from the equations above that for the linearized system, the in-plane and out-of-plane motion is decoupled for each equilibrium point. Note that in general, no claims may be made about the motion for the nonlinear system.

Meirovitch defines the conditions for stability that can be applied to characterize the equilibrium points (and motion near them) in this linear stability analysis. He states, “If all the characteristic exponents associated with [equation (72)] possess negative real parts, then the periodic [or equilibrium] solution of the complete system [equation (62)] is asymptotically stable” [13]. The characteristic exponents are the eigenvalues of the  $A$  matrix for the system, or the roots of the characteristic equation. He continues, “If there is at least one characteristic exponent associated with [equation (72)] with a positive real part, then the periodic [or equilibrium] solution of the

complete system [equation (62)] is unstable” [13]. The definition goes on to explain that if roots are purely imaginary, oscillatory motion is exhibited and the solution is marginally stable [13, 25].

If the system contains at least one root that is positive real and at least one that is negative real, the solution is unstable by Lyapunov stability, but is commonly said to be “nonstable” and characterized as a saddle point in terms of the “flow” of stability. Isochronous correspondence between a solution and its reference as it is used here leads to this definition of Lyapunov stability, which is just one of numerous stability definitions that could be applied to this analysis [1]. The characteristic equation for the out-of-plane motion produces pure imaginary roots, associated with marginal stability. Since  $U_{zz0}^*$  is a negative constant, the out-of-plane motion is a simple harmonic oscillator in the  $\hat{z}$  direction in the form  $\ddot{\zeta} + \omega^2\zeta = 0$ . The period of oscillation for each point can be calculated using:

$$T = \frac{2\pi}{\sqrt{\|U_{zz0}^*\|}}, \quad (82)$$

where, in fact, this is exactly  $2\pi$  for the triangular points ( $L_4$  and  $L_5$ ). The out-of-plane motion is characterized as a marginally stable, 2-D center [1, 25, 32]. Though the equilibrium points are characterized as marginally stable in terms of their out-of-plane behavior in the linear system, a prediction for the stability of the points in the nonlinear system may not be made [1]. To conduct a stability analysis of in-plane motion near the equilibrium points,  $\det(\lambda I - A_{eq}) = 0$  is evaluated for  $\delta\dot{\vec{X}} = A_{eq}\delta\vec{X}$  to get the characteristic equation of the linearized system:

$$\lambda^4 + (4 - U_{xx}^* - U_{yy}^*)\lambda^2 + (2U_{xy}^* - U_{yx}^*)\lambda + (U_{xx}^*U_{yy}^* - U_{xy}^{*2}) = 0, \quad (83)$$

where the second term is zero since  $U_{xy}^* = U_{yx}^*$ . Considering the collinear libration

points,  $L_1$ ,  $L_2$ , and  $L_3$ , note that  $y_{Li} = z_{Li} = 0$ ,  $U_{xx}^* > 0$ , and  $U_{yy}^* < 0$ . For simplicity,  $\lambda = \pm\Lambda^{\frac{1}{2}}$ ,

$$\beta_1 = 2 - \left( \frac{U_{xx}^* + U_{yy}^*}{2} \right), \quad (84)$$

and,

$$\beta_2^2 = -U_{xx}^* U_{yy}^* > 0 \quad (85)$$

are defined. The quadratic formula then gives,

$$\Lambda_1 = -\beta_1 + (\beta_1^2 + \beta_2^2)^{\frac{1}{2}} > 0 \quad (86)$$

and,

$$\Lambda_2 = -\beta_1 - (\beta_1^2 + \beta_2^2)^{\frac{1}{2}} < 0, \quad (87)$$

which implies that  $\lambda_{1,2} = \pm\sqrt{\Lambda_1}$  represent the real roots of the characteristic equation (equation (83)) and  $\lambda_{3,4} = \pm\sqrt{\Lambda_2}$  represent the imaginary roots. Solutions then take the typical form for ordinary linear differential equations [36]:

$$\xi = \sum_{i=1}^4 M_i e^{\lambda_i t} \quad (88)$$

$$\eta = \sum_{i=1}^4 N_i e^{\lambda_i t} \quad (89)$$

In general, there is always one term with a positive real root in the exponent that indicates an unbounded value for  $\xi$  and  $\eta$  as  $t \rightarrow \infty$ . This ascertains that the solution is unstable [1, 13, 25]. Since this analysis characterizes the linearized system, only under certain conditions can the stability of the nonlinear system be made. The sufficient condition for determining if the nonlinear system is locally asymptotically stable (with respect to that equilibrium point) is met if the linear system is classified as asymptotically stable by observing the eigenvalues with all



negative real parts [1]. If any of the real parts are positive, the equilibrium point is classified unstable [1]. The stability exponents for Hamiltonian systems such as this one also occur as positive/negative pairs, so unstable and purely imaginary values are the only cases permitted [20]. If some of the roots are zeros or are purely imaginary, no stability claims can be made about the nonlinear system. In this analysis, the indication of instability also holds true for the nonlinear system. Also note that the coefficients  $M_i$  and  $N_i$  are not independent, but related by  $\alpha_i$ , defined below:

$$N_i = \left( \frac{\lambda_i^2 - U_{xx}^*}{2\lambda_i} \right) M_i = \alpha_i M_i \quad (90)$$

The initial conditions can then be written,

$$\xi_0 = \sum_{i=1}^4 M_i e^{\lambda_i t_0} \quad (91)$$

$$\dot{\xi}_0 = \sum_{i=1}^4 \lambda_i M_i e^{\lambda_i t_0} \quad (92)$$

$$\eta_0 = \sum_{i=1}^4 \alpha_i M_i e^{\lambda_i t_0} \quad (93)$$

$$\dot{\eta}_0 = \sum_{i=1}^4 \lambda_i \alpha_i M_i e^{\lambda_i t_0} \quad (94)$$

and the initial conditions associated with the  $N_i$  terms are of similar form. It is also possible to express the coefficients  $M_i$  and  $N_i$  in terms of these initial conditions [1]. By defining stability by the presence of an unbounded term in the solution, the collinear equilibrium points themselves are “unstable” [1,13]. However, the motion in the vicinity of each point may exhibit interesting characteristics or “modes.” These modes are associated with the characterization of subspaces within the 6-D dynamical “flow.” The initial conditions may be manipulated in such a way as to suppress the

unbounded behavior and only generate bounded motion [1, 25]. Notice the  $M_1$  and  $M_2$  coefficients are associated with the positive real exponents,  $\lambda_1$  and  $\lambda_2$ , which express the unstable motion [1, 13]. The initial conditions may then be chosen such that  $M_1 = M_2 = 0$ , and the resulting particular solutions contain only  $M_3$  and  $M_4$ , which exhibit oscillatory behavior in the linear model [1, 13]. These different modes are connected to the stable and unstable subspaces associated with the phase space “flow.” In the CR3BP, each collinear libration point is characterized as a nonstable 2-D center  $\times$  2-D center  $\times$  2-D saddle (2-D center  $\times$  2-D saddle in the planar CR3BP) [13, 25, 32].

Recall the characteristic equation (equation (83)) and consider the triangular equilibrium points. The  $x$  and  $y$  positions of  $L_4$  and  $L_5$  are,

$$x_{L_{4,5}} = \frac{1}{2} - \mu \quad (95)$$

and

$$y_{L_{4,5}} = \pm \frac{\sqrt{3}}{2}. \quad (96)$$

This results in the simplified characteristic equation,

$$\Lambda^2 + \Lambda + \frac{27}{4}\mu(1 - \mu) = 0. \quad (97)$$

Defining  $g = 1 - 27\mu(1 - \mu)$ ,

$$\Lambda = \frac{1}{2} - 1 \pm \sqrt{g}, \quad (98)$$

which leads to the linear stability of  $L_4$  and  $L_5$  with a dependence on the mass ratio of the system,  $\mu$ . When  $0 < g \leq 1$ , the mass ratio is in the range  $0 < \mu \leq \mu_0$ , where  $\mu_0$  is the critical mass ratio value, and the triangular points are marginally stable [1, 25]. This leads to imaginary roots of the characteristic equation, and the linearized motion

is bounded [1,25]. This 4-D center characterization is a superposition of two harmonic oscillators with different frequencies [1,25]. Similar to the collinear points, the proper choice of initial conditions may excite one frequency and suppress the other to achieve a certain desired result. Periodic orbits about these points may also be obtained when both frequencies are present if the ratio of their values is a rational number for some  $\mu$  [1,25]. When  $g = 0$ ,  $\mu = \mu_0 = \frac{(1-\sqrt{\frac{23}{27}})}{2} = 0.0385$ . If a system has this mass ratio, the two frequencies are equal, and periodic motion is exhibited in the linear model. Lastly, when  $g < 0$ ,  $\mu > \mu_0$ , and the resultant roots are complex conjugates [1,25]. This leads to unbounded behavior in the linear system, and it can then be claimed that both the linear and nonlinear systems are unstable [1,25]. Notice that for most systems in the solar system, including the Earth-Moon CR3BP, a triangular point is characterized as a marginally stable 2-D center  $\times$  2-D center  $\times$  2-D center (or a 6-D center). A notable exception of this observation is seen in the Pluto-Charon CR3BP, in which the triangular points are classified as unstable.

## 2.11 State Transition Matrix

To examine a trajectory in the CR3BP, a set of initial conditions is selected, and the equations of motion are numerically integrated for a selected amount of time to generate a specific simulation for those conditions. It is possible that the integrated trajectory shown by this solution does not have the desired characteristics for the mission design. While that simulation displays the trajectory in question, there is no information available about nearby solutions. To examine how nearby solutions behave, a mission planner may try a selection of nearby initial conditions, but this would lead to an infinite number of simulations to numerically integrate and observe in the total phase space. The standard way to obtain information about the nearby trajectories is by utilizing the variational equations and the State Transition

Matrix (STM). This method assumes that the integrator used is reliable and that the astrodynamicist has some insight into how the nearby solutions act [20]. The STM, also called the “guidance matrix” or “sensitivity matrix,” determines how sensitive the final trajectory is to the initial conditions input to the system [20, 25].

Considering the variational equations of motion in equation (72), notice that because this is a linear set of equations, the addition of any two solutions to the set is also a solution, and the general solution is constructed from a fundamental set of solutions,  $\vec{\phi}_i(t)$ . Contained in this fundamental solution vector are  $n$  independent solutions to equation (72) with initial conditions such that  $\phi_{ij}(t_0) = \delta_{ij}$ , where  $\delta_{ij}$  is the Kroenecker delta. A solution satisfying a general set of initial conditions is represented by a scaled combination of solutions,

$$\delta\vec{X}(t) = \sum_{j=1}^n \vec{\phi}_j(t) \delta x_j(t_0). \quad (99)$$

A solution function at the initial time,  $t_0$ , with initial conditions of the form in equation (99) is also a solution at some other time,  $t$ . Since equation (99) has the correct initial conditions for any nearby trajectory, it is the general solution to equation (72). Replacing equation (99) with a matrix formulation, the STM,  $\Phi(t, t_0)$ , is defined to be a square matrix with the  $n$  independent solutions,  $\vec{\phi}_i$ , as columns. With initial conditions,

$$\Phi(t_0, t_0) = I, \quad (100)$$

$\Phi$  satisfies the differential equation,

$$\dot{\Phi}(t, t_0) = A(t)\Phi(t, t_0), \quad (101)$$

which is the governing equation for the STM. Equation (99) can then be written

$$\delta \vec{X}(t) = \Phi(t, t_0) \delta \mathbf{x}(t_0), \quad (102)$$

which is also the general solution to equation (72). The STM also has two useful properties:

$$\Phi(t_2, t_0) = \Phi(t_2, t_1) \Phi(t_1, t_0) \quad (103)$$

and

$$\Phi(t_0, t_1) = \Phi^{-1}(t_1, t_0) \quad (104)$$

The STM is mathematically defined as the derivative of the state solution at a given  $t$  with respect to the initial conditions at  $t_0$ , or the Jacobian matrix of the solution [8].

In terms of the partial derivatives, the STM is defined:

$$\Phi(t, t_0) = \begin{bmatrix} \frac{\partial x(t)}{\partial x(t_0)} & \frac{\partial x(t)}{\partial y(t_0)} & \frac{\partial x(t)}{\partial z(t_0)} & \frac{\partial x(t)}{\partial \dot{x}(t_0)} & \frac{\partial x(t)}{\partial \dot{y}(t_0)} & \frac{\partial x(t)}{\partial \dot{z}(t_0)} \\ \frac{\partial y(t)}{\partial x(t_0)} & \frac{\partial y(t)}{\partial y(t_0)} & \frac{\partial y(t)}{\partial z(t_0)} & \frac{\partial y(t)}{\partial \dot{x}(t_0)} & \frac{\partial y(t)}{\partial \dot{y}(t_0)} & \frac{\partial y(t)}{\partial \dot{z}(t_0)} \\ \frac{\partial z(t)}{\partial x(t_0)} & \frac{\partial z(t)}{\partial y(t_0)} & \frac{\partial z(t)}{\partial z(t_0)} & \frac{\partial z(t)}{\partial \dot{x}(t_0)} & \frac{\partial z(t)}{\partial \dot{y}(t_0)} & \frac{\partial z(t)}{\partial \dot{z}(t_0)} \\ \frac{\partial \dot{x}(t)}{\partial x(t_0)} & \frac{\partial \dot{x}(t)}{\partial y(t_0)} & \frac{\partial \dot{x}(t)}{\partial z(t_0)} & \frac{\partial \dot{x}(t)}{\partial \dot{x}(t_0)} & \frac{\partial \dot{x}(t)}{\partial \dot{y}(t_0)} & \frac{\partial \dot{x}(t)}{\partial \dot{z}(t_0)} \\ \frac{\partial \dot{y}(t)}{\partial x(t_0)} & \frac{\partial \dot{y}(t)}{\partial y(t_0)} & \frac{\partial \dot{y}(t)}{\partial z(t_0)} & \frac{\partial \dot{y}(t)}{\partial \dot{x}(t_0)} & \frac{\partial \dot{y}(t)}{\partial \dot{y}(t_0)} & \frac{\partial \dot{y}(t)}{\partial \dot{z}(t_0)} \\ \frac{\partial \dot{z}(t)}{\partial x(t_0)} & \frac{\partial \dot{z}(t)}{\partial y(t_0)} & \frac{\partial \dot{z}(t)}{\partial z(t_0)} & \frac{\partial \dot{z}(t)}{\partial \dot{x}(t_0)} & \frac{\partial \dot{z}(t)}{\partial \dot{y}(t_0)} & \frac{\partial \dot{z}(t)}{\partial \dot{z}(t_0)} \end{bmatrix}. \quad (105)$$

The equations of variation (equation (101)) can be numerically integrated simultaneously with the nonlinear EOMs (equation (62)) at every time step, and a time history of the elements in  $\Phi(t, t_0)$  is generated [20, 25]. Since there is no closed-form analytical solution to the CR3BP, observing the system response to a set of initial conditions through the STM is valuable. Targeting algorithms and continuation schemes utilize the STM in searching for trajectories near a reference solution.

Another useful characteristic of the STM is that because of its initial conditions

(equation (100)), the determinant of the STM is exactly equal to one. Liouville’s theorem validates that it should also remain equal to one for all time as the STM is integrated simultaneously with the EOMs. The theorem describes the motion of an element of the phase space as a volume element of a fluid; in general, the element changes shape, but has a constant volume, and the nearby particles remain close [37]. Liouville’s theorem implies that the phase space of the CR3BP is incompressible, so the determinant of the STM should always be equal to one. The constant unity determinant of the STM gives another metric (along with  $JC$ ) to track the error in a numerical simulation.

## 2.12 Periodic Orbits

Famously known as his conjecture on periodic orbits, Poincaré stated: “If a particular solution of the restricted problem is given, one can always find a periodic solution (with period which might be very long) such that the difference between these two solutions is as small as desired for any length of time” [1]. His conjecture suggests using a periodic orbit as a reference orbit [1]. First order linear approximations for periodic orbits near the non-stable, collinear libration points are used to obtain families of these orbits. A periodic orbit in the CR3BP is never found in a singular isolated occurrence; there are also other members of an orbital “family” nearby. This is due to the nature of the eigenvalues of the STM for one revolution of a periodic orbit: two eigenvalues are equal to one, which is associated with the periodicity of the orbit and an indication that there are other orbits nearby that have similar characteristics.

Near the collinear libration points, orbit families with different characteristics such as Lyapunov, Halo, Vertical, and Axial families may be generated using various targeting algorithms, which will be discussed further in Section 3.1 [38]. Each orbit in the respective grouping of orbits is a “member” of the family and is in some way

related to the previous family member [25, 39, 40]. Each orbit is generated from the last, so the next orbit somehow resembles the last in some or all parts of the phase space. Stability of a single orbit depends on the eigenvalues of the monodromy matrix, or the STM of the orbit for one complete period [25, 39, 40]. Stability trends are seen as family members are examined, and a bifurcation occurs where a change in stability is observed between family members [25, 39]. The Jacobi Constant also changes with each family member, and the period of a specific orbit in the family can be unique for each member. The periodic orbit families may be relatively easily generated with a continuation algorithm, and the information about each family member may be recorded for the purpose of choosing a specific family member depending on design constraints or specific needs of a mission. In order to exploit the properties of certain periodic orbits in the CR3BP, a stability analysis is done to determine the types of possible motion in the space. The eigenvalues associated with the monodromy matrix provide the stability information for analysis [25, 39, 40]. While the linearized stability analysis of an equilibrium point refers to a definition of isochronous correspondence and characterization based on Lyapunov stability, the analysis of orbital stability in this investigation uses normal correspondence, where the perturbed solution,  $\vec{X}(t)$ , is defined in a direction exactly normal from the reference state,  $\vec{X}^*(t)$ , on the reference trajectory, depicted in Figure 13 [1].

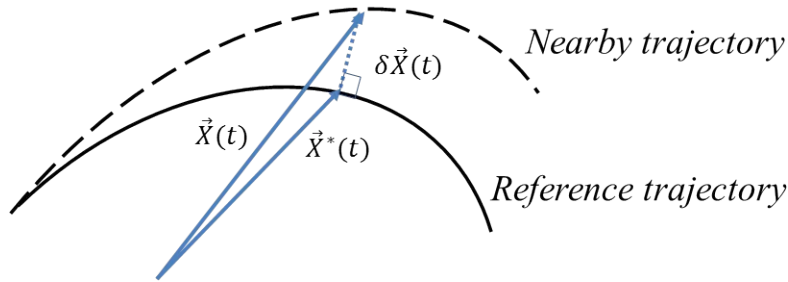


**Figure 13. Notional Variation of a Nearby Trajectory with Respect to a Reference Trajectory by Normal Correspondence (Adapted from Szebehely [1]).**

While normal correspondence is associated with orbital stability analysis, Floquet

Theory gives a relation that lets an astrodynamicist treat the system in the same way as with a Lyapunov stability analysis (see Section 2.10). Recall that the  $A$  matrix is in general time-varying, but it is a constant coefficient matrix when linearizing about the equilibrium points [20]. In the case of linearizing about a periodic orbit, the  $A$  matrix is periodic [20]. Floquet discovered the solution to the periodic coefficient linear system, which gives stability information about the orbit similar to solving the constant coefficient linearized equations about an equilibrium point [20]. Floquet theory indicates that the STM can be written in the form:

$$\Phi(t, 0) = F(t)e^{Jt}F^{-1}(0), \quad (106)$$

where  $F(t)$  is a periodic matrix, and  $J$  is a Jordan normal form matrix and usually diagonal, where the diagonal elements are the system frequencies [20]. When describing a periodic orbit that starts and ends at the same point,  $t = T$  and  $F(T) = F(0)$ , where  $T$  is one orbital period. Inserting this information and rearranging equation (106), the result is

$$e^{Jt} = F^{-1}(0)\Phi(T, 0)F(0), \quad (107)$$

which is an explicit statement that  $F(0)$  is a constant matrix of the eigenvectors corresponding to the monodromy matrix,  $\Phi(T, 0)$ , from the definition of eigenvectors,  $\Phi(t_0 + T, t_0)\vec{v}_i(t_0) = \lambda_i\vec{v}_i(t_0)$ . The statement in equation (107) also indicates that

$$\lambda_i = e^{\omega_i t}, \quad (108)$$

which states that the eigenvalues,  $\lambda_i$  are related to  $\omega_i$ , the Poincaré exponents of  $J$  (or the system frequencies). In other words, the Poincaré exponents may be treated like the eigenvalues of a constant coefficient system. In general, for Hamiltonian systems without dissipation (such as this case), the only cases for a pair of  $\omega_i$  are (1)



positive/negative pure imaginary numbers or (2) positive/negative real numbers [20]. From the relation in equation (108), this indicates that the eigenvalues of the monodromy matrix will occur in reciprocal pairs [1, 13, 20, 25, 32]. The linear system can now be evaluated as a discrete time problem; instead of characterizing the eigenvalues based on if their locations are on the left or right side of the complex plane, the characteristic multiplier values are evaluated based on if their locations are inside or outside the unit circle. The monodromy matrix computed in an analysis of a 3-D orbit possesses six eigenvalues. Two of these will be equal to one on the real axis and on the unit circle (also with unit magnitude). These unity eigenvalues are associated with the periodicity of the orbit and also indicate marginal stability (a 2-D center) [1, 13, 25].

For a periodic orbit in the spatial CR3BP, there is typically at least one positive/negative conjugate pair on the unit circle (each with unit magnitude), which is associated with marginal stability (classified as a 2-D center). For the planar CR3BP, there is one pair equal to one, and the other pair may be on the unit circle or on the real axis. An eigenvalue that is outside the unit circle indicates instability, while an eigenvalue inside the unit circle implies asymptotic stability. When one eigenvalue in a pair lies inside the unit circle, and the other lies outside, this is associated with a 2-D saddle. In the spatial CR3BP, it is possible to observe a 2-D center x 2-D center x 2-D saddle (2-D center x 2-D saddle in the planar problem), which is referred to as an unstable periodic orbit (UPO). A periodic orbit classified as a 6-D center is referred to as a “stable” periodic orbit, though marginal stability is the best stability an orbit can achieve through the linear analysis. The statements about nonlinear stability conclusions based on the linear stability analysis when classifying the equilibrium points also hold true for the stability of periodic orbits. Since marginal stability is the “most” stable classification that an orbit may have, orbits that are asymptotically

stable are not observed in the CR3BP. When the linear stability analysis of a periodic orbit reveals marginally stable behavior, no claims on the stability of the orbit in the nonlinear system can be made. When an orbit is classified as unstable or “nonstable” in the linear stability analysis, this indicates that the orbit is also unstable in the nonlinear system.

A bifurcation occurs when there is a change in stability examined while investigating a larger group of orbits, or a family of the same type of orbit [38]. Another type of orbit, or another family altogether, may result from a change of stability, stemming from the closest orbit found near the bifurcation point. For example, as the stability information is examined of the periodic “Lyapunov” orbit family about the  $L_1$  equilibrium point (looking from the smallest to the largest members of the family), a bifurcation is approached as one pair of characteristic multipliers (either associated with the stable and unstable subspaces or the center subspace) approaches  $\pm 1$  from the real axis or from along the unit circle. When this pair is exactly  $\pm 1$ , this is possibly the intersection of two different families (a bifurcation point). There are multiple continuation methods that exploit this observation to compute families of orbits (see Section 3.2).

The exact location of bifurcation orbits can be approximated using continuation and a method of bisections. This location is found by observing a change in eigenstructure. One way this can happen is when a characteristic multiplier leaves the unit circle and goes to the real axis (or comes to the unit circle from the real axis). During a continuation process, this change in eigenstructure can occur between two computed solutions. Consider the family of planar Lyapunov orbits around  $L_1$ . The initial state for exactly midway between these two solutions can be computed using the lower of the two solution states surrounding the bifurcation solution where  $\Delta x$  is a defined step size ( $\Delta x = 0.0006$  nondimensional units was typically used in this

investigation) that moves along the  $x$ -axis,

$$\vec{\mathbf{X}}^{midway} = \vec{\mathbf{X}}^{lower} + \frac{\Delta x}{2} \cdot \vec{\mathbf{X}}^{lower}. \quad (109)$$

The eigenstructure of the midway orbit is then observed to determine whether the bifurcation solution is between  $\vec{\mathbf{X}}^{lower}$  and  $\vec{\mathbf{X}}^{midway}$ , or above  $\vec{\mathbf{X}}^{midway}$ . Redefining the “lower” solution, the new midway state can be computed:

$$\vec{\mathbf{X}}^{midway} = \vec{\mathbf{X}}^{lower} + \frac{\Delta x}{4} \cdot \vec{\mathbf{X}}^{lower}. \quad (110)$$

This process is continued until the bifurcation is detected to be sufficiently close, or when the characteristic multiplier approaching a change in stability is within some tolerance of  $\pm 1$ , where the step size is reduced by a factor of 2 with every prediction. Since a bifurcation is a potential indication of the presence of another orbit family, a perturbation in the direction of the suspected family member may give a successful initial guess to target those orbits. The stability analysis of periodic orbits also leads to structures in the phase space called invariant manifolds. The application of these structures for use in mission design begins with the study of Dynamical Systems Theory.

### 2.13 Dynamical Systems Theory

Dynamical Systems Theory (DST) presents a modern and potentially fuel-saving set of tools for mission design in a multi-body environment. Different modes of dynamical “flow” can exist for a nonlinear system in a multi-body environment, like the CR3BP. The phase space can be analyzed to evaluate the “flow” of trajectories in the vicinity of points or bodies of interest [20]. In this study, invariant manifolds associated with unstable periodic orbits around the Earth-Moon libration points are

exploited to investigate favorable trajectory options near the Earth or equilibrium points in the Earth-Moon system. An intersection in the full phase space of trajectories on these manifolds present an opportunity for theoretically “free” (zero- $\Delta V$ ) transfers from one orbit to another. The Genesis spacecraft mission trajectory employed these methods [41]. The stable manifold of an unstable periodic orbit contains the set of all possible trajectories that approach the unstable periodic orbit in infinite time. The stable manifold associated with an unstable periodic orbit around the Sun-Earth libration point between the Earth and the Sun, L1, was examined in the Genesis mission design [41].

The present investigation also explores the use of unconventional transfers between mission orbits using some of DST’s techniques. Libration point orbits (LPOs) are studied to compute families of orbits and to provide potential starting and destination points in some contingency options in test cases. Note the use of orbits about libration points in the Earth-Moon and other systems is not currently considered of utmost military importance; however, the concepts and tools used for complex dynamical analysis for more prominent military missions can be investigated and showcased in missions leading to and from orbits about libration points. Using periodic orbits around libration points can give spacecraft on those particular trajectories a close-up and consistent view of the closest primary body. Spacecraft traveling close to libration point locations also may have the opportunity of utilizing the minimal (theoretically “free”)  $\Delta V$  transfers between stable and unstable invariant manifolds of unstable periodic orbits.

The International Sun-Earth Explorer-3 (ISEE-3) was the first spacecraft with a mission to travel to one of these LPOs. Launched in 1978, ISEE-3 went into orbit around the  $L_1$  libration point of the Sun-Earth system where it investigated the boundaries of the Earth’s magnetosphere and examined the structure of the solar

wind near the Earth [42, 43]. Later, launched in 1995, the Solar and Heliospheric Observatory (SOHO) traveled to the same point for an unobstructed view of the Sun to study from its deep core to the outer corona and solar wind [44]. SOHO gives up to three days notice for Earth-directed disturbances like Coronal Mass Ejections (CMEs) and radiation storms [45]. The Advanced Composition Explorer (ACE) also resides at the Sun-Earth  $L_1$  libration point, giving early warning of potentially hazardous geomagnetic storms since its launch in 1997 [46]. As of 2009, the Planck spacecraft orbits the Sun-Earth  $L_2$  libration point, looking into the cosmic microwave background and giving the best view of the earliest moments in cosmic history [47]. The advantages of spacecraft in LPOs led to further study of lower-energy methods for transfer. Hiten was the first spacecraft to demonstrate one of these lower-energy trajectories as it passed by the Earth-Moon  $L_4$  and  $L_5$  libration points and completed ten lunar fly-bys before orbiting around and landing on the Moon [48, 49]. In 1968, Conley published a preliminary description of low-energy transfers in the Earth-Moon system using orbits transiting near the collinear equilibrium points in the restricted three-body problem [50].

Others took Conley's work further, developing other useful tools in DST to design lower-energy transfers. There are many recent examples of research in this area. Davis, Anderson, and Born specifically explored the mission design of a low-energy transfer beginning in LEO, inserting onto a stable manifold trajectory of an LPO in the Earth-Moon system to ultimately arrive in GEO [51]. In 2001, the Genesis mission was the first project to actualize the trajectory design concept of using invariant manifolds as pathways for transfers. The Genesis spacecraft's mission was to collect solar wind samples from a region beyond the Earth's magnetosphere and return them to Earth [41]. The spacecraft was directly inserted onto a stable manifold trajectory associated with an unstable periodic orbit around the Sun-Earth  $L_1$

libration point. The spacecraft traveled to the unstable periodic orbit, performed its sample collection, and started its return trip on an unstable manifold trajectory leading from the unstable periodic orbit. The spacecraft took advantage of a “heteroclinic” connection between the unstable manifold associated with  $L_1$  periodic orbit and performed a deterministically “free” (zero- $\Delta V$ ) maneuver to a stable manifold trajectory associated with an unstable periodic orbit around the Sun-Earth  $L_2$  libration point [8]. The spacecraft completed a loop around  $L_2$  on the stable manifold trajectory before returning to Earth on an unstable manifold trajectory associated with the unstable periodic orbit around  $L_2$  [41]. Methods making use of DST as first utilized in the Genesis mission are further examined in this investigation to design spacecraft missions for practical military applications.

As stated, using a multi-body dynamical model expands the design options for a mission design problem, and all applicable solutions should be considered when planning trajectories. Modern technology and supercomputers have transformed previously unthinkable problems to solve by hand into possible feats that, in most cases, can be solved accurately in a relatively miniscule amount of time. Though advanced technology gives immense computing power, trying to search all available solutions in a multi-body space dynamics problem still poses problems. Searching all possible solutions for a general spacecraft problem that wants the “best” solution will leave a computer with an infinite search. Using visual tools available in multi-body problems can let the mission planner gain insight into the problem. This leads the astrodynamicist to narrow the all-solution search by clarifying potential initial conditions, midpoints, end boundaries, and specific trajectory behaviors that may be possible in a given problem. Using tools developed from DST commonly incorporates looking at the given system in less intuitive coordinates of the phase space, usually implemented with simple visual presentations. One possibility when using visual tools is

to use the available information to make a guess for an initial design, and then use technological resources to refine and potentially optimize that guess and the nearby solutions. A focus in this research is to use visual mapping tools to gain insight into the behavior of the solution space of trajectories, inputting an initial guess into a Newton-Raphson algorithm and utilizing computational power to refine the solution. The first step in integrating DST techniques in this research is to compute invariant manifolds associated with unstable periodic orbits.

## 2.14 Invariant Manifolds

DST serves to introduce the increasingly more popular space mission design concept of using invariant manifolds associated with unstable periodic orbits as means for orbital transfers. Wiesel defines these structures as “surface[s] of lower dimension imbedded within the phase space” [20]. In the CR3BP, manifolds are notionally linked to the stability of the equilibrium points and periodic orbits of which they are associated. Consider the  $n$ -dimensional linearized system represented by equation (62). As mentioned earlier, the eigenvalues,  $\lambda_i$ , of the constant  $A$  matrix for the linearized system evaluated at an equilibrium point,  $\vec{X}_{eq}$ , play a role in characterizing the specified solution’s stability. In general, the system’s  $n$ -dimensional space obeys  $rank(A) = n = n_s + n_u + n_c$ , where  $n_s$  is the number of eigenvalues with negative real parts (Lyapunov stable),  $n_u$  is the number of eigenvalues with positive real parts (Lyapunov unstable), and  $n_c$  is the number of eigenvalues with purely imaginary parts (marginally stable) [25, 34, 52, 53]. The space  $\mathbb{R}^n$  is usually represented in terms of three subspaces associated with the eigenvalues: the stable subspace ( $E^s$ ), the unstable subspace ( $E^u$ ), and the center subspace ( $E^c$ ) [25, 34, 52, 53]. These eigenvalues also have associated, linearly independent eigenvectors,  $\vec{v}_i$ , that span  $\mathbb{R}^n$  and each define a direction tangent to the associated subspace. A solution in a specified

subspace also remains in that subspace for all time, indicating the existence of local stable and unstable invariant manifolds,  $W_{loc}^s$  and  $W_{loc}^u$ , associated with  $E^s$  and  $E^u$  in the linear system [25, 34, 52, 53]. The local stable manifolds represent the set of the initial conditions in the neighborhood of the equilibrium points such that the “flow” initiated at these points asymptotically approaches the point as  $t \rightarrow \infty$ . Similarly, the local unstable manifold is the comparable set such that the “flow” asymptotically approaches the equilibrium point as  $t \rightarrow -\infty$ . Figure 14 represents an example planar projection of the dynamical “flow” near an equilibrium point.

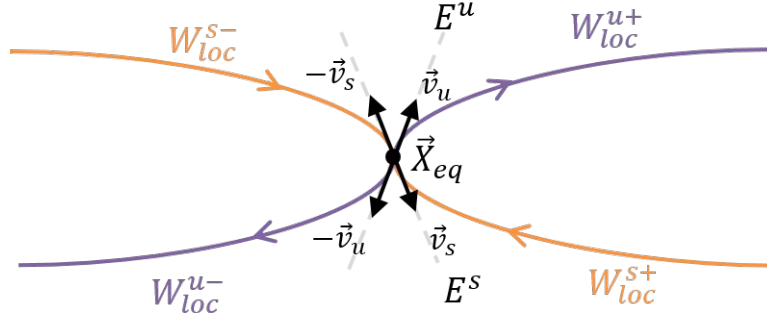


**Figure 14. Notional Representation of the Dynamical “Flow” Near a 2-D Saddle Equilibrium Point.**

The figure shows how the “flow” of the local half manifold branches are represented by their associated eigenvectors:  $W_{loc}^{s+}$  is defined by  $+\vec{v}_s$ , and likewise for  $W_{loc}^{s-}$ ,  $W_{loc}^{u+}$ , and  $W_{loc}^{u-}$  defined by  $-\vec{v}_s$ ,  $+\vec{v}_u$ , and  $-\vec{v}_u$ , respectively. The associated eigenspaces ultimately rely on the linearized variational equations for each case, therefore note that these values and directions are only approximations of the nonlinear dynamics. The nonlinear, global manifolds may be approximated by taking a small step and propagating along the appropriate eigenvector directions, in negative time for  $W_{loc}^s$  and in positive time for  $W_{loc}^u$ . For both the stable and unstable subspaces, the positive and negative half manifolds make up the global manifold approximations,  $W^s$  and  $W^u$ , respectively. Figure 14 also represents a hyperbolic fixed point with no center



subspace, or  $n_c = 0$  when evaluated at that point [34]. A center subspace associated with an equilibrium point encompasses all the periodic and quasi-periodic motion seen in the vicinity.

Invariant manifolds are also found with respect to periodic orbits. Recall that a periodic orbit is classified as unstable if an eigenvalue of the orbit's STM for one period (monodromy matrix) lies outside of the unit circle. In this case, the characterization of eigenvalues evaluated at a fixed point on the periodic orbit determine the subspaces that exist in the dynamical “flow” in the vicinity. The eigenvalues  $\lambda_i$  (with corresponding eigenvectors,  $\vec{v}_i$ ) that lie inside and outside of the unit circle are associated with the stable and unstable subspaces. To approximate the global manifolds associated with a periodic orbit, first the local manifolds for a chosen point along the orbit are computed by propagating initial conditions perturbed in the direction of the associated eigenvectors. A representation for all the global manifolds may be computed in the same fashion for all (or a selection of) fixed points along the periodic orbit, calculating eigenvalues and eigenvectors for each point individually to numerically integrate manifold trajectories in the appropriate direction. For a less computationally intensive process, it may be shown that the eigenvalues of the monodromy matrix are independent of the starting point along the orbit, which allows the STM to be utilized in approximating the manifolds. The relationship between the STM at one time on the periodic orbit,  $t_0$ , may be related to a later time,  $t_1$ , where  $T$  is one period of the orbit:

$$\Phi(t_1 + T, t_1) = \Phi(t_1 + T, t_0 + T)\Phi(t_0 + T, t_1). \quad (111)$$

Since  $T$  represents the same amount of time whether it is added to  $t_0$  or  $t_1$ , and

$\Phi(t_1 + T, t_0 + T) = \Phi(t_1, t_0)$ , equation (111) becomes

$$\Phi(t_1 + T, t_1) = \Phi(t_1, t_0)\Phi(t_0 + T, t_0)\Phi^{-1}(t_1, t_0), \quad (112)$$

since  $\Phi(t_0 + T, t_1) = \Phi(t_0 + T, t_0)\Phi^{-1}(t_1, t_0)$ . Noticing from equation (112) that  $\Phi(t_1 + T, t_1)$  and  $\Phi(t_0 + T, t_0)$  are similar matrices, they must also have the same eigenvalues. This conclusion implies that if invariant manifolds exist for one fixed point on a periodic orbit, then they exist for all points along the orbit, since the eigenvalues determining their existence are associated with each point making up the orbit. To compute a representation of the global manifolds, a number of fixed points evenly spaced in time may be chosen along the orbit, and the invariant manifolds associated with each point may be propagated, together representing the invariant manifold tubes associated with a periodic orbit. The local manifolds may be computed for the first fixed point on the orbit, and since the eigenvalues are the same at each point around the orbit, the linearized “flow” transitions exactly, and the STM between the last point and the next may be used to determine the eigenvectors at the  $i^{th}$  point, i.e.,

$$\vec{v}_i(t_1) = \Phi(t_1, t_0)\vec{v}_i(t_0). \quad (113)$$

In other words, the eigenvectors may be transitioned along the periodic orbit by the STM as it is numerically integrated simultaneously with the orbit [25, 54, 55, 56].

Similar to the manifolds accompanying equilibrium points, the local stable manifolds,  $W_{loc}^s$ , asymptotically approach the orbit in forward time, while the local unstable manifolds,  $W_{loc}^u$ , asymptotically approach the orbit in negative time. Each manifold trajectory originating at each fixed point is tangent to the subspace directions defined by the eigenvectors,  $\vec{v}_i$ , at each point. To numerically approximate the manifold trajectories from an unstable periodic orbit, a fixed point is first defined on a given

unstable periodic orbit. The initial state for propagation is determined by taking a small step off the periodic orbit, in the direction of the associated eigenvector. For example, to determine the initial state for the positive stable half manifold,  $\vec{X}^{s+}$ , a step  $p$  is taken in the direction of  $\vec{v}_s$  from the fixed point,  $\vec{X}_{FP}$ ,

$$\vec{X}^{s+} = \vec{X}_{FP} + p\vec{v}_s, \quad (114)$$

where the eigenvector is defined  $\vec{v}_s = [x_s \ y_s \ z_s \ \dot{x}_s \ \dot{y}_s \ \dot{z}_s]^T$ . The velocity of the associated eigenvector is normalized by the distance components, therefore a “step” in the vector direction can be described in terms of a disturbance in distance after the vector is multiplied by a scalar step in distance. The step is a displacement in both position and velocity, but is normalized by distance. The initial state for the approximation is then defined,

$$\vec{X}^{s+} = \vec{X}_{FP} + l\vec{v}^{ws}, \quad (115)$$

where  $l$  is the step in distance and

$$\vec{v}^{ws} = \frac{\vec{v}_s}{\sqrt{x_s^2 + y_s^2 + z_s^2}}. \quad (116)$$

For the Earth-Moon system, a step off the periodic orbit by  $l = 20 - 50$  km provides results that still give a decent approximation for the manifold in a reasonable amount of computation time, while departing the periodic orbit quickly enough to yield trustworthy numerical integration data [25, 32]. To obtain the remaining local half manifolds, initial states for  $W_{loc}^{s-}$ ,  $W_{loc}^{u+}$ , and  $W_{loc}^{u-}$  are found similarly, stepping in the respective directions of the associated eigenvectors,  $-\vec{v}_s$ ,  $+\vec{v}_u$ , and  $-\vec{v}_u$ . From these initial states around a fixed point on an unstable periodic orbit, the positive and

negative stable manifolds are propagated from these initial states in negative time to approximate trajectories that lead to the periodic orbit in forward time. Conversely, the positive and negative unstable manifolds are propagated in forward time to approximate the trajectories that depart the orbit. As in the case with manifolds near the equilibrium point, the combining of  $W_{loc}^{s+}$  and  $W_{loc}^{s-}$  forms the approximation for the global stable manifold asymptotically approaching the unstable periodic orbit in forward time in the nonlinear system, and likewise,  $W_{loc}^{u+}$  and  $W_{loc}^{u-}$  form the unstable manifold approaching the orbit in negative time. Manifold trajectories “originating” from a periodic orbit also share the same  $JC$  value as their reference orbit. In the nonlinear system, the collection of manifold trajectories (each 1-D) leading to and away from the periodic orbit as  $t \rightarrow \infty$  form manifold “tube” structures that are 2-D surfaces in the 6-D phase space. Approximated projections of the stable (orange) and unstable (purple) manifold tubes associated with an unstable periodic Lyapunov orbit around the Earth-Moon  $L_1$  libration point are seen in Figure 15. A zoomed view of the stable and unstable manifold trajectory approximations as they asymptotically approach and depart the periodic Lyapunov orbit, respectively, is seen in Figure 16. The manifold trajectories seen in the figure were approximated by choosing twenty fixed points along the Lyapunov orbit, spaced evenly in time.

Note that the symmetric properties of the CR3BP may also be utilized here by reflecting solutions across the  $x$ -axis to decrease calculations and integration time. A stable manifold trajectory propagated in negative time from a point along the periodic orbit above the  $x$ -axis is also a solution when reflected over the axis, departing the periodic orbit in forward time, and ultimately originating from the orbit from the reflected point below the axis.

If a trajectory is “on” a manifold (at the correct position and velocity) at a given time, it remains on the manifold for all time [25, 32, 52]. This implies that a

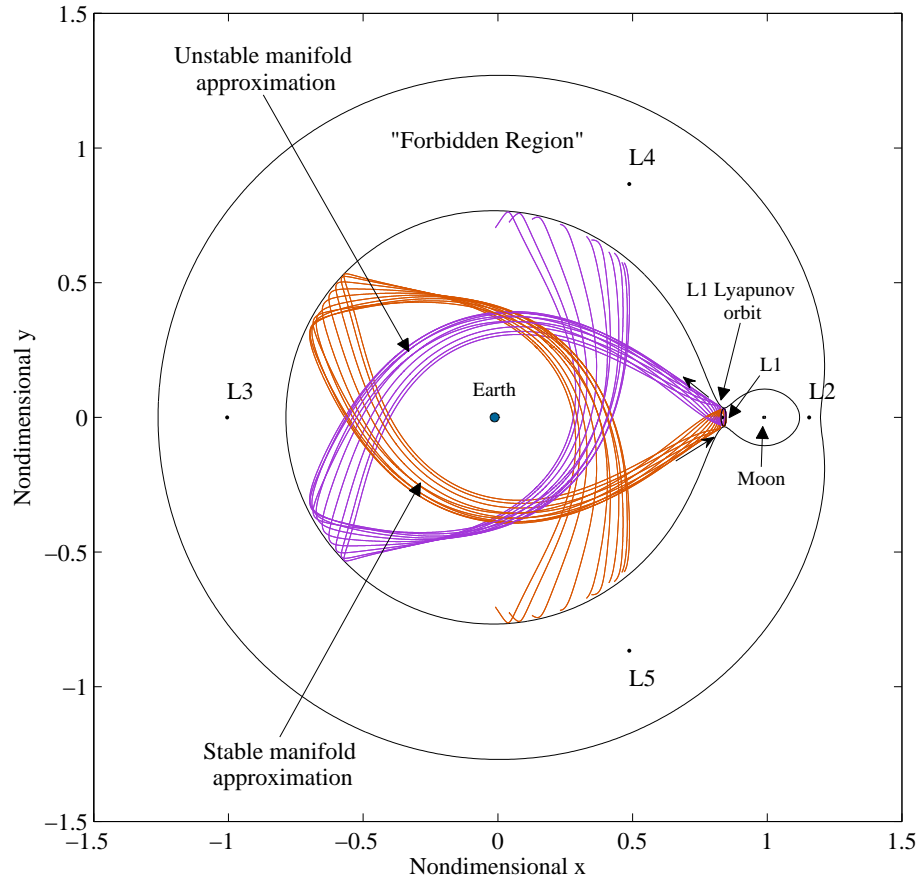


**Figure 15. Stable and Unstable Invariant Manifold “Tube” Approximations Associated with Unstable Periodic  $L_1$  Lyapunov Orbit in Barycentric Rotating Frame.**

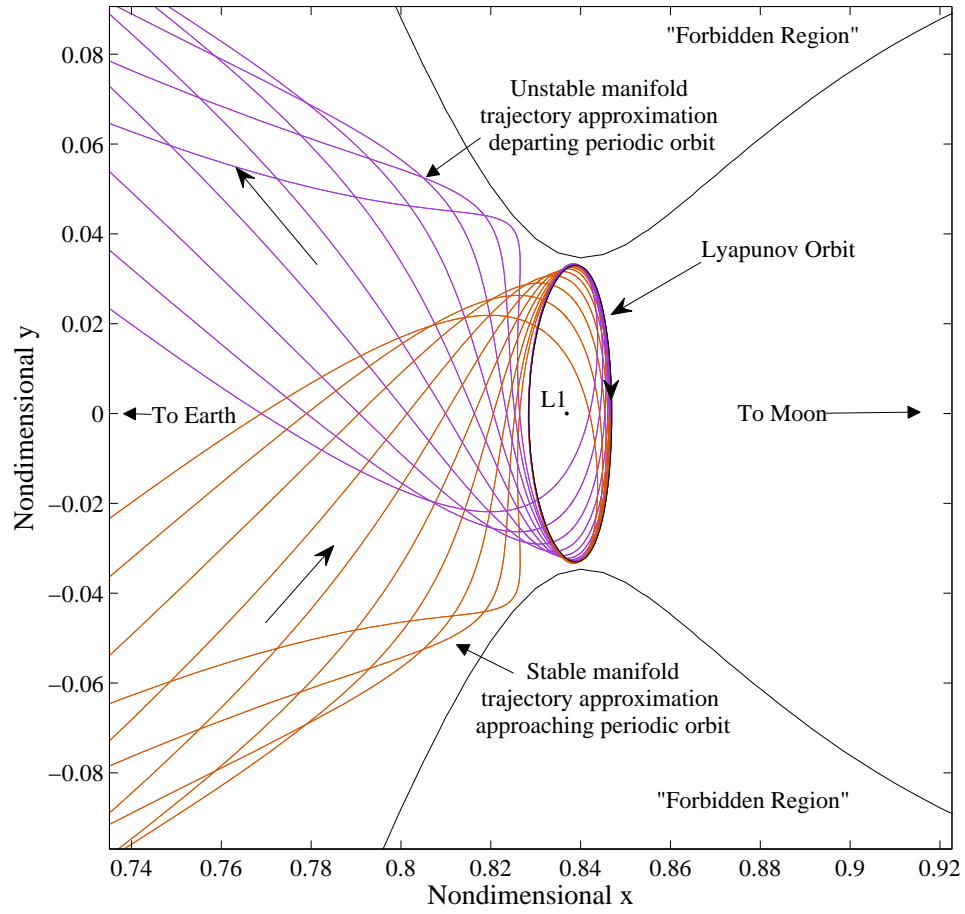


Figure 16. Zoomed View of Stable and Unstable Invariant Manifold “Tube” Approximations Associated with Unstable Periodic  $L_1$  Lyapunov Orbit in Barycentric Rotating Frame.

spacecraft trajectory may not cross an invariant manifold in the full phase space. The time-invariance of the manifolds gives mission designers motivation to explore these structures for space operations. As suggested by Figure 15, the manifold trajectories may travel exceedingly far from their reference orbit, and considerably close to bodies that are distant compared to the periodic orbit. If a spacecraft were to intersect a manifold trajectory in position, the difference in energy level between it and the manifold trajectory would dictate the velocity change needed in order to be “on” the manifold in the full phase space, which may have reasonably small magnitude. A spacecraft that performs a maneuver to be on a stable manifold trajectory would then follow the manifold to approach the original unstable periodic orbit (in forward time). Since a manifold trajectory approaches the orbit in infinite time, a small maneuver may be performed once the trajectory is sufficiently close to the periodic orbit. Another small maneuver in the correct direction (depending on the departure point) may then place the spacecraft on the unstable manifold, eventually leading away from the periodic orbit.

An intersection (in the full phase space) can also exist between a stable manifold of an orbit, proceeding in negative time, and an unstable manifold of the same orbit in forward time, termed a “homoclinic” connection. When the stable and unstable manifolds originate from different orbits, the connection is called “heteroclinic.” Note that since the manifold trajectories share a  $JC$  value with their associated periodic orbit, a heteroclinic connection may only exist between manifolds originating from periodic orbits with equivalent energy levels. These connections would theoretically allow for a “free” (zero- $\Delta V$ ) transfer between the periodic orbits. A series of these connections may also theoretically lead a spacecraft from one part of the solar system to another. Within the second volume of Poincaré’s *Les Méthodes Nouvelles de la Mécanique Céleste*, he applied the theory of asymptotic solutions to the restricted

three-body problem, where he explained the concept of homoclinic solutions as “doubly asymptotic solutions” [57]. The sensitivity of these solutions to their initial conditions led Poincaré to explore the notion of chaos. Guckenheimer and Holmes observe that when the reference vector field and perturbed systems are defined as “close,” the solutions may be suspected to be close, but it turns out that this is not the case, and small perturbations may lead to radical changes to the structure [34]. However, this chaotic behavior is typically seen near limiting, asymptotic behavior, and the unperturbed and perturbed solutions may be close for finite time periods [34]. For this reason, perturbations and steps near equilibrium points and periodic orbits are kept sufficiently small for their specific situations. Nevertheless, other methods for characterizing the stability and structure of the solution space are useful for mission design. Poincaré maps may offer this capability, as described in Section 2.16.

## 2.15 Resonant Orbits

Studying the use of resonant orbits and lunar fly-bys in spacecraft mission design has steadily increased since the 1960s with Minovitch and JPL’s work with “gravity assist” fly-by techniques in spacecraft trajectory design [57, 58, 59]. Early studies of comets near Jupiter showed that their trajectories before a close approach to the planet were much different than their resulting trajectories after the fly-by. Minovitch was able to mathematically explain and predict the path of a spacecraft as well as its increased velocity after traveling close to a Sun-orbiting planet [58, 59]. His gravity assist technique was first used in 1973 when Mariner 10 journeyed to Venus and Mercury [59]. In a two-body sense, the orbital energy is decreased and increased with a series of fly-bys, but in reality, there is a transfer of momentum between the spacecraft and the fly-by planet [57, 58]. This exchange of momentum is what allows a resonant orbit that is influenced by the Moon’s gravitational field to offer



a pathway of reduced  $\Delta V$  for a transfer from one place in the primary system to another. In 2000, Strange and Longuski introduced this concept with their graphical method of employing gravity assists in trajectory design [60]. Bringing in three-body dynamics, they incorporate an analytical technique that is directly related to Tisserand’s criterion, which is an approximation of the Jacobi Constant of the CR3BP expressed by orbital elements [57, 60]. The AsiaSat-3/HGS-1 design method based its analytical guess to input into a targeting algorithm on the Tisserand criterion [6].

Some modern applications in mission design involve the concept of traveling to or from resonant orbits as a starting point or destination orbit, typically planning to utilize the shape of the resonant orbit to visit a different area of the system or take advantage of the orbit’s periodicity as it relates to the smaller primary’s orbit about the larger primary. Parker and Lo explored Earth-Moon mission designs using planar, symmetric families of periodic orbits. They also studied the invariant manifolds from unstable orbits in these families, focusing on using resonant orbits that fly by the Moon [61]. Anderson examined resonant orbits for use in low-thrust mission design utilizing resonant fly-bys as well as trajectories designed to travel along invariant manifolds originating from or asymptotically approaching unstable periodic resonant orbits [57]. The use of resonant orbits is also seen in Garber’s mission orbit selection process used to set up his “fundamental equation” analysis [62]. Garber focuses on choosing orbits with natural shape and motion that would closely match the constraints of the problem [62]. Lantoine, Russell, and Campagnola used a patched three-body model to enable “resonant-hopping” gravity assists to design and optimize inter-moon transfers of the Jovian system [63]. The transfer technique of transferring a spacecraft from one resonant orbit about one moon to a second orbit with a different resonance has inspired exploration of the relationship between invariant manifolds of select unstable resonant orbits and their utility in orbital transfers using more

modern tools and numerical schemes. More recently, Vaquero investigated unstable resonant orbits and their relationship with the associated invariant manifolds and potential transfers between resonances [40]. She also cataloged a wide selection of resonant orbit families in the Earth-Moon CR3BP and explored the use of these families in different applications based on their specific patterns and routes through the system [53]. Vaquero and Howell studied employing resonant orbits as transfer mechanisms between non-resonant orbits, examining design scenarios that transfer spacecraft from LEO to LPOs [64]. In 2014, Anderson and Lo showed that the stable manifolds of planar Lyapunov orbits can give insight into the resonances that are required for the final approach to a body [65]. The use of fly-by gravity assists, resonant orbits, and invariant manifolds is continuing to become a more extensive area of research as the lower-energy transfer options in trajectory design consistently introduce promising options for future missions.

The basic definition of resonance describes the condition in which there is a “simple numerical relationship between frequencies or periods” [66]. Orbits are classified to have orbit-orbit resonance (or “coupling”) when a body  $A$  completes  $q$  orbits about a primary body in the same time it takes a body  $B$  to complete  $p$  orbits about the primary [53, 66]. Resonant orbits are commonly described in terms of their  $p:q$  ratio. In the Earth-Moon two-body model, a resonant orbit occurs when there is a simple integer ratio between its period and the period of the Moon about the Earth ( $p:q$ , where  $p$  = number of spacecraft revolutions of the Earth and  $q$  = number of lunar revolutions of the Earth) [66, 67]. “Exterior” and “interior” resonant orbits exist, where the spacecraft travels along the outer boundaries of the primary system or within  $P_2$ ’s orbit, respectively [53, 66]. A ratio where  $p < q$  corresponds to an exterior resonant orbit, while interior orbits have ratios where  $p > q$ . In the CR3BP, the gravity of additional bodies causes the time it takes for a body to complete one

revolution to deviate slightly, even for a closed, periodic trajectory. Consequently, the  $p:q$  ratio of resonant orbits is not exactly equal to the ratio of resonant bodies' orbital periods. The ratio in multi-body problems is instead an approximate rational fraction, where the spacecraft completes  $p$  revolutions in the approximate time it takes the Moon to travel  $q$  orbits [53, 66].

Examining resonant orbits in the rotating frame shows that every time a spacecraft passes through an apse location, a “loop” appears in the resonant trajectory. This occurrence is only observed in the rotating frame, where the number of loops correspond to the value of  $p$ . As an example, a 4:1 resonant orbit is seen in Figure 17. A spacecraft traveling along this orbit completes four revolutions of the Earth in the same time that the Moon completes one revolution.

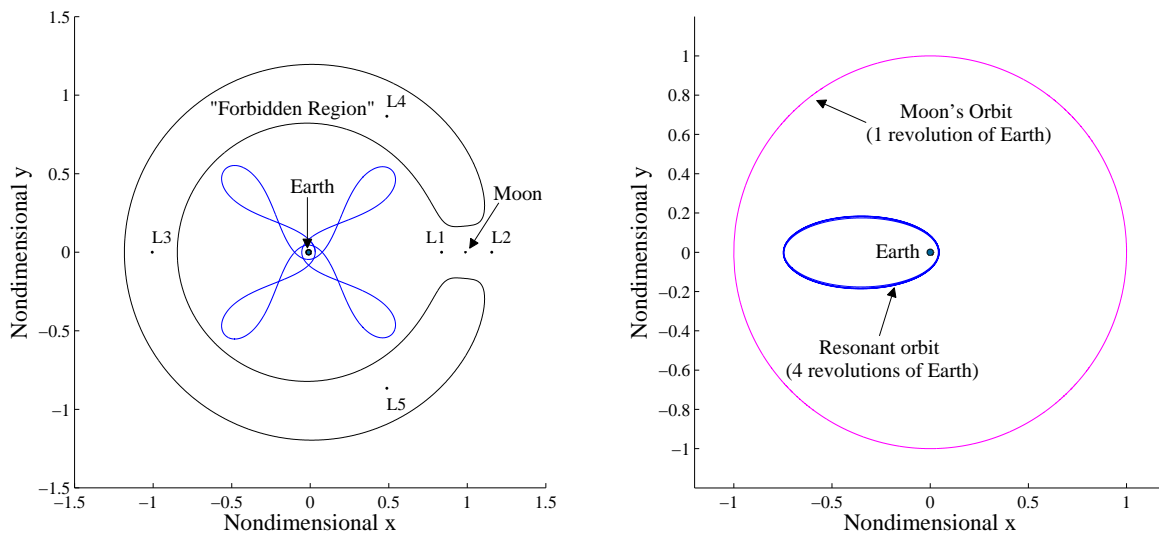


**Figure 17. Member of Periodic 4:1 Resonant Orbit Family in Barycentric Rotating and Inertial Frames.**

In order to find a resonant orbit in the CR3BP, a multiple-shooting targeting scheme (described in Section 3.1) is applied, and the converged solution is a closed, periodic trajectory with an approximate rational fraction  $p:q$  ratio. Initial guesses for the patch points, or select initial guesses along the orbit, are the apses of a

resonant trajectory, chosen so that the trajectory begins and ends at an apse location on the  $x$ -axis. This implies that there is no component of the velocity in the  $x$ -direction. For a planar resonant orbit,  $z_0 = \dot{z}_0 = 0$ , so the initial state vector is then  $\vec{X}_0 = [x_0 \ 0 \ 0 \ 0 \ y_0 \ 0]^T$  when starting and ending on the  $x$ -axis. The error vector for targeting resonant orbits is driven to zero to within  $10^{-12}$  nondimensional units, and since the error vector is made up of the distances and velocities between each patch point state, this tolerance corresponds to a total error of sub-cm and even smaller sub-mm/s accuracy for each state defined along the periodic orbit. See Section 3.1 for further description. A continuation method (Section 3.2) can be applied to find other orbits with similar characteristics and the same resonant ratio, or a selection of a  $p:q$  resonant orbit family.

A catalog of various resonant orbit families exhibiting orbit-orbit resonance between a spacecraft and the Moon about the Earth are seen in Vaquero’s work [53]. Different families of resonant orbits illustrate various directions of motion near the primaries and unique paths throughout the system. In this investigation, a resonant orbit family in the Earth-Moon system is selected for a particular mission based on its natural shape and itinerary around the Earth. A specific resonant orbit in the family can be chosen based on its distinctive characteristics, like distance from a primary or known maneuver point in the system. A piece of this resonant orbit, or a resonant “arc,” is used to generate an initial guess to input into a multiple-shooting targeting algorithm searching for a desired mission trajectory.

## 2.16 Poincaré Maps

Wiesel explains that numerical integration is not only used as a mathematical tool for computing and examining a single orbit; it also serves as a method to see into the behaviors and inner-workings of nonlinear systems [20]. One way that a

numerical simulation can explain previously unseen characteristics of a system is through Poincaré maps. Wiggins outlines three different advantages that come from reducing the study of a continuous time system (or a “flow”) to the study of a discrete time system (through a Poincaré map) while examining ordinary differential equations [52]:

- (1) “Dimension reduction”: a Poincaré map offers the advantages of always reducing the dimension of the problem by eliminating at least one variable.
- (2) “Global dynamics”: the map view provides an “insightful and striking” visual of the global dynamics of systems with four or less dimensions (4-D phase space).
- (3) “Conceptual clarity”: the map displays a “succinct statement” of the potentially complicated characteristics of different facets of the system on the map [52].

In 1881, Henri Poincaré envisioned a visualization tool to analyze stability behaviors in dynamical systems called a Poincaré map. When looking at the data on a Poincaré map, also called first-return map, trajectories or groups of trajectories may exhibit structures or features that signify certain behaviors. These characteristics may otherwise be unknown or difficult to see from looking at a selection of trajectories in other configurations or typical spaces.

The Poincaré map is one particular dynamical tool used in this investigation that allows the mission planner to gain visual insight into the scenario by “slicing” the design space and reducing the dimensionality of the problem. The Jacobi Constant has utility when designing Poincaré maps, as defining an energy level of an orbit or set of trajectories reduces the dimension of the entire data set by one. Portraying this system information with a Poincaré map reduces the problem by another dimension when defining a surface of section. Considering an  $n$ -dimensional, continuous time system, the surface of section is a defined  $(n - 1)$ -dimensional hypersurface that de-

scribes a cross-section of the dynamical “flow” of the system [34,68]. In this analysis, 2-D Poincaré maps, defined with a certain energy level (by specifying a value of Jacobi Constant that holds true for all trajectories represented on the map), are used to analyze a particular cross-section of the planar CR3BP. A 4-D space defined by the state is reduced to a 2-D space on the map. Generating Poincaré maps for the spatial CR3BP (6-D phase space) would require a 4-D map, which is difficult to visualize. Various methods for producing maps for the spatial problem can be seen in the work of Froeschlé [69], Gómez et al. [70], Koon et al. [71], Craig Davis and Howell [72], Geisel [32], and Haapala [73]. In 1964, Hénon generated 2-D Cartesian phase space maps for various Jacobi Constant values in the planar Copenhagen problem, in which the primaries are defined with equal mass [74]. There are many examples of Poincaré maps that define the surface of section as a physical plane. In his work searching for low-energy transfers in the Earth-Moon system, Conley developed a proof that described how invariant manifolds associated with planar, periodic orbits in the vicinity of the collinear libration points can be classified based on their behavior within their accessible region [50]. Expounding upon Conley’s work, the use of invariant manifolds as a transfer method was explored using Poincaré sections by Koon et al. and Gómez et al. [70,71].

Another method of defining the surface of section for a Poincaré map is with the plane of periapsis. In a two-body sense, a periapse is commonly referred to as the point on a closed orbit that is closest to the central primary, while an apoapse refers the farthest point. In the CR3BP, an apse occurs at a point along an orbit when the radial velocity with respect to the primary is zero. Periapsis satisfies the condition for an apse, and the radial acceleration is positive. Conversely, apoapsis occurs when the radial velocity is zero and acceleration is less than zero (see Section 3.3). Creating this type of map allows a physically intuitive display of the periapsis information in

the configuration space. Periapsis maps have been generated to show the periapses of the stable and unstable manifolds of unstable periodic orbits around libration points that may serve as transfer pathways into and out of the system or as an opportunity for a heteroclinic or homoclinic connections at a certain energy level.

Mission design methods have been developed from visual insight gained from the map based on the trajectories' short- and long-term behavior within the region close to a primary, typically  $P_2$ . Villac and Scheeres first exploited the periapsis Poincaré map to identify regions of escape from the vicinity of  $P_2$  in the planar Hill three-body problem, which is a limiting case of the CR3BP [75, 76]. Later, Paskowitz and Scheeres employed periapsis Poincaré maps to explore low-energy transfers between orbits with different long-term classifications in the  $P_2$  region [77]. More recently, Haapala used manifold periapse structures to design planar trajectories with predetermined characteristics like long-term capture and transit behavior near and through the  $P_2$  region [30]. Haapala and Howell also used periapsis Poincaré maps to construct transfers between libration point orbits in various three-body systems and explored strategies for representing systems in the spatial CR3BP, including observing the natural motion of captured Jupiter-family comets and searching for periodic orbits in the system [73, 78]. Craig Davis developed a design process of orbits in the  $P_2$  region in the Saturn-Titan and Earth-Moon CR3BP systems, and the Sun-Saturn-Titan restricted four-body system [79]. She studied the effects of the tidal acceleration due to  $P_1$  on individual and groups of orbits, investigated the short- and long-term behaviors of various orbit types based on initial conditions in different systems with multiple energy levels, and predicted trajectories of fly-bys combined with a tidally-influenced environment [79]. Howell and Craig Davis classified various types of escaping and captured orbits in the  $P_2$  region based on initial conditions, designing missions by selecting orbits with desired behaviors with specific focus in

the Saturnian system [72, 80]. Howell et al. also investigated the evolution of trajectories in the vicinity of the smaller primary and computed orbits with desired sets of characteristics in the region [81].

A Poincaré map may be generated for any nonlinear system of equations. The following development of Poincaré maps is based on discussion and definitions used in the work of Parker and Chua [68] as well as Guckenheimer and Holmes [34], along with adaptations by Haapala [73]. Again consider an  $n$ -dimensional phase space with an autonomous, continuous-time system in the form of equation (62), where  $\vec{f}(\vec{X})$  is a vector field. Within the system, an  $(n - 1)$ -dimensional hypersurface, or surface of section, can be defined,  $\Sigma$ . The surface of section is transverse to the dynamical “flow,”  $\vec{\phi}(\vec{X} t)$ , generated by  $\vec{f}(\vec{X})$  [25, 34, 68]. In general, the hypersurface is not restricted to a plane, but must be selected so that the flow is transverse to it everywhere. This means that some component of the flow must be perpendicular to the hyperplane surface. A trajectory associated with the flow may intersect the hyperplane at a point,  $x$ . Let  $\Sigma^+$  be defined as the hypersurface of which the component of the flow normal to the hyperplane changes from the negative side of the surface to the positive side. Conversely, let  $\Sigma^-$  be defined as the hypersurface of intersections from the opposite direction, and  $\Sigma$  will be more specifically defined as the hypersurface with intersections occurring from either direction. A Poincaré map,  $P$ , maps one surface of section,  $\Sigma_1$ , to another,  $\Sigma_2$ . The two hyperplanes are usually specified such that they are the same [34, 68, 73]. The Poincaré map would then illustrate intersections of one hypersurface,  $\Sigma_1 = \Sigma_2$ . The first return of the trajectory defines the nonlinear map  $P : \Sigma_1 \rightarrow \Sigma_2$ , and  $P(\vec{X}_0) = \vec{X}(\vec{X}_0)$ , where  $\vec{X}_0$  is the initial state of the trajectory. In Figure 18, the sequence  $\{x_1, x_3, x_5, \dots\}$  lies on the one-sided map,  $P^+$ , and the sequence  $\{x_2, x_4, \dots\}$  lies on the one-sided map,  $P^-$ . The point  $x_3$  corresponds to the first crossing of  $\Sigma^-$ , and likewise,  $x_4$  corresponds to



the first crossing of  $\Sigma^+$ . The complete set of points  $\{x_1, x_2, x_3, x_4, x_5\}$  belongs on the two-sided map,  $P$ , corresponding to a set of intersections of the surface of section,  $\Sigma$ .

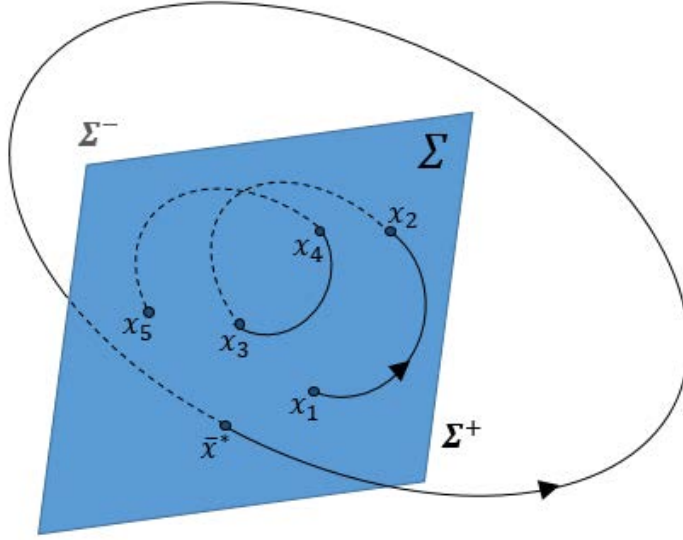


**Figure 18. Notional Representation of a Poincaré Surface of Section.**

Considering an example periodic orbit with initial state conditions,  $\vec{X}_0$ , and map intersection,  $\vec{X}^*$ , the figure shows that the orbit returns to the same point on the map at which it started.  $P : \Sigma \rightarrow \Sigma$  maps  $\vec{X}^*$  to itself repetitively, so  $P(\vec{X}) = \vec{X}^*$ . Such a state is known as a fixed point on the map. In his *Méthodes Nouvelles*, Henri Poincaré regards the subject of periodic orbits as one of the only ways to see deeper into the dynamical complexity of the problem of three bodies, and by extension, specifically the CR3BP [1].

A non-periodic trajectory is seen as a set of points on the map. In the CR3BP, the Jacobi Constant reduces the dimension of the problem by one when held fixed. Choosing a surface of section and plotting the intersections of a set of trajectories on a Poincaré map further reduces the data by one dimension. In the planar CR3BP, 4-D trajectories can be represented in 2-D with a fixed Jacobi Constant on a Poincaré

map. The trajectory’s entire state space is represented on the plane in the projection. The possible visual clues that explain different areas of the space can be described more easily by observing a Poincaré map. The map in Figure 19 shows a Poincaré map for a surface of section defined at the  $y = 0$  plane of the planar CR3BP for the Earth-Moon system with  $JC = 3.1$ . In other words, the original 4-D space of the set of trajectories is reduced to a 2-D map. Initial conditions for each planar trajectory represented on the map are taken in steps in  $x$  along the  $\dot{x} = 0$  axis, so the initial state for each of the 60 trajectories presented is in the form  $\vec{X} = [x_0 \ y_0 \ \dot{x}_0 \ \dot{y}_0]^T$ , where  $y_0 = \dot{x}_0 = 0$ . With the given  $JC$ , a  $\pm\dot{y}_0$  value may be determined as  $x$  values are defined. For a two-sided map, all surface of section intersections would be shown for trajectories with both positive and negative  $\dot{y}_0$  values. However, the map in Figure 19 is a one-sided map, initialized with trajectories with  $\dot{y}_0 > 0$ . Each trajectory is also numerically integrated for 150 revolutions of the primaries (about 11 years) with the goal of producing a map that is sufficiently filled out with points to determine the behavior.

Poincaré maps provide a broad view of the types of orbits in the selected region at the associated energy level. Returns on the map that correspond to quasi-periodic behavior tend to form structures that resemble concentric closed curves. These curves emerge with an ordered placement of the subsequent returns, as seen in Figure 19. Quasi-periodic behavior is also seen in “islands” of similar arrangement surrounding the larger ordered structures. Zooming in to these ordered regions would reveal that these islands and curves are actually made up of smaller islands and curves, and according to Wiesel, “this hierarchical structure continues forever, at even finer scales” [20]. At the “center” of the quasi-periodic structure (not necessarily the geometric center), even if it does not appear on the map with this set of trajectories, a periodic orbit (or a single, fixed point on the map) is expected to exist. Initial

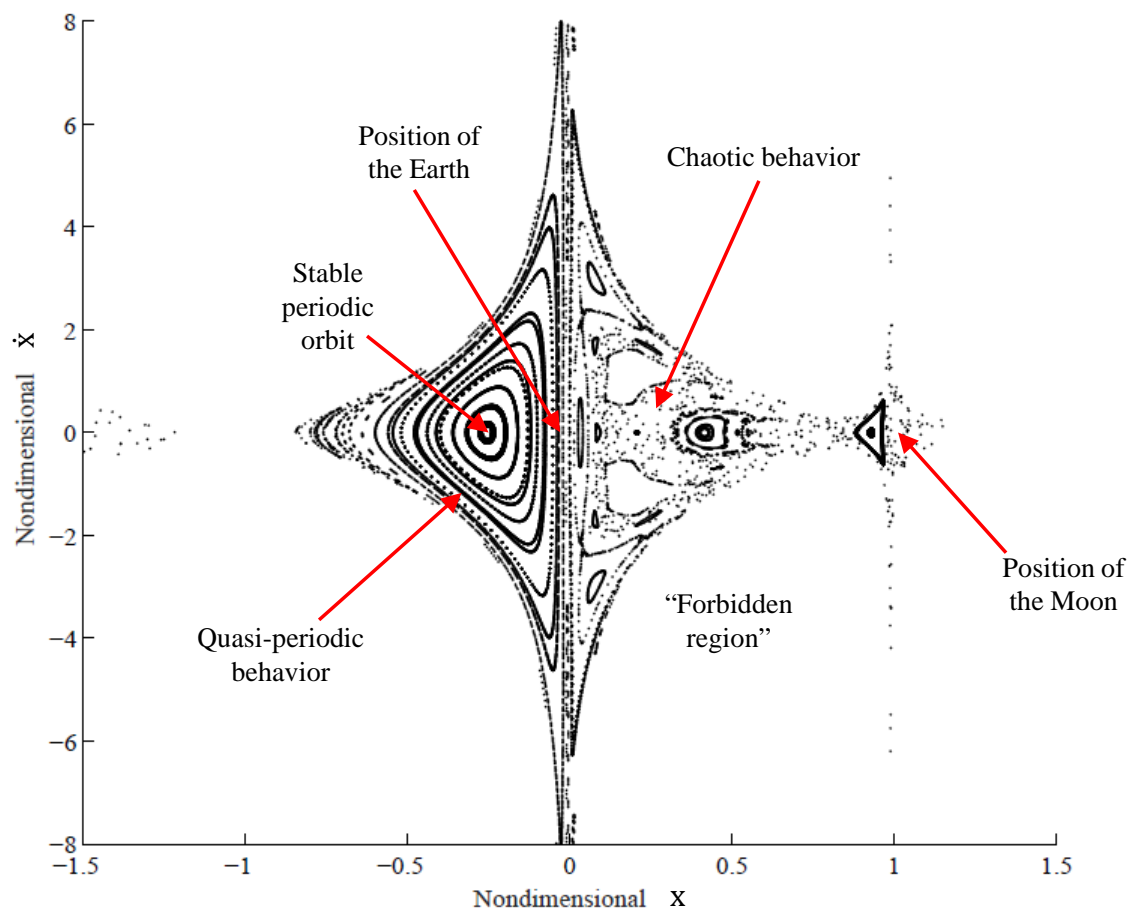
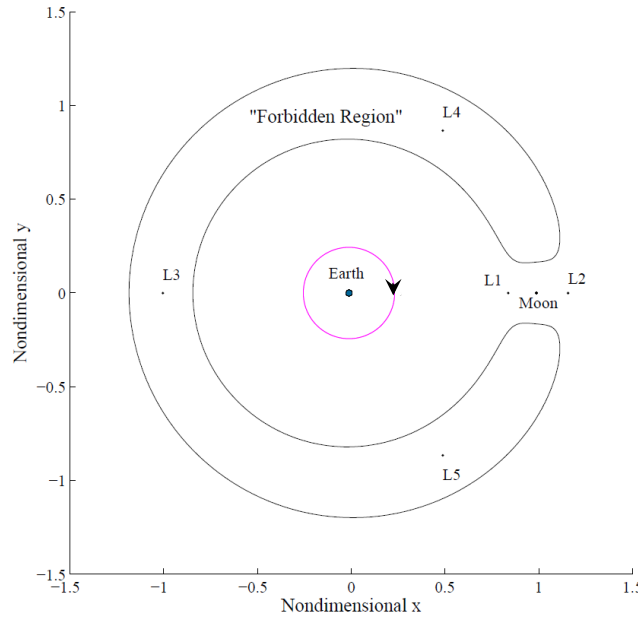


Figure 19. Poincaré Map for Earth-Moon System,  $JC = 3.1$ , 60 Trajectories Numerically Integrated for 150 Revolutions of the Primaries (About 11 Years).

conditions for the approximate location of this fixed point may be taken from the map (where  $\dot{x}_0 = 0$ , indicating a perpendicular crossing of  $y = 0$ ) and input into a targeting algorithm to compute a periodic orbit. The ordered region around this periodic orbit indicates that the periodic orbit would be classified as linearly stable. A periodic orbit with perpendicular crossings of the  $y = 0$  axis using the initial conditions approximated from the map (labeled “stable periodic orbit” in Figure 19) was targeted using a single-shooting algorithm. The resulting converged periodic orbit is seen in the configuration space in Figure 20.



**Figure 20. Periodic Orbit Targeted By Single-Shooting With Initial Guess from Poincaré Map for Earth-Moon System,  $JC = 3.1$ , Integration Time=1.356 nondimensional units (About 6 days).**

One shortcoming of Poincaré maps comes with searching for unstable periodic orbits. There is not obvious structure surrounding unstable orbits as with the periodic or quasi-periodic case, but indications of instability are found in between the island structures indicating stable motion. “The breakdown from order to chaos begins in the vicinity of unstable periodic orbits,” says Wiesel [20]. Regions on the map in Figure 19 also shows regions of seemingly random points, which is a sign of chaotic

behavior in that region. The large areas on the map that do not contain any points are associated with “forbidden regions” defined by the ZVCs. Smaller “holes” of empty regions on the map are observed because the particular initial conditions selected do not result in map returns in those areas during the integration time.

Similar maps of multiple energy levels may be compared to give the mission designer insight into how the different types of orbits are seen to “evolve” as energy level changes. An example of evolving structure and other behaviors are revealed by periapsis Poincaré maps in Chapter 4. Defining a map that only presents trajectories at one energy level may be seen as another disadvantage, but individual maps may still be helpful. Furthermore, since maps can be created with different initial conditions and for different integration times, looking at a series of maps with different energy levels may reveal trends of structure in certain areas. For example, periodic orbits may appear closer and closer together in certain regions as the value of  $JC$  is increased. As another example, if unstable behavior is observed on the map of one energy level, but an unstable periodic orbit is sought at a different energy level, then the evidence on the first map may be enough proof to go looking for unstable behavior in the corresponding area on the map of a different energy level.

## 2.17 Chapter 2 Summary

In this chapter, a historical overview is provided to set up the research presented with a foundational background originally stemming from the world’s earliest and most influential philosophers and scientists. The theories of general and special perturbations are introduced, as well as the use of numerical integration to determine particular solutions for a problem with no known closed-form analytical solution. A summary of the 2BP equations of motion and solutions are given, and the simplifying assumptions and equations of motion are justified and derived for the CR3BP.

Nondimensional units are defined, and the transformation to and from the inertial and rotating frames is described, giving an initial explanation of the side-by-side plots of trajectories in these frames that will be shown throughout this research. Also described is the Jacobi Constant ( $JC$ ), the one known integral of the motion admitted by the CR3BP, and how it leads to “accessible” and “forbidden regions” delineated by the ZVCs. Observations of special features in the rotating frame are described, including the five equilibrium points and the symmetry properties of solutions. The equilibrium points and periodic orbits are studied through a linear stability analysis, and an explanation of the resulting invariant manifold approximations is given, setting the groundwork for DST approaches to mission design. The STM is introduced as a way to compute the manifold trajectories associated with unstable periodic orbits, and to observe the “flow” of dynamics. Resonant orbits are presented and defined, and an introduction to Poincaré maps is provided, leading the way to the design methods that are specific to this research. Targeting schemes and continuation methods, as well as periapsis Poincaré maps are numerical tools specifically developed to aid in finding the solutions to design scenarios proposed in the next section.

### 3. Design Methodology and Numerical Tools

The algorithms for single- and multiple-shooting that target trajectories from one specified point to another, which are utilized in Test Case I, are described in this chapter. These targeting algorithms are also used to compute periodic orbits about the Earth-Moon  $L_1$  libration point, as well as periodic resonant orbits in the Earth-Moon system. Single-parameter and pseudo-arclength continuation methods that search for members of periodic orbits are also detailed. The initial guess for some resonant orbits are found from picking initial conditions off the Earth-Moon Poincaré map shown in Section 2.16 that indicated a periodic orbit that returned to the same point on the map multiple times. Once the first orbit is found, pseudo-arclength continuation serves to find the next member in the periodic resonant orbit family, utilizing a sophisticated program that steps in the direction of the closest family member. These continuation methods were employed to generate a family of the periodic orbits around Earth-Moon  $L_1$  as well as a family of periodic resonant orbits. The initial guesses for each of these resonant orbit family members' patch points are the apses of the orbit, or the intersections of the periapsis surface of section. The hyperplane associated with the condition of periapsis is also introduced in this chapter, along with the method to produce two types of periapsis Poincaré maps, which are used in the test cases.

Each simulation in this investigation uses MATLAB<sup>®</sup> to find solutions. Depending on a problem's complexity, all programs successfully produce results within a total time ranging from a few seconds to a few hours. The generation of Poincaré maps lasts from a few minutes to over a full day's time, depending on the number of trajectories represented and the numerical integration times for trajectories. In this work, MATLAB<sup>®</sup> version 8.1.0.604 (R2013a) was used, with benchmark task elapsed times: 0.3120, 0.3502, 0.2497, 0.3397, 0.8810, 3.8939. All simulations were performed on a

Windows 2007 computer using an Intel<sup>®</sup> Celeron<sup>®</sup> Central Processing Unit E3400 @ 2.60 GHz with 4.00 GB of RAM.

### 3.1 Targeting Strategies

Single- and multiple-shooting algorithms are targeting strategies employed to find periodic orbits or specific trajectories in the CR3BP. Both are iterative differential corrections processes that incrementally correct the initial conditions of a trajectory or trajectory segments to ultimately drive the differences between the end conditions and the desired end conditions to zero (to within a satisfactory tolerance). These methods also utilize the STM as a linear approximation of nearby trajectories. Consider a reference solution,  $\vec{\mathbf{X}}^*$ , with initial state,

$$\vec{\mathbf{X}}_0^* = \begin{bmatrix} x_0 \\ y_0 \\ z_0 \\ \dot{x}_0 \\ \dot{y}_0 \\ \dot{z}_0 \end{bmatrix}, \quad (117)$$

at the initial time  $t_0$ . The targeting algorithm constrains the end state  $\vec{\mathbf{X}}^t$  to become the desired end state at some time  $t_f$ . Using a generalization of constraints and design variables, let  $\vec{\mathbf{Q}}$  be the design variable vector comprised of  $n$  free variables  $[Q_1, Q_2, \dots, Q_n]$  that may be adjusted or “controlled.” The variation between the design variable at the desired state and the design variable defined at the reference,  $\delta\vec{\mathbf{Q}}$ , is given by:

$$\delta\vec{\mathbf{Q}} = \vec{\mathbf{Q}}_d - \vec{\mathbf{Q}}^*, \quad (118)$$



where  $\vec{Q}_d$  and  $\vec{Q}^*$  represent the design variables evaluated at  $\vec{X}_d$  and  $\vec{X}^*$ , respectively, i.e.,  $\vec{Q}(\vec{X}_d) = \vec{Q}_d$  and  $\vec{Q}(\vec{X}^*) = \vec{Q}^*$ . The constraints vector  $\vec{F}(\vec{Q})$  contains  $m$  constraint equations that are driven to  $\vec{0}$  (to within a satisfactory tolerance) by the nature of the corrections process. The constraints may be specified simply at the end condition, or at multiple points along the trajectory. An iterative targeting process like single- or multiple-shooting initializes on a first guess for each design variable. In order for the automated algorithm to converge to a solution, the initial guess must be close enough to the solution. The single-shooting method, or a simple targeting method, considers a trajectory or orbit in a single segment. The constraints are designed such that the fixed end state is reached by altering the initial conditions. For an initial  $\vec{Q}$  close to a reference variable  $\vec{Q}^*$ ,  $\vec{F}(\vec{Q})$  can be approximated using a first-order Taylor series expansion [35],

$$\vec{F}(\vec{Q}) = (\vec{F}(\vec{Q}^*) + D\vec{F}(\vec{Q}^*)(\vec{Q} - \vec{Q}^*)), \quad (119)$$

where

$$D\vec{F}(\vec{Q}^*) = \frac{\partial \vec{F}}{\partial \vec{Q}} = \begin{bmatrix} \frac{\partial F_1}{\partial Q_1} & \frac{\partial F_1}{\partial Q_2} & \dots & \frac{\partial F_1}{\partial Q_{n-1}} & \frac{\partial F_1}{\partial Q_n} \\ \frac{\partial F_2}{\partial Q_1} & \frac{\partial F_2}{\partial Q_2} & \dots & \frac{\partial F_2}{\partial Q_{n-1}} & \frac{\partial F_2}{\partial Q_n} \\ \vdots & \vdots & \vdots & \vdots & \vdots \\ \frac{\partial F_{m-1}}{\partial Q_1} & \frac{\partial F_{m-1}}{\partial Q_2} & \dots & \frac{\partial F_{m-1}}{\partial Q_{n-1}} & \frac{\partial F_{m-1}}{\partial Q_n} \\ \frac{\partial F_m}{\partial Q_1} & \frac{\partial F_m}{\partial Q_2} & \dots & \frac{\partial F_m}{\partial Q_{n-1}} & \frac{\partial F_m}{\partial Q_n} \end{bmatrix}. \quad (120)$$

Notice that the STM can be used to populate the elements of equation (120). Desiring  $\vec{F}(\vec{Q}) = \vec{0}$ , equation (119) becomes,

$$\vec{F}(\vec{Q}^j) + D\vec{F}(\vec{Q}^j)(\vec{Q}^{j+1} - \vec{Q}^j) = \vec{0}, \quad (121)$$

where  $\vec{Q}^j$  represents the current value for  $\vec{Q}$ , and  $\vec{Q}^{j+1}$  symbolizes the next value. Equation (121) is solved iteratively until  $\vec{F}(\vec{Q}^{j+1}) = \vec{F}(\vec{Q}^*)$  and  $\vec{F}(\vec{Q}) = \vec{0}$  is satisfied, or  $\|\vec{F}(\vec{Q}^{j+1})\| \leq \epsilon$  where  $\epsilon$  is the convergence tolerance (in this investigation,  $10^{-12}$  nondimensional units is the given tolerance).

Notice that the right-most expression multiplied in equation (121) (the difference between  $\vec{Q}^{j+1}$  and  $\vec{Q}^j$ ) determines precisely how to change the state on the next iteration. In general, if  $D\vec{F}(\vec{Q})$  (size  $m \times n$ ) is a square matrix ( $n = m$ ), then the update equation is a rearrangement of equation (121) using the inverse of  $D\vec{F}(\vec{Q})$ ,

$$\vec{Q}^{j+1} = \vec{Q}^j - [D\vec{F}(\vec{Q}^j)]^{-1} \vec{F}(\vec{Q}^j), \quad (122)$$

which computes one unique solution using Newton's Method. When there are more design variables than constraints ( $n \geq m$ ), the  $D\vec{F}(\vec{Q})$  matrix (size  $m \times n$ ) is not square and therefore not able to be inverted and used in the update equation in equation (122). In general, there are infinitely many solutions for this case. However, a unique solution can be identified by selecting a  $\vec{Q}^{j+1}$  that is the closest solution to  $\vec{Q}^j$ , namely the minimum-norm solution, which uses a "pseudo-inverse" of the non-invertible matrix (minimizing the 2-norm of the difference between the next solution and the current solution [82]). Note that other methods may be used to compute a solution, but the minimum-norm solution was examined in this investigation for problems with non-square  $D\vec{F}(\vec{Q})$  matrices. The update equation for the minimum-norm solution is seen below:

$$\vec{Q}^{j+1} = \vec{Q}^j - D\vec{F}(\vec{Q}^j)^T [(\vec{F}(\vec{Q}^j)(\vec{F}(\vec{Q}^j)^T)^{-1} \vec{F}(\vec{Q}^j)]. \quad (123)$$

This method searches for the closest solution that (if possible) inherits most of the characteristics of  $\vec{Q}^j$ . One potential issue associated with this solution method is

having a small radius of convergence for finding a solution, possibly indicating a more unstable algorithm [25].

Single-shooting can be used to search for planar periodic orbits in the CR3BP. The symmetry of the CR3BP is commonly exploited in similar targeting schemes so that a solution that starts on the  $x$ -axis at  $t_0$  ends at a different point on the  $x$ -axis at later time,  $t_f$ . The complete periodic orbit is found by reflecting the solution over the  $x$ -axis. Consider a fixed-time scenario with a specified desired position,

$$\vec{Q}_d = \vec{X}_d = \begin{bmatrix} x_d \\ y_d \end{bmatrix}, \quad (124)$$

and allow the initial velocity and time to vary. The design variables are then defined:

$$\vec{Q} = \begin{bmatrix} \dot{x}_0 \\ \dot{y}_0 \end{bmatrix}. \quad (125)$$

The constraints vector, made up of two constraint equations, can then be written,

$$\vec{F}(\vec{Q}) = \begin{bmatrix} x_d - x_0^t(\dot{v}_0) \\ y_d - y_0^t(\dot{v}_0) \end{bmatrix}, \quad (126)$$

where the resultant position components are functions of the initial velocity,  $\dot{v}_0 = [\dot{x}_0 \ \dot{y}_0]^T$ . The  $D\vec{F}(\vec{Q})$  matrix can be constructed using the chain rule to be

$$D\vec{F}(\vec{Q}) = \frac{\partial \vec{F}}{\partial \vec{Q}} = \left( \frac{\partial \vec{F}}{\partial \vec{r}} \right) \left( \frac{\partial \vec{r}}{\partial \vec{v}_0} \right) = \frac{\partial \vec{F}}{\partial \vec{v}_0}, \quad (127)$$

where  $\vec{r} = [x \ y]^T$ , and  $\frac{\partial \vec{r}}{\partial \vec{v}_0}$  can be taken from the upper right-hand corner of the planar

STM ( $4 \times 4$ ), computed during that iteration. In matrix form, this becomes

$$D\vec{F}(\vec{Q}) = \begin{bmatrix} \frac{\partial F_1}{\partial x} & \frac{\partial F_1}{\partial y} \\ \frac{\partial F_2}{\partial x} & \frac{\partial F_2}{\partial y} \end{bmatrix} \begin{bmatrix} \frac{\partial x}{\partial \dot{x}_0} & \frac{\partial x}{\partial \dot{y}_0} \\ \frac{\partial y}{\partial \dot{x}_0} & \frac{\partial y}{\partial \dot{y}_0} \end{bmatrix} = \begin{bmatrix} -1 & 0 \\ 0 & -1 \end{bmatrix} \frac{\partial \vec{r}}{\partial \vec{v}_0} = -I \frac{\partial \vec{r}}{\partial \vec{v}_0}. \quad (128)$$

Since equations (127) and (128) represent a square matrix, the update equation for this scenario follows in the form of equation (122),

$$\begin{bmatrix} \dot{x}_0 \\ \dot{y}_0 \end{bmatrix}^{j+1} = \begin{bmatrix} \dot{x}_0 \\ \dot{y}_0 \end{bmatrix}^j - \begin{bmatrix} -I \frac{\partial \vec{r}}{\partial \vec{v}_0} \end{bmatrix}^{-1} \begin{bmatrix} x_d - x^t(\vec{v}_0) \\ y_d - x^t(\vec{v}_0) \end{bmatrix}, \quad (129)$$

where equation (129) is iterated until  $\|\vec{F}(\vec{Q})\| < 10^{-12}$ .

Time can also be set as a design variable when employing a single-shooting method. In this case, time will be added as a design variable and the  $D\vec{F}(\vec{Q})$  matrix will incorporate elements of the recently computed STM, as well as the time derivatives of the current iteration.

When initial guesses for patch points are available, multiple-shooting provides a method for targeting that may be a more powerful technique for more challenging design problems. Near chaotic regions of the design space, small modifications to the initial conditions of a trajectory may lead to substantial changes in the end state. Breaking the trajectory into smaller sections and applying a differential corrections process across all sections simultaneously may create an algorithm that has a higher likelihood to find an overall solution, and/or it may not require as close of an initial guess as a single-shooting algorithm would require. Multiple-shooting is essentially a collection of single-shooting processes in one overall targeting scheme, with an initial setup depicted in Figure 21.

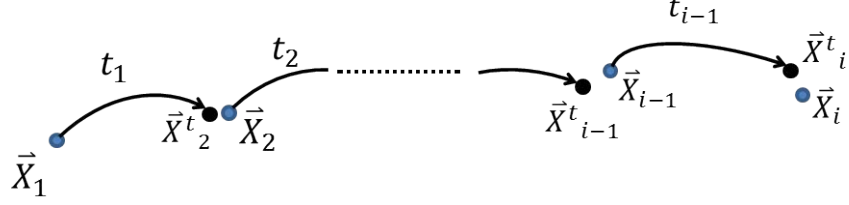


**Figure 21. Notional Multiple-Shooting Targeting Process with Fixed Initial and Final Positions.**

The overall reference solution for a multiple-shooting algorithm is a concatenation of each reference segment. The initial guess for this method is a set of “patch points” that identify different points along the reference path. Each segment on the trajectory begins at a fixed initial position with initial state condition,  $\vec{X}_i$ . The initial conditions of each point are altered such that the difference between their end state,  $\vec{X}_i^t$ , and the next state,  $\vec{X}_{i+1}$ , is driven to zero, i.e.,  $\vec{X}_{i+1}^t(\vec{X}_i) = \vec{X}_{i+1}$  for all  $i$ . A new set of discrete points (as close as possible to the old set) form a continuous trajectory in the entire phase space (seen in Figure 22).

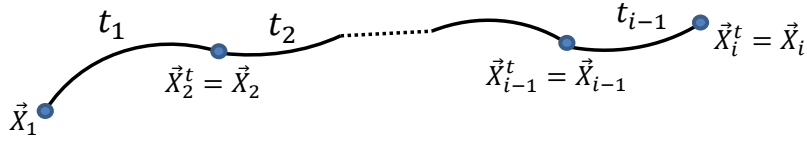


**Figure 22. Notional Multiple-Shooting Targeting Process with Forced Continuity in Position and Velocity.**

The design variable vector,  $\vec{Q}$ , can include any or all of the state vectors for the patch points, as well as the time for each segment,  $t_i$  to  $t_{i-1}$ , or other quantities that are functions of the states or their times. As an example, consider a trajectory with four separate segments ( $i = 4$ ). The  $\vec{Q}$  vector may be assembled of the five initial points connecting the segments,  $\vec{Q} = [\vec{X}_1 \ \vec{X}_2 \ \vec{X}_3 \ \vec{X}_4 \ \vec{X}_5]^T$ , and to ensure continuity

from the beginning state to the end state, the constraints vector is constructed,

$$\vec{F}(\vec{Q}) = \begin{bmatrix} \vec{X}_2^t(\vec{X}_1) - \vec{X}_2 \\ \vec{X}_3^t(\vec{X}_2) - \vec{X}_3 \\ \vec{X}_4^t(\vec{X}_3) - \vec{X}_4 \\ \vec{X}_5^t(\vec{X}_4) - \vec{X}_5 \end{bmatrix}. \quad (130)$$

Note that to target a closed, periodic orbit from beginning to end, the first and last points can be defined so that they are the same, and the distance between them is driven to zero by the nature of the algorithm. Consider this example in the spatial CR3BP. Since the variable vector contains five patch points, and each patch point defines a state of length six, this gives  $\vec{Q}$  a length of thirty ( $n = 30$ ). The constraints vector contains four equations constraining states of length six, giving  $\vec{F}(\vec{Q})$  a length of twenty-four ( $m = 24$ ). The  $D\vec{F}(\vec{Q})$  matrix is then expected to have size  $m \times n = 24 \times 30$ . This matrix assembles the partial derivatives of each constraint equation with respect to each design variable, defined below:

$$\vec{F}(\vec{Q}) = \begin{bmatrix} \frac{\partial \vec{F}_1}{\partial \vec{Q}_1} & \dots & \frac{\partial \vec{F}_1}{\partial \vec{Q}_5} \\ \vdots & \ddots & \vdots \\ \frac{\partial \vec{F}_4}{\partial \vec{Q}_1} & \dots & \frac{\partial \vec{F}_4}{\partial \vec{Q}_5} \end{bmatrix}. \quad (131)$$

Notice that each numerically integrated end state in an iteration is a function of the previous state, expressed in the first quantity in each constraint equation (equation

(130)). The beginning and end states can then be input to equation (131), giving,

$$D\vec{F}(\vec{Q}) = \begin{bmatrix} \frac{\partial \vec{X}_2^t(\vec{X}_1)}{\partial \vec{X}_1} & -I_{6 \times 6} & 0_{6 \times 6} & \cdots & 0_{6 \times 6} \\ 0_{6 \times 6} & \frac{\partial \vec{X}_3^t(\vec{X}_2)}{\partial \vec{X}_2} & -I_{6 \times 6} & \ddots & \vdots \\ \vdots & \ddots & \frac{\partial \vec{X}_4^t(\vec{X}_3)}{\partial \vec{X}_3} & -I_{6 \times 6} & 0_{6 \times 6} \\ 0_{6 \times 6} & \cdots & 0_{6 \times 6} & \frac{\partial \vec{X}_5^t(\vec{X}_4)}{\partial \vec{X}_4} & -I_{6 \times 6} \end{bmatrix}, \quad (132)$$

which is expanded and simplified to become,

$$D\vec{F}(\vec{Q}) = \begin{bmatrix} \Phi_1(t_1, t_0) & -I_{6 \times 6} & 0_{6 \times 6} & \cdots & 0_{6 \times 6} \\ 0_{6 \times 6} & \Phi_1(t_2, t_1) & -I_{6 \times 6} & \ddots & \vdots \\ \vdots & \ddots & \Phi_1(t_3, t_2) & -I_{6 \times 6} & 0_{6 \times 6} \\ 0_{6 \times 6} & \cdots & 0_{6 \times 6} & \Phi_1(t_4, t_3) & -I_{6 \times 6} \end{bmatrix}. \quad (133)$$

Since  $D\vec{F}(\vec{Q})$  is not a square matrix, the update equation for the minimum-norm solution (equation (123)) is solved iteratively until  $\|\vec{F}(\vec{Q}^{j+1})\| \leq \epsilon$ . The free variable vector  $\vec{Q}^*$  then represents the solution for a converged orbit.

### 3.2 Continuation Methods

As stated previously, periodic orbits in the CR3BP always exist as families of periodic orbits. For each periodic orbit, two eigenvalues of the monodromy matrix are equal to one. One of these eigenvalues is associated with the periodicity of the orbit, and since each eigenvalue comes in a reciprocal pair, there is another eigenvalue equal to one. This second unity eigenvalue indicates that there are other periodic orbits nearby that have similar characteristics as the original orbit. Once a periodic orbit is converged with single- or multiple-shooting, a continuation procedure searches for next ( $k^{th}$ ) solution,  $\vec{Q}^{k+1}$ , using the original, converged orbit,  $\vec{Q}^*$ , as an initial guess. Single-parameter continuation searches for the next solution by perturbing the first

solution's initial condition by stepping in some physical direction. In this investigation, several members of the planar Lyapunov orbit family is computed around the  $L_1$  libration point. After using single shooting to compute the first periodic orbit, other family members were generated by perturbing the  $x_0$  component of the initial state of the first periodic orbit by  $\delta x$  along the  $x$ -axis. This slightly perturbed state is the initial guess for the second orbit in a single-shooting algorithm, where equation (122) is employed to compute the next periodic Lyapunov orbit family member. The procedure is repeated to solve for other members in the family, displayed in Figure 23.

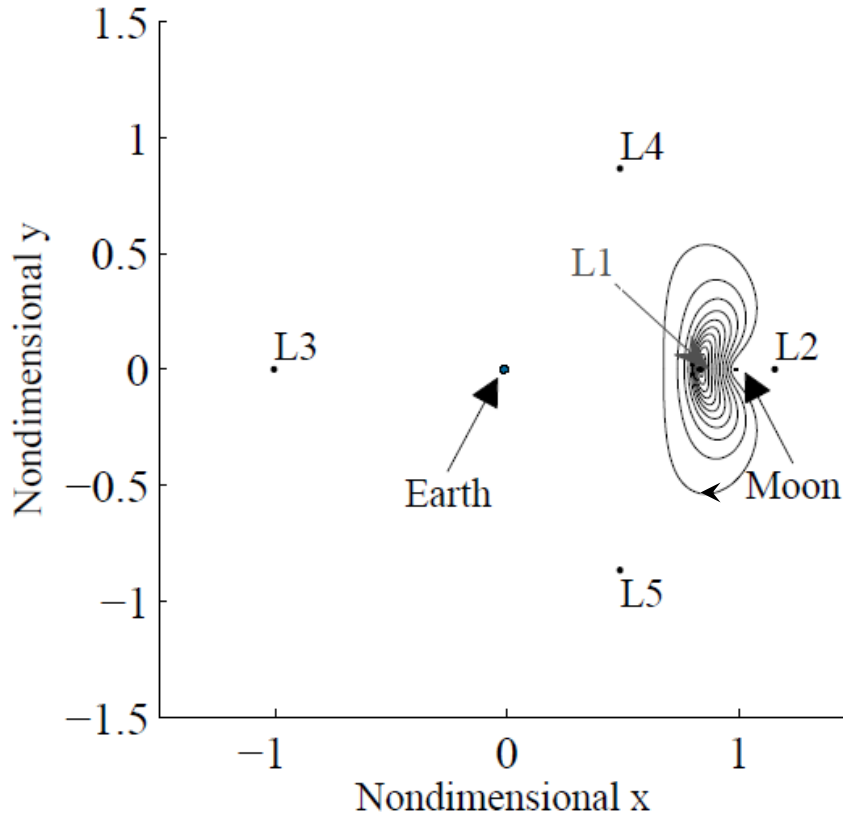


**Figure 23. Several Members in Planar  $L_1$  Lyapunov Orbit Family in Barycentric Rotating Frame.**

Another method of continuing an orbit family is by pseudo-arclength continuation (PAC). The PAC method is a more robust type of single-parameter continuation. PAC



uses the previous family member and searches for the next member with no *a priori* knowledge of the evolution of the particular family, while requiring an additional constraint equation [38, 39, 53]. Traditional single-parameter continuation computes family members by searching in a spatial direction or by increasing or decreasing another orbital parameter, such as  $JC$  or orbital period. Using the PAC method, the continuation parameter moves in fixed steps, but is not required to be a physical quantity or to be stepping in a predetermined direction relating to the evolution of the family. PAC uses the null space of the Jacobian matrix to take a nonphysical step exactly tangent to the previous family member. In this research, a pseudo-arclength continuation scheme is implemented with a multiple-shooting algorithm used to search for families of resonant orbits, using the apses of each orbit as patch points. Planar members of the periodic 4:3 resonant orbit family are found by PAC. The 3-D axial members of this family are found by first finding the planar bifurcation orbit using the method of bisections described in Section 2.12. PAC is then implemented to find the closest 3-D member from the bifurcation orbit, using a slight velocity perturbation in the  $z$ -direction (about 10 mm/s was used in this investigation) to seed the initial 3-D orbit's initial state.

The multiple-shooting variables for this objective are listed below:

$$\vec{Q} = \begin{bmatrix} \vec{X}_1 \\ \vec{X}_2 \\ \vdots \\ \vec{X}_N \\ t_1 \\ \vdots \\ t_{N-1} \\ \beta \end{bmatrix} \quad (134)$$

$$\vec{F}(\vec{Q}) = \begin{bmatrix} \vec{X}_2^t - \vec{X}_2 \\ \vdots \\ \vec{X}_N^t - \vec{X}_N \\ x_N - x_1 \\ y_N - y_1 \\ z_N - z_1 \\ \dot{x}_N^t - \dot{x}_1 \\ \dot{z}_N^t - \dot{z}_1 \\ \dot{y}_N^t + \beta^2 \\ \vec{r}_1 \cdot \vec{v}_1 \\ \vdots \\ \vec{r}_{N-1} \cdot \vec{v}_{N-1} \end{bmatrix} \quad (135)$$

This algorithm defines the final patch point to be almost the same as the initial patch point, enforcing continuity for the trajectory and finding a closed orbit. Notice the constraint  $\dot{y}_N^t + \beta^2$  in equation (135). In order to avoid over-constraining the problem, the difference between all components in the initial and final states is driven to zero, except for the final velocity component in the  $y$ -direction,  $\dot{y}_N^t$ . The constraint for  $\dot{y}_N^t$  defines a slack variable,  $\beta$  such that  $\dot{y}_N^t$  must be negative (and consistent with the direction of spacecraft motion for this case). Since the value for  $JC$  is constant along any trajectory, the  $JC$  for this case defines the *magnitude* of the velocity in the  $y$ -direction at the end of the trajectory, and  $\beta$  forces the *direction* to be negative, thereby enforcing continuity along the entire orbit. The initial guess for  $\beta$  is  $-\sqrt{\|\dot{y}_1\|}$ .

$$D\vec{F}(\vec{Q}) = \frac{\partial \vec{F}(\vec{Q})}{\partial \vec{Q}} =$$

$$= \begin{bmatrix} \frac{\partial \vec{X}_2^t}{\partial \vec{X}_1} & \frac{-\partial \vec{X}_2}{\partial \vec{X}_2} & 0_{6 \times 6} & 0_{6 \times 6} & \frac{\partial \vec{X}_2^t}{\partial t_1} & 0_{6 \times 6} & \cdots & 0_{6 \times 6} & 0 \\ 0_{6 \times 6} & & & 0_{6 \times 6} & 0_{6 \times 6} & \ddots & 0_{6 \times 6} & \vdots & \vdots \\ \vdots & \ddots & \ddots & 0_{6 \times 6} & 0_{6 \times 6} & \ddots & \ddots & 0_{6 \times 6} & \vdots \\ 0_{6 \times 6} & 0_{6 \times 6} & \frac{\partial \vec{X}_N^t}{\partial \vec{X}_{N-1}} & \frac{-\partial \vec{X}_N}{\partial \vec{X}_N} & 0_{6 \times 6} & \cdots & 0_{6 \times 6} & \frac{\partial \vec{X}_N^t}{\partial t_{N-1}} & \vdots \\ \left[ \begin{array}{c} J_{6 \times 6} \\ 0_{6 \times 6N-3} \\ K_{6 \times 6} \\ L_{6 \times 6} \end{array} \right] & & & & \begin{array}{c} 0 \\ \vdots \\ \vdots \\ \vdots \\ \vdots \\ 0 \\ 0 \end{array} & \begin{array}{c} 0 \\ \vdots \\ \vdots \\ \vdots \\ \vdots \\ 0 \\ \cdots \end{array} & \begin{array}{c} 0 \\ \vdots \\ \vdots \\ \vdots \\ \vdots \\ 0 \\ 0 \end{array} & \begin{array}{c} 0 \\ \vdots \\ \vdots \\ \vdots \\ \vdots \\ 0 \\ \frac{\partial y_N^t}{\partial t_{N-1}} \end{array} & \begin{array}{c} \vdots \\ \vdots \\ \vdots \\ \vdots \\ \vdots \\ 0 \\ 2\beta \end{array} \\ \left[ \begin{array}{c} \frac{\partial \vec{X}_2^t}{\partial \vec{X}_1} \\ \frac{-\partial \vec{X}_2}{\partial \vec{X}_2} \\ 0_{6 \times 6} \\ 0_{6 \times 6} \\ \frac{\partial \vec{X}_2^t}{\partial t_1} \\ 0_{6 \times 6} \\ \cdots \\ 0_{6 \times 6} \\ 0 \end{array} \right] & & & & & & & & \end{bmatrix}, \quad (136)$$

where, noticing various diagonal terms that are equivalent to the STMs for each segment, identity matrices, and time derivatives at the end states, the submatrices in equation (136) are defined and simplified further:

$$J_{6 \times 6} = \begin{bmatrix} \frac{\partial x_N - x_1}{\partial x_1} & 0 & \cdots & \cdots & \cdots & 0 \\ 0 & \frac{\partial y_N - y_1}{\partial y_1} & 0 & \cdots & \cdots & \vdots \\ \vdots & 0 & \frac{\partial z_N - z_1}{\partial z_1} & 0 & \cdots & \vdots \\ \vdots & \cdots & 0 & \frac{\partial \dot{x}_N - \dot{x}_1}{\partial \dot{x}_1} & 0 & 0 \\ \vdots & \cdots & \cdots & \cdots & 0 & \frac{\partial \dot{z}_N - \dot{z}_1}{\partial \dot{z}_1} \\ 0 & \cdots & \cdots & \cdots & \cdots & 0 \end{bmatrix}$$

$$= \begin{bmatrix} \begin{bmatrix} & & & \\ & & & \\ -I_{4 \times 4} & & & \\ & & & \end{bmatrix} & \begin{matrix} 0 & 0 \\ \vdots & \vdots \\ \vdots & \vdots \\ 0 & 0 \end{matrix} \\ 0 \dots \dots \dots 0 & -1 \\ 0 \dots \dots \dots \dots & 0 \end{bmatrix}, \quad (137)$$

$$K_{6 \times 6} = \begin{bmatrix} \begin{bmatrix} & & & & \\ & & & & \\ & & 0_{5 \times 6} & & \\ & & & & \\ & & & & \end{bmatrix} \\ 0 \dots \dots 0 \frac{\partial(\dot{y}_N + \beta^2)}{\partial \dot{y}_{N-1}} 0 \end{bmatrix}$$

$$= \begin{bmatrix} \begin{bmatrix} & & & & \\ & & & & \\ & & 0_{5 \times 6} & & \\ & & & & \\ & & & & \end{bmatrix} \\ 0 \dots \dots 0 \Phi(t_N, t_{N-1}) 0 \end{bmatrix}, \quad (138)$$

$$L_{6 \times 6} = \begin{bmatrix} \frac{\partial x_N - x_1}{\partial x_N} & 0 & \dots & \dots & \dots & 0 \\ 0 & \frac{\partial y_N - y_1}{\partial y_N} & 0 & \dots & \dots & \vdots \\ \vdots & 0 & \frac{\partial z_N - z_1}{\partial z_N} & 0 & \dots & \vdots \\ \vdots & \dots & 0 & \frac{\partial \dot{x}_N - \dot{x}_1}{\partial \dot{x}_N} & 0 & 0 \\ \vdots & \dots & \dots & \dots & 0 & \frac{\partial \dot{z}_N - \dot{z}_1}{\partial \dot{z}_N} \\ 0 & \dots & \dots & \dots & \dots & 0 \end{bmatrix}$$

$$= \begin{bmatrix} \begin{bmatrix} & & & \\ & I_{4 \times 4} & & \\ & & & \end{bmatrix} & \begin{matrix} 0 & 0 \\ \vdots & \vdots \\ \vdots & \vdots \\ 0 & 0 \end{matrix} \\ 0 & \dots & \dots & \dots & 0 & 1 \\ 0 & \dots & \dots & \dots & \dots & 0 \end{bmatrix}, \quad (139)$$

and

$$\alpha_{N-1 \times 7N} = \begin{bmatrix} \frac{\partial(\vec{r}_1 \cdot \vec{v}_1)}{\vec{X}_1} & 0_{6 \times 6} & \dots & \dots & 0_{6 \times 6} & \frac{\partial(\vec{r}_1 \cdot \vec{v}_1)}{t_1} & 0_{6 \times 6} & 0_{6 \times 6} & 0_{6 \times 1} \\ 0_{6 \times 6} & \ddots & \ddots & \dots & \dots & 0_{6 \times 6} & \ddots & 0_{6 \times 6} & \vdots \\ \vdots & \vdots & \ddots & 0_{6 \times 6} & \dots & 0_{6 \times 6} & \ddots & 0_{6 \times 6} & \vdots \\ 0_{6 \times 6} & \dots & 0_{6 \times 6} & \frac{\partial(\vec{r}_{N-1} \cdot \vec{v}_{N-1})}{\vec{X}_N} & 0_{6 \times 6} & \dots & 0_{6 \times 6} & \frac{\partial(\vec{r}_{N-1} \cdot \vec{v}_{N-1})}{t_{N-1}} & 0_{6 \times 1} \end{bmatrix}$$

$$= \begin{bmatrix} [\vec{v}_1, \vec{r}_1] & 0 & \dots & 0 \\ 0 & [\vec{v}_2, \vec{r}_2] & \ddots & \vdots \\ \vdots & \ddots & \ddots & 0 \\ 0 & \dots & 0 & [\vec{v}_{N-1}, \vec{r}_{N-1}] \end{bmatrix}. \quad (140)$$

In this configuration of multiple-shooting variables, the free variable vector,  $\vec{Q}$  (length  $7N$ ), and constraints vector,  $\vec{F}(\vec{Q})$  (length  $7N - 1$ ), form a  $D\vec{F}(\vec{Q})$  matrix that is not square—there is one more design variable than constraint equation. The multiple-shooting targeter uses the minimum-norm equation (123) to compute a solution, satisfying  $\vec{F}(\vec{Q}) = \vec{0}$ . The next solution  $\vec{Q}^{k+1}$  is then predicted by using the previously converged solution  $\vec{Q}^* = \vec{Q}^k$  and stepping in some scalar step size  $\Delta s$ , defined tangent to the family by the null vector. The nullspace of the Jacobian matrix for the recent solution,  $D\vec{F}(\vec{Q})$ , provides the null vector,  $\Delta\vec{Q}^k$ . A linear step is taken

in this direction from the reference solution, shown by the simple equation,

$$\vec{Q}^{k+1} = \vec{Q}^k + \Delta s \cdot \Delta \vec{Q}^k. \quad (141)$$

To require that the next member in the family is a fixed step size from the previous solution, a scalar constraint equation is added to the constraints vector  $\vec{F}(\vec{Q})$ , to construct the augmented constraint vector for the new prediction,  $\vec{G}(\vec{Q})$ , defined,

$$\vec{G}(\vec{Q}^{k+1}) = \begin{bmatrix} \vec{F}(\vec{Q}^{k+1}) \\ (\vec{Q}^{k+1} - \vec{Q}^k)^T \Delta \vec{Q}^k - \Delta s \end{bmatrix}. \quad (142)$$

The addition of this constraint results in an equal number of variables and constraints, forming a square, augmented Jacobian matrix,

$$D\vec{G}(\vec{Q}^{k+1}) = \frac{\partial \vec{G}(\vec{Q}^{k+1})}{\partial \vec{Q}^{k+1}} = \begin{bmatrix} D\vec{F}(\vec{Q}^{k+1}) \\ \Delta \vec{Q}^{kT} \end{bmatrix}. \quad (143)$$

Recall equation (122) for obtaining a unique solution for the next member of the family by inverting the Jacobian matrix and iteratively updating the result,

$$\vec{Q}_{j+1}^{k+1} = \vec{Q}_j^{k+1} - \left[ D\vec{G}(\vec{Q}_j^{k+1}) \right]^{-1} \vec{G}(\vec{Q}_j^{k+1}). \quad (144)$$

Once a solution is determined (the next family member is found), the entire algorithm repeats and a given number of family members may be calculated. Figure 27 shows members of the Earth-Moon 4:3 resonant orbit family, calculated using this method. PAC is particularly useful when little information is known about a particular family or when a parameter obeying a simple trend is difficult to find. In general, PAC does not require prior information to find families and collections of orbits.

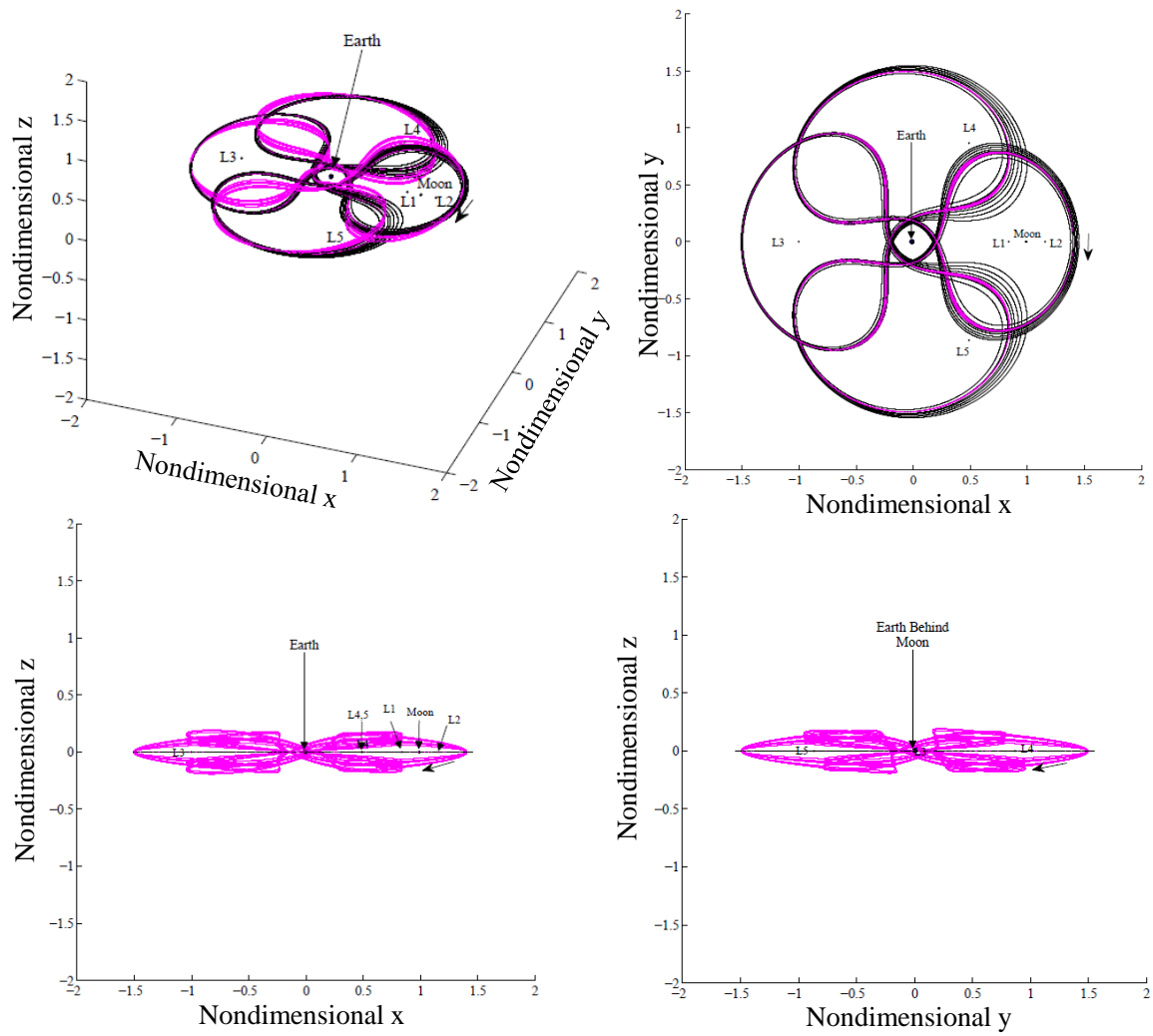


Figure 24. Planar and Axial Members of Periodic 4:3 Resonant Orbit Family.

### 3.3 Periapsis Poincaré Maps

In Section 2.16, Poincaré maps with Cartesian phase space surfaces of section were described, in which the hyperplane ( $y = 0$ ) was a plane in the configuration space. In general, the surface of section does not have to be a plane in the configuration space, but rather, can be a plane specified by a condition associated with the phase space, including the velocity space. Such is the case with periapsis Poincaré maps, defined by the plane of periapsis passage. In the two-body problem, a periapse occurs when a point on a trajectory reaches a minimum distance to the primary, and conversely, an apoapse reflects the greatest distance from the gravitational body [75, 76, 77]. In the CR3BP, an apse is the condition of having zero velocity in the radial direction from the chosen reference primary. In previous research, the periapses are often defined with respect to the smaller primary,  $P_2$ , due to the interest of different applications for trajectories in the vicinity of moons [30, 53, 73, 75, 76, 77]. In this investigation, the focus goes toward the characterization and application of trajectories near the Earth (or  $P_1$  in the Earth-Moon CR3BP), and for this reason,  $r$  is defined as the radial distance between the Earth and the spacecraft ( $P_1$  and  $P_3$ ). Periapsis satisfies the apse condition of  $\dot{r} = 0$ , giving a local minimum of the position magnitude of the spacecraft with respect to the Earth, and occurs specifically when  $\ddot{r} \geq 0$ . Apoapsis is then when  $\dot{r} = 0$  and  $\ddot{r} \leq 0$ . One useful feature of a periapsis surface of section is that it may be projected directly into the more intuitively understood configuration space, rather than a mixed position-velocity phase space, as in Figure 19. For this research, only the planar CR3BP periapsis maps will be generated, creating 2-D maps. The following explanation of the periapsis condition in the CR3BP is based on Villac and Scheeres's development, along with Haapala's adaptations [30, 73, 75]. The position



vector of  $P_3$  with respect to  $P_1$ ,  $\vec{q}$ , and its derivative,  $\dot{\vec{q}}$ , are then defined

$$\vec{q} = [x + \mu \ y]^T, \quad \dot{\vec{q}} = [\dot{x} \ \dot{y}]^T. \quad (145)$$

The magnitude of the radial acceleration can then be written:

$$\ddot{r} = \frac{1}{r}(\dot{\vec{q}}\dot{\vec{q}}^T) - \frac{1}{r^3}(\vec{q}\dot{\vec{q}}^T)^2. \quad (146)$$

The periapsis condition in terms of Cartesian coordinates can then defined by

$$\vec{q}^T \dot{\vec{q}} = 0 \quad (147)$$

and with  $v = \|\dot{\vec{q}}\|$ ,

$$v^2 + \vec{q}^T \ddot{\vec{q}} = 0, \quad (148)$$

where equation (147) sets the last term in equation (146) to zero, producing equation (148) [75]. Thus, the condition of periapsis occurs when  $\vec{q}$  is orthogonal to  $\dot{\vec{q}}$ . Though the vector  $\vec{q}$  and its derivative may be expressed in any coordinate frame, the definitions above are frame independent, therefore a periapse in the rotating frame is also defined as a periapse in the inertial frame. The periapsis Poincaré maps produced in this investigation are categorized into two types: (1) maps showing the periapses of the stable and unstable manifolds of unstable periodic orbits, used for observing opportunities for transfer; and (2) maps with initial conditions starting with a periapse near GEO altitude in the planar CR3BP, used to explore end conditions for a given time interval. Each of these types of periapsis maps represent a 4-D polar coordinate phase space by a 2-D map, yet, the periapses are ultimately plotted in Cartesian coordinate configuration space in the rotating frame.

### 3.3.1 Periapsis Poincaré Maps Representing Stable and Unstable Invariant Manifold Trajectories

The first type of the periapsis Poincaré maps described in the preceding section shows the periapses of the stable and unstable manifolds departing from an unstable periodic Lyapunov orbit around  $L_1$  in negative and forward time, respectively. The periapses are colored based on their association with the stable or unstable manifolds. These maps may give insight into the location of a homoclinic connection between the stable and unstable manifolds of the same periodic orbit. If exact homoclinic connections are not observed, periapses of the manifolds that *almost* intersect in the full phase space are recorded, and the periapse information for one of the “close” points may be used as the transfer point, at which performing a small maneuver from the original manifold may satisfy mission objectives. The design goals of this analysis also focus on the physical regions of periapses near certain altitudes from the Earth for transfer design. Since a periapse has no radial velocity, an impulsive maneuver to/from a manifold trajectory from/to an initial orbit around the Earth would indicate a tangent burn at the periapse location (completely perpendicular to the radial direction defining the periapse). Both types of maps as well as some of these applications are explored in the next chapter.

### 3.3.2 Periapsis Poincaré Maps Displaying Near-Earth Trajectories

The second type of periapsis map in this investigation uses initial conditions in polar coordinates of the form  $\vec{X}_0 = [r_0 \ \theta_0 \ \dot{r}_0 \ \dot{\theta}_0]$  where  $\theta$  is the angle measured counter-clockwise from the  $x$ -axis in the configuration space. Trajectories beginning with periapses where  $r_0$  is defined at GEO altitude for the planar CR3BP are used, where  $\theta$  is incremented around the Earth in steps of  $10^\circ$ , determining 36 different trajectories for the map. The  $\dot{r}_0$  component is zero for each initial condition from the

definition of periapsis, and the  $\dot{\theta}$  value is determined from a given  $JC$  for the map. The sign of  $\dot{\theta}$  in this analysis was defined as positive, giving trajectories that are initially prograde with respect to the Earth. Although all trajectories are initially prograde, subsequent periapse points may be prograde or retrograde, in general. These maps are color-coded according to each trajectory’s condition at the end of the integration time, arbitrarily chosen to be 155 revolutions of the primaries (about 11.5 years). Trajectories that stay “bounded” within the Earth region are recorded in one color, while trajectories that pass through the  $L_1$  “gateway,” or the  $L_2$  “gateway” when they are open are represented in a different color. The periapses on the map that are labeled a certain color belong to a trajectory that eventually has the specified condition. This implies that if a spacecraft is on a trajectory and reaches a periapse in one of the regions of specific periapse behavior, looking at the map will tell the observer the end condition of the spacecraft. Applications of these maps may include mission design with a desired end behavior, as well as the analysis of the predictability of an observed trajectory (seen in Section 4.3).

### 3.4 Chapter 3 Summary

In this chapter, the specific numerical methods used in this investigation are introduced and derived. Single- and multiple-shooting algorithms are explained, which will be used to find a trajectory solution from one point in the Earth-Moon system to another. A pseudo-arclength continuation method is described, using points satisfying the CR3BP periapsis condition to find periodic resonant orbit family members. These methods are applied in specific design scenarios, each contributing to final mission designs presented in the next chapter. The multiple-shooting code that is imbedded in the pseudo-arclength continuation algorithm is used to find single resonant orbits. Test Case I uses the 4:3 periodic resonant orbit family members found

in the PAC process to find an initial guess for a multiple shooting algorithm that is employed to find a transfer trajectory to and from Earth-centered orbits. Finally, a description of the periapsis surface of section and the associated Poincaré maps are introduced. Both Test Case II and Test Case III implement periapsis Poincaré maps. Test Case II examines the periapsis map of invariant manifold trajectories from a Lyapunov orbit about the Earth-Moon  $L_1$  libration point. This map shows the stable and unstable periapse points in different colors to show opportunities for transfer using these trajectories. Test Case III examines periapsis Poincaré maps displaying periapse information for a set of orbits starting near GEO altitudes (while remaining in the Earth-Moon plane). These points are colored according to the behavior of the orbit by the end of the integration time. These maps may be used to design a mission with a desired “end” behavior (at least by a specified integration time) or to use observed periapse information of an unknown spacecraft trajectory to determine the behavior of the unknown orbit.

## 4. Test Cases: Results and Analysis

Test cases and specific scenarios are observed using the tools mentioned in Chapter 3 aid in mission design. The analysis following each test case also offers some discussion of the advantage to the “warfighting mission assurance.” The *Space Domain Mission Assurance: A Resilience Taxonomy* white paper put out by the Office of the Assistant Secretary of Defense for Homeland Defense and Global Security describes the concept of “resilience” in space systems as the “warfighting mission assurance benefit” [12]. The paper examines three interrelated approaches for mission assurance: (1) “Defensive Operations” (actions made to provide insight of an unknown spacecraft’s operations), (2) “Reconstitution” (bringing new components on-line as a plan for contingency or to replace decommissioned assets), and (3) “Resilience” (ability of the space operations to have mission success if unforeseen circumstances arise) [12]. Some of these approaches are enveloped in the analysis of the following test cases.

In Test Case I, the natural shapes of resonant orbits computed by pseudo-arclength continuation are examined to choose an initial resonant orbit arc to use to determine initial patch points to input in a multiple-shooting algorithm. This multiple-shooting algorithm searches for a solution that transfers a spacecraft from perigee of an initial geosynchronous transfer orbit to a final geostationary orbit for less  $\Delta V$  than standard transfer methods. The results of this design process are compared to the “nominal trajectory” in the AsiaSat-3/HGS-1 rescue mission as well as to the values for two-body transfer methods. The converged solution trajectory is propagated further, and contingency options are explored that correspond to the “figure-8” structure that emerges in the rotating frame. The contingency plans are examined in order to increase the design’s “resiliency” as outlined by the white paper [12].

In Test Case II, a periapsis Poincaré map gives insight into the design space

with information on periapses of invariant manifolds near the Earth. The stable and unstable manifold trajectory approximations are represented in different colors on the map, and a transfer is designed between Earth-centered orbits in the plane of the Earth and Moon. The initial orbit is a “Tundra” orbit that has apogee and perigee altitudes close to that of a standard Tundra orbit about the Earth, but is not a true Tundra orbit because it is in the plane of the Moon’s orbit about the Earth. The final orbit for this case is a “GEO-like” orbit also in the plane of the primaries that has a final altitude slightly smaller than typical GEO. The design’s “resilience” as referred to in the aforementioned white paper is also increased, as contingency options are also explored for this test case.

In Test Case III, the second type of periapsis Poincaré map is examined. Maps of multiple energy levels and integration times are presented. The periapse points on the map are color-coded according to the behavior of an orbit at the end of the chosen integration time. Orbits that start near GEO altitudes are examined on these maps and colored according to whether they impact the Earth or Moon, stay around the Earth region, or depart the Earth region. The applications of these maps as a means for transfer design when specific “end” behaviors are desired at the end of an integration time are discussed. The potential for these maps as a tool for predicting the future behavior or location of an unknown spacecraft is also explored, offering utility as a “defensive operation” described by the white paper [12].

#### **4.1 Test Case I: “Rescue” Mission**

To demonstrate the potential mission design capabilities of resonant orbits by exploiting the natural resonant orbit shape and to showcase the utility of robust targeting algorithms, a transfer scenario is created to closely resemble the AsiaSat-3/HGS-1 “rescue” mission described in Section 1.3. Consider a spacecraft left “stranded” in



the ascending node of the initial GTO was defined to be in line with the ascending node of the Moon's orbit about the Earth at the initial time,  $t_0$ . According to the Jet Propulsion Laboratory (JPL) HORIZONS web-interface data with the defined epoch, on this date, the Moon's inclination was  $18.6003^\circ$  with respect to Earth's equatorial plane. A constant inclination of  $19^\circ$  was used in both Ocampo's analysis and in this investigation for more equivalent comparison. This date also corresponds to a specific lunar right ascension of the ascending node or,  $\Omega = 5.26^\circ$ , and the specified setup of the Moon in this scenario defines  $\phi = \omega + \nu - t = 90^\circ - t$ , where  $\omega$  is the argument of perigee of the Moon and  $\nu$  is its true anomaly. A notional illustration of these initial angles is seen in Figure 26.

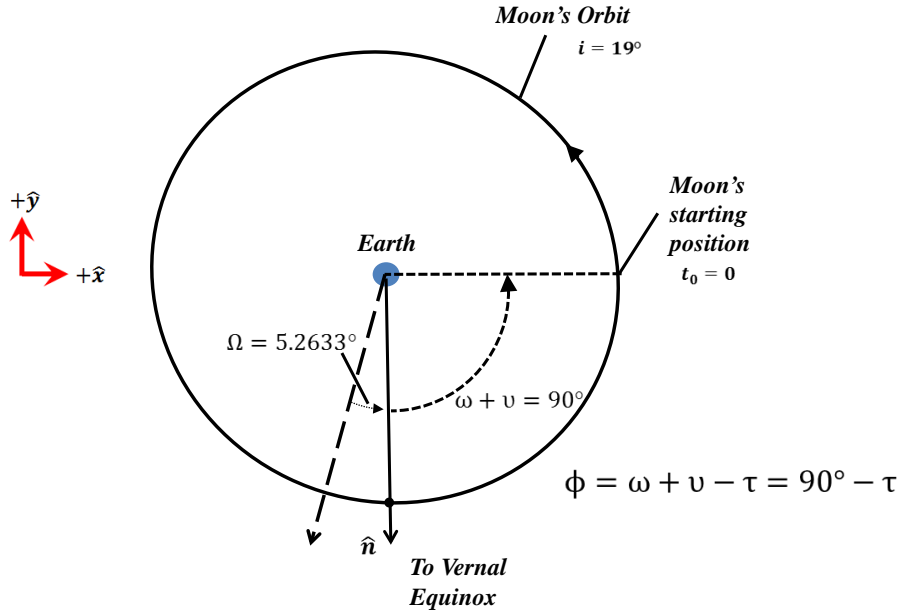


**Figure 26.** Notional Mission Setup of Earth and Moon Positions for Initial Geosynchronous Transfer Orbit (GTO) Transfer to Final Geosynchronous Orbit (GEO) via Lunar Fly-By.

Knowing that lunar fly-bys take advantage of the gravity of the Moon in a momentum transfer as the spacecraft approaches and departs close to the body, a resonant orbit with the same basic characteristics may be chosen as a model on which to base an initial guess for the transfer. A pathway shape is roughly defined between the ini-



tial GTO and final GEO that resembles a piece, or an “arc,” of a resonant orbit that uses the gravity of the Moon to change inclination from the highly inclined GTO to a minimally inclined GEO-altitude orbit. The 4:3 resonant orbit families were studied in greater detail in order to choose an appropriate resonant arc to use in the targeter. Recall the collection of the planar and axial 4:3 resonant orbit families in Figure 27.

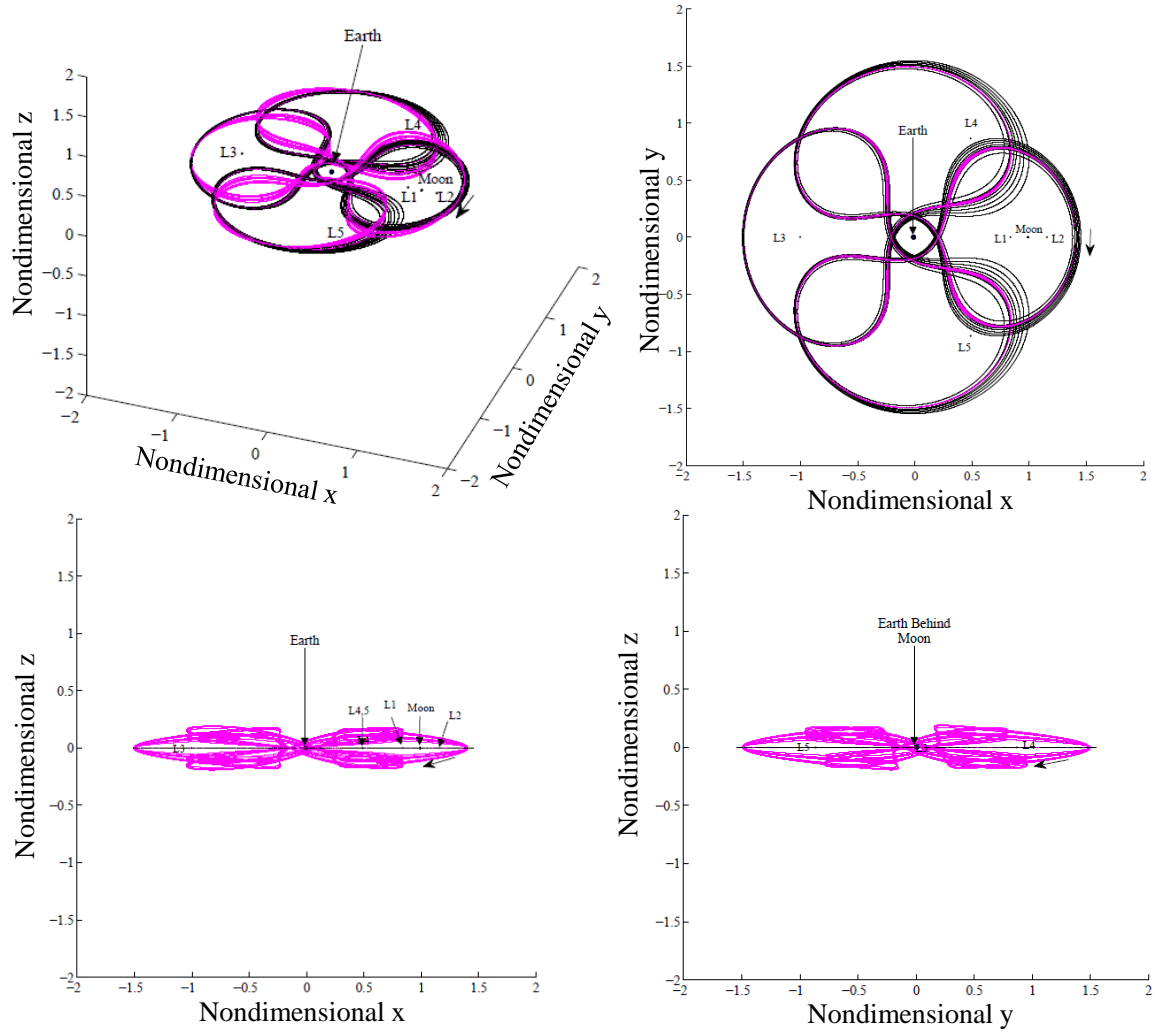


**Figure 27. Planar and Axial Members of Periodic 4:3 Resonant Orbit Family.**

The 4:3 resonant orbits in Figure 27 are computed with a pseudo-arclength continuation scheme that takes advantage of periapses as patch points. All members of

the family shown are classified as unstable periodic orbits that travel through four orbits about the Earth in the same time that the Moon completes three revolutions of the Earth. The 3-D family members of this family are found by perturbing the planar bifurcation orbit by adding a small initial velocity in the out-of-plane direction,  $\dot{z}_0$ . The other out-of-plane members are computed using the same PAC method as the planar members. Once this resonant orbit family is identified as a potentially useful orbit family for the “rescue” scenario, an “initial guess orbit” is identified. A specified segment, or the resonant arc, of this chosen orbit is used to generate patch points for a targeting algorithm that will constrain the locations of the initial and final maneuver points (from perigee of the GTO to any point on a GEO), giving freedom to the internal patch points to move. The initial guess orbit chosen from a collection of planar and 3-D 4:3 resonant orbit families is seen in Figure 28.

This orbit is chosen by a numerical process that compares an approximated initial state at perigee of the GTO to each state of a resonant orbit for every time step in the numerical integration of the orbit. The approximated initial state estimates the first maneuver using the initial  $\Delta V$  magnitude used for the “nominal trajectory” in the AsiaSat-3/HGS-1 mission. This process is continued for all orbits in the collection of the 4:3 resonant orbit family. The orbit that possesses the minimum difference between this state and the approximated initial maneuver state is then chosen as the initial guess orbit. The location of the point with the minimum difference in the phase space with the approximated initial maneuver point is highlighted in Figure 28. The Earth-centered inertial frame view of this chosen resonant orbit is seen in Figure 29, with the resonant arc highlighted in blue.

Five patch points were used to input into a multiple-shooting algorithm. Three patch points evenly spaced in time along this magenta arc are input, along with the approximated initial state at perigee of the GTO, and an approximated end

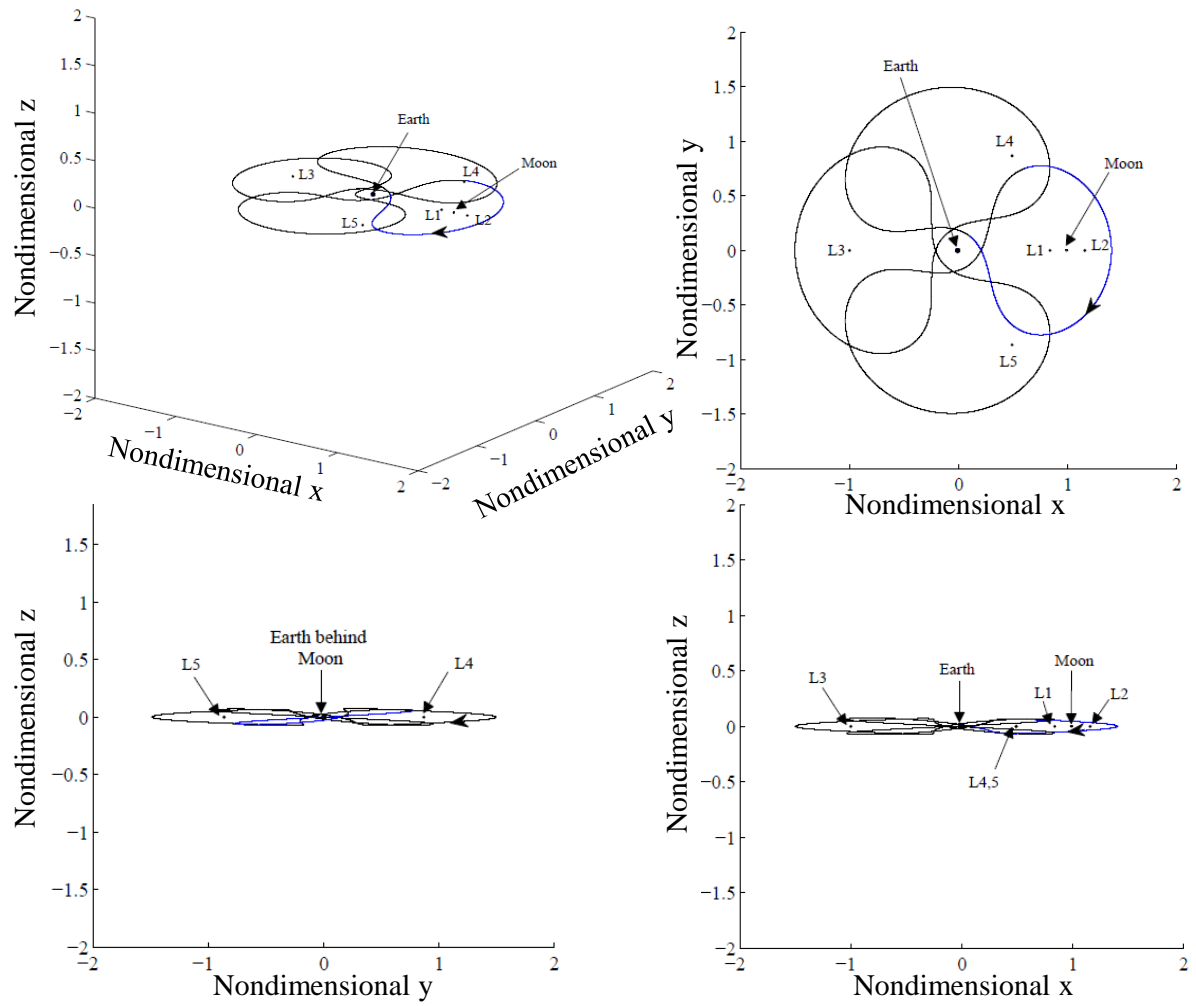


**Figure 28. Orbit Chosen from a Collection of Planar and 3-D 4:3 Resonant Orbit Families to Produce Initial Guess Patch Points for Multiple-Shooting Algorithm.**

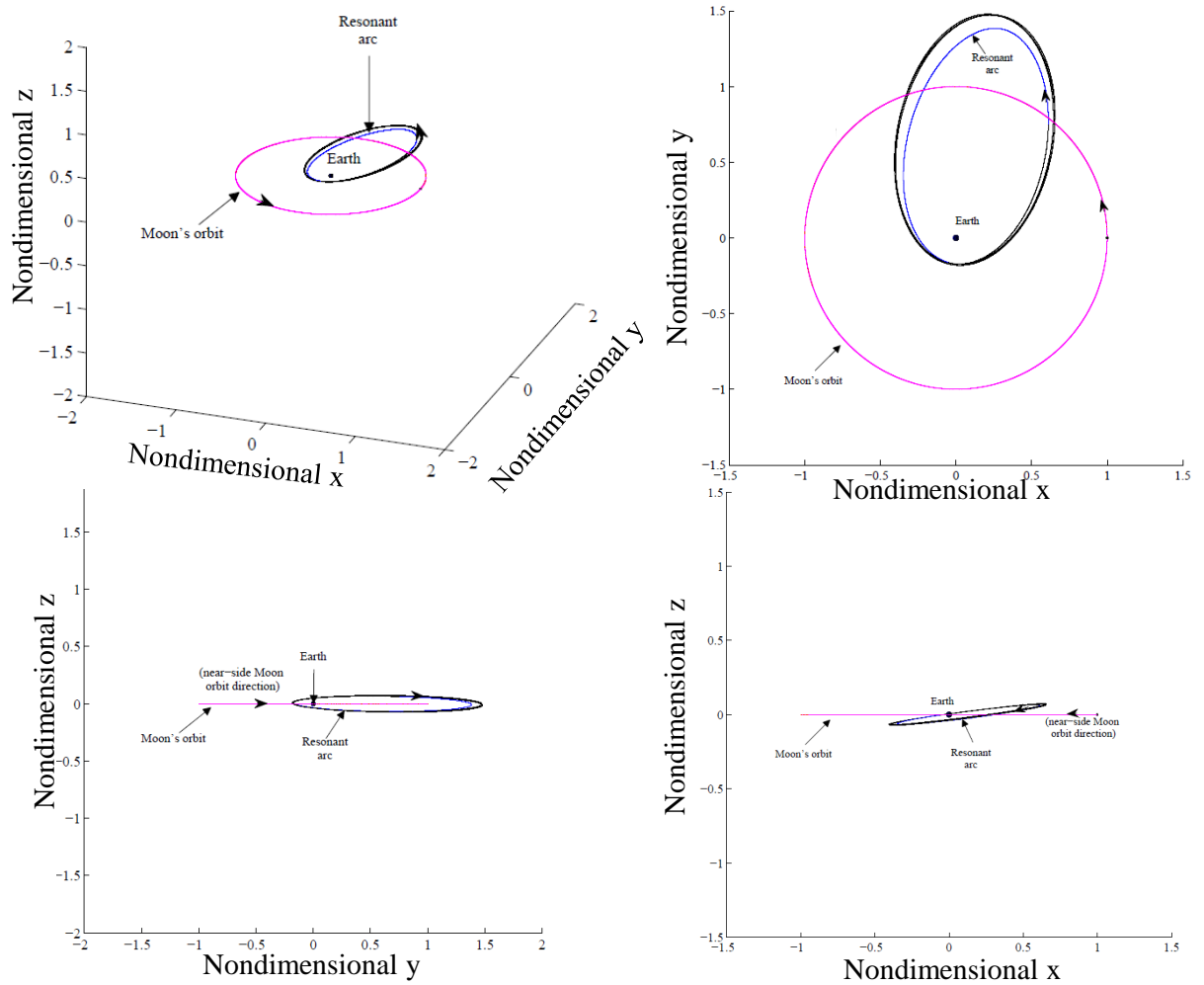


**Figure 29. Orbit Chosen from a Collection of Planar and 3-D 4:3 Resonant Orbit Families to Produce Initial Guess Patch Points for Multiple-Shooting Algorithm in Earth-Centered Inertial Frame.**

state located in GEO using two-body velocity values. The targeter allowed all patch points, except the initial position in the GTO, to vary (in both position and velocity) in order to converge to a continuous, “flyable” trajectory. The constraints vector that was driven to zero for this algorithm included all states of the five patch points (both position and velocity values). The trajectory was converged to within a total tolerance of  $10^{-12}$  nondimensional units, which, if all components of each state in the vector shared equal error, corresponds to each patch point location component having an accuracy to within  $1.28 \times 10^{-4}$  cm and each velocity component in each state having an accuracy to within  $3.42 \times 10^{-10}$  cm/s. The converged trajectory shown in Figures 30 and 31 yields a path similar to the resonant orbit arc, beginning at the specified point and ending the trajectory *near* GEO.

The converged trajectory specifications are seen in Table 2 as they compare to the “nominal trajectory” design for AsiaSat-3/HGS-1 as well as a two-body calculation for the  $\Delta V$  requirement to perform the inclination change from the GTO to GEO. Recall the first maneuver was constrained to stay at the same position, but the velocity was able to vary using the targeter. The resulting first burn was slightly off the tangent direction from perigee of the GTO, pointing slightly below the plane of the GTO. The second and final burn occurs at the end of the fly-by transfer arc when the trajectory reaches GEO altitude. The natural dynamics of the transfer arc take advantage of the gravitational field of the Moon, performing an inclination change from  $i = 51.619^\circ$  in the initial GTO to  $i = 9.55^\circ$  in the final orbit. The cost of performing a combined plane change and circularization maneuver at this final point is documented in Table 2 and incorporated into the final calculations.

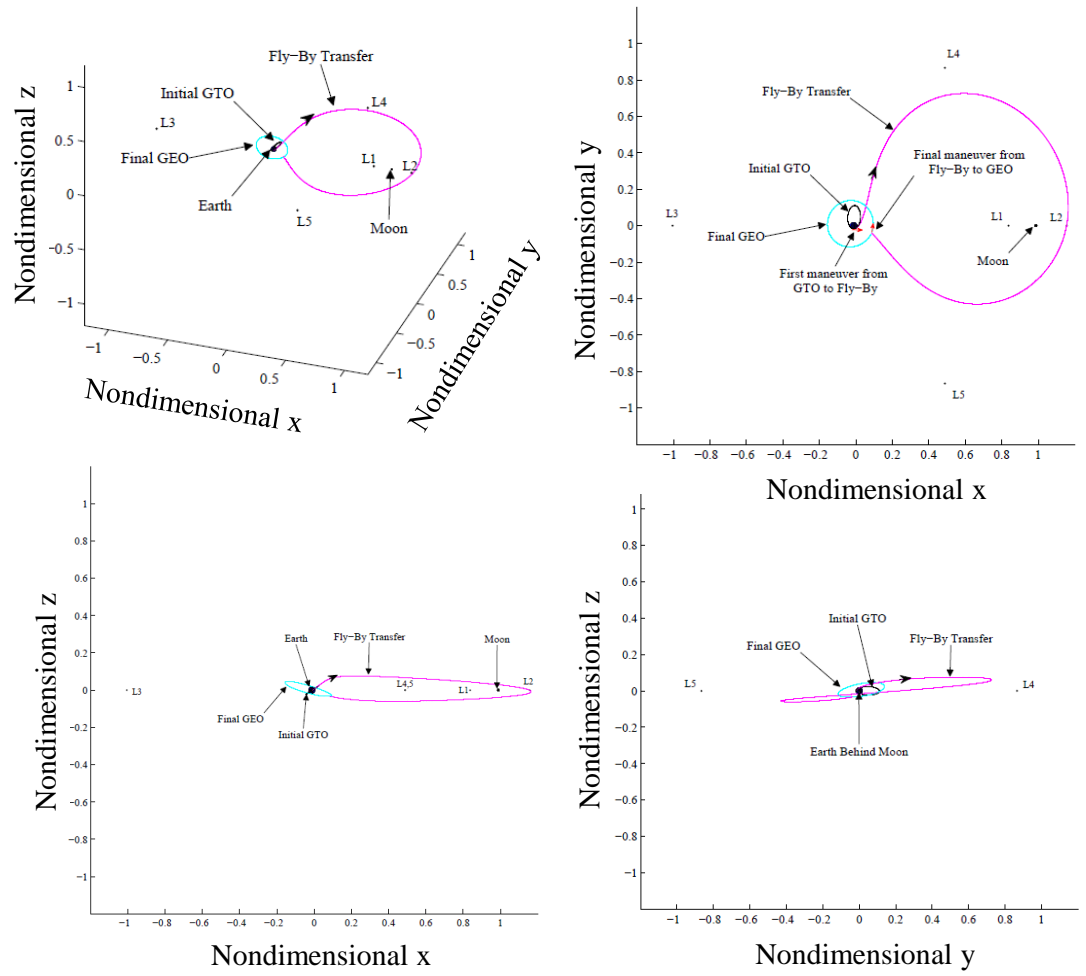


Figure 30. Converged Spacecraft Trajectory Transferring from Initial GTO to Final GEO via Lunar Fly-by in Barycentric Rotating Frame.

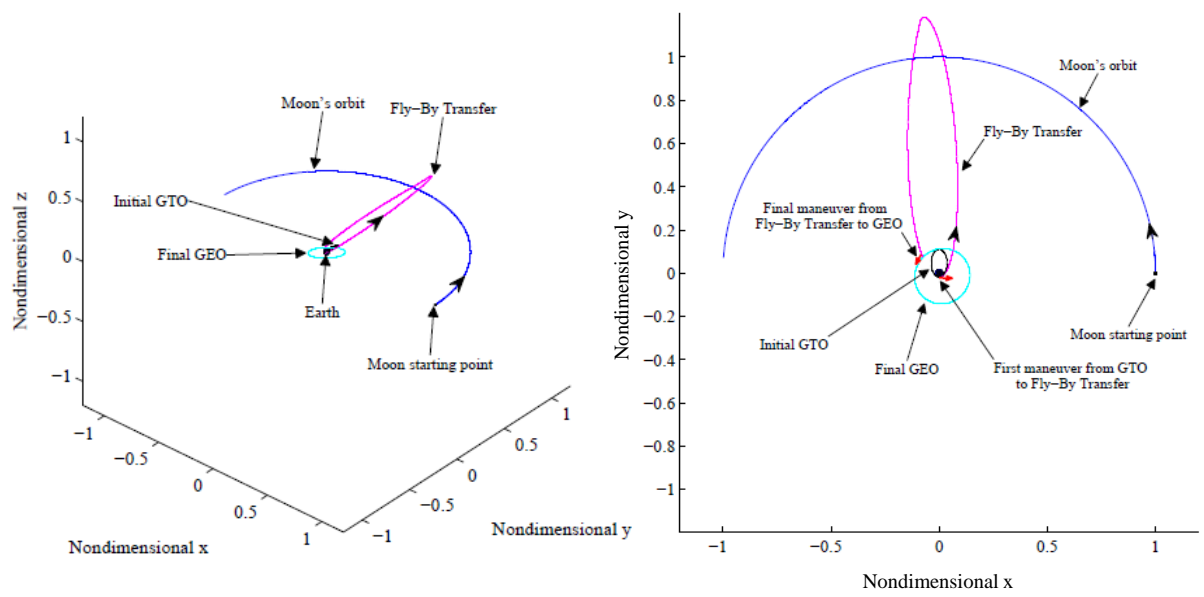


Figure 31. Converged Spacecraft Trajectory Transferring from Initial GTO to Final GEO via Lunar Fly-by in Earth-Centric Inertial Frame (Left: 3-D Inertial View, Right: Inertial x-y View).

Table 2. Compared Values for Two-body Calculations, the AsiaSat-3/HGS-1 “Nominal Trajectory” from Ocampo’s Analysis, and the Converged Design Using a Resonant Arc as an Initial Guess for a Multiple-Shooting Scheme.

	Two-Body Analysis	AsiaSat-3/HGS-1 “Nominal Trajectory”	Converged Design
Inclination After Fly-By (degrees)	-	0.000	9.551
Inclination of Final Orbit (degrees)	0.000	0.000	0.000
Final Semi-Major Axis (km)	42,376.813	42,376.813	42,527.795
Time of Flight (days)	0	$\approx 8$	11.985
Closest Distance to Moon’s Surface (km)	-	5,233.915	61,472.573
Furthest Distance From Earth’s Surface	-	614,217.311	456,004.214
$\Delta V_1$ (km/s)	-	0.683733 (tangent burn)	0.669003 (nontangent burn)
$\Delta V_2$ (km/s)	-	1.131441(tangent circularization burn)	1.186346
Total $\Delta V$ (km/s)	2.424565	1.815174	1.855349



For all situations compared in Table 2, the initial GTO orbit inclination is defined at  $51.619^\circ$ , with a perigee altitude of 204.70 km and apogee altitude of 36,150.20 km (all taken from the AsiaSat-3/HGS-1 “nominal trajectory” analysis [6]).

In order to better understand the results of the “rescue” mission, the two-body orbital elements of each leg in the transfer (initial GTO, lunar fly-by, and final GEO) are calculated at each time step while numerically integrating each leg of the transfer. To calculate the osculating (instantaneous) orbital elements of the orbits and trajectories numerically integrated in the CR3BP, a rotation from the barycentric rotating frame of the CR3BP to the geocentric equatorial frame is necessary. The osculating orbital elements are expressed in an Earth-centered, inertial reference frame with angles measured with respect to the geocentric equatorial plane referenced by the vernal equinox direction and the stars that are sufficiently “fixed” in space [8]. The osculating orbital elements of the trajectories computed in the numerical simulation are also based on the Moon’s osculating elements at the selected epoch [32]. The process begins by transforming the state vectors in the barycentric rotating frame generated in the numerical simulation to corresponding vectors in the Earth-centered inertial frame of the CR3BP along each time step with the transformation seen in Section 2.6. Recall that the Earth-centered inertial frame is based on the plane of the primaries and is initially aligned with the rotating frame. The conversion from the Earth-centered inertial frame of the CR3BP to the geocentric equatorial reference frame is a 3-1-3 set of rotations through the Euler angles: right ascension of the ascending node,  $\Omega$ , inclination,  $i$ , and  $\phi = \omega + \nu - t$ , all defined in Figure 26. The osculating elements for a spacecraft starting in a highly inclined GTO that maneuvers to perform a fly-by of the Moon, decreasing in inclination as it travels back toward the Earth to perform a combined plane change and circularization maneuver to ultimately arrive in GEO, are seen in Figure 32. Each osculating element in Figure 32

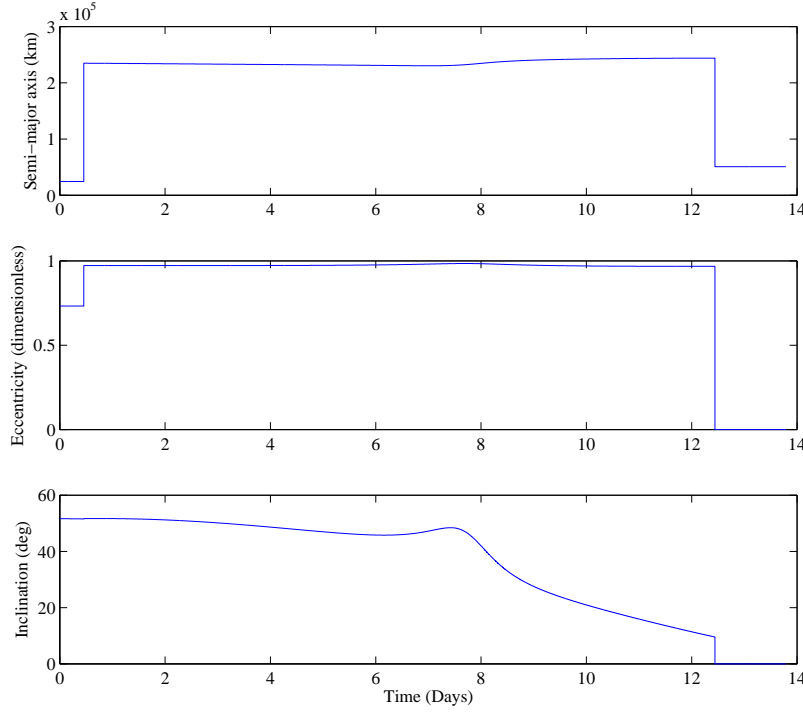


**Figure 32. Osculating Elements of Full Transfer Mission from an Initial Geosynchronous Transfer Orbit (GTO) to Final Geosynchronous Orbit (GEO) via Lunar Fly-By.**

show three separate stages of the transfer: initial GTO, lunar fly-by, and final GEO. The osculating semi-major axis and eccentricity each show initial “jumps” from the GTO to the fly-by trajectory ( $\approx 0.2$  days in Figure 32), indicating the change from an orbit with a relatively smaller semi-major axis and eccentricity of 0.75. After this transition, semi-major axis and eccentricity both increase, reflecting the insertion onto the fly-by trajectory. Notice the eccentricity of the fly-by trajectory approaches, but does not reach, the value of one. This indicates that the fly-by trajectory does not “escape” the influence of the Earth, but remains as a “closed” orbit in the system for the duration of the lunar encounter. This detail foreshadows the contingency options explored in the next section, observing how the fly-by trajectory, if propagated further, returns repeatedly to close to its initial altitude from the Earth. With the insertion into GEO ( $\approx 12.2$  days in Figure 32), semi-major axis decreases, but ends at a value larger than the original. Eccentricity drops to zero, indicating the maneuver

to final, circular GEO. Finally, the inclination at the first maneuver at  $\approx 0.2$  days is nearly undetectable without the information from the above osculating elements since the first burn is nearly tangent to the initial GTO. The fly-by trajectory ends at GEO altitude with an inclination of  $9.55^\circ$ , and a final, nontangent burn is performed here to insert the spacecraft into its final GEO.

#### 4.1.1 Test Case I: Analysis

The differences between the AsiaSat-3/HGS-1 “nominal trajectory” and the converged trajectory in this investigation offer insight into the nature of the problem as they are examined. The differences between the two problems originate in the different targeting algorithms designed in a CR3BP model. The scenario presented in the previous section aligns the ascending node of the GTO with the ascending node of the Moon’s orbit. This detail stays fixed, also fixing the GTO’s right ascension of the ascending node,  $\Omega_{GTO}$ , argument of perigee,  $\omega_{GTO}$ , and the definition of the Moon’s location in time. In the setup in the AsiaSat-3/HGS-1 mission, a numerical targeting algorithm found the locally optimal trajectory for the lowest  $\Delta V$  possible. This targeter used a design variable vector that did not use the states of patch points; it included the initial time defining the location of the Moon at GTO perigee, the right ascension of the ascending node of the GTO, the argument of perigee of the GTO, the  $\Delta V$ , and the time of flight as design variables for the lowest  $\Delta V$ . The multiple-shooting algorithm used in this investigation is not designed to give an optimal solution, so no claims of optimality can be made for the solutions in this investigation.

Another difference is the fixed tangent burn maneuvers in the AsiaSat-3/HGS-1 “nominal trajectory.” The algorithm in the present investigation did not restrict the maneuvers to tangent burns. The last difference observed between the solutions is

that the final inclination in Ocampo’s paper was forced to end at zero, while the end condition in this investigation looked for an end altitude equivalent to GEO altitude, at any inclination. The nature of the patch point method in multiple-shooting created a scenario where either the final location is fixed (also fixing GEO’s  $\Omega$ ), not allowing for any other GEO insertion options at another point on the final orbit, or the simulation must stop numerically integrating when the trajectory reaches GEO altitude. The design in the current investigation opted for the latter choice which considers a combined plane change and circularization maneuver at the end point. Another option that would be available instead of this plane change is to perform the circularization burn (with no plane change) to get into an inclined “GEO” orbit and let the Moon’s natural perturbations decrease the inclination. These perturbations were utilized in the actual AsiaSat-3/HGS-1 mission, with a preliminary model that forced a constraint to obtain a favorable ascending node (necessary to take advantage of the Moon’s perturbations) with higher fidelity compared to the AsiaSat-3/HGS-1 “nominal trajectory” [6].

Finally, note that the orbital setup designed to replicate conditions in Ocampo’s “nominal trajectory” and the coordinating converged trajectory are designed to specifically correspond to the epoch of 25 Jan 1998, where the inclination of the Moon with respect to the Earth’s equatorial plane is modeled to be  $19^\circ$ . The outcome of the transfer in this investigation only depends on the inclination of the Moon with respect to the Earth’s equatorial plane, and not on the Moon’s other initial orbital elements. The inclination of the Moon with respect to Earth’s equatorial plane actually oscillates between about  $18.29^\circ$  to  $28.59^\circ$  in a cycle that lasts roughly 18 years for the inclination starting at the minimum to return back to the same minimum value [83,84]. As reported by the JPL Horizons web-interface, future dates when the Moon’s inclination returns to approximately  $19^\circ$  and the orbital configuration would

allow for this transfer to happen include: Apr 2017, Dec 2032, Nov 2035, Jul 2051, May 2054, and Feb 2070 [85]. As the lunar inclination moves through its 18 year cycle, it passes  $19^\circ$  right before and right after it reaches its minimum of  $18.29^\circ$ , which accounts for the closer dates (Dec 2032 to Nov 2035 and Jul 2051 to May 2054). It takes longer for the inclination to reach its maximum ( $28.59^\circ$ ) and to come back to  $19^\circ$ , which accounts for the longer times between dates (Apr 2017 to Dec 2032, Nov 2035 to Jul 2051, and May 2054 to Feb 2070).

The differences between the designs were mainly a result of different targeting schemes, but overall, the comparison shows that the design method used in this investigation, using a resonant arc and multiple-shooting to find a solution, offers an alternate avenue to approach the same transfer scenario and advantageous results in terms of  $\Delta V$  compared to 2BP methods (shown in Table 2).

The design strategy in this investigation also presents several disadvantages. First, the method of using a resonant orbit arc requires some knowledge of the basic transfer orbit and the velocities involved. If the same design approach was to be used for a different transfer scenario, a catalog of resonant orbit families may be examined for potential utility in the transfer, but ultimately, it may take multiple guesses of different resonant arcs from different families to come close to a feasible design, if such a transfer even exists for the scenario. Also, the initial  $\Delta V$  for the first maneuver at perigee of the GTO was known to be a decent guess since it was used in the AsiaSat-3/HGS-1 “nominal trajectory.” It may be reasonable to choose an initial speed that causes the trajectory to leave the initial orbit and fly to near Moon altitudes, but too much of a deviation from the speed used in this example may cause the targeter to converge to a different solution entirely. The design mindset may be to start with the available  $\Delta V$  and decrease the value until a flyable trajectory is no longer achieved. Though the algorithm is relatively quick to run (less than one minute to convergence),

and this “trial and error” method may work, it is also inefficient. The simplicity in this design also fixes the initial configuration of the GTO to the Moon’s position, which limits the available solutions.

As stated in Section 1.5.2, the converged trajectories in this investigation are not claimed to be optimal. The design method presented in this investigation did not explicitly optimize the  $\Delta V$  or restrict the final inclination as to see how the natural dynamics would produce a trajectory to get from one orbit to another. Since the exact numerical solution in the AsiaSat-3/HGS-1 report was not replicated, any observations listed below are attributed to the solution designed by the method described in Section 4.1.

The comparison between Ocampo’s “nominal” transfer mission and the converged design in this scenario shows that an alternate unconventional, higher altitude transfer method is possible to construct, leading to a converged design with low overall  $\Delta V$  cost compared to usual, 2BP methods. When Ocampo’s design was studied in 1998, using a fly-by of the Moon was a surprising method to examine. Offering this technique with resonant arc provides yet another way to design the same transfer, and depending on the design constraints and specifications, this method may even prove to be more useful in some situations.

#### **4.1.2 Test Case I: Contingency Options**

Another main advantage of the method using a resonant orbit arc for an initial guess is the wide assortment of contingency options available that take advantage of the converged orbit’s natural motion, increasing the design’s “resiliency” by exploring different options in case the chosen maneuver does not happen [12]. Various contingency plans are explored for the “rescue” mission designed above. Since the initial guess for this analysis relied on a resonant orbit, the converged transfer solution

takes on characteristics reminiscent of a resonant orbit. If the same trajectory used for the lunar fly-by is not terminated in GEO, propagating for five revolutions of the primaries reveals structure similar to that of resonance. This continued orbit is seen in Figure 33.

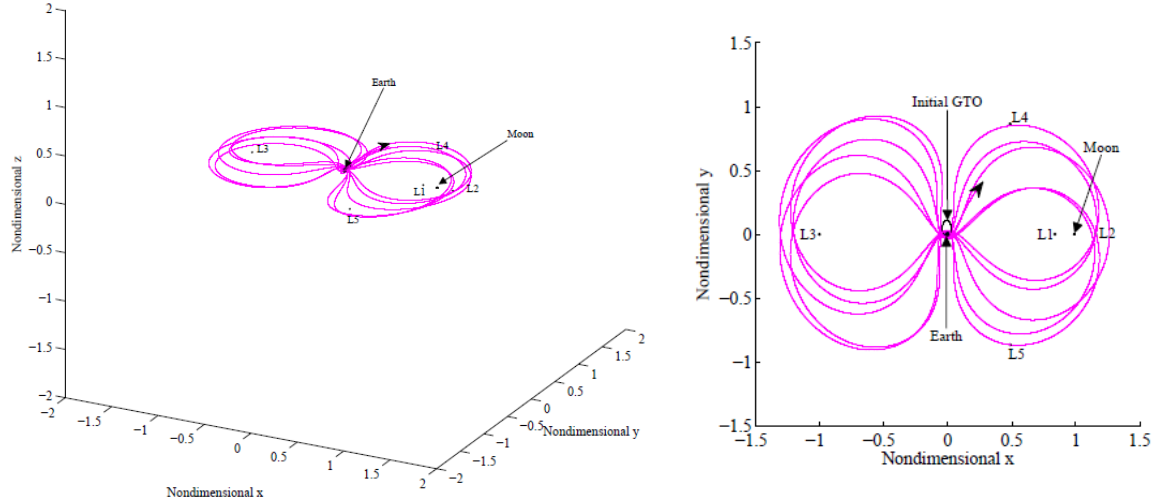


**Figure 33. Lunar Fly-by Trajectory Propagated for 5 Revolutions of the Primaries in Barycentric Rotating Frame.**

Although the projected trajectory does not possess perfect resonance, each “petal” of the orbit is completed in about half the time it takes for the Moon to complete one revolution of the Earth. In other words, one approximate “period” of this trajectory is about equal to the time it takes for the Moon to complete one orbit. If the spacecraft waits one “period” of this orbit, this positions the spacecraft not at the original end position (GEO altitude, inclined  $9.55^\circ$ ), but at the same altitude, inclined at  $15.66^\circ$ . Completing a combined plane change and circularization maneuver requires a  $\Delta V$  of 1.41 km/s. Another plan may be to end in an inclined high-LEO mission orbit. The first option for transfer would be to wait 12.08 days (just a few hours longer than the original plan), and ending at an altitude of 1,563.25 km, inclined at  $17.70^\circ$  with a final transfer  $\Delta V$  of 3.83 km/s. Figure 34 shows the  $x$ - $y$  view of the fly-by orbit propagated for 12.08 days to insert into a final LEO orbit in both the barycentric

rotating frame.

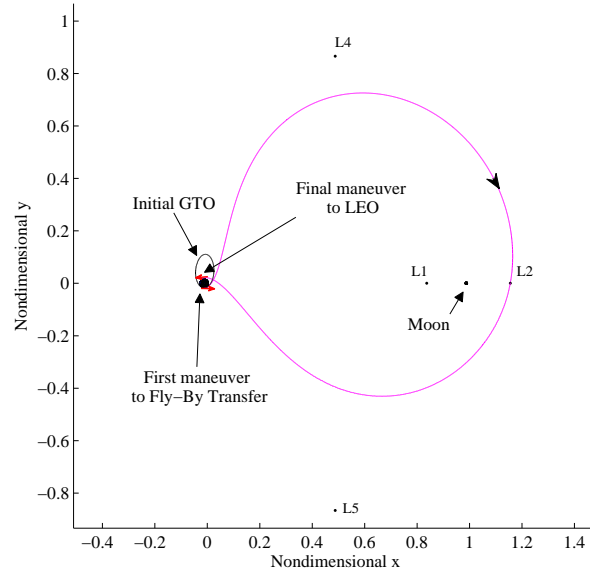


**Figure 34. Trajectory Transferring from Initial GTO to Final LEO via Lunar Fly-by in Barycentric Rotating Frame ( $x$ - $y$  view).**

This trajectory returning to LEO after 12.08 days is seen in the Earth-centered inertial frame in Figure 35. Notice the “petal” structure seen in the rotating frame is undetectable in the inertial frame, where the transfer appears as a large ellipse.

Consider a scenario with the same setup, but the goal of the transfer investigation is now to characterize the opportunity to make the final burn into GEO at some later phasing time, taking advantage of the loose structure of the orbit. This problem is reminiscent of a coplanar rendezvous scenario where an “intercepting” spacecraft needs to wait a specific amount of time before transferring to rendezvous with a “target” satellite in a different orbit. In this case, the “intercepting” spacecraft is traveling on this “figure-8” orbit and the target’s position is in the final “GEO” or LEO altitude orbit. Table 3 summarizes the times at which the spacecraft would “return” to an inclined “GEO” or LEO altitude orbit (to within 3.84 km of 35,000 km or 600 km for “GEO” and LEO altitudes, respectively). Total integration time for this analysis is about 1.25 years from the first maneuver at perigee of the GTO.



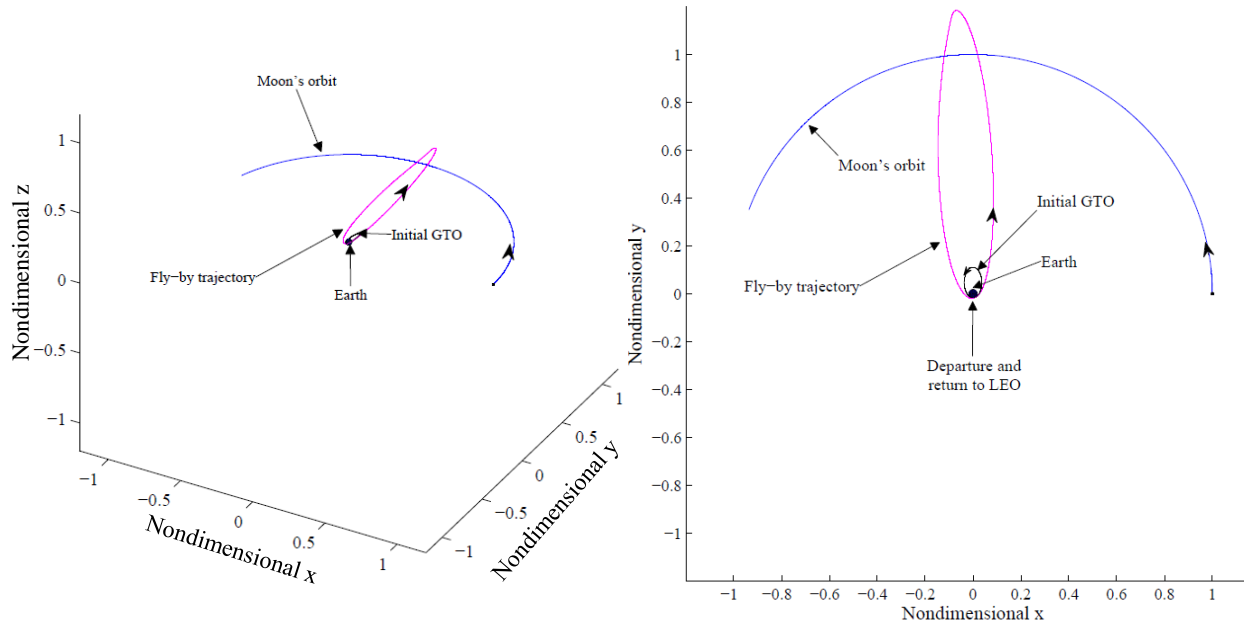


**Figure 35. Trajectory Transferring from Initial GTO to Final LEO via Lunar Fly-by in Earth-Centered Inertial Frame (Left: 3-D View, Right:  $x$ - $y$  view).**

Returning inclinations and  $\Delta V$  values for circularization maneuvers into the final orbits are also listed. Notice the return to the “GEO” altitude orbit after one “period” and the return to the higher-altitude LEO after 12.08 days are not listed since the final altitudes examined are constrained to more common “GEO” and LEO altitudes. Observing Table 3, the returns for “GEO” altitudes seem to occur every 12-14 days (with a few outlying returns that reach up to around 100 days between them). This seems to make sense when recognizing that the “period” of this orbit is about half that of the period of the primaries, or about 13.64 days. The inclination values of these returns (ranging on average between  $30^\circ$  and  $65^\circ$ ) are seemingly random at first, but a broad pattern can be seen in about every other (or every two) returns, switching between a lower and higher value of the total inclination range. A wider range of return altitudes may also be observed for a larger list of potential final maneuver points.

**Table 3. Times, Altitudes, Inclinations, and Final Maneuver  $\Delta V$  Values of Approximate Returns to Inclined “GEO” or LEO by a Lunar Fly-By Transfer Trajectory Propagated for 1.25 Years Since First Maneuver.**

Time from First Maneuver (days)	Final Altitude (km)	Final Inclination ( $^{\circ}$ )	$\Delta V$ Value for Maneuver into Final Orbit (km/s)
25.95	1, 199.14	43.13	2.905331
26.05	34, 998.44	43.20	1.050479
38.64	34, 997.38	8.65	1.050614
135.38	35, 000.55	67.72	1.049951
147.43	35, 003.73	31.90	1.049836
173.28	34, 999.62	26.30	1.050069
188.14	35, 000.30	61.22	1.049960
216.81	34, 997.54	62.12	1.049971
230.58	35, 003.10	32.77	1.049666
261.38	35, 003.05	46.72	1.050069
277.64	34, 999.08	51.99	1.050385
293.52	34, 997.78	66.12	1.050090
324.35	35, 001.02	59.46	1.049991
338.27	34, 999.19	21.43	1.050025
368.94	35, 003.19	46.22	1.050205
384.90	35, 003.17	56.98	1.050576
401.10	35, 000.36	65.41	1.050345
416.74	35, 002.94	37.24	1.049742
446.24	34, 999.00	28.69	1.049835

A different conclusion can be drawn from the LEO observations. In the time of 2 years from the initial maneuver from the GTO, only one return to LEO altitude between 200 – 1200 km exists at about the 26 day mark. The LEO returns were then propagated for 3 more years, the results of which are in Table 4.

**Table 4. Times, Altitudes, Inclinations, and Final Maneuver  $\Delta V$  Values of Approximate Returns to LEO by a Lunar Fly-By Transfer Trajectory Propagated for 5 Years Since First Maneuver.**

Time from First Maneuver (days)	Final Altitude (km)	Final Inclination ( $^{\circ}$ )	$\Delta V$ Value for Maneuver into Final Orbit (km/s)
25.95	1,199.14	43.13	2.905331
1,390.86	599.85	34.22	3.035707
1,403.95	600.24	24.96	3.035615
1,416.72	602.83	53.82	3.035009
1,428.45	600.90	54.59	3.035455
1,440.17	600.99	39.29	3.035434
1,452.26	600.68	64.84	3.035508
1,464.67	602.84	29.72	3.035014

These returns seem to happen about every 12 – 14 days as well, with variable inclinations at return, which reveal a similar pattern as the “GEO” returns. For the first and second returns, the inclinations are about  $10^{\circ}$  and are in the lower range of observed inclinations for the LEO returns (about  $\approx 25^{\circ} - 35^{\circ}$ ). The third and fourth returns are about  $1^{\circ}$  apart, in the higher range of observed inclinations for the LEO returns ( $\approx 55^{\circ} - 65^{\circ}$ ). Each individual return then comes back to about the same altitude (600 km) every 13 days or so, alternating between a “lower” or “higher” inclination. This loose pattern may be useful for predicting returns to LEO altitudes, or to assist in solving a rendezvous/phasing problem with one of the many satellites in low Earth orbit today.

In examining the future options for returns to LEO and “GEO” altitudes, insight is gained about the structure of this converged trajectory path. Rather than using a computer algorithm to simply get the spacecraft from the initial point to the final

point, the trajectory calculated using the design method employing a resonant arc gives options for alternate mission goals. Space assets are expensive, in terms of both cost to get a spacecraft into orbit and the onboard technology, with the potential for knowledge gained once in orbit. Looking at the contingency options available due to the structured “figure-8” pattern of the trajectory may offer vital mission alternatives. This design method therefore offers low- $\Delta V$  solutions to both the problem presented and future transfer opportunities. The phasing options for this “figure-8” patterned (but not resonant) orbit lead to many transfer opportunities, all of which are explored by examining the trajectory in the rotating frame.

## 4.2 Test Case II: Planar Orbit Transfer Design

The previous test case shows how designing in the CR3BP may give advantageous mission options to consider for a satellite in its geosynchronous transfer orbit and/or that has a large inclination change to overcome in order to reach the final orbit. Further investigation of the Moon fly-by transfer used in this design suggests connections to other behaviors examined in the CR3BP. The next transfer example is simplified further by considering a planar transfer. The planar case does not provide the same obstacles as a spatial problem would (like potential inclination changes) since a trajectory beginning in the plane (in both position and velocity) of the Earth and Moon will remain in the plane for all finite time in the CR3BP. Examining the planar case provides analysis of nearby behaviors in the plane that may naturally lead to observation of similar behaviors out of the plane and apply to 3-D applications. Periapsis Poincaré maps of planar orbits are utilized here to examine transfer opportunities.

Consider a scenario where a spacecraft in a planar “Tundra” orbit is scheduled or re-tasked to a final mission orbit in a planar “GEO” orbit. A notional representation of this scenario is seen in Figure 36. The goal of this test case is to design an

“unpredictable” pathway between the initial and final orbits. Invariant manifold trajectories associated with an unstable periodic orbit about the Earth-Moon  $L_1$  libration point are employed to let a spacecraft in the “Tundra” orbit travel in a seemingly random pattern until the spacecraft is ultimately inserted into its final mission orbit for similar  $\Delta V$  as compared to conventional transfer methods.

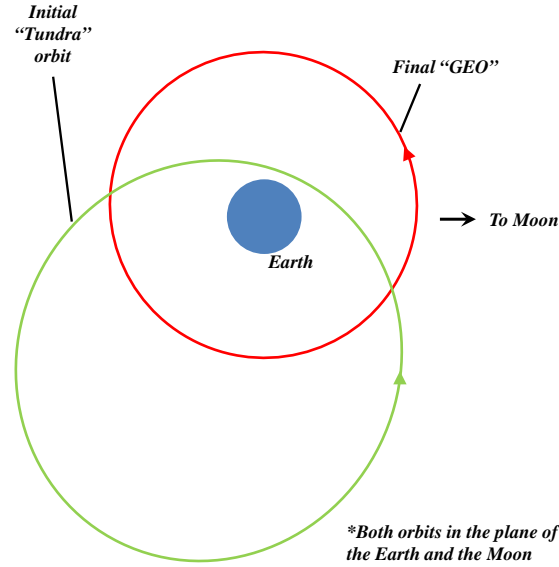


**Figure 36. Zoomed View of Notional Mission Setup for Transfer from Initial “Tundra” Orbit (green) to Final “GEO” (red), Both in the Plane of the Primaries.**

Conventional, inclined Tundra orbits may have potential future military capability, classified into a broad category of highly inclined, highly elliptical orbits (HEOs). HEOs are home to the X-Ray Multi-Mirror Mission (XMM-Newton) designed by the European Space Agency (ESA), studying celestial X-ray sources unblocked by the Earth’s atmosphere, and the ESA’s International Gamma-Ray Astrophysics Laboratory (INTEGRAL), characterizing the gamma-ray sources with sophisticated detecting and mapping instruments [86,87]. XMM-Newton and INTEGRAL perform their missions in HEOs with inclinations of about  $67.2^\circ$  and  $51.6^\circ$ , respectively [88,89]. These missions take advantage of HEO’s distance from Earth’s atmosphere and range

of observing distances both toward the Earth and other areas of the system, while appreciating the continuous communication with 48 and 72 hour orbital periods, respectively [86, 87]. Tundra orbits are similar to Molniya (or Russian “lightning”) orbits in that they both utilize a unique  $63.4^\circ$  inclination that prevents the orbit’s  $\omega$  precession due to J2 perturbations. Both have a high-altitude apogee, allowing long dwell time and periods of contact in apogee, fixed in the northern hemisphere due to the critical inclination. Tundra and Molniya orbits are useful for Earth observations, filling the gap north of  $55^\circ$  that GEO satellites miss [11]. Tundra orbits also have an orbital period of exactly one sidereal day, while Molniya periods are half of this, roughly 12 hours [11]. Spacecraft in Tundra orbits return to the same position over the Earth each sidereal day, but they do not remain over the Earth in a fixed position like geostationary spacecraft [11]. Tundra orbits specifically are home to Sirius Satellite Radio and the Russian EKS satellites, part of an early warning constellation designed for missile detection [90].

The initial “Tundra” orbit in Test Case II, as mentioned earlier, remains in the plane of the primaries, defined by Tundra altitudes (70,648.676 km apogee and 1,000 km perigee) and has an orbital period equal to one sidereal day. Note that actual Tundra orbits are designed to have a critical value for inclination equal to  $63.4^\circ$ , which is not true for the planar “Tundra” orbit in this test case. While a planar “Tundra” orbit is periodic in the inertial frame, the rotating frame of the CR3BP shows how the apogee (and perigee) point of the orbit changes as the Moon rotates about the Earth. This pattern is seen in Figures 37 and 38.

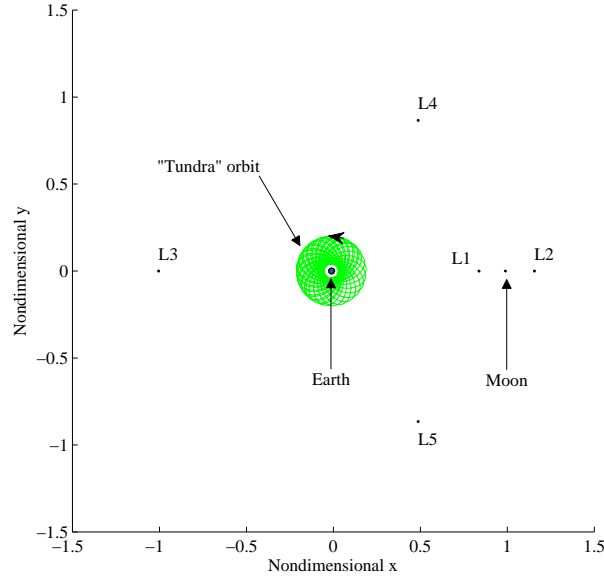


**Figure 37. Initial “Tundra” Orbit in Barycentric Rotating Frame of the CR3BP.**

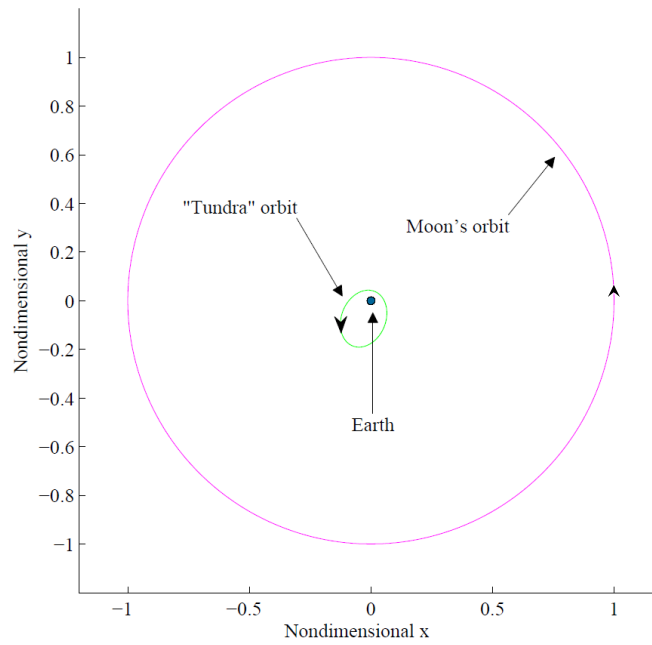


**Figure 38. Initial “Tundra” Orbit in Earth-Centered Inertial Frame of the CR3BP.**

A final mission orbit is defined by a “GEO,” or GEO-like orbit, also in the Earth-Moon plane, defined slightly smaller than actual GEO altitude, at 33,699.789 km altitude. Since this orbit is circular, the trajectory appears periodic in both the inertial and rotating frames and will be characterized as a periodic, circular orbit

in this scenario (although further analysis would reveal that a GEO orbit in the rotating frame would deviate from an exact periodic path). Conventional two-body Hohmann transfer option  $\Delta V$ s from “Tundra” to “GEO” are compared to a transfer with an unpredictable pathway in Table 5. In order to examine unpredictable path options, approximations of stable and unstable manifold trajectories associated with a Lyapunov orbit around the Earth-Moon  $L_1$  libration point are propagated from the unstable periodic orbit in negative and forward time, respectively. The manifold “tube” structure approximations are projected in the configuration space in Figures 39 and 40, propagated for about two months.

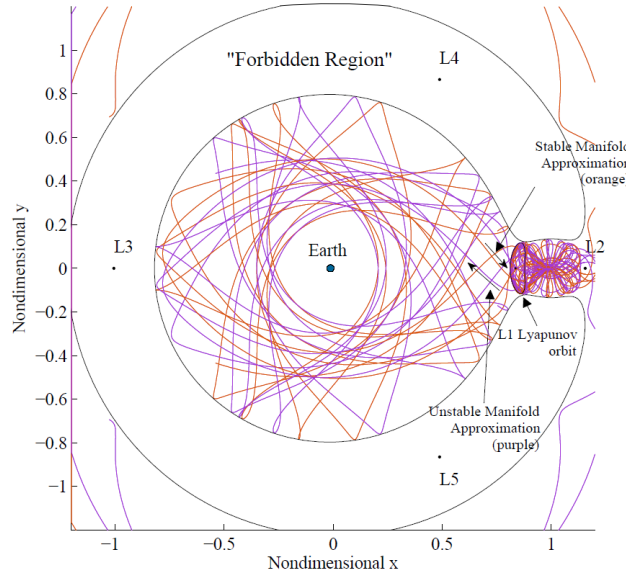


**Figure 39. Stable and Unstable Invariant Manifold “Tube” Approximations Associated with Unstable Periodic  $L_1$  Lyapunov Orbit in Barycentric Rotating Frame ( $JC = 3.1327$ ).**



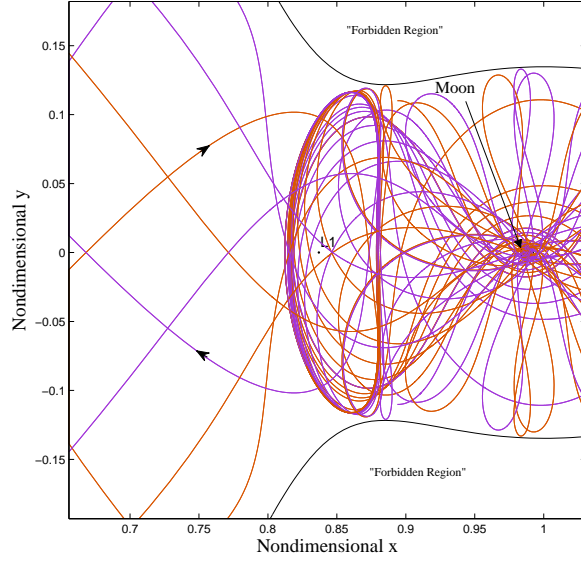


**Figure 40. Zoomed View of  $L_1$  Region with Stable and Unstable Invariant Manifold “Tube” Approximations Associated with Unstable Periodic  $L_1$  Lyapunov Orbit in Barycentric Rotating Frame ( $JC = 3.1327$ ).**

Continuing the propagation for 300 revolutions of the primaries (or about 22 years), a periapsis Poincaré map is generated. The map in Figure 41 shows the periapses for 80 total stable (orange) and unstable (purple) manifold trajectories “originating” from the Lyapunov orbit in negative or forward time. Notice the ZVCs, the blank space between the ZVCs, and the region where the periapse points exist. Based on the definition of periapsis, the blank region surrounding the points on the map and near the interior boundary of the ZVCs is where apoapsis points would occur. The “holes” within the region of periapse returns are empty because the specific manifold trajectories chosen do not have returns in these areas. Poincaré maps may be defined in terms of all apses, or alternately apoapsis points, but points of periapsis were chosen for this investigation to uniquely choose initial conditions and display locations of points closer to the Earth. Periapses are typically the traditional choice in literature for these reasons.

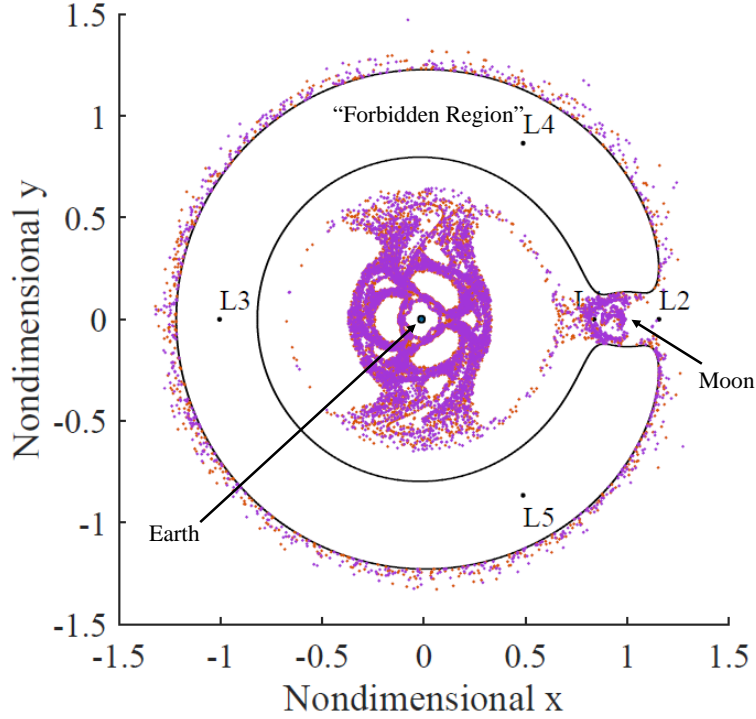


**Figure 41. Periapsis Poincaré Map for Stable and Unstable Invariant Manifold Approximations Associated with Unstable Periodic Lyapunov Orbit About Earth-Moon  $L_1$  in Barycentric Rotating Frame,  $JC = 3.1327$ , 80 Trajectories Numerically Integrated for 300 Revolutions of the Primaries (About 22 Years).**

Periapse points of these trajectories are potentially useful near the Earth, or at “Tundra” or “GEO” altitudes, when considering transfer opportunities to or from the specified orbits. Periapsis, by definition, determines a point where the magnitude of the radial velocity (from the Earth to the periapse position, in this case) is zero, so the velocity at this point is completely in a direction perpendicular to the radial direction defining the periapse. This means that if a spacecraft is at the apogee or perigee location in an Earth orbit and also satisfies the periapsis condition of a manifold trajectory, the positions would intersect, and a maneuver to/from the “Tundra” or “GEO” orbits would be possible. An impulsive burn ( $\Delta V$ ) at these specific points would also be exactly tangent to the Earth orbit by the definition of the manifold periapsis. Exploiting this idea, the periapsis Poincaré map is examined near planar “Tundra” apogee altitudes; zooming in to the Earth region, Figure 42 shows potential

periapse points near “Tundra” apogee altitude in the highlighted region.

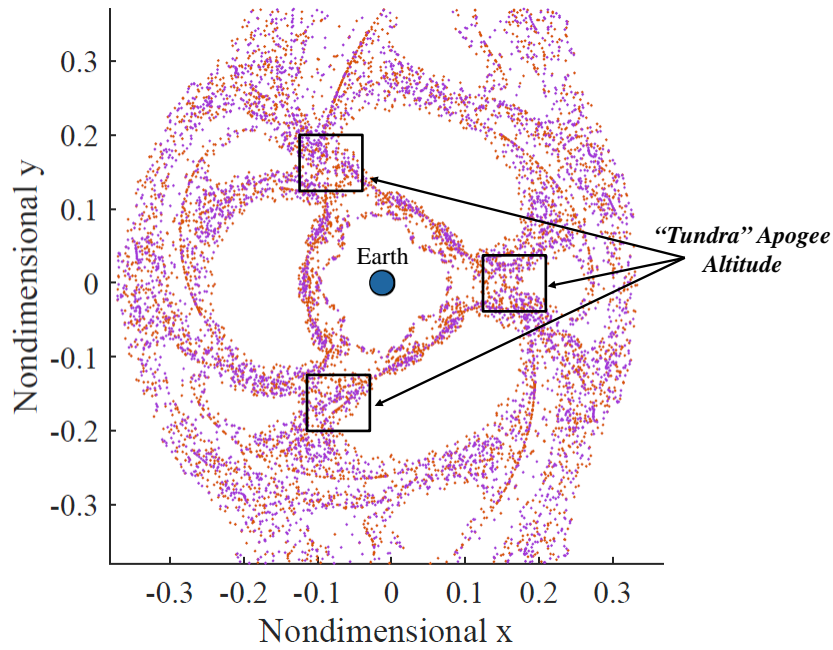


**Figure 42. Zoomed View of Periapsis Poincaré Map for Stable and Unstable Invariant Manifold Approximations Associated with Unstable Periodic  $L_1$  Lyapunov Orbit in Barycentric Rotating Frame, Showing “Tundra” Altitude Locations,  $JC = 3.1327$ , 80 Trajectories Numerically Integrated for 300 Revolutions of the Primaries (About 22 Years).**

A periapse belonging to the approximation of an unstable manifold trajectory at one of these points was chosen to perform a tangent impulsive maneuver from the apogee of the planar “Tundra” orbit. The manifold trajectory on which this periapse resides initially departs from the unstable periodic orbit in forward time, then meets up with this chosen periapse point. The unstable manifold trajectory can then be propagated further in time from this point to see where a spacecraft that has maneuvered onto the manifold will travel. The transfer from planar “Tundra” (green) to the unstable manifold (purple) is seen in Figure 43.

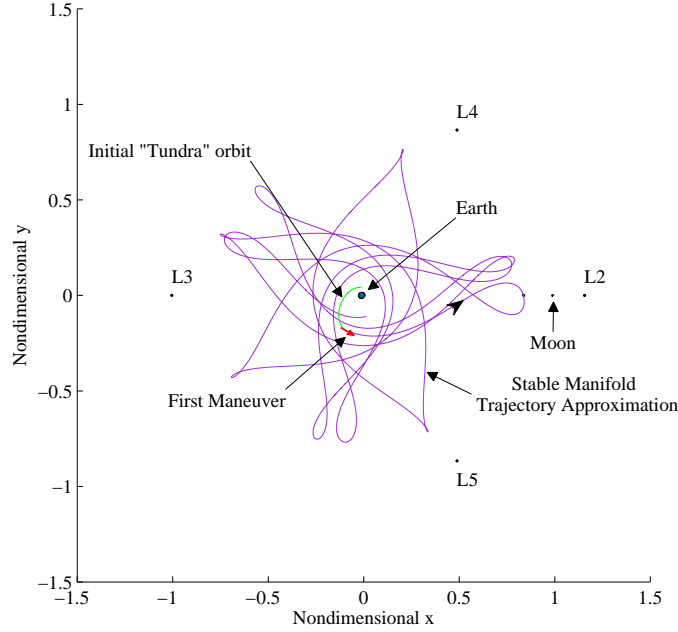


**Figure 43. Maneuver from Initial “Tundra” Orbit to Stable Manifold Trajectory in Barycentric Rotating Frame.**

Other transfer opportunities that are observable from the periapsis map are potential homoclinic connections between the stable and unstable invariant manifolds in the full phase space (position *and* velocity). Homoclinic connections can be found while generating the map by calculating the “distance” (in the full phase space) between periapse points for all the trajectories represented on the map and finding where these “distances” are close to zero (to within a  $10^{-12}$  tolerance). This type of connection would require zero- $\Delta V$  to get from one manifold trajectory to another, and therefore a spacecraft could depart the periodic LPO and eventually return back to the same LPO for “free.” A homoclinic connection was not used for this test case because all potential intersecting points in this scenario correspond to extremely long times of flight for the transfer (multiple years). Another type of opportunity that may be calculated while generating the map is an intersection of the stable and unstable manifolds in *only* position. A position intersection could allow for a transfer from one trajectory to another with a small  $\Delta V$ . Particularly if the trajectories are observed

to be traveling in the same direction with respect to the Earth, this velocity discontinuity is potentially extremely small. The unstable manifold trajectory maneuvered to from the “Tundra” orbit in this scenario is observed to have a “close enough” periapse intersection with an approximation for a stable manifold trajectory. This intersection of periapse points in question is “close” to within a tolerance of 0.0005 nondimensional units, or about 192 km. For a maneuver, this difference between the unstable and stable manifolds is obviously not “close enough,” and the stable and unstable manifold trajectories each have their own “intersection points.” However, an approximated trajectory with an initial state originating from the “intersection” periapse of the unstable trajectory may produce a solution that resembles the stable manifold trajectory associated with that “intersection.” The “intersection” periapses of the stable (orange) and unstable (purple) manifold trajectories are in the region of the periapse Poincaré map highlighted in Figure 44.

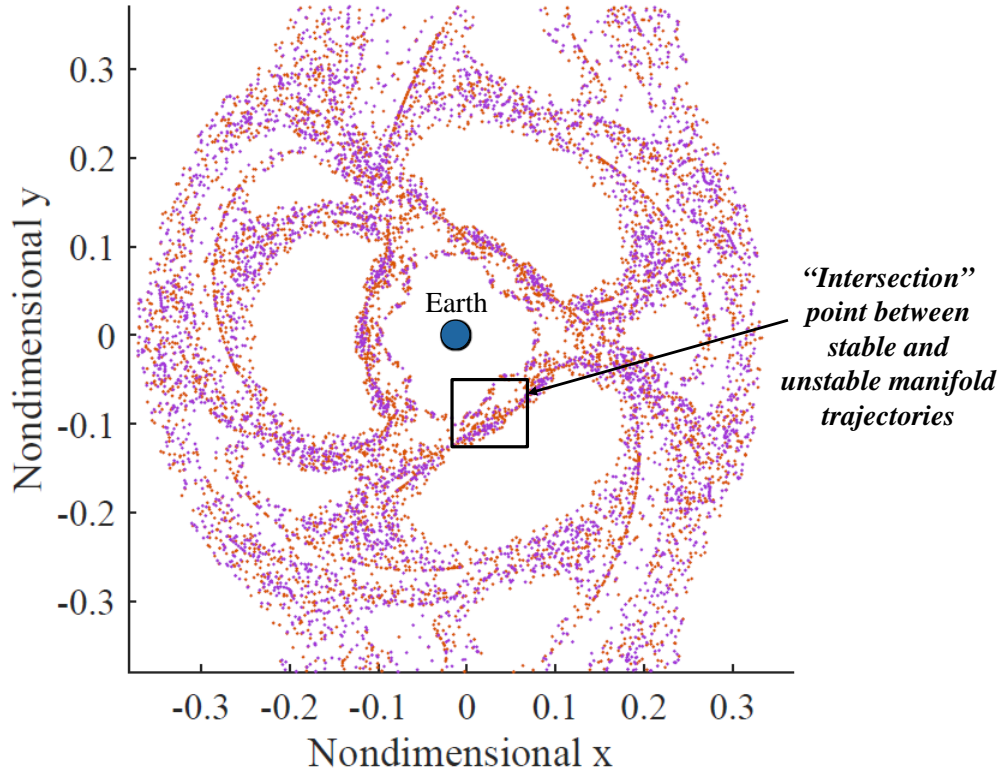


Figure 44. Zoomed View of Periapsis Poincaré Map for Stable and Unstable Invariant Manifold Approximations Associated with Unstable Periodic  $L_1$  Lyapunov Orbit in Barycentric Rotating Frame, Showing “Intersection” Point Location Between Manifold Trajectories (80 Trajectories Numerically Integrated for 300 Revolutions of the Primaries (About 22 Years),  $JC = 3.1327$ ).

This “intersection” is originally chosen for examination (rather than a more *exact* intersection) because of the stable manifold’s behavior after its periapse at the “intersection.” Propagating the stable manifold associated with this “intersection,” the trajectory’s subsequent periapse point is seen to be near planar “GEO” altitude. Figure 45 highlights the region where the stable manifold trajectory associated with the “intersection” periapse comes close to planar “GEO” altitude orbits.

This behavior is observed for the stable manifold associated with the “intersection,” which is an unattainable trajectory from the unstable manifold, but this behavior may be a decently accurate indication of the behavior nearby, approximated

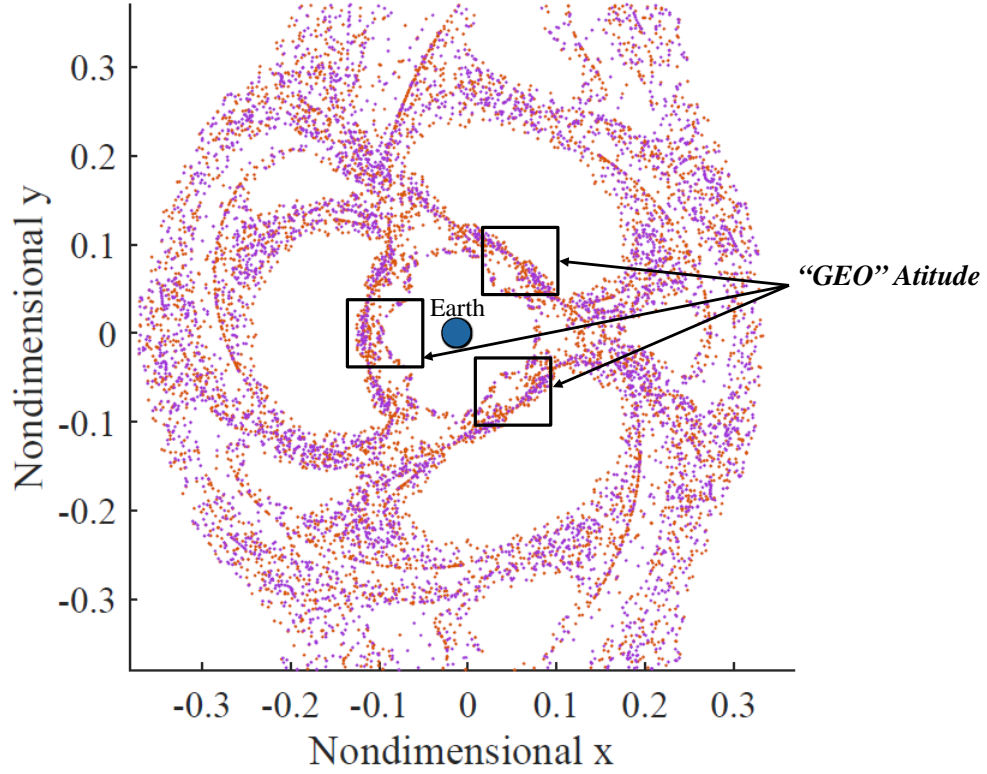
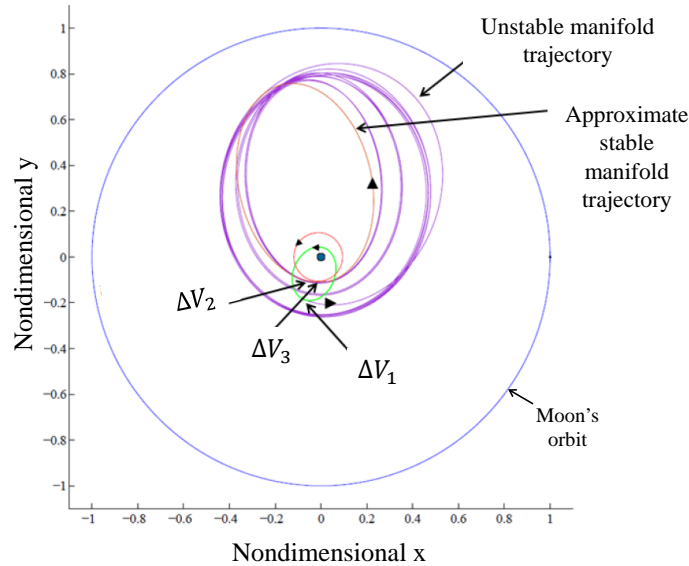


Figure 45. Zoomed View of Periapsis Poincaré Map for Stable and Unstable Invariant Manifold Approximations Associated with Unstable Periodic  $L_1$  Lyapunov Orbit in Barycentric Rotating Frame, Showing “GEO” Altitude Regions,  $JC = 3.1327$ , 80 Trajectories Numerically Integrated for 300 Revolutions of the Primaries (About 22 Years).

trajectory originating at the unstable manifold’s “intersection” periapse point. The end position of the unstable manifold trajectory at the “intersection” periapse point and the initial velocity of the stable manifold trajectory at its “intersection” periapse point were used as the initial condition to integrate a trajectory that exactly intersects the unstable manifold trajectory at its periapse. The magnitude of the maneuver at this location is equal to the discontinuity between the velocity of the unstable manifold at its periapse and the velocity of the stable manifold at its periapse. The integrated trajectory has similar behavior to the stable manifold, reaching its next periapse point near “GEO” altitude. The final maneuver to complete the “Tundra” to “GEO” transfer is to perform a circularization maneuver at the final periapse point of the orange trajectory to the “GEO” altitude orbit. Since this occurs at a periapse, this impulsive maneuver is also a tangent burn into the planar “GEO” orbit. The transfer from this trajectory (orange) to planar “GEO” (red) is seen in the entire transfer representations in both the barycentric rotating frame and Earth-centered inertial frame, seen in Figures 46 and 47.



**Figure 47. Full Transfer Plan from Initial “Tundra” Orbit to Final “GEO” Orbit Using Stable and Unstable Manifold Trajectories in Earth-Centered Inertial Frame.**



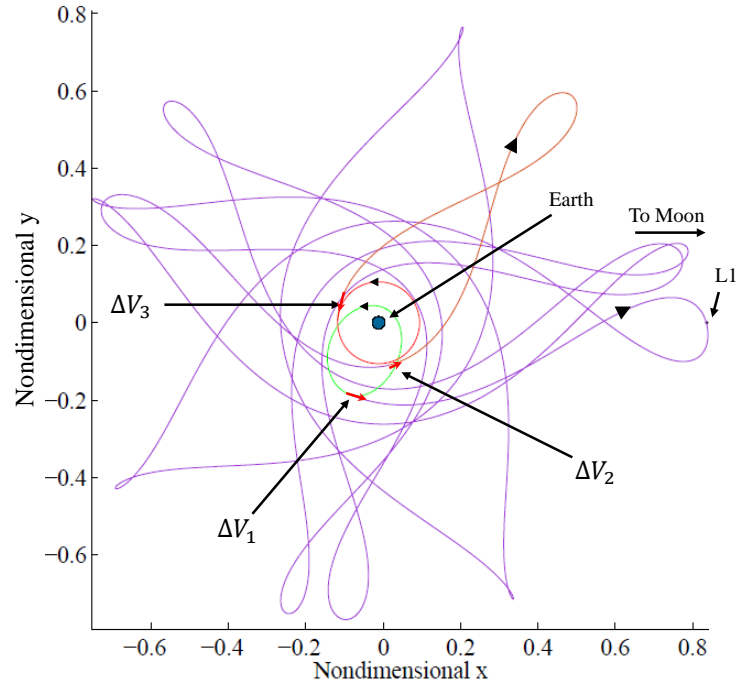


**Figure 46. Full Transfer Plan from Initial “Tundra” Orbit to Final “GEO” Orbit Using Stable and Unstable Manifold Trajectories in Barycentric Rotating Frame.**

The time of flight and  $\Delta V$  values for this case as well as two body transfers from the apogee or perigee of the “Tundra” orbit to the “GEO” orbit are seen in Table 5.

Table 5. Values for Two-Body Calculations for a Transfer from Planar “Tundra” Orbit to Planar “GEO” as Compared to Design Utilizing Invariant Manifold Trajectories for Transfer

	Two-Body Transfer (“Tundra” Perigee to “GEO”)	Two-Body Transfer (“Tundra” Perigee to “GEO”)	Manifold Transfer
Initial “Tundra” Orbit to Unstable Manifold Trajectory, $\Delta V_1$ (km/s)	6.776292	3.129447	1.546809
Unstable Manifold Trajectory to Stable Manifold Trajectory Approximation $\Delta V_2$ (km/s)	-	-	0.010823
Stable Manifold Trajectory to Final “GEO”, $\Delta V_3$ (km/s)	-	-	1.811925
Total $\Delta V$	6.776292	3.129447	3.369557
Time of Flight Between $\Delta V_1$ and $\Delta V_2$	-	-	108.58 days ( $\approx 3$ months, 19 days)
Time of Flight Between $\Delta V_2$ and $\Delta V_3$	-	-	8.47 days
Total Time of Flight	5.05 hours	19.58 hours	117.06 days ( $\approx 3$ months, 27 days)

### 4.2.1 Test Case II: Analysis

The process for designing a transfer from one orbit to another in the plane of the primaries using periapsis Poincaré maps has both advantages and disadvantages. Table 5 shows how a transfer of this type is relatively low-cost when utilizing higher-altitude options like invariant manifold trajectories. Comparing the methods, there is also an obvious trade-off between an unpredictable path transfer and its time of flight. The “Tundra” perigee to “GEO” option is obviously the quickest method, taking just hours, while the manifold transfer method requires months. Although the maneuvers in the design use impulsive tangent burns to increase efficiency, having one more transfer left to go through and having longer flight times in the transfer process may introduce more opportunity for error or equipment malfunction.

There are also some other disadvantages specific to this design method. First, in observing transfer options on the periapsis map, the velocity components of each point on the map are not visually available. There is no guarantee that continuity in position according to the map means that there is a continuous, “flyable” option at the chosen point. The periapsis maps display 4-D information on a 2-D map with the chosen surface of section and  $JC$  value. The *magnitudes* of velocity for both trajectories may match exactly in an exact intersection of position, potentially indicating a zero- $\Delta V$  transfer. However, velocity direction for both trajectories intersecting in the configuration space must be verified to ensure that a trajectory does not require the spacecraft to drastically switch its thruster direction when maneuvering from the initial path. Another potentially disadvantageous observation is that the manifold transfer depends on a particular epoch for which the “Tundra” apogee location is in the correct setup in the rotating frame. This specific orientation in the rotating frame needs to be taken into account when choosing a start epoch. On the other hand, the timing issue is only observed in the rotating frame. If a spacecraft in a

planar “Tundra” orbit is given the order to perform an orbit transfer to a new mission orbit that was to be undetectable to anyone attempting to monitor the operations, using the periapsis map approach with specific orientations of the initial orbit may be beneficial.

Another downfall of this design method is that only one unstable periodic orbit with its associated manifolds (all of the same  $JC$ ) were studied for transfers. Since this design only used the manifolds between Earth orbits, the unstable periodic orbits about the Earth-Moon  $L_2$  and  $L_3$  points may also have been examined. All different periodic orbits that may be examined also have different associated energy levels, which means that the potential  $\Delta V$ s for similar transfers could be reduced. Although Poincaré maps reduce the dimension of the problem, if there are not constraints that define energy levels and specific transfer parameters, examining maps one energy level at a time may be inefficient and tedious work.

Another design consideration relates to the integration times used for the maps. The integration time used for a periapsis Poincaré map must also be taken into consideration when examining the trajectories represented on the map. In order to gain more insight into the structure of the map, longer integration times are typically used to generate Poincaré maps. When using these maps for transfer design, a mission planner must be wary of the solutions that would take years to complete, when a similar transfer point may be available with a shorter time of flight. An example of this would be to explore all potential points that may have been viable for transfer from the planar “Tundra” orbit (which may have any argument of perigee value), looking at all periapses at the apogee altitudes with all  $\omega$  values. The different options may have provided shorter or longer transfer times. Also, the integration time of the map may not significantly matter if only pieces of the trajectories are used for transfers, as they were in this scenario.

This design is not claimed to be a globally or even locally optimal solution, but it is a continuous solution designed using the periapsis map to take advantage of naturally lower-energy transfers both between manifold trajectories and to/from planar Earth orbits at periapses.

#### 4.2.2 Test Case II: Contingency Options

As with the previous test case, there are many contingency options to explore with this test case scenario that increase the transfer options and “resiliency” for the mission [12]. When the spacecraft reaches the unstable manifold trajectory, there may be either a true homoclinic connection or an exact intersection in just position with a stable manifold trajectory. This option could provide a zero- $\Delta V$  (for a true homoclinic connection) or a low- $\Delta V$  (exact intersection in position, and perhaps small discontinuity in velocity) transfer option between the manifold trajectories.

Another option may be to maneuver from the initial Earth orbit directly to an approximate stable manifold trajectory leading to the Lyapunov orbit studied to generate the manifolds. Time of flight for this transfer from an Earth orbit depends on the transfer point selected to insert the spacecraft onto a stable manifold leading to the unstable periodic orbit in forward time. For a transfer point near “Tundra” apogee altitude, time of flight is near two months to get close to the periodic orbit selected for this scenario. Based on the first  $\Delta V$  in the test case from the initial “Tundra” orbit to the unstable manifold trajectory approximation ( $\Delta V_1 = 1.546809$  km/s), the required  $\Delta V$  for the total transfer from “Tundra” to an LPO would be expected to be less than 2 km/s. Since the manifold trajectories in the true, nonlinear system approach the periodic orbit in infinite time, a very small  $\Delta V$  may be performed in order to insert into the periodic orbit from the approaching trajectory. Another possibility could start with a spacecraft in the associated Lyapunov orbit. With

the nature of unstable periodic orbits, a slight amount of stationkeeping may be required to keep the spacecraft on the specified orbit already, but in theory, a small  $\Delta V$  could be performed at the precise location and direction to insert the spacecraft onto the unstable manifold used in this test case’s scenario. The second and third burns described in the original case could also eventually be executed, completing the scenario in the planar “GEO” altitude orbit. If a spacecraft were already orbiting the  $L_1$  libration point in the selected orbit in this scenario and wanted to come back to a different type of Earth orbit, a periapsis map of just the unstable manifold trajectories associated with the periodic orbit may be useful to examine to find a trajectory that intersects the desired altitude at a periapse.

### 4.3 Test Case III: Periapsis Poincaré Maps for Predicting Behaviors

In Test Case II, a periapsis Poincaré map is used to design a transfer mission from one Earth orbit to another. Another main utility of periapsis maps is the ability to show the long-term end behaviors of a given set of trajectories, creating a directory of initial conditions that may be exploited for certain end behaviors. In past research examples, periapsis maps have been generated that show the periapses of the stable and unstable manifolds of unstable periodic orbits around libration points that may serve as pathways into and out of the smaller primary’s vicinity at certain energy levels. Trajectories were characterized as they continued to stay near the smaller primary, transited through the region between  $L_1$  and  $L_2$ , reached a certain number of periapses before leaving the vicinity, etc. [30, 72, 73, 75, 76, 80, 81]. As an alternate view of this information, spacecraft with observed periapses at the defined points may be identified in order to predict the future outcome of that particular orbit. The periapsis maps below are of the second type described in Section 3.3, generated to characterize spacecraft trajectories based on future behavior. The initial conditions,

$\vec{X}_0$ , for the 36 trajectories represented on each map are determined by the periapsis condition in polar coordinates. The initial positions are established by first choosing a  $JC$  value, and then selecting a starting point in planar “GEO” ( $r_0 = 42,164.14$  km altitude) that satisfies the periapsis condition ( $\dot{r}_0 = 0$ ) and varying the  $\theta$  value by incrementing around the Earth in  $10^\circ$  steps. All initial periapse points are defined to begin moving prograde with respect to the Earth, or  $\dot{\theta} > 0$ . All trajectories are then numerically integrated for a specified period of time. Maps of various Jacobi Constant values are compared to show how the structure evolves as the energy level is decreased (as  $JC$  is increased). Periapsis Poincaré maps of trajectories near the Earth in the Earth-Moon CR3BP are examined to determine long-term behaviors in the region. A map of this type, numerically integrated for 155 revolutions of the primaries (about 11.5 years) is shown in Figures 48 and 49. Note the Earth, Moon, and example returns are indicated on the first periapsis map but are left off on all others in order to better observe the coded colors and structure.

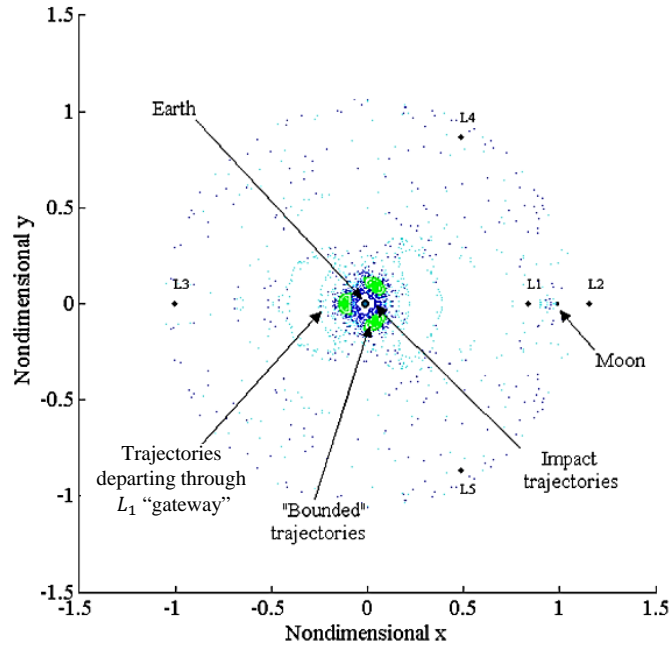
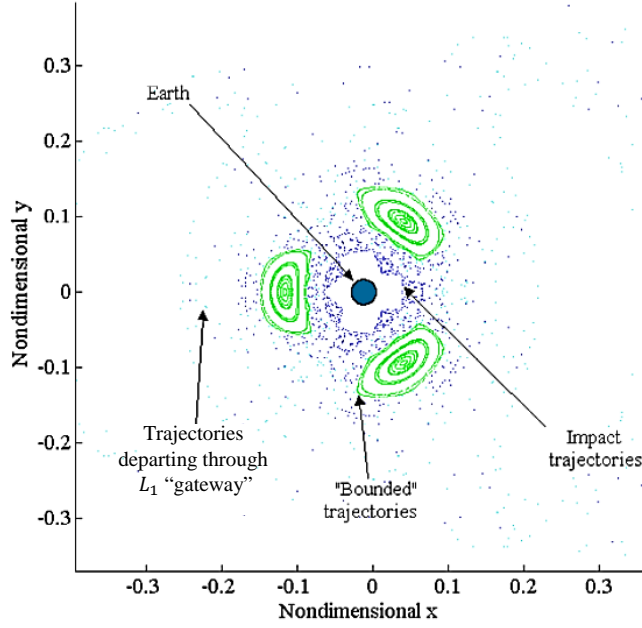


Figure 48. Periapsis Poincaré Map,  $JC = 2.95$ , 36 Trajectories Numerically Integrated for 155 Revolutions of the Primaries (About 11.5 Years), Cyan=Trajectories Departing  $L_1$  "Gateway," Green=Trajectories "Bounded" for Integration Time, Blue=Trajectories that Impact Earth.





**Figure 49. Zoomed View of Periapsis Poincaré Map,  $JC = 2.95$ , 36 Trajectories Numerically Integrated for 155 Revolutions of the Primaries (About 11.5 Years), Cyan=Trajectories Departing  $L_1$  “Gateway,” Green=Trajectories “Bounded” for Integration Time, Blue=Trajectories that Impact Earth.**

The green trajectories seen in each map are the trajectories that stay bounded within the Earth interior region as defined by  $x = x_{L3}$  to  $x = x_{L1}$  and  $y = y_{L5}$  to  $y = y_{L4}$ , or the ZVCs, whichever boundaries are closer to the Earth. Cyan points on the map represent trajectories that pass through the  $L_1$  “gateway” at some point during the integration time. In general, trajectories may pass through both “gateways” within their lifetime, but the color reflected on the map corresponds to their first departure from the near-Earth region. Dark blue points impact the Earth during their lifetime. Such trajectories would not be considered for trajectory design after an impact point, but the integration of these paths are continued and their subsequent periapse points are still shown for their contribution to the overall structure. Notice the map in Figures 48 and 49 corresponds to an energy level with no ZVCs on the  $x$ - $y$  plane. A first look at this map shows many impacts to the Earth and Moon (dark blue points), which may indicate that 155 revolutions of the primaries, or 11.5 years,

is an excessive amount of time to observe. Maps of various energy levels are created for trajectories that are numerically integrated for 15 revolutions of the primaries, or about 1.12 years, seen in Figures 50 and 52.

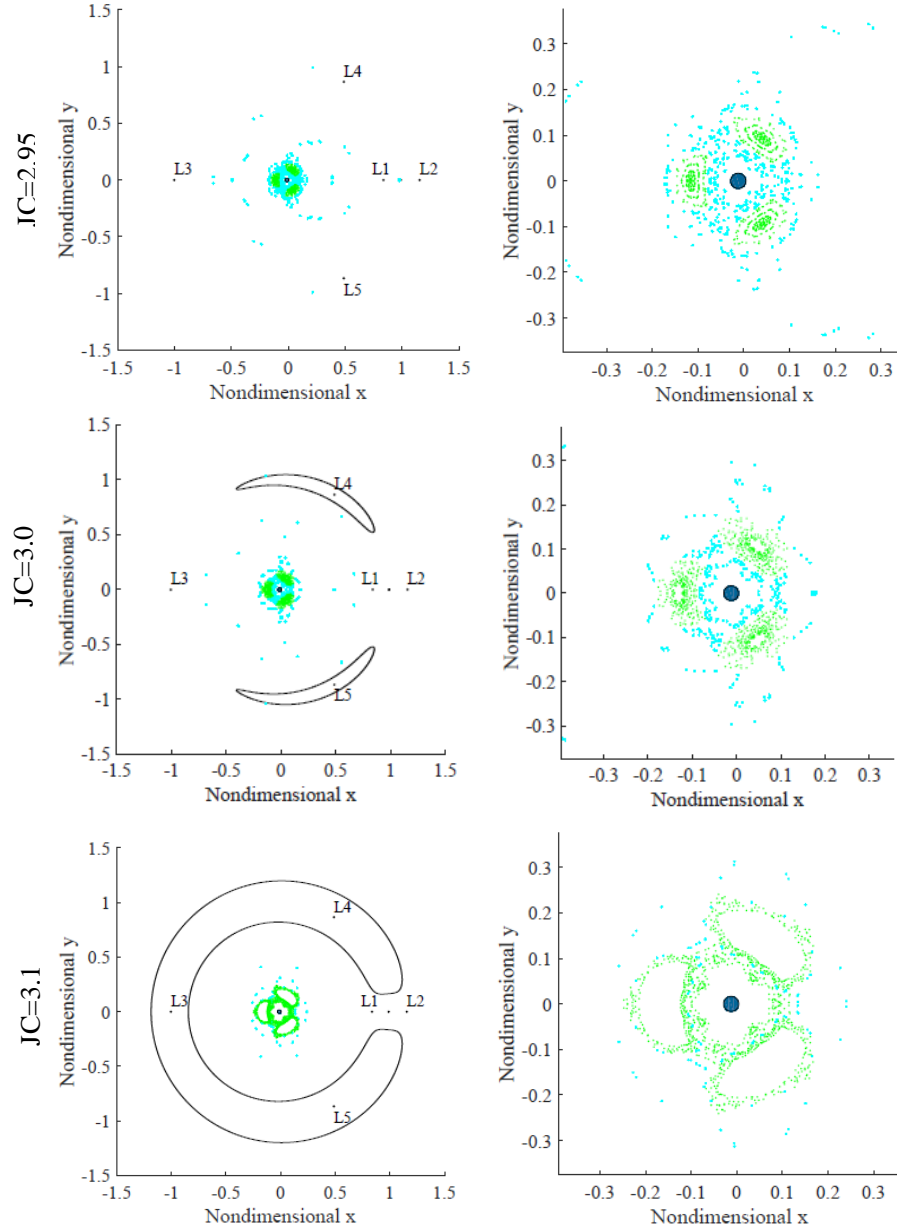


**Figure 50.** Periapsis Poincaré Map,  $JC = 2.95, 3.0, \text{ and } 3.1$ , 36 Trajectories Numerically Integrated for 15 Revolutions of the Primaries (About 1.12 Years), Cyan=Trajectories Departing  $L_1$  “Gateway,” Green=Trajectories “Bounded” for Integration Time, Blue=Trajectories that Impact Earth (Left: Barycentric Rotating Frame, Right: Zoomed View).

Using the periapse map defined at  $JC = 3.15$ , example trajectories of each characterized type are shown in the rotating frame in Figure 51. Note that all plotted periapses are shown on the map, and the example trajectories' periapses are not explicitly highlighted as it passes through the colored periapsis regions. Also, each trajectory is numerically integrated for 15 revolutions of the primaries (about 1.12 years).

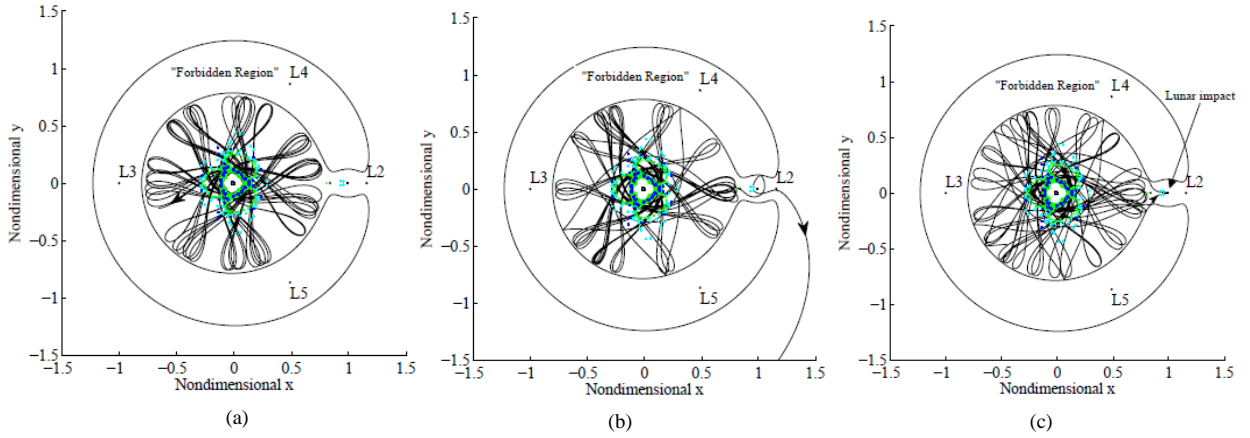


**Figure 51. Periapsis Poincaré Map for 36 Trajectories Numerically Integrated for 15 Revolutions of the Primaries (About 1.12 Years),  $JC = 3.15$ , Shown with Example Trajectories Corresponding to Initial Conditions for a (a) Bounded Trajectory, (b) Escape Trajectory Through the  $L_1$  “Gateway,” and (c) Impact Trajectory. Cyan=Trajectories Departing  $L_1$  “Gateway,” Green=Trajectories “Bounded” for Integration Time, Blue=Trajectories that Impact Earth.**

#### 4.3.1 Test Case III: Analysis

As energy level changes, different behaviors appear on the maps. Since all trajectories start near the Earth at planar “GEO” altitude, if the  $JC$  defined ZVCs with a closed  $L_1$  “gateway” (or  $JC > JC_{L1}$ ) all trajectories remain bounded, as seen in Figure 52 ( $JC = 3.2$ ), below.

As energy level increases, more trajectories pass through the  $L_1$  “gateway,” and more cyan points are seen. Looking at a specifically colored region on the map and choosing a point in that region allows a mission designer to use this point’s data as the

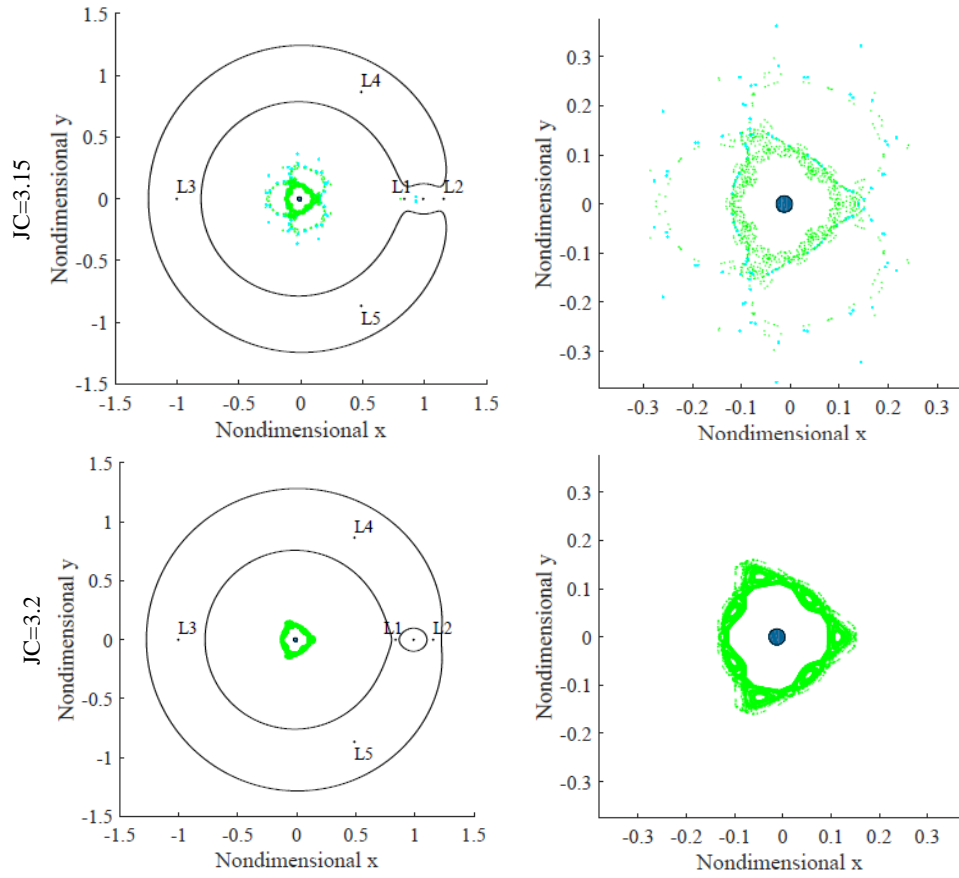


**Figure 52.** Periapsis Poincaré Map for 36 Trajectories Numerically Integrated for 15 Revolutions of the Primaries, or 1.12 Years ( $JC = 3.15$  and  $JC = 3.2$ ), Cyan=Trajectories Departing  $L_1$  “Gateway,” Green=Trajectories “Bounded” for Integration Time, Blue=Trajectories that Impact Earth (Left: Barycentric Rotating Frame, Right: Zoomed View).

initial condition to then propagate the trajectory forward. Due to the time-invariance of the CR3BP, redefining the initial conditions to a periapse that appears on the map leads to a trajectory that adheres to the behavior of the original chosen point. For this reason, initial conditions are not specifically labeled on the map, and all points are potential initial conditions that will produce a trajectory with the chosen outcome.

These Poincaré maps may be used for a specific “predictability” analysis for the trajectories. The “predictability” discussion in this investigation mainly offers insight into the movement of unknown spacecraft as a “defensive operation,” as the prediction of future behaviors and locations provides visual insight for the users of the maps. Recall the transfer design in Test Case II. Mentioned in the analysis was the fact that the initial “Tundra” orbit had to be in a specific orientation in the rotating frame in order for the transfer to take place as designed. Examining the inertial plot of the entire transfer (Figure 47), the insertion point onto the unstable manifold trajectory is seemingly random as seen by the “Tundra” orbit in this frame. The potential to then maneuver to a stable manifold trajectory is also undetectable from the inertial frame. Applying this rationale to Test Case III, consider the example trajectory in Figure 51 (b), shown by its periapse classification that it will depart the Earth interior region through the  $L_1$  “gateway.” The rotating and inertial views of the beginning of this trajectory are seen below in Figure 53.

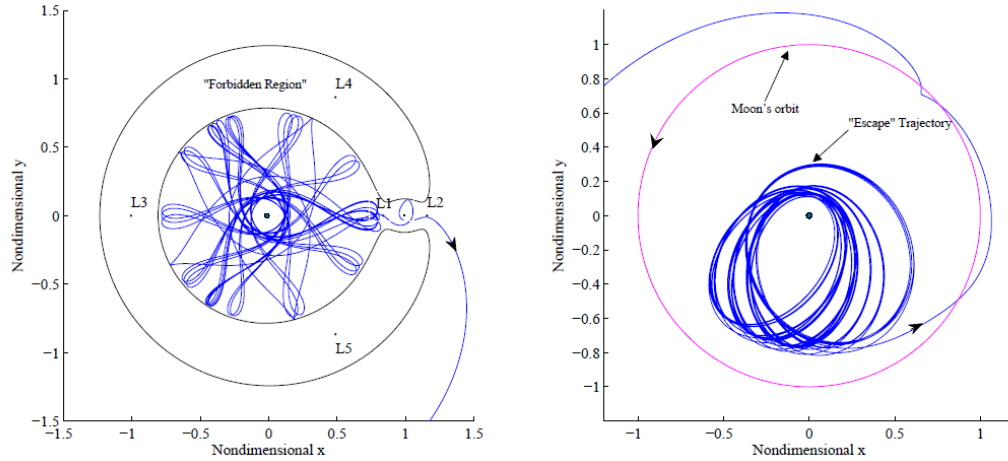


**Figure 53. Escape Trajectory Through the  $L_1$  “Gateway” in the Barycentric Rotating Frame and Earth-Centered Inertial Frame.**

If the inertial plot of the trajectory was the only source for analysis, the figure would show a trajectory that appears as a slightly perturbed, typical two-body orbit. Examining the rotating view plot shows how there is motion bounded within the ZVCs until the trajectory finally reaches an opportunity to “escape” the Earth interior region. While the trajectory initially appears to stay close to a reference two-body orbit, this longer propagation shows that a spacecraft following this trajectory diverges from the two-body orbit and travels away from the Earth, leaving the Earth interior region near  $L_1$ . Examining the orbit in the inertial frame shows no other indication of the dramatic change until the trajectory actually changes. More information is gathered in the rotating frame, where the trajectory seems to hug the inside curve of the ZVCs, and once the trajectory is in the proper position to go through the  $L_1$  “gateway,” the trajectory departs the Earth interior region for the remainder of the simulation.

Studying this trajectory with the periapse map tells the observer at first glance what to expect from the orbit, at least by a set integration time. If periapse information of an unknown spacecraft’s orbit is observed, a periapsis Poincaré map such as

these may give insight into where the orbit will end up in a given time period. With exact initial conditions, a trajectory may simply be numerically integrated to predict the outcome. With the colored regions of the map, a *guess* for the periapse may be enough to narrow down the region of the map in which the point may reside. The periapse points on the map not only show information for those specific points, but their locations (and colors associated with their characterization) also indicate the behavior of points in the same various regions that are not actually plotted on the map. Any point in the region may be chosen as the initial condition to numerically integrate a trajectory that exhibits the same behavior of the trajectories represented by the periapse points that are plotted on the map. The condition of periapsis indicates that a spacecraft approaching a periapse would be moving in a direction toward the Earth until it reaches its periapse point, and then it would travel in a direction away from the Earth. This description makes calculating a potential periapse point on an unknown trajectory potentially easier, and simple changes in direction may be observed and recorded to determine an approximate periapse.

The structural information on the map may also tell the overall behavior of the trajectory, indicating chaotic motion, or a more ordered trajectory orbit, like a quasi-periodic or even a periodic orbit. The stability information of these orbits may also be available from the map. It may be possible to make a guess for the initial periapse information of a trajectory in question, locate the potential trajectory on the map and find that it may be a periodic orbit. If other observations confirm the periodic (or quasi-periodic) condition of the trajectory, the map could also indicate whether the orbit would be stable or unstable. This information may point out how “stable” the orbit is: if the orbit returns to the same point every time, indicating a true periodic orbit, or if the orbit returns to *approximately* the same position, with a specific return pattern that may be available information on the map. A “less stable”

trajectory may require more stationkeeping to keep the spacecraft on the chosen orbit. Consequently, if a very small maneuver is made on a trajectory characterized in this way, or a natural external disturbance slightly perturbs the spacecraft orbit, the resulting trajectory may be radically different than the initial path. Though it is not expanded upon in this investigation, this concept may be exploited to make more unpredictable maneuvers between orbits and trajectories. This idea is suggested in Section 5.5.

Looking at the same topic from the viewpoint of a mission designer, the periapsis maps tell the designer a range of points where initializing a trajectory will produce a desired outcome. The map would also help the mission planner narrow down the choice for an initial condition by observing the stability information of the considered points. This may help to design a trajectory that specifically exhibits chaotic, quasi-periodic, or periodic motion while still giving the desired end behavior. The stability information of the orbits may also help the decision by comparing stable orbits versus unstable orbits with the desired behavior.

Although the periapsis Poincaré maps presented in this test case offer valuable information, there are also some disadvantages to note. First, in order to use the maps to predict an unknown spacecraft’s end behavior or orbit type, a periapse must be observable. If very little information is known about the spacecraft trajectory in question, periapse may not be useful at all. Just like the previous test case, there are also limitations that come with using Poincaré maps in general. Each map must correspond to one particular energy level, and only a selection of the available trajectories in the region are used to generate the map. The long-term “end” behaviors observed in each map also depend on the numerical integration time for each trajectory. This is useful when a specified time is provided when computing the map data, but if a chosen end behavior is needed at a different time than presented,



then the behavior observed from the map is not guaranteed for the new time.

Another potential drawback comes with defining all initially prograde trajectories in the initial conditions. All periapse points on the maps in this investigation may have either prograde or retrograde motion at subsequent periapses, but each initial periapse (the initial condition) of all trajectories on the periapsis maps have initially prograde motion. At every initial periapse point defined for each trajectory represented on the map, there is also a solution that is moving initially retrograde, and the subsequent periapse points for those trajectories are not shown. On one hand, this neglects potentially different end behaviors from the same initial points, which would create a denser, more detailed map and increase the number of characterized points in each category, but this is also a design parameter specified in order to exactly define the shown trajectories. Trajectories initially retrograde with respect to the Earth may be added to the map, but there is no distinguishing characteristic that delineates between initially retrograde or prograde trajectories.

Additionally, colors only correspond to the first departure point for the Earth region and do not reflect information regarding the other behaviors of the trajectory or the regions it visits during the integration time. A cyan-colored periapse point may indicate that a trajectory departs the Earth-region close to  $L_1$ , but this same pathway may eventually lead to another libration point, or it may fly-by the Moon once and return to the Earth region for rest of the time. More colors could have been used to showcase other categories of end behaviors, allowing the map information to be useful for more specific missions.

#### **4.4 Chapter 4 Summary**

In this chapter, three test cases showcase the numerical tools and unconventional methods developed in the CR3BP environment. The trajectories and transfers in the

test cases are not claimed to be optimal. Test Case I presents a “rescue” mission that transfers a stranded satellite in a highly inclined geosynchronous transfer orbit to an equatorial geosynchronous orbit with a design method that utilizes the natural shape and motion of resonant orbits as patch points for a multiple-shooting method. The converged design not only reaches mission objectives by overcoming a large inclination change during transfer, but reveals a “figure-8” structure with similar orbital characteristics as a resonant orbit. Numerous and convenient contingency plans are available based on the use of this structure and the potential phasing opportunities, increasing the “resilience” of this mission plan [12].

Test Case II uses a design process using a periapsis map to observe the transfer opportunities from a “Tundra” orbit defined in the planar CR3BP (different than actual Tundra orbits with  $63.4^\circ$  inclination) to a “GEO” orbit in the same plane (with different inclination and slightly smaller altitude than actual GEO). A tangent burn is made to maneuver the spacecraft from the initial orbit to an unstable manifold trajectory associated with an unstable periodic orbit about the  $L_1$  libration point. From the unstable manifold, a “close intersection” is found at a periapse nearly intersecting the periapse of a stable manifold trajectory associated with the same periodic orbit. From the end point on the unstable manifold, a tangent maneuver is completed to put the spacecraft onto a trajectory resembling that of the stable manifold, and a final transfer is made to finalize the mission in a planar “GEO” orbit. Contingency options are explored for this case that would increase the “resiliency” of the mission design [12].

Test Case III uses periapsis Poincaré maps to characterize specific long-term “end” behaviors for a range of orbits near the Earth and offer a method to employ “defensive operations” and gain insight into an unknown spacecraft’s trajectory [12]. As energy level changes, the structure of the maps evolve and trajectories exhibit different end

conditions. The maps can be used to choose initial conditions coded to yield specific behaviors. Predictions of future behaviors, trajectory structure, and orbital stability may also be determined based on observed periapse guesses.

## 5. Summary, Conclusions, and Future Work

In the present investigation, design processes using the tools and methods brought about by modeling in a multi-body dynamical environment are presented and evaluated. These processes begin by expanding the design space to observe the available opportunities. For various scenarios, each solution comes with contingency plans that also lend specific advantages.

### 5.1 Summary

The research in this study of military applications follows directly in line with the Air Force decision step of “deciding,” helping a mission planner to examine a vast space of design options as astrodynamical problems present themselves. Unconventional tools and methods in this analysis directly line up with goals listed in Department of Defense documents, motivating study with advanced methods. Success stories that have used multi-body dynamics to solve problems provide inspiration for test cases, such as the AsiaSat-3/HGS-1 mission employing a lunar fly-by to complete an inclination change between Earth orbits with less  $\Delta V$  than conventional methods. The two-body model may provide a decent first guess for the motion of a satellite close to the Earth, but taking the gravitational field of the Moon into account as well is often necessary for higher-altitude spacecraft trajectories. The circular restricted three-body problem lends itself to the design process. While no known closed-form analytical solution to the CR3BP is available, the problem formulation in the barycentric rotating frame offers an alternate view of possible solutions and their utility to real-world problems. The Jacobi Constant, the CR3BP’s one known integral of the motion, defines regions of accessible and inaccessible space and offers a valuable constant for tracking error in the numerical tools used in this investigation. Special

perturbations methods are applied to astrodynamics, continually opening doors to sophisticated and computationally intensive methods that are gaining popularity as technology allows. Numerical integration and Poincaré maps are used extensively in this work to explore the solution space of specific test cases. Stability analysis of equilibrium points and periodic orbits in the CR3BP leads to the computation of invariant manifolds. These structures contain trajectories that offer unique and low- $\Delta V$  transfers from one point in a CR3BP system to another. Periodic orbits, such as resonant orbits, are used to generate invariant manifolds or to provide information for an initial guess into a numerical program. Targeting methods and continuation schemes are derived and implemented to search the design space for solutions to problems, finding answers to reach problem objectives while satisfying constraints. These procedures are coupled with trajectories' condition of periapsis with respect to the Earth, allowing more robust algorithms to provide particular solutions.

Test Case I presents a “rescue” mission that transfers a stranded satellite in a highly inclined geosynchronous transfer orbit to a geostationary orbit. The natural pathway of the 4:3 periodic resonant orbit family is chosen to act as a guide to search for a transfer solution. Pseudo-arclength continuation is used to generate members of this family both in the plane of the primaries and out-of-plane. An individual orbit was identified to give state information for patch-points to input into a multiple-shooting targeting algorithm. A transfer solution is found that uses the Moon’s gravity to transfer the spacecraft from the highly inclined GTO to a slightly inclined “GEO” altitude orbit. With a combined plane change and circularization maneuver performed at the final point, the total  $\Delta V$  for this transfer is less than a two-body combined plane change and circularization maneuver to GEO and comparable to the “nominal solution” produced in the AsiaSat-3/HGS-1 analysis. Comparisons are made between each method, and contingency solutions are explored that take

advantage of the “figure-8” patterned structure of the transfer path and “phasing” options due to its near-resonant behavior.

Test Case II uses periapsis Poincaré maps in the design process of transferring from an orbit in the plane of the primaries in the CR3BP with “Tundra” altitudes (with different inclination than real Tundra orbits) to another orbit in the same plane with “GEO-like” altitude (with slightly smaller altitude and different inclination than real GEO). A pathway is designed that departs with a tangent burn from apogee of the “Tundra” orbit to an unstable invariant manifold emanating from an unstable periodic orbit around the Earth-Moon  $L_1$  libration point that possess a periapse at the transfer point. A small  $\Delta V$  is then made at a periapse point on the unstable manifold that is *close* to a periapse of a stable manifold associated with that same unstable periodic orbit. This leads to a trajectory that resembles the stable manifold trajectory associated with the nearby periapse. A final maneuver is made at the path’s next periapse point to end up in a final “GEO” altitude orbit. Contingency options are examined for this scenario, discussing the use of invariant manifolds as transfer means to/from other destinations.

Test Case III examines periapsis maps catered to different applications. Long-term “end” behaviors of trajectories are coded on the map, giving the observer the structural and stability information of a Poincaré map, as well as identifying areas of trajectories that impact a primary, depart the area, or are “bounded” for the integration time associated with the map. The utility of these maps are evaluated for predicting the future behavior based on the observed periapsis information of a spacecraft and for choosing initial conditions based on a desired outcome.

## 5.2 The Employment of Numerical Methods and Dynamical Systems Theory Are Essential for Contemporary Mission Design

Developing and implementing the design processes in this research has led to several conclusions concerning the efficacy of the presented tools for military applications. First, applying numerical integration, other numerical methods, and Dynamical Systems Theory are essential to this research. Computing particular solutions, converging iterative algorithms to target or continue specific classifications of orbits, and generating esoterically defined maps are only a small subset of the capabilities of numerical methods to assist in this type of design. Speaking to special perturbations, Wiesel claims “this is almost certainly the future of orbital mechanics” [20]. Although the CR3BP allows more design options than the two-body problem, it is still a highly-simplified model of the actual dynamics. Any solution computed in the CR3BP would then become an initial guess to input into an ephemeris-based model incorporating the gravitational fields from other celestial bodies (the Sun being the next body to consider) and additional influences of the space environment capable of modeling. Additionally, all solutions offered in this investigation do not determine the “statistical  $\Delta V$ ” for any of the transfers. It is important to look at the *actual* cost of these designs, including the stationkeeping cost for following exactly along a transfer trajectory. Though it is not the most accurate model, design using a CR3BP does offer numerous advantages for preliminary design and potentially for military applications. Employing concepts from Dynamical Systems Theory, including the generation of Poincaré maps representing stable and unstable invariant manifolds, as well as examining the structures that emerged from the maps, is instrumental in designing low- $\Delta V$  missions and gaining insight into a trajectory’s long-term behavior.

### 5.3 The Barycentric Rotating Frame Gives Significant Insight

Engineers are often told to “think outside the box.” Though cliché, examining each problem in the rotating frame gives mission designers a clear avenue to do just that. The rotating frame lets the observer see structure and characteristics that are not readily noticeable in the inertial frame. The existence of the Jacobi Constant; the observation of patterns, periodicity, and resonance; and the locations of equilibrium points are all easily seen in the rotating frame and exploited in this investigation. The first test case, involving a “rescue” mission similar to that of AsiaSat-3/HGS-1, demonstrates the usefulness of the rotating frame. Of course, this specific solution was created with a resonant orbit that was determined by already studying the motion in the rotating frame, but examining a solution in the rotating frame that was previously developed from an inertial perspective is useful in the same way. The solution generated from a resonant arc has an unexpected path in the inertial frame; the transfer arc from the GTO departs, almost appears as a large 2BP Hohmann transfer arc, visits around the Moon, and returns in a similar pattern. The inertial frame tells the basic “rescue” story, but it leaves out possibly critical information about the designed solution. When the trajectory is propagated longer and put in the CR3BP, another facet of the story is revealed. In the rotating frame, the trajectory is able to be analyzed by its specific patterns (like the “figure-8” pattern observed in Test Case I, Section 4.1.2) and resonant-like qualities, which may make it useful for other mission design scenarios.

Poincaré maps also give insight when examining a set of trajectories integrated with the equations of motion developed in the rotating frame. The study of periodic orbits and specific structural patterns characterizing stability can give the mission planner significant insight into the problem. An initial guess can be chosen directly from the Poincaré map and input into an automated computer algorithm to obtain



a precise solution to a problem. Picking initial conditions for a stable periodic orbit, as described in Section 2.16, is an example of how human observation/visual insight can be used to start the process for finding a computer-generated solution converged to a given tolerance. Periapsis points can also be examined by the mission designer looking at specific scenario-driven altitudes, such as in Section 4.2. In this case, instead of choosing an initial guess to put into a computer program that outputs a solution, the state data from the map and the pattern of subsequent returns of the examined points can give useful, direct information about where a specific orbit is at its periapse point at a given altitude and what altitude it will be at when it reaches its next periapse. In general, due to the definition of the periapsis condition, and the resulting description of the concavity of a trajectory as seen from the Earth, a periapse location will be a *locally* minimum altitude from the Earth. The periapse points also represent where the spacecraft would be moving exactly tangent to the apogee (or perigee) of a closed, near-Earth orbit at that altitude. These characteristics of the points present the periapses as efficient locations for maneuvers to/from Earth orbits, defined and easily shown on periapsis Poincaré maps.

In another application of Poincaré maps, described in Section 4.3, initial conditions for a desired end behavior for a given time period can be easily picked from the periapsis map, simply by selecting an initial condition in the corresponding region to the desired behavior. Actual periapse points shown on the map may be chosen, as well as other points in the region of interest that are not actually plotted on the map. Using the same mentality of choosing periapses for transfer locations from Earth orbits, initial conditions with the desired end behavior that are also at a desired Earth orbit altitude may be chosen as convenient maneuver points from Earth orbit, into a trajectory that gives a desired end behavior that is seemingly unpredictable from the Earth-centered inertial frame observations. Human insight gained from examining

solutions in the rotating frame (whether in the configuration space or on Poincaré maps) is a useful advantage of modeling and using the tools available in the CR3BP.

#### 5.4 Specific Solutions Originate from a Vast Collection of Mission Options with Map-Based Design

While studying Poincaré maps is useful for mission design in general, they also provide an expansive solution set to work from, while at the same time displaying specific information. Poincaré maps are a tool that can be extremely useful for problems that can benefit from observing trajectories at a specific  $JC$  and for a set integration time. There are many ways to define a Poincaré map, and there may be many ways to present the same, or slightly different, information relating to each scenario. One utility of using maps is seeing an abundance of information about a large selection of trajectories at a specific energy level at one time, hopefully gaining an overall picture of what is going on in the region observed. The second and third test cases show how periapsis maps examined for the Earth-region (rather than within the vicinity of  $P_2$  commonly seen in other research [30, 53, 73, 75, 76, 77]) can be useful for mission design by using a map to design a mission from a planar “Tundra” orbit to a planar “GEO” (Test Case II) and by observing long-term behaviors of spacecraft trajectories (Test Case III). Obvious from the design process with the periapsis maps, it is possible to observe copious potential mission paths for each scenario. The periapsis maps may be defined with different variables to cater to a specific scenario’s requirements: surface of section, unique or ambiguous initial conditions for trajectories represented on the map, number of trajectories represented, invariant manifolds of the same or many periodic orbits, integration time, energy level, overlaid maps at different energy levels, etc. Since individual scenarios are examined in each test case, gaining an overall knowledge of the related, or physically nearby, solutions is useful for problems with

less stringent constraints or for exploring unconventional options. For this reason, there is also importance in exploring and developing contingency plans in order to gain more insight into the available options. Overall, there is no general process for map-based mission design, and each Poincaré map is mission-dependent. The level of efficacy for a Poincaré map may rely on how clever the map designer is in generating the display for a specific problem, which is useful for facilitating simpler observations of the map, but may lead to accidentally neglecting pertinent information.

## 5.5 Recommendations for Future Work

The more work that was completed in effort to fully scrutinize the models, tools, algorithms, and test cases in this research, the more scenarios and ideas emerged that leave work to be explored. Recommendations for extending the analyses and numerical experiments of this work in contribution to the field include the following:

- *Implement map design for more practical orbit transfer scenarios.*

Perhaps the most impractical details of this investigation were seen in the full transfer design in Section 4.2, managing the transfer between two Earth orbits that happen to both lie in the plane of the primaries, as well as the planar periapsis map applications used for design from “Tundra” to “GEO” orbits (which are defined differently than real Tundra and GEO orbits) in Section 4.3. Of course, there could be some operational advantage of these orbits, and the Moon’s inclination with respect to Earth’s equatorial plane changes from about  $18.29^\circ$  to  $28.59^\circ$ , so it may actually be realistic to assume an initial orbit has an inclination equal to the higher end of the range (nearly equal to the latitude of Cape Canaveral) [83,84]. However, completing a full transfer design in this plane may only be useful for a small assortment of missions. Designing missions through a similar process may then be appropriate, albeit challenging,

for the spatial CR3BP. Poincaré map design for the spatial problem adds two dimensions to consider (requiring 4-D maps), which adds complexity both by the task of describing four dimensions on a map (difficult to visualize) and adding more variables to define for specific maps (as discussed in Section 5.4).

- *Study the specific stability characteristics seen on periapsis Poincaré maps.*

Stability information foretold by the specific structured regions of a map were not explicitly studied on the periapsis maps in this investigation, though the maps studied did contain a variety of stability information. Specifically, close to the Earth, quasiperiodic and periodic orbits with multiple returns to the periapsis map were observed, possibly indicating different resonant orbits. Figure 54 shows just a few examples of the structures observed in the periapsis maps of this investigation that may be studied further.

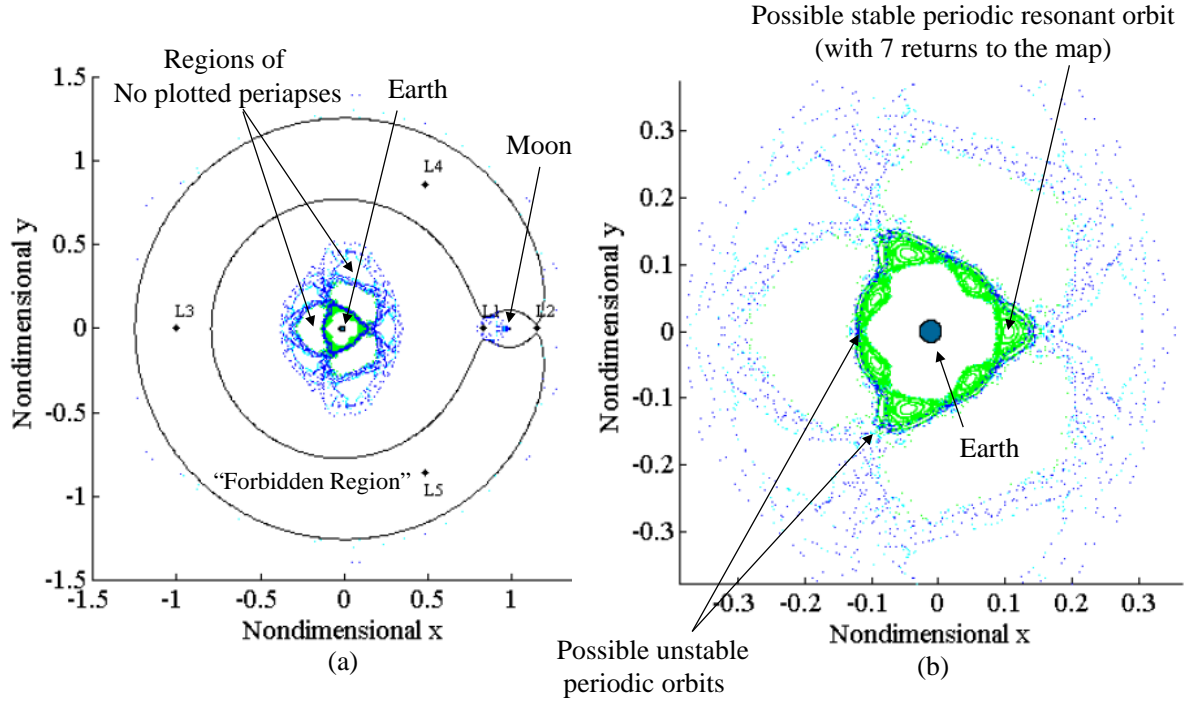


**Figure 54. Earth-Moon Periapsis Poincaré Map Showing Possible Structure (a) Barycentric Rotating Frame (b) Zoomed View of Barycentric Rotating Frame ( $JC = 3.17$ , Integration Time = 15 Revolutions of the Primaries), Cyan=Trajectories Departing  $L_1$  “Gateway,” Green=Trajectories “Bounded” for Integration Time, Blue=Trajectories that Impact Earth.**

Figure 54 (a) shows regions where periapses are not observed, and (b) shows possible initial guesses for stable and unstable periodic orbits in the Earth-Moon system at  $JC = 3.17$ . The blank spaces in Figure 54 (a) represent regions where no returns to the map are plotted for the trajectories represented on the map, but in general, periapses are possible in these regions. Apoapses would occur in the region surrounding the periapses that are plotted, just inside the “interior” ZVC boundary. It would be interesting to study and classify the types of initial conditions that return to specific regions.

Small changes that lead to radically different behavior can also be more readily recognized when looking at the problem in a different formulation. Chaos is characterized by a results’ sensitivity to the initial conditions, and in general,

chaotic behavior is exhibited in the CR3BP. One way these differences in behavior may be observed is by Poincaré maps. The chaotic regions seen on the maps (seemingly random “seas” of points, as explained in Section 2.16) and this information may be used to either avoid or exploit these regions based on the goals of the mission. The structures observed and the possibility of chaotic trajectories could also aid in predicting an unknown spacecraft’s future whereabouts. A visual analysis of the structure on the map may tell how a small perturbation or a small yet deliberate maneuver may send the spacecraft into an orbit that does not resemble its original trajectory in the slightest. This information may also indicate to the mission planner that stationkeeping should be a more significant concern when planning to remain on a chosen unstable periodic orbit. Conversely, these structural indications may lead to choosing a stable orbit so that a spacecraft may naturally require less stationkeeping.

This structure analysis also coincides with predicting the “end behavior” seen in Test Case III (Section 4.3). If the prediction for a specific spacecraft trajectory is inaccurate, there is an associated expectation of how stable the actual trajectory may be based on its approximate location on the map. There are multiple coded “end behavior” colors seen in the structured regions on the map, so multiple behaviors are observed for trajectories of various stability characterizations. These combinations may lead to additional indications (or simply verification) of what kind of behavior the unknown spacecraft’s trajectory might exhibit.

- *Explore the evolution of apses on families of periodic orbits.*

While periapsis criteria imbedded in the continuation scheme used in this research offered utility for specific purposes, this led to difficulties when trying to find a large collection of resonant orbits in families. The inclusion of these

points may be necessary for convergence, but experimentation with numbers of patch points, or the selection of which points to use, may give a more efficient process for finding more complete families. Exploring the specific evolution of apse points along resonant orbit (or other) families (as energy level increases or decreases) may reveal interesting information. Periapsis as well as apoapsis information may be recorded separately on a periapsis Poincaré map for a selection of members in a single family. The subsequent returns can be numbered and examined, comparing each numbered return of each family. This can be done to see if apsides ever “disappear” from an orbit family, or if apoapses turn to periapses and vice versa. This information can be applied to a periapse point chosen for maneuvering. If this periapse point belongs to a family of orbits, and periapse points for other members in the same family stay close, then this point may be available as a maneuver location for many energy levels and may place a spacecraft on trajectories of similar behavior (or at least resonance), since members of resonant orbit families share specific characteristics. This may lead to the discovery of maneuvering points on/off a resonant orbit that are available at many energy levels.

- *Generate a wide variety of Poincaré maps with a more efficient computing system.*

Exploring periapsis Poincaré maps with different energy levels, integration times, and “end” condition criteria was mentioned. The generation of many plots with MATLAB<sup>®</sup> would be impractical for producing data in a timely manner [22] and maintaining an integration tolerance of  $10^{-12}$  nondimensional units (with trajectory data at sub-cm and sub-cm/s precision for position and velocity data, respectively). A more efficient computing program is recommended for creating many detailed Poincaré maps. Creating more maps would make observability of the evolving structure and stability dynamics easier to

see, as well as create more opportunities for analysis.

- *Explore more contingency options for solutions computed in the rotating frame.*

There may be a plethora of contingency options for the “figure-8” orbit in Test Case I (Section 4.1.1) as well as for orbits and trajectories with similar patterned behavior. The boundedness of maximum orbit altitude and the return inclination at each approximate returning point for the solution in the test case may have a relationship to be exploited. Osculating elements may be interesting to compare between subsequent returns of the spacecraft as it completes each “orbit,” and general patterns may exist for trajectories of similar type.

Expanding the discussion of utilizing contingency operations for the purpose of protecting military assets in space, particular interest may be found in unusually shaped “holding” or “parking” orbits. These “parking orbits” may simply be in a GEO, a “GEO-like” orbit, or they may take advantage of more unconventional structure observed in the rotating frame that is seemingly random or just uninteresting in the inertial frame. Perhaps a resonant orbit may serve as an example. Exploring the different structures in the rotating frame may present a resonant orbit or other structured trajectory that would be useful. Replacing space assets, should something happen, is both expensive and takes a considerable amount of time to get from the ground to space. Additional spacecraft could be placed in the “parking orbit” to wait. This “parking orbit” may hold a spacecraft waiting for the appropriate opportunity to insert into mission orbit should one satellite in a mission constellation malfunction or reach its end-of-life. Or, a spacecraft in this unusual “parking orbit” may simply be applying the “phasing” concepts discussed in Section 4.1.1 in order to seize the calculated opportunity to insert into a particular orbit. A spacecraft in one of these orbits may remain there until it is given a mission task and



is reconstituted. Depending on orbit shape and structure, a spacecraft in the “parking orbit” may be able to transfer to a variety of mission orbits in a timely manner. Additionally, a seemingly unimportant shape in the inertial frame may allow these transfer opportunities to be completed without being obvious to an observer. The cost effectiveness of these “parking orbits,” as well as the benefits from undetectability/unpredictability may be assessed.

- *Expand the observed “end” behaviors for predictability analysis using periapsis Poincaré maps.*

A specific scenario applying the prediction analysis described in Test Case III (Section 4.3.1) would bring about particular long-term “end” behavior to explore. Similar maps reflecting these (possibly numerous) behaviors would divide and categorize the map further to aid in mission design and predicting motion. Additional “end” behaviors may include involving trajectories departing the Earth’s vicinity “ahead of” or “behind” the Moon (with initial departure coordinates above or below  $y = 0$ , respectively). Another idea would be to plot the same behaviors in this analysis, but with different indicators that correspond to different integration times.

To quote Szebehely, “Sir Isaac established the rules, Poincaré presented the challenges” [91]. While current tools and technologies are sufficient to conduct space operations, the next level of designing space missions comes with the advanced techniques that attempt to tackle these “challenges” described by Szebehely. The practices seen in this research have particular use for the military, leading to a more comprehensive understanding of Earth’s environment and its available spacecraft trajectories, both near and far. Implementing advanced dynamical methods is necessary for improving the current astrodynamical analyses used for military applications in space.

## Bibliography

1. V. G. Szebehely, *Theory of Orbits*. New York, NY: Academic Press, 1967.
2. T. C. Brandt, "Military Uses for Space," *Air University Review*, 1985. [Online]. Available: <http://www.airpower.maxwell.af.mil/airchronicles/aureview/1985/nov-dec/brandt.html>
3. J. R. Boyd, "The Essence of Winning and Losing," 1995, pp. 1–5.
4. U. S. Air Force, "Air Force Smart Operations for the 21st Century CONOPS," vol. 4, 2006. [Online]. Available: [www.501csw.usaf.af.mil/shared/media/document/AFD-080212-052.pdf](http://www.501csw.usaf.af.mil/shared/media/document/AFD-080212-052.pdf)
5. S. Rhodes, "Problem-Solve Like an Air Force Pilot," *Air Force Print News Today*, 2012.
6. C. Ocampo, "Trajectory Analysis for the Lunar Flyby Rescue of AsiaSat-3 / HGS-1," vol. 253, pp. 232–253, 2005.
7. National Research Council of the National Academies, *Continuing Kepler's Quest: Assessing Air Force Space Command's Astrodynamics Standards*. Washington, DC: National Academies Press, 2012.
8. W. E. Wiesel, *Spaceflight Dynamics*, 3rd ed. Beavercreek, OH: Aphelion Press, 2010.
9. U. S. Joint Chiefs of Staff, "Joint Publication 3-14," *Joint Publication 3-14*, no. May, 2013.
10. Office of the U. S. Air Force Chief Scientist, *Technology Horizons: A Vision for Air Force Science and Technology 2010-30*, 2011.
11. Dutch, "Some Major Orbit Types," 2012. [Online]. Available: <https://www.uwgb.edu/dutchs/AstronNotes/Orbits0.HTM> [Date Accessed: 2015-09-01]
12. Office of the Assistant Secretary of Defense for Homeland Defense and Global Security, "Space Domain Mission Assurance: A Resilience Taxonomy White Paper," Tech. Rep., 2015.
13. L. Meirovitch, *Methods of Analytical Dynamics*. New York, NY: McGraw-Hill, 1970.
14. L. A. Willson, "Polaris Project," 2000. [Online]. Available: <http://www.polaris.iastate.edu/credits.htm> [Date Accessed: 2015-12-08]

15. V. G. Szebehely, *Adventures in Celestial Mechanics: A First Course in the Theory of Orbits*, 1st ed. Austin, TX: University of Texas Press, 1989.
16. N. J. Cornish, “The Lagrange Points,” 2012. [Online]. Available: [http://map.gsfc.nasa.gov/mission/observatory\\_l2.html](http://map.gsfc.nasa.gov/mission/observatory_l2.html) [Date Accessed: 2015-12-15]
17. P. Holmes, “Poincaré, Celestial Mechanics, Dynamical-Systems Theory and Chaos,” *Physics Reports*, vol. 193, no. 3, pp. 137–163, 1990.
18. G. D. Birkhoff, “On The Periodic Motion of Dynamical Systems,” Cambridge, MA, 1927.
19. J. B. Tatum, “General Perturbation Theory,” in *Celestial Mechanics*, 2015, ch. 14.
20. W. E. Wiesel, *Modern Astrodynamics*, 2nd ed. Beavercreek, OH: Aphelion Press, 2010.
21. J. Fletcher, “The Comet’s Tale,” *Newsletter of the Comet Section of the British Astronomical Association*, vol. 8, no. 15, pp. 9–11, 2001.
22. MathWorks Inc., “MATLAB,” Natick, MA, 2015.
23. Bindel, “The Runge-Kutta Concept,” in *Intro to Scientific Computing (CS 3220)*. Cornell University, 2012, ch. 13, pp. 1–7.
24. L. Shampine and M. Reichelt, “The MATLAB ODE Suite,” *SIAM Journal on Scientific Computing*, pp. 1–22.
25. C. Geisel, “MECH733A Graduate Course: Numerical Methods for Orbit Design.” Wright-Patterson Air Force Base, OH: Air Force Institute of Technology, 2015.
26. E. W. Weisstein, “Semilatus Rectum.” [Online]. Available: <http://mathworld.wolfram.com/SemilatusRectum.html> [Date Accessed: 2016-03-07]
27. T. Ballistiy and C. Warrilow, “Vernal Equinox: Science Behind the First Day of Spring,” 2015. [Online]. Available: <https://weather.com/science/weather-explainers/news/vernal-equinox-first-day-of-spring-2015> [Date Accessed: 2016-03-07]
28. Shield, “NonDimensionalization.” [Online]. Available: <https://www.aem.umn.edu/people/faculty/shield/software/truss/nondim.htm> [Date Accessed: 2016-03-07]
29. D. L. Kunz, *MECH512 Intermediate Dynamics Text*, fall 2014 ed., Beavercreek, OH, 2014.
30. A. F. Haapala, *Trajectory Design Using Periapse Maps and Invariant Manifolds*, Thesis, Purdue University, 2010. [Online]. Available: [https://engineering.purdue.edu/people/kathleen.howell.1/Publications/Masters/2010\\_Haapala.pdf](https://engineering.purdue.edu/people/kathleen.howell.1/Publications/Masters/2010_Haapala.pdf)

31. V. G. Szebehely, "Application of the Restricted Problem of Three Bodies to Space Mechanics," *Space Science Reviews*, vol. 2, no. 2, 1963. [Online]. Available: <http://adsabs.harvard.edu/full/1963SSRv....2..219S>
32. C. Geisel, *Spacecraft Orbit Design in the Circular Restricted Three-Body Problem Using Higher-Dimensional Poincaré Maps*, Dissertation, Purdue University, 2013. [Online]. Available: [https://engineering.purdue.edu/people/kathleen.howell.1/Publications/Dissertations/2013\\_Geisel.pdf](https://engineering.purdue.edu/people/kathleen.howell.1/Publications/Dissertations/2013_Geisel.pdf)
33. A. E. Roy, *Orbital Motion*, 4th ed. London, England: Institute of Physics Publishing, 2005.
34. P. Holmes and J. Guckenheimer, *Nonlinear Oscillations, Dynamical Systems, and Bifurcations of Vector Fields*. New York, NY: Springer-Verlag New York Inc., 1983.
35. E. W. Weisstein, "Taylor Series." [Online]. Available: <http://mathworld.wolfram.com/TaylorSeries.html> [Date Accessed: 2016-01-05]
36. H. M. Schey, *Quantitative Understanding in Biology Module IV : ODEs Lecture I : Introduction to ODEs*, Ph.D. dissertation, Cornell University, 2011.
37. D. T. Greenwood, *Classical Dynamics*. Englewood Cliffs, NJ: Prentice-Hall, Inc., 1997.
38. E. J. Doedel, V. a. Romanov, R. C. Paffenroth, H. B. Keller, D. J. Dichmann, J. Galán-Vioque, and A. Vanderbauwhede, "Elemental Periodic Orbits Associated with the Libration Points in the Circular Restricted 3-Body Problem," *International Journal of Bifurcation and Chaos*, vol. 17, no. 08, pp. 2625–2677, 2007.
39. T. A. Pavlak, *Mission Design Applications in the Earth-Moon System: Transfer Trajectories and Stationkeeping*, Thesis, Purdue University, 2010. [Online]. Available: [https://engineering.purdue.edu/people/kathleen.howell.1/Publications/Masters/2010\\_Pavlak.pdf](https://engineering.purdue.edu/people/kathleen.howell.1/Publications/Masters/2010_Pavlak.pdf)
40. T. M. Vaquero Escribano, *Poincare Sections and Resonant Orbits in the Restricted Three-Body Problem*, Thesis, Purdue University, 2010. [Online]. Available: [https://engineering.purdue.edu/people/kathleen.howell.1/Publications/Masters/2010\\_Vaquero.pdf](https://engineering.purdue.edu/people/kathleen.howell.1/Publications/Masters/2010_Vaquero.pdf)
41. M. W. Lo, B. G. Williams, W. E. Bollman, D. Han, Y. Hahn, J. L. Bell, E. A. Hirst, R. A. Corwin, P. E. Hong, K. C. Howell, B. Barden, and R. Wilson, "Genesis Mission Design," *American Institute of Aeronautics and Astronautics, Inc*, 1998.

42. R. W. Farquhar, "The Flight of ISEE-3/ICE: Origins, Mission history, and a Legacy," *AIAA/AAS Astrodynamics Specialist Conference and Exhibit*, no. AIAA-1998-4464, 1998.
43. H. J. Kramer, "ISEE-3/ICE (International Cometary Explorer) Mission," 2002. [Online]. Available: <https://directory.eoportal.org/web/eoportal/satellite-missions/i/isee-3> [Date Accessed: 2015-04-11]
44. B. Fleck, "SOHO Fact Sheet," 2003. [Online]. Available: [http://sohowww.nascom.nasa.gov/about/docs/SOHO\\_Fact\\_Sheet.pdf](http://sohowww.nascom.nasa.gov/about/docs/SOHO_Fact_Sheet.pdf) [Date Accessed: 2015-04-04]
45. "SOHO to Give Early Warning of Radiation Storms," 2008. [Online]. Available: [http://www.nasa.gov/mission\\_pages/soho/soho\\_radiation.html](http://www.nasa.gov/mission_pages/soho/soho_radiation.html) [Date Accessed: 2015-04-11]
46. E. R. Christian and A. J. Davis, "Advanced Composition Explorer (ACE) Mission Overview," 2012. [Online]. Available: [http://www.srl.caltech.edu/ACE/ace\\_mission.html](http://www.srl.caltech.edu/ACE/ace_mission.html) [Date Accessed: 2015-04-14]
47. "Planck: Exploring the Birth of Our Universe," 2009. [Online]. Available: [http://www.nasa.gov/mission\\_pages/planck/overview.html](http://www.nasa.gov/mission_pages/planck/overview.html) [Date Accessed: 2015-04-12]
48. "Hiten," 2014. [Online]. Available: <http://nssdc.gsfc.nasa.gov/nmc/spacecraftDisplay.do?id=1990-007A> [Date Accessed: 2015-04-21]
49. K. Uesugi, "Results of the Muses-a "HITEN" Mission," *The Institute of Space and Astronautical Science*, p. 1, 1996.
50. C. Conley, "Low Energy Transit Orbits in the Restricted Three-Body Problem," *SIAM Journal Of Applied Mathematics*, vol. 16, no. 4, p. 732, 1968.
51. K. Davis, R. Anderson, and G. Born, "Preliminary Study of Geosynchronous Orbit Transfers from LEO using Invariant Manifolds," *The Journal of the Astronautical Sciences*, pp. 1–19, 2011.
52. S. Wiggins, *Introduction to Applied Nonlinear Dynamical Systems and Chaos*. New York, NY: Inc, Springer-Verlag New York, 1990.
53. T. M. Vaquero Escribano, *Spacecraft Transfer Trajectory Design Exploiting Resonant Orbits in Multi-body Environments*, Dissertation, Purdue University, 2013. [Online]. Available: [https://engineering.purdue.edu/people/kathleen.howell.1/Publications/Dissertations/2013\\_Vaquero.pdf](https://engineering.purdue.edu/people/kathleen.howell.1/Publications/Dissertations/2013_Vaquero.pdf)
54. B. T. Barden, *Using Stable Manifolds to Generate Transfers in the Circular Restricted Problem of Three Bodies*, Thesis, Purdue University, 1994.

[Online]. Available: [https://engineering.purdue.edu/people/kathleen.howell.1/Publications/Masters/1994\\_Barden.pdf](https://engineering.purdue.edu/people/kathleen.howell.1/Publications/Masters/1994_Barden.pdf)

55. G. Gomez, A. Jorba, J. Masdemont, and C. Simo, "Study of the Transfer From the Earth to a Halo Orbit Around the Equilibrium Point L1," *Celestial Mechanics and Dynamical Astronomy*, vol. 56, no. 4, pp. 541–562, 1993.
56. B. Marchand, *Temporary Satellite Capture of Short-Period Jupiter Family Comets From the Perspective of Dynamical Systems*, Thesis, Purdue University, 2000.
57. R. L. Anderson, *Low Thrust Trajectory Design for Resonant Flybys and Captures Using Invariant Manifolds*, Dissertaion, University of Colorado, 2005.
58. D. Doody, "Interplanetary Trajectories," 2015. [Online]. Available: <https://solarsystem.nasa.gov/basics/bsf4-1.php> [Date Accessed: 2016-01-02]
59. J. Moltzan, "2013 Starship Congress Keynote Speaker Announcement Dr. Michael A. Minovitch: On the Possibility of Achieving Interstellar Space Travel at Near Optical Velocities," 2013.
60. N. J. Strange and J. M. Longuski, "Graphical Method for Gravity-Assist Trajectory Design," *Journal of Spacecraft and Rockets*, vol. 39, no. 1, pp. 9–16, 2002.
61. M. W. Lo and J. S. Parker, "Unstable Resonant Orbits near Earth and Their Role in Planetary Missions," *AIAA/AAS Astrodynamics Specialist Conference*, no. August, pp. 1–29, 2004.
62. D. D. Garber, *Application of the Fundamental Equation to Celestial Mechanics and Astrodynamics*, Dissertation, University of Southern California, 2012.
63. G. Lantoine, R. P. Russell, and S. Campagnola, "Optimization of Low-Energy Resonant Hopping Transfers Between Planetary Moons," *Acta Astronautica*, vol. 68, no. 7, pp. 1361–1378, 2011.
64. T. M. Vaquero Escribano and K. C. Howell, "Leveraging Resonant-Orbit Manifolds to Design Transfers Between Libration-Point Orbits," *Journal of Guidance, Control, and Dynamics*, vol. 37, no. 4, pp. 1143–1157, 2014.
65. R. L. Anderson and M. W. Lo, "Spatial Approaches to Moons from Resonance Relative to Invariant Manifolds," *Acta Astronautica*, vol. 105, no. 1, pp. 355–372, 2014.
66. C. Murray and S. Dermott, *Solar System Dynamics*. New York, NY: Cambridge University Press, 1999.
67. C. Marchal, *The Three-Body Problem*. New York, NY: Elsevier Science Publishing Company Inc., 1990.

68. L. O. Chua and T. S. Parker, *Practical Numerical Algorithms for Chaotic Systems*. New York, NY: Springer-Verlag New York Inc., 1989.
69. C. Froeschlé, “Numerical Study of Dynamical Systems with Three Degrees of Freedom: I. Graphical Displays of Four-Dimensional Sections,” *Astronomy and Astrophysics*, vol. 4, pp. 115–128, 1970.
70. G. Gómez, W. Koon, and M. Lo, “Invariant Manifolds, the Spatial Three-Body Problem and Space Mission Design,” *AIAA/AAS Astrodynamics Specialist Conference*, no. 301, 2001.
71. W. S. Koon, M. W. Lo, J. E. Marsden, and S. D. Ross, “Resonance and Capture of Jupiter Comets,” *Celestial Mechanics and Dynamical Astronomy*, vol. 81, pp. 27–38, 2001.
72. K. C. Howell and D. Craig Davis, “Trajectory Evolution in the Multi-Body Problem with Applications in the Saturnian System,” *Acta Astronautica*, vol. 69, pp. 1038–1049, 2011. [Online]. Available: [https://www.researchgate.net/publication/228576819\\_Trajectory\\_evolution\\_in\\_the\\_multi-body\\_problem\\_with\\_applications\\_in\\_the\\_Saturnian\\_System](https://www.researchgate.net/publication/228576819_Trajectory_evolution_in_the_multi-body_problem_with_applications_in_the_Saturnian_System)
73. A. F. Haapala, *Trajectory Design in the Spatial Circular Restricted Three-Body Problem Exploiting Higher-Dimensional Poincare Maps*, Dissertation, Purdue University, 2014. [Online]. Available: [https://engineering.purdue.edu/people/kathleen.howell.1/Publications/Dissertations/2014\\_Haapala.pdf](https://engineering.purdue.edu/people/kathleen.howell.1/Publications/Dissertations/2014_Haapala.pdf)
74. M. Hénon, “Numerical Exploration of the Restricted Three-Body Problem,” *The Theory of Orbits in the Solar System and in Stellar Systems*, pp. 157–169, 1964.
75. B. F. Villac and D. J. Scheeres, “On the Concept of Periapsis in Hills Problem,” *Celestial Mechanics and Dynamical Astronomy*, vol. 90, no. January 2016, pp. 165–178, 2004.
76. B. F. Villac and D. J. Scheeres, “Escaping Trajectories in the Hill Three-Body,” *Journal of Guidance, Control, and Dynamics*, vol. 26, no. 2, pp. 224–232, 2003.
77. M. Paskowitz and D. Scheeres, “Robust Capture and Transfer Trajectories for Planetary Satellite Orbiters,” *Journal of Guidance, Control, and Dynamics*, vol. 29, no. 2, pp. 342–353, 2006.
78. A. F. Haapala and K. C. Howell, “Representations of Higher-Dimensional Poincaré Maps with Applications to Spacecraft Trajectory Design,” *Acta Astronautica*, no. 96, pp. 23–41, 2014. [Online]. Available: [https://engineering.purdue.edu/people/kathleen.howell.1/Publications/Journals/2014\\_AA\\_HaaHow.pdf](https://engineering.purdue.edu/people/kathleen.howell.1/Publications/Journals/2014_AA_HaaHow.pdf)

79. D. Craig Davis, *Multi-Body Trajectory Design Strategies Based on Periapsis Poincare Maps*, Dissertation, Purdue University, 2011. [Online]. Available: [https://engineering.purdue.edu/people/kathleen.howell.1/Publications/Dissertations/2011\\_CraigDavis.pdf](https://engineering.purdue.edu/people/kathleen.howell.1/Publications/Dissertations/2011_CraigDavis.pdf)
80. K. C. Howell and D. Craig Davis, “Long-Term Evolution of Trajectories Near the Smaller Primary in the Restricted Problem,” *Advances in the Astronautical Sciences*, vol. 10, no. 184, pp. 1–20, 2010. [Online]. Available: [https://www.researchgate.net/publication/265004183\\_Long-term-evolution\\_of\\_trajectories\\_near\\_the\\_smaller\\_primary\\_in\\_the\\_restricted\\_problem](https://www.researchgate.net/publication/265004183_Long-term-evolution_of_trajectories_near_the_smaller_primary_in_the_restricted_problem)
81. K. C. Howell, D. C. Davis, and A. F. Haapala, “Application of Periapse Maps for the Design of Trajectories Near the Smaller Primary in Multi-Body Regimes,” *Mathematical Problems in Engineering*, vol. 2012, pp. 1–22, 2012. [Online]. Available: <http://www.hindawi.com/journals/mpe/2012/351759/>
82. J. Lambers, “Minimum Norm Solutions of Underdetermined Systems,” in *MAT 419/519 Lecture 15*. University of Southern Mississippi, 2011.
83. J. Davis, “Of Inclinations and Azimuths,” 2012. [Online]. Available: <http://www.planetary.org/blogs/guest-blogs/jason-davis/3450.html> [Date Accessed: 2016-02-11]
84. E. W. Weisstein, “Moon,” 1996. [Online]. Available: <http://scienceworld.wolfram.com/astronomy/Moon.html> [Date Accessed: 2016-02-11]
85. J. P. L. S. S. Dynamics, “JPL HORIZONS Web-Interface.” [Online]. Available: <http://ssd.jpl.nasa.gov/horizons.cgi> [Date Accessed: 2016-01-20]
86. “XMM-Newton Fact Sheet,” 2015. [Online]. Available: [http://www.esa.int/Our\\_Activities/Space\\_Science/XMM-Newton\\_factsheet](http://www.esa.int/Our_Activities/Space_Science/XMM-Newton_factsheet) [Date Accessed: 2015-09-01]
87. “Integral Fact Sheet,” 2015. [Online]. Available: <http://sci.esa.int/integral/47360-fact-sheet/> [Date Accessed: 2015-09-01]
88. ITPROSTAR, “INTEGRAL Orbit Information,” 2016. [Online]. Available: <http://www.n2yo.com/satellite/?s=27540> [Date Accessed: 2016-03-10]
89. “XMM-Newton Orbit/Navigation,” 2011. [Online]. Available: <http://sci.esa.int/xmm-newton/31349-orbit-navigation/> [Date Accessed: 10 March 2016]
90. C. Bergin and W. Graham, “Soyuz 2-1B Launches EKS-1 to Upgrade Russian Early Warning System,” 2015.
91. M. J. Valtonen, “The Few Body Problem : Proceedings of the 96th Colloquium of the International Astronomical Union Abstract,” in *Astrophysics and Space Science Library*, Turku, Finland, jun 1987, pp. 1–2.



REPORT DOCUMENTATION PAGE					Form Approved OMB No. 0704-0188	
<p>The public reporting burden for this collection of information is estimated to average 1 hour per response, including the time for reviewing instructions, searching existing data sources, gathering and maintaining the data needed, and completing and reviewing the collection of information. Send comments regarding this burden estimate or any other aspect of this collection of information, including suggestions for reducing this burden to Department of Defense, Washington Headquarters Services, Directorate for Information Operations and Reports (0704-0188), 1215 Jefferson Davis Highway, Suite 1204, Arlington, VA 22202-4302. Respondents should be aware that notwithstanding any other provision of law, no person shall be subject to any penalty for failing to comply with a collection of information if it does not display a currently valid OMB control number. <b>PLEASE DO NOT RETURN YOUR FORM TO THE ABOVE ADDRESS.</b></p>						
1. REPORT DATE (DD-MM-YYYY)		2. REPORT TYPE		3. DATES COVERED (From — To)		
24-03-2016		Master's Thesis		Aug 2014 - Mar 2016		
4. TITLE AND SUBTITLE				5a. CONTRACT NUMBER		
Military Applications of High-Altitude Satellite Orbits in a Multi-Body Dynamical Environment Using Numerical Methods and Dynamical Systems Theory				5b. GRANT NUMBER		
				5c. PROGRAM ELEMENT NUMBER		
				5d. PROJECT NUMBER		
6. AUTHOR(S)				5e. TASK NUMBER		
Wilmer, Meredith M., 2d Lt, USAF				5f. WORK UNIT NUMBER		
7. PERFORMING ORGANIZATION NAME(S) AND ADDRESS(ES)				8. PERFORMING ORGANIZATION REPORT NUMBER		
Air Force Institute of Technology Graduate School of Engineering and Management (AFIT/EN) 2950 Hobson Way WPAFB OH 45433-7765				AFIT-ENY-MS-16-M-247		
9. SPONSORING / MONITORING AGENCY NAME(S) AND ADDRESS(ES)				10. SPONSOR/MONITOR'S ACRONYM(S)		
AFRL Space Vehicles Directorate 3550 Aberdeen Avenue SE Kirtland AFB NM 87117-5776 POC: N/A				AFRL/RV		
				11. SPONSOR/MONITOR'S REPORT NUMBER(S)		
Principal DoD Space Advisor Staff 1670 Air Force Pentagon Washington DC 20330-1670C 703-693-5799 POC: Maj Stuart A. Stanton						
12. DISTRIBUTION / AVAILABILITY STATEMENT						
Distribution Statement A. Approved for public release; Distribution Unlimited.						
13. SUPPLEMENTARY NOTES						
This material is declared a work of the U.S. Government and is not subject to copyright protection in the United States.						
14. ABSTRACT						
<p>The circular restricted three-body problem (CR3BP) is a simplified dynamical model for a satellite under the gravitational influence of both the Earth and the Moon, maintaining closer fidelity to the gravitational environment experienced by a high-altitude Earth-orbiting spacecraft than modeling in the Earth-satellite two-body problem. Resonant orbit arcs are used to determine an initial guess to input into an algorithm that computes a trajectory solution with specific design requirements and constraints. A test case uses this method to compute a lunar "fly-by" transfer solution requiring less <math>\Delta V</math> than two-body transfer methods and offers an unusual pathway that adds an "unpredictability" element to the design. Multiple-shooting and pseudo-arclength continuation methods are used to target trajectories and compute periodic orbits in the CR3BP to within a satisfactory tolerance. Invariant manifolds from an unstable periodic orbit around a libration point in the Earth-Moon system are used as unpredictable transfer pathways when traveling from one Earth orbit to another, utilizing a map-based design process. Periapsis Poincaré maps are also constructed to characterize the observed behaviors of orbits in the Earth-Moon system for a specified time, demonstrating utility for both designing trajectories with desired end characteristics and predicting an unknown spacecraft's future behavior.</p>						
15. SUBJECT TERMS						
Orbital transfer, Multi-body dynamical environment, Manifold, Dynamical Systems Theory, Lunar fly-by, Poincaré map, Periapsis, Circular restricted three-body problem, Resilience, Predictability						
16. SECURITY CLASSIFICATION OF:			17. LIMITATION OF ABSTRACT	18. NUMBER OF PAGES	19a. NAME OF RESPONSIBLE PERSON	
a. REPORT	b. ABSTRACT	c. THIS PAGE			Maj Christopher D. Geisel, Ph.D., AFIT/ENY	
U	U	U	UU	217	19b. TELEPHONE NUMBER (include area code)	
					(937)255-3636 x4237; christopher.geisel@afit.edu	